



# UNIVERSITAT DE BARCELONA

## Control of active flows through soft interfaces

Pau Guillamat Bassedas

**ADVERTIMENT.** La consulta d'aquesta tesi queda condicionada a l'acceptació de les següents condicions d'ús: La difusió d'aquesta tesi per mitjà del servei TDX ([www.tdx.cat](http://www.tdx.cat)) i a través del Dipòsit Digital de la UB ([diposit.ub.edu](http://diposit.ub.edu)) ha estat autoritzada pels titulars dels drets de propietat intel·lectual únicament per a usos privats emmarcats en activitats d'investigació i docència. No s'autoritza la seva reproducció amb finalitats de lucre ni la seva difusió i posada a disposició des d'un lloc aliè al servei TDX ni al Dipòsit Digital de la UB. No s'autoritza la presentació del seu contingut en una finestra o marc aliè a TDX o al Dipòsit Digital de la UB (framing). Aquesta reserva de drets afecta tant al resum de presentació de la tesi com als seus continguts. En la utilització o cita de parts de la tesi és obligat indicar el nom de la persona autora.

**ADVERTENCIA.** La consulta de esta tesis queda condicionada a la aceptación de las siguientes condiciones de uso: La difusión de esta tesis por medio del servicio TDR ([www.tdx.cat](http://www.tdx.cat)) y a través del Repositorio Digital de la UB ([diposit.ub.edu](http://diposit.ub.edu)) ha sido autorizada por los titulares de los derechos de propiedad intelectual únicamente para usos privados enmarcados en actividades de investigación y docencia. No se autoriza su reproducción con finalidades de lucro ni su difusión y puesta a disposición desde un sitio ajeno al servicio TDR o al Repositorio Digital de la UB. No se autoriza la presentación de su contenido en una ventana o marco ajeno a TDR o al Repositorio Digital de la UB (framing). Esta reserva de derechos afecta tanto al resumen de presentación de la tesis como a sus contenidos. En la utilización o cita de partes de la tesis es obligado indicar el nombre de la persona autora.

**WARNING.** On having consulted this thesis you're accepting the following use conditions: Spreading this thesis by the TDX ([www.tdx.cat](http://www.tdx.cat)) service and by the UB Digital Repository ([diposit.ub.edu](http://diposit.ub.edu)) has been authorized by the titular of the intellectual property rights only for private uses placed in investigation and teaching activities. Reproduction with lucrative aims is not authorized nor its spreading and availability from a site foreign to the TDX service or to the UB Digital Repository. Introducing its content in a window or frame foreign to the TDX service or to the UB Digital Repository is not authorized (framing). Those rights affect to the presentation summary of the thesis as well as to its contents. In the using or citation of parts of the thesis it's obliged to indicate the name of the author.

DOCTORAT EN NANOCIÈNCIES



UNIVERSITAT DE  
BARCELONA

# Control of active flows through soft interfaces

Pau Guillamat Bassedas

Advisors: Drs. J. Ignés Mullol<sup>1,2</sup> and F. Sagués Mestre<sup>1,2</sup>

Tutor: Dr. J. Ignés Mullol

<sup>1</sup>Departament de Ciència dels Materials i Química Física, Universitat de Barcelona.

<sup>2</sup>Institut de Nanociència i Nanotecnologia de la Universitat de Barcelona (IN<sup>2</sup>UB).

The research described in this thesis has been carried out at the group “Self-Organized Complexity and Self-Assembled Materials” of the Department of Materials Science and Physical Chemistry of the University of Barcelona, and part of the Institute of Nanotechnology of the same university (IN<sup>2</sup>UB).

The work has been financially supported by the Generalitat de Catalunya through a FI-DGR pre-doctoral fellowship and MINECO Project FIS 2013-41144P.

# Contents

Abstract .....	7
List of figures.....	9
List of videos .....	13
List of abbreviations and symbols.....	17
Preface .....	19
Chapter 1. Introduction .....	21
1. Liquid crystals.....	23
1.1. Main classification .....	23
1.1.1. Colloidal Liquid Crystals .....	24
1.2. Liquid crystal phases .....	24
1.3. Order in liquid crystals .....	26
1.4. Anisotropy: main manifestations .....	27
1.4.1. Dielectric anisotropy.....	28
1.4.2. Diamagnetic anisotropy .....	29
1.4.3. Optical anisotropy: Birefringence.....	29
1.4.4. Rheological anisotropy: The shear viscosity .....	30
1.5. Distortions in nematic liquid crystals .....	31
1.5.1. Long-range distortions: Free energy .....	31
1.5.2. LCs at interfaces: anchoring .....	32
1.5.3. Application of external fields: The Fréedericksz transition.....	33
1.5.4. Short-range distortions: Topological defects .....	34
1.5.5. Spherical inclusions in nematic liquid crystals .....	37



1.6.	Structure of the smectic-A phase: effects on rheology .....	38
2.	Active Matter.....	41
2.1.	Main observations and experiments.....	41
2.1.1.	Living Active Matter systems .....	41
2.1.2.	Artificial Active Matter.....	46
2.2.	Active liquid crystals .....	50
2.2.1.	Active defects and meso-scale turbulence.....	51
2.2.2.	Our experimental system: The Active Nematic .....	53
2.3.	Alteration and control of active flows: state of the art.....	55
3.	Materials and methods .....	61
3.1.	The active gel .....	61
3.1.1.	Purification of tubulin .....	61
3.1.2.	Polymerization of microtubules.....	61
3.1.3.	Expression of kinesin .....	62
3.1.4.	Clustering of molecular motors .....	62
3.1.5.	ATP hydrolysis and regeneration system .....	62
3.1.6.	Active gel assembly.....	63
3.2.	The liquid crystals.....	65
3.2.1.	Rheological measurements of 8CB .....	66
3.3.	Experimental setups.....	67
3.3.1.	Open cell.....	67
3.3.2.	LC flow cell.....	68
3.4.	Active emulsions .....	68
3.5.	Surface treatments.....	68

3.5.1.	Polymeric brush .....	68
3.5.2.	Hydrophobization by self-assembled monolayers of silanes.....	68
3.5.3.	Polymeric coatings .....	70
3.6.	Surfactants .....	70
3.6.1.	Preparation of lipid vesicles.....	71
3.7.	Application of external fields and temperature control.....	73
3.7.1.	Electric fields .....	73
3.7.2.	Magnetic fields.....	73
3.7.3.	Temperature control.....	73
3.8.	Imaging .....	74
3.8.1.	Polarized-light microscopy .....	74
3.8.2.	Fluorescence microscopy.....	75
3.8.3.	Confocal laser-scanning microscopy.....	76
3.9.	Image and Data analysis .....	77
3.9.1.	Image velocimetry.....	77
3.9.2.	Particle tracking.....	77
3.9.3.	Vorticity and Okubo-Weiss fields .....	77
3.9.4.	Active nematic director field .....	78
3.9.5.	Spatial autocorrelation functions .....	79
4.	Main goal and objectives .....	81
Chapter 2.	Interfacing the active nematic with isotropic oils.....	83
Chapter 3.	Control of active flows with addressable soft interfaces .....	97
Chapter 4.	Active droplets in nematic liquid crystals.....	113

Chapter 5. Closing remarks .....	125
1. Conclusions .....	127
2. Open questions .....	128
3. Future perspectives.....	129
List of references.....	131
List of Publications.....	145
Resum .....	147
Acknowledgements.....	163

# Abstract

Groups of animals, bacterial colonies, tissues and assemblies of subcellular extracts are some examples of experimental systems studied in the field of Active Soft Matter. All of them are composed of autonomous self-propelled units that consume and transform energy to generate mechanical work. The interaction between these motile units lead to the emergence of cooperative spatiotemporal patterns, not observed in complex fluids in equilibrium. Despite the morphology and dynamics of these systems are being studied in detail, there is still absence of true control capabilities, which could bring new possibilities in the use or application of active flows. To this end, this work has essentially focused on the coupling of an active material with flow-damping soft interfaces.

The experimental system used here is an active gel based on a mixture of cytoskeletal proteins, created in the laboratory of Z. Dogic from Brandeis University (MA, USA) in 2012. In brief, ATP-fuelled kinesin motor clusters crosslink and drive bundled microtubules, giving rise to an active network of biofilaments that develops far from thermodynamic equilibrium. The active gel can also self-organize at soft interfaces, forming a quasi-2d active nematic liquid crystal, which features spontaneous turbulent-like flows. In this thesis, first, we report experimental evidence of the existence of strong hydrodynamic coupling at the oil/water interface, where the active nematic resides, and the influence of the rheological properties of the oil phase. By changing the viscosity of the contacting oily fluid, we alter the morphology and dynamics of the active nematic, which we have characterized. In addition, in collaboration with M. C. Marchetti and S. Shankar from Syracuse University (NY, USA), we have fitted specific data to a hydrodynamical model in order to extract an estimate value for the viscosity of the active material. Second, based on these observations, and with the objective of steering the active flows, we impose viscosity patterns at the interface. To this purpose, we use a thermotropic liquid crystal, which self-assembles in well-known structures with marked anisotropic viscosity, externally- and *in situ*-tuneable by means of temperature and/or external fields. Under such rheological constraints, the active nematic flows are commanded at will, rapidly organizing either in localized rotating swirls or parallel stripes of aligned microtubule bundles. Through this process, we have also had the opportunity to study the interaction between active and passive nematic liquid crystals. The latter, in this case, serve as reporters of the active flows. Finally, we emulsify the active gel in different fluids to create droplets with an active nematic spherical shell, which develops in geometrically and topologically constrained conditions. Due to the confinement restrictions, the active nematic develops strikingly periodic dynamics that transmit coherent flows into the confining phase. Here, with our experiments and simulations carried out by M. Ravnik and Ž. Kos from the University of Ljubljana (Slovenia), we study emulsions of droplets with an active nematic shell dispersed in thermotropic nematic liquid crystals. In particular, we focus on the interaction between active flows and the usually static topological defects induced around inclusions in liquid crystals.

To conclude, this work not only increases our fundamental knowledge of both thermotropic (passive) and active nematic liquid crystals but it serves as a starting platform to explore the interaction between these two fluid ordered analogues at the interface. Special emphasis will be put on the implementation of anisotropic patterns at interfaces as it has demonstrated to be key towards controlling active flows.



# List of figures

- Fig. 1. The liquid crystalline phase. Page 23.
- Fig. 2. Structure of nematogens in thermotropic liquid crystals. Page 24.
- Fig. 3. Liquid crystal phases. Page 25.
- Fig. 4. Relationship between Spherical and Cartesian coordinates. Page 26.
- Fig. 5. The distribution function  $f(\theta)$  for a system of cylinders in a nematic phase. Page 26.
- Fig. 6. Graphical representation of anisotropy for a general physical property  $P$  in temperature-dependent liquid crystals. Page 27.
- Fig. 7. Interaction between liquid crystal molecules and an electric field. Page 28.
- Fig. 8. Birefringent crystals between crossed polarizers. Page 30.
- Fig. 9. Fundamental geometries for viscosity measurements. Page 30.
- Fig. 10. Long-range distortions of nematic liquid crystals. Page 31.
- Fig. 11. Orientation of nematic liquid crystal constituents near a solid surface. Page 32.
- Fig. 12. The Fréedericksz transition. Page 33.
- Fig. 13. Defects in nematic liquid crystals. Page 34.
- Fig. 14. The Schlieren texture. Page 35.
- Fig. 15. Wall line defects. Page 36.
- Fig. 16. Liquid crystal defects around spherical inclusions. Page 38.
- Fig. 17. Schematic representation of the smectic-A phase. Page 38.
- Fig. 18. Structure of toroidal focal conic domains. Page 39.
- Fig. 19. The bookshelf texture. Page 40.
- Fig. 20. Drone footage of a sheep spiral. Page 42.
- Fig. 21. A typical starling flock and its 3D reconstruction. Page 42.
- Fig. 22. Dynamic clusters of bacteria. Page 43.
- Fig. 23. Migration of cells within a confluent monolayer. Page 43.
- Fig. 24. Collective patterns in cytoplasmic streaming in an oocyte of *Drosophila melanogaster*. Page 44.
- Fig. 25. Microtubule structure. Page 44.
- Fig. 26. Dynamic instability of microtubules. Page 45.
- Fig. 27. Self-organization of light-activated self-propelled colloids. Page 46.
- Fig. 28. Schematic of a motility assay and phase behaviour as a function of the filament density. Page 47.
- Fig. 29. Self-organization of microtubules and kinesin motor complexes. Page 48.


- Fig. 30. Different large-scale patterns formed through self-organization of microtubules and motors. Page 48.
- Fig. 31. Active microtubule networks. Page 50.
- Fig. 32. Active nematic of vibrated rods. Page 51.
- Fig. 33. Turbulence in a bacterial bath. Page 52.
- Fig. 34. Active nematic liquid crystal. Page 53.
- Fig. 35. Dynamics of 2D streaming nematics confined to fluid interfaces. Page 54.
- Fig. 36. Flocks of rolling colloids through obstacle-decorated channels. Page 56.
- Fig. 37. Tissue flows controlled by geometric constraints. Page 57.
- Fig. 38. Defect dynamics of an active nematic film on the surface of a spherical vesicle. Page 57.
- Fig. 39. Unipolar circular flows of bacteria in the periodic pattern of defects. Page 59.
- Fig. 40. Skeletal formula of deprotonated Adenosine triphosphate (ATP). Page 62.
- Fig. 41. Regeneration of ATP by pyruvate kinase (PK). Page 63.
- Fig. 42. Skeletal formula of 4-pentyl-4'cyanobiphenyl (5CB). Page 65.
- Fig. 43. Skeletal formula of 4-octyl-4'cyanobiphenyl (8CB). Page 65.
- Fig. 44. Rheology measurements for 8CB. Page 66.
- Fig. 45. Schematic representation of the experimental setup. Page 67.
- Fig. 46. Formula of DMOAP. Page 69.
- Fig. 47. Formula of a fluoroctylsilane, the main ingredient of Aquapel. Page 69.
- Fig. 48. Formula of Pluronic. Page 71.
- Fig. 49. Formula of Tween-80. Page 71.
- Fig. 50. Formulas of the employed phospholipids. Page 72.
- Fig. 51. Structure for the assembly of the array of magnets. Page 73.
- Fig. 52. Polarized-light microscopy. Page 74.
- Fig. 53. Custom-built inverted fluorescence microscope. Page 75.
- Fig. 54. Principal light pathways in confocal laser-scanning microscopy. Page 76.
- Fig. 55. Confocal micrographs in different imaging modes. Page 76.
- Fig. 56. Parametric representation of a line in Cartesian coordinates. Page 78.
- Fig. 57. Active nematic director field. Page 78.
- Fig. 58. Active nematic contacting oils with different viscosities. Page 87.
- Fig. 59. Relation between defect density and defect speed. Page 88.
- Fig. 60. Speed and defect density variations with activity. Page 90.
- Fig. 61. Defect density variation with a relation between activity and speed. Page 90.
- Fig. 62. Formation of vortices in high viscosity oils. Page 91.

- Fig. 63. Structure of the active turbulent flow. Page 92.
- Fig. 64. Director field of the active nematic. Page 93.
- Fig. 65. Spatial correlation functions. Page 93.
- Fig. 66. Decay lengths for active nematics in contact with different oil viscosities. Page 94.
- Fig. 67. Active flows reported by a nematic liquid crystal. Page 101.
- Fig. 68. Self-assembly of the active nematic in contact with the patterned interface. Page 102.
- Fig. 69. Soft confinement of the active nematic. Page 103.
- Fig. 70. Defect structure in active nematic swirls. Page 104.
- Fig. 71. Defect dynamics in active nematic swirls. Page 105.
- Fig. 72. Flows induced by active nematic swirls. Page 106.
- Fig. 73. Alignment of the active nematic with a magnetic field. Page 107.
- Fig. 74. Regular destabilization of the aligned active material via bending deformations. Page 108.
- Fig. 75. Oscillatory instability of the aligned active nematic. Page 108.
- Fig. 76. Active flow along self-organized lanes. Page 109.
- Fig. 77. Activity dependence of the self-organized flows. Page 110.
- Fig. 78. Defect trajectories in small active nematic shells. Page 117.
- Fig. 79. Active nematic shells in contact with a solid substrate. Page 117.
- Fig. 80. Interaction between active droplets of different sizes. Page 118.
- Fig. 81. Active nematic shell in a thermotropic nematic liquid crystal. Page 118.
- Fig. 82. Periodically-oscillating Saturn ring defects. Page 119.
- Fig. 83. Coupling of the active defect trajectories to the passive nematic. Page 120.
- Fig. 84. Activity-triggered Saturn ring configurations. Page 121.
- Fig. 85. Oscillation in hexadecapolar configurations. Page 122.
- Fig. 86. Boojum defects dragged by active flows. Page 123.
- Fig. 87. Distorted Saturn ring around an active nematic shell with irregular dynamics. Page 123.





# List of videos

Below, find a list of videos that complement some of the figures of this thesis. Figures with supplementary videos present the symbol  in their caption.

- **Video 1. The active nematic.** Fluorescence micrographs showing how an active gel based on fluorescent microtubules and molecular motor complexes develops in contact with a soft interface, where it is organized into a quasi-two-dimensional active nematic liquid crystal. Dark regions are devoid of microtubules and constitute topological defects. Images are 350  $\mu\text{m}$  wide.
- **Video 2. Morphologic and dynamical changes of the active nematic facing oils with different viscosities.** Fluorescence micrographs of the active nematic show an increase in the number of defects and a decrease of their speeds when in contact with increasing oil viscosities: 0.05, 5 and 300 Pa·s from left to right. Green spots indicate the location of  $+1/2$  defects.
- **Video 3. Structure of active turbulent flows.** (Top) Confocal fluorescence micrograph of the active nematic in the turbulent regime when in contact with an isotropic oil. (middle) Instantaneous flow field (vector plot) and computed Okubo-Weiss parameter field (density plot, arbitrary units), which is employed to determine the location and size of the vortices. (bottom) Binary image corresponding to the Okubo-Weiss field. Black regions are  $\text{OW} < 0$ .
- **Video 4. Flow coupling between active and passive nematics.** Polarization micrographs of a thermotropic liquid crystal featuring nematic phase and in contact with the active nematic.
- **Video 5. Active nematic swirls under toroidal focal conic domains (TFCDs).** Reflection confocal (left) and fluorescence (right) micrographs show how, in contact with big enough TFCDs, the active nematic organizes swirls, led by the circular patterns at the oil/water interface. Notice that small focal conics do not trigger the formation of swirls.
- **Video 6. Influence of activity on the defect trajectories of confined active nematics.** Reflection confocal micrographs with superimposed  $+1/2$  defect trajectories evidence the difference between circularly confined active nematics in different activity conditions. At the interface with domains of equal size, the active nematic with high activity (left) gives rise to more circulation of defects. Defects in the low-activity active nematic (right) are only scattered by the circular patterns at the interface.
- **Video 7. Preservation of the topological charge inside active nematic swirls.** The video contains superimposed images of fluorescence and reflection confocal microscopy centred on a large active nematic swirl. The active nematic (in green) is forced to follow the concentric direction of the TFCDs in the oil phase (grayscale), with an accumulated defect charge constrained by the topology of a full circle ( $s=+1$ ). The total number of defects may vary but this topological constraint is satisfied at all times.

- **Video 8. Bending instability in active nematic swirls.** Fluorescence micrographs show how rotation of  $+1/2$  defects organize a corona of MT bundles at the periphery of big swirls. Due to the extensile nature of the active material this ordered state is prone to suffer the bending instability, which disassembles the swirls by creating defects in the radial direction. New defects adapt to the rheological constraints at the interface and start to rotate again to reconstitute a new corona of MT bundles.
- **Video 9. Localized flows induced by active nematic swirls.** Bright field micrographs of TFCDs in contact with the active nematic with dispersed polystyrene spherical particles (1.7  $\mu\text{m}$ ). The superimposed trajectories evidence how the flows induced by the active nematic swirls effectively drag the particles towards the periphery of the interfacial domains in spiral trajectories. Notice that one of the tracers (near the centre of the TFCD and whose trajectory has been highlighted in green) moves in perfect circles. In this case, the tracer is moving adsorbed at the lamellar planes, which flow within the TFCD.
- **Video 10. Unidirectional alignment of the active nematic.** The normally turbulent active nematic dynamics is organized into unidirectional patterns of laminar flow by the indirect action of a magnetic field. Transition from the nematic (35 °C) to the smectic-A (25 °C) phase of the passive liquid crystal 8CB leads to the formation of a bookshelf configuration of the mesogen molecules under the influence of a homogeneous magnetic field (4 kG). The interface presents now strong uniaxial anisotropy of the shear stress, which forces the active nematic underneath. The biofilaments assemble now in stripes surrounded by defect lanes, which organize antiparallel flows along the direction of the less viscous axis, perpendicular to the magnetic field (horizontally oriented).
- **Video 11. *In-situ* rotation of the aligned active nematic.** The aligned active nematic spontaneously transits from laminar to turbulent flow upon melting 8CB into the nematic phase at 35 °C. We subsequently rotate the magnetic field by 90°, and reverse the phase transition back into the smectic-A phase. The active nematic re-establishes the aligned state following the new easy axis, at 90° from the initial configuration.
- **Video 12. Proliferation of  $+1/2$  defects during disruption of the aligned active nematic.** High magnification reflection confocal micrographs show the instabilities experienced by aligned active nematic. Bending deformations disrupt the aligned state by generating defects. Here, we highlight the position of  $+1/2$  defects during three consecutive disruptions of the laminar flow state. The experiment is performed with an ATP concentration of 140  $\mu\text{M}$ . Velocity oscillations are accompanied with the periodic onset of defect proliferation. Since shear stress is much higher in this direction, transversally moving defects are more densely packed and advance more slowly than those along the laminar flow lanes.
- **Video 13. Periodic disruption of the aligned active nematic.** Bend instability periodically appears in the aligned stripes between defect lanes. This mechanism releases the extensile stresses accumulated in the active nematic while causing a transversal flow that disrupts the

directional dynamics of the active phase. The instability gives rise to new defects that will either annihilate or incorporate into pre-existing defect lanes.

- **Video 14. Opposite unidirectional flows in the aligned active nematic.** Passive tracer particles are dragged along the defect lanes in antiparallel directions. Particle trajectories are highlighted in green and blue. When new defects proliferate, a transversal flow originates, making particles deviate from the original rectilinear trajectories and incorporate into pre-existing adjacent lanes, thus reversing their direction.
- **Video 15. Active shells in contact with solid surfaces.** Fluorescence micrographs show the robust rotational motion of an active droplet dispersed in a low-viscosity isotropic oil. The grey circle depicts the trajectory of the active droplet. Arrow heads indicate the sense of motion.
- **Video 16. Interaction between active droplets.** Fluorescence micrographs show how active droplets hydrodynamically interact with each other giving rise to random motions.
- **Video 17. Oscillatory dynamics of a Saturn ring defect.** (left) Polarization images of an active droplet surrounded by a Saturn ring defect, which is driven far from its equilibrium position. (right) Simulations reproduce the experimentally observed phenomenon. Blue regions depict the position of the active defects. Green arrows represent the velocity field.
- **Video 18. Saturn ring oscillations driven by active defects.** Fluorescence images of an active nematic shell (diameter,  $\sim 50 \mu\text{m}$ ) show how regular oscillations of the passive disclination defect are only attainable for specific trajectories of the active defects. Coloured lines indicate the trajectories of the active defects.
- **Video 19. Dynamic regimes of the Saturn ring.** Polarization micrographs of the same droplet (diameter,  $\sim 60 \mu\text{m}$ ) showing different dynamical states of the Saturn ring.
- **Video 20. Dynamic Hexadecapolar configuration.** Different active droplets featuring the hexadecapolar configuration in planar (left, bright-field microscopy) and homeotropic (right, polarization microscopy) far-fields. Both images are  $100 \mu\text{m}$  wide.
- **Video 21. Boojums dragged by active flows.** Bright-field micrographs showing a short oscillation of a double boojum defect configuration.
- **Video 22. Distorted Saturn ring configurations triggered in large droplets.** Polarization images of an active droplet of  $130 \mu\text{m}$  in diameter. Surrounding Saturn ring presents completely irregular dynamics.



# List of abbreviations and symbols

Below, find a list of abbreviations and symbols for important terms and concepts used in this thesis.

- $\Gamma_M$  – magnetic torque
- $Q_{ij}$  – tensorial order parameter
- $f_e$  – electric contribution to the free energy density
- $f_m$  – magnetic contribution to the free energy density
- $l_\alpha$  – active length scale
- $r_a$  – rate of defect annihilation
- $r_c$  – rate of defect creation
- $\varepsilon_a$  – dielectric anisotropy
- $L$  – extrapolation length
- $R_g$  – radius of gyration
- Re – Reynolds number
- SR – Saturn ring
- $\chi_a$  – diamagnetic anisotropy
- 5CB – 4-pentyl-4'-cyanobiphenyl (liquid crystal, nematic phase)
- 8CB – 4-octyl-4'-cyanobiphenyl (liquid crystal, nematic and smectic phases)
- ALC – active liquid crystal
- AN – active nematic
- ATP - adenosine triphosphate
- CB – cyanobiphenyl
- CLC – colloidal liquid crystal
- $\mathbf{D}$  – electric displacement
- $\mathbf{E}$  – electric field
- GTP - guanosine triphosphate
- $\mathbf{H}$  – magnetic field
- LC – liquid crystal
- LLC – lyotropic liquid crystal
- $\mathbf{M}$  - magnetization
- MT – microtubule
- $\mathbf{n}$  – director vector
- $\mathbf{n}(\mathbf{r})$  – director vector field
- OW – Okubo-Weiss parameter
- PEG – polyethylene glycol
- PFCD – parabolic focal conic domain
- R – optical retardance
- SmA – smectic-A phase
- SmC – smectic-C phase

- $T_c$  – clearing temperature (liquid crystal to isotropic phase)
- TFCD – toroidal focal conic domain
- $th$  – threshold value
- TLC – thermotropic liquid crystal
- $T_m$  – melting point
- UV – ultraviolet
- $W$  – anchoring strength coefficient
- $F$  – elastic free energy density
- $P$  – the pitch spacing in cholesterics
- $S$  – scalar order parameter
- $l$  – penetration length
- $n$  – number of defects
- $s$  – topological strength
- $v$  – speed of defects
- $\alpha$  – activity parameter
- $\gamma$  – rotational viscosity
- $\delta$  – Kronecker delta
- $\varepsilon$  – dielectric permittivity
- $\eta$  – viscosity coefficient
- $\theta$  – polar angle
- $\varphi$  – azimuthal angle
- $\chi$  – diamagnetic susceptibility
- $\omega$  - vorticity
- $K_i$  – elastic constant of liquid crystals.  $i=1, 2, 3$  for splay, bend and twist distortions, respectively

# Preface

This dissertation has been written on the basis of the experiments performed in the group “Self-Organized Complexity and Self-Assembled Materials” in the Department of Materials Science and Physical-Chemistry and in the Institute of Nanotechnology (IN<sup>2</sup>UB) of the University of Barcelona, in the period between September 2013 and April 2017. The research described herein has been conducted under the supervision of professors J. Ignés and F. Sagués.

The text has been structured in five main chapters. **Chapter 1** is an introduction to the fields of Liquid Crystals and Active Matter, including a section with the state-of-the-art strategies for control of active flows that contextualizes my research. At the end of this chapter, I have also included a Materials and methods section in which I present the protocols for the preparation and characterization of the experimental realizations. Following, **Chapter 2, 3** and **4** consist on a summary of our contributions to the field of Active Matter. They all include an introductory section, a summary of the obtained results, and conclusions. In **Chapter 5**, I expose closing remarks including general conclusions, open questions and future perspectives of this work.

Pau Guillamat  
April 2017





# **Chapter 1.**

# **Introduction**



---

# 1. Liquid crystals

Liquid Crystals (LCs) are viscous fluids that feature states of matter intermediate between isotropic liquids and crystalline solids [1–4]. Even though, macroscopically, they behave like ordinary liquids (they flow easily), LCs present some degree of internal order, which resembles the solid crystalline state (Fig. 1). For this reason, they are also called mesomorphic phases or mesophases [2]. The source of their properties lies on the fact that LCs are formed by anisometric units that interact with each other. This interaction enhances the orientational ordering of LC constituents, meaning that, on average, they will locally point in the same directions.

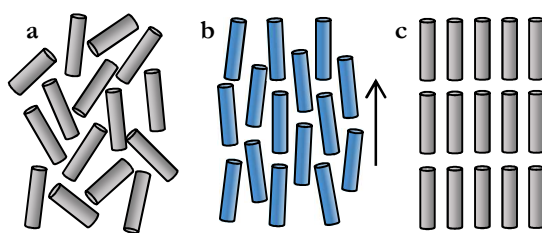


**Fig. 1. The liquid crystalline phase.** Rigid cylinders representing the configuration of (a) an isotropic liquid, with neither orientational nor positional order, (b) a liquid crystal, with orientational order and (c) a crystal, exhibiting both orientational and positional order. The arrow in (b) indicates the average orientation of the LC constituents.

Because of their internal order, LCs exhibit anisotropy in many physical properties, i.e. their values along and perpendicular to the preferred axis are not equivalent. The main manifestations of this anisotropy will be detailed in forthcoming sections.

## 1.1. Main classification

Depending on the nature of their constituents, LCs can be classified in two main categories: lyotropic and thermotropic.

Lyotropic LCs (LLCs) are based on either concentrated aqueous solutions of amphiphiles [5,6], aromatic compounds (chromonic LCs) [7] or polymers [8,9], or dense dispersions of anisometric colloids [10,11]. The degree of order in LLCs depends both on the concentration of their constituents, hence the prefix *lyo-* indicating dispersion or dissolution, and, secondarily, on temperature. In contrast to LLCs, thermotropic LCs (TLCs) are obtained by melting a crystalline solid, hence the prefix *thermo-*. They are oily substances composed of organic molecules, which within a certain temperature range (above the melting point,  $T_m$ , and below the clearing temperature,  $T_c$ ) self-assemble into liquid-like ordered phases.

Molecules forming TLCs usually share common structural features that enhance molecular ordering: most of them are elongated with a flexible tail and a central rigid core that contains flat segments, like benzene rings, that define the long axis of the molecules (Fig. 2a). In addition, LC molecules usually carry strong dipoles and easy polarizable groups, an important fact that will affect how these materials interact with external electromagnetic fields. Common examples of TLCs are 4,4'-azoxyanisole (PAA),

N-(4-Methoxybenzylidene)-4-butylaniline (MBBA), and cyanobiphenyl (CB) derivatives like 4-pentyl-4'-cyanobiphenyl (5CB) (Fig. 2*b*).

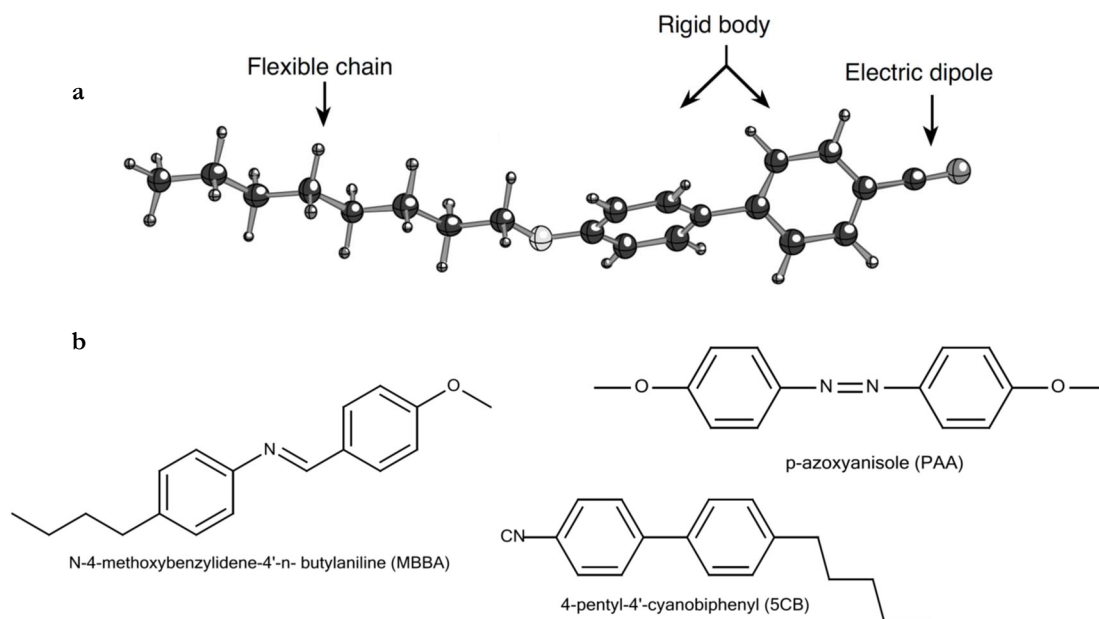


**Fig. 2. Structure of nematogens in thermotropic liquid crystals.** a) Basic structural features of TLC molecules. b) Chemical structure of the most representative nematic TLC molecules. PAA exhibits the nematic mesophase only at high temperatures, between 116 and 135°C, while MBBA is nematic from 20 to 47°C, thus facilitating experimentation. Cyanobiphenyl derivatives like 5CB, are more stable and LCs at room-temperature, and so they are widely used nowadays. Adapted from ref. [3].

### 1.1.1. Colloidal liquid crystals

As mentioned before, LLCs can be constituted of dense suspensions of anisometric colloids. In these case, the hard-core steric interactions between the constituents suffice to order them in thermal equilibrium [12]. Above a critical concentration, orientational entropy is sacrificed for gains in translational entropy, which increases due to the reduction in excluded volume. Therefore, crowding alone can drive the formation of colloidal liquid crystalline phases [10,13–15], which, differently from the others, are temperature-independent.

Together with TLCs, colloidal LCs (CLCs) have a great relevance in this thesis, as they set the basis for the emergence of experimental active matter.

## 1.2. Liquid crystal phases

The organization in LCs varies depending, basically, on the structure of their constituents, which can self-assemble into different mesophases that differ, essentially, on their symmetry [16]. The main LC phases are the nematic, the cholesteric, the smectic and the columnar:

- The nematic is the less ordered LC phase; its components only feature orientational order, which results from the tendency of its constituents to align with each other along a preferred direction (Fig. 3*a*). Although a certain amount of short-range order may exist as in ordinary liquids, nematics are

characterized by featuring only orientational order. Since nematogen building blocks are free to slide past one another, there is no long-range order in the positions of their centers of mass.

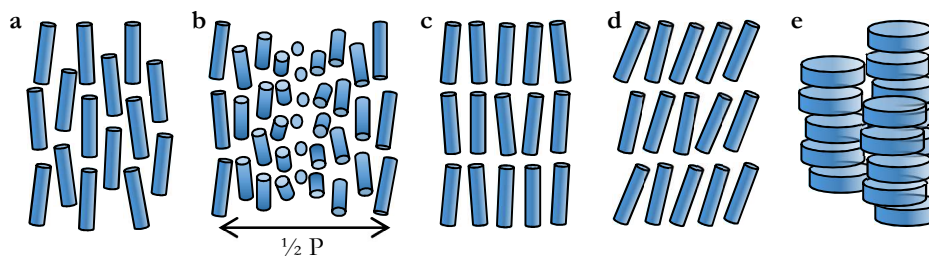


**Fig. 3. Liquid crystal phases.** The building blocks of the LCs are represented as rigid rods and disks. **a)** The nematic phase. The constituents tend to have the same alignment but their positions are not correlated. **b)** The cholesteric phase. The alignment of the constituents varies regularly along a direction perpendicular to the molecular axes, with a periodicity distance  $P/2$ . As in the nematic case, the positions of the constituents are not correlated. **c)** The smectic-A phase. The constituent units organize in planes perpendicular to the average constituents' axis. **d)** The smectic-C phase. The building blocks organize in planes, with the constituents tilted with respect of these planes. **e)** The columnar phase. Usually composed of disk-like objects that form cylindrical structures, which stack in regular arrays.

- The cholesteric phase, or chiral nematic phase, shares the basic features of the nematics, that is to say, long-range orientational order and short-range positional order. However, the constitutive units now are chiral, and the interaction between them leads to a variation of their orientation in a regular way throughout the medium. In particular, the units gradually rotate perpendicularly to their long axis giving rise to a periodic helical structure. The spacing within units separated by a full rotation of the orientation with respect to the twist axis is called the pitch ( $P$ ). Nevertheless, as half rotation is indistinguishable from a full rotation, the spatial period is one half of  $P$  (Fig. 3b).

Differently from the nematic and the cholesteric phases, the centres of gravity of the constituents of smectic and columnar phases present long-range order.

- In the smectic phase, the constitutive entities organize in layers with well-defined inter-layer spacing (one-dimensional order in three dimensions). Although different classes of smectic phases have been recognized [17], only the smectic-A (SmA) phase will be introduced, as it has been relevant for this work. In the SmA phase, the LC building blocks are aligned perpendicular to the layers, which can slide freely over one another (Fig. 3c). As a matter of fact, the ability of flowing in preferred directions confers a marked rheologically anisotropic behaviour to these materials, which will have a crucial role in Chapter 3.

- Finally, the columnar phase can be described as an array of liquid tubes as its constituents pack in columns that self-organize in periodic structures (two-dimensional order in three dimensions) (Fig. 3e). While nematic, cholesteric and smectic phases are usually enhanced in LCs constituted by elongated units (calamitic LCs), columnar phases are often found in LCs made of disk-like objects (discotic LCs).

Although most of the considerations below apply both to LLCs and TLCs, we will be generally considering TLCs and in particular nematics, as they represent the simplest phase for introducing the

most characteristic features of LCs, and are the most important for the purpose of this thesis. A lot of emphasis will be also given to the structures of smectic-A phase in following sections.

### 1.3. Order in liquid crystals

LCs feature lower symmetry than an isotropic fluid as their constituents tend to be parallel to some common axis. This can be defined by the unitary vector  $\mathbf{n}$ , which is called the director. Practically all the interesting phenomena arising from LCs involve the geometry and dynamics of this preferred axis, so it is useful to define a vector field  $\mathbf{n}(\mathbf{r})$  that gives its local orientation. Rigid cylinders are the simplest type of objects that allow to easily describe nematic behaviour. The axis of these cylinders is labelled by a unit vector  $\mathbf{a}$ . Then, we can define  $\mathbf{a}$  by its polar angles  $\theta$  and  $\phi$  (Fig. 4).

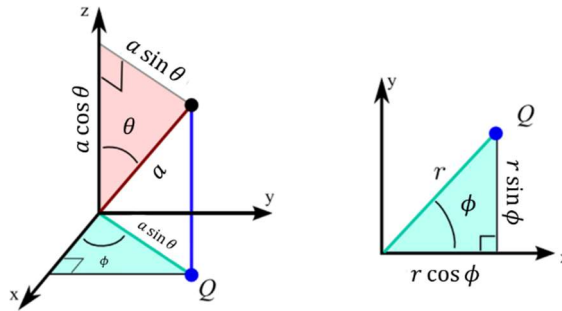


**Fig. 4. Relationship between Spherical and Cartesian coordinates.** As  $r = a \sin \theta$ , then  $a_x = \sin \theta \cos \phi$ ,  $a_y = \sin \theta \sin \phi$  and  $a_z = \cos \theta$ .

The state of alignment of the cylinders can be described by a distribution function  $f(\theta, \phi)d\Omega$ , which gives the probability of finding cylinders in a small solid angle  $d\Omega = \sin \theta d\theta d\phi$  around the direction  $(\theta, \phi)$ . As the nematic phase has a complete cylindrical symmetry about  $\mathbf{n}$ ,  $f(\theta, \phi)$  is independent of  $\phi$  and thus the distribution function takes the form  $f(\theta)$ , whose general appearance is shown in Fig. 5.

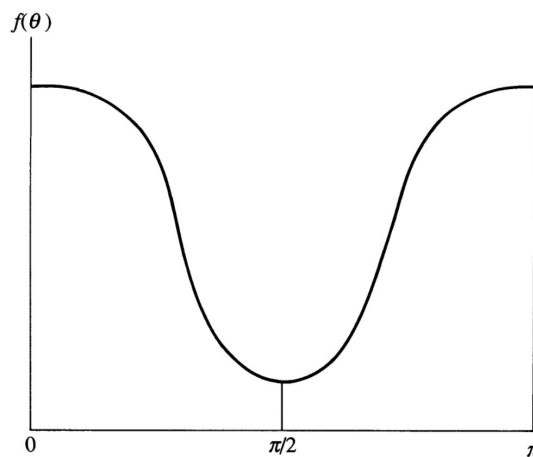


**Fig. 5. The distribution function  $f(\theta)$  for a system of cylinders in a nematic phase.** Here, we assume that the average orientation of  $\mathbf{n}$  is along the z axis.  $f(\theta)$  is large around  $\theta=0$  or  $\pi$ , i.e. for constituents parallel to  $\mathbf{n}$ , and it is small for  $\theta \sim \pi/2$ . Source: ref. [2].

In order to define an order parameter  $S$  for a nematic phase, which is non-zero for a LC but that vanishes, for symmetry reasons, in the isotropic phase, one can compare the orientation of every single constituent of the LC with the average preferred direction defined by  $\mathbf{n}$  [18]. For symmetry reasons, the first non-trivial moment of the distribution function is

$$S = \frac{1}{2} \langle 3\cos^2 \theta - 1 \rangle = \int_0^\pi f(\theta) \frac{1}{2} (3\cos^2 \theta - 1) \sin \theta \, d\theta,$$

If  $f(\theta)$  is peaked around  $\theta=0$  or  $\pi$  (parallel alignment),  $\cos^2 \theta = 1$  and  $S = 1$ . On the other hand, if  $f(\theta)$  is peaked around  $\theta = \pi/2$  (perpendicular alignment) then  $\cos^2 \theta = 0$  and  $S = -\frac{1}{2}$ . Finally, if the orientation were totally random (isotropic state),  $f(\theta)$  is independent of  $\theta$  and  $\langle \cos^2 \theta \rangle = \frac{1}{3}$ , giving  $S = 0$ . Thus  $S$  is a measure of the alignment [2].

From a more macroscopic point of view, we can consider that in an ideal nematic LC, the molecules are (on average) aligned along one common direction  $\pm \mathbf{n}$ . Here, we can define a tensorial order parameter that has the form

$$Q_{ij} = S(n_i n_j - \frac{1}{3} \delta_{ij})$$

Where  $S$  is the scalar order parameter, previously described in the microscopic approach.

## 1.4. Anisotropy: main manifestations

As they present internal order, LCs exhibit properties with different values when measured along axes in different directions. This feature is called anisotropy, and it is the quintessential property of these materials. LCs thus feature anisotropic behaviour in practically all their physical properties, which will normally have two components, corresponding to parallel and perpendicular orientations with respect to the director  $\mathbf{n}$  (Fig. 6).

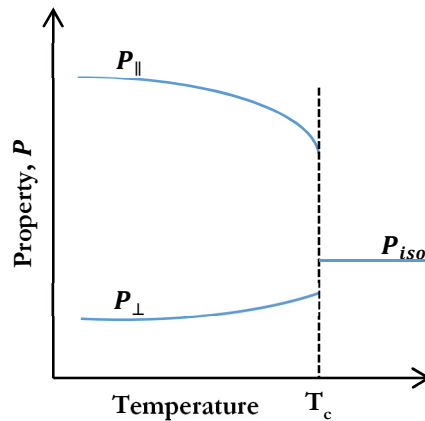


**Fig. 6. Graphical representation of anisotropy for a general physical property  $P$  in temperature-dependent liquid crystals.** In a LC,  $P$  presents different values when measured parallel ( $P_{\parallel}$ ) or perpendicular ( $P_{\perp}$ ) to  $\mathbf{n}$ . Above a critical temperature ( $T_c$ ), the fluid loses its internal order and with it, the anisotropic properties.  $P_{iso}$  is the property value in the isotropic phase.



Here, the most relevant manifestations of this quality are briefly introduced, namely, dielectric, diamagnetic, optical and viscous anisotropy.

#### 1.4.1. Dielectric anisotropy

LCs can be constituted by polar or non-polar molecules. The first ones present a permanent dipole moment arising from the charge separation in the molecule. In contrast, non-polar molecules feature a dipole moment only under an electric field, which induces the charge separation. Although induced dipoles are weaker than permanent dipoles, electric fields have the same influence on both. The electric permittivity ( $\epsilon$ ) quantifies the susceptibility of a material to polarize in response to an applied electric field. In the case on LCs, this quantity is different when measured along ( $\epsilon_{\parallel}$ ) or normal ( $\epsilon_{\perp}$ ) to the director axis. The difference between these constants may be positive and negative, depending on the chemical structure of the constituent molecules, and it defines the dielectric anisotropy of the material ( $\epsilon_a = \epsilon_{\parallel} - \epsilon_{\perp}$ ).

The global effect of an electric field  $\mathbf{E}$  on a nematic LC is measured by the electric displacement  $\mathbf{D}$ :

$$\mathbf{D} = \epsilon_{\parallel} \mathbf{E} \quad \text{if } \mathbf{E} \text{ is parallel to } \mathbf{n}$$

$$\mathbf{D} = \epsilon_{\perp} \mathbf{E} \quad \text{if } \mathbf{E} \text{ is normal to } \mathbf{n}$$

We can write down a more generic equation when  $\mathbf{E}$  is oriented with an arbitrary angle with respect to  $\mathbf{n}$ :

$$\mathbf{D} = \epsilon_{\perp} \mathbf{E} + \epsilon_a (\mathbf{n} \cdot \mathbf{E}) \mathbf{n}$$

Under an electric field, the material evolves to minimize the electric contribution to the thermodynamic potential, which is obtained from the free energy density

$$f_e = -\frac{\epsilon_{\perp}}{8\pi} \mathbf{E}^2 - \frac{\epsilon_a}{8\pi} (\mathbf{n} \cdot \mathbf{E})^2$$

The first term is independent of orientation, i.e. independent of  $\mathbf{n}$ . However, the second term, which includes  $\mathbf{n}$ , favours parallel alignment ( $\mathbf{n} \parallel \mathbf{E}$ ) if  $\epsilon_{\parallel} > \epsilon_{\perp}$  and thus  $\epsilon_a > 0$ . In this case, molecules carry a dipole moment along its long axis so they can be oriented efficiently along an external electric field. If, on the contrary, the dipole moment is normal to the long axis of the molecules,  $\epsilon_{\parallel} < \epsilon_{\perp}$  and  $\epsilon_a < 0$  and, consequently, perpendicular orientation of  $\mathbf{n}$  to respect to the  $\mathbf{E}$  is enhanced (Fig. 7) [2].

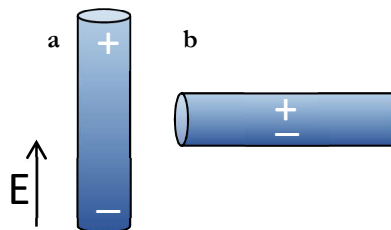


**Fig. 7. Interaction between liquid crystal molecules and an electric field.** a) Molecules will align along the field direction if  $\Delta\epsilon > 0$ . b) Contrarily, they will dispose perpendicular to the field direction when  $\Delta\epsilon < 0$ .

---

The presence of charged impurities in TLCs, makes the use of high frequency (kHz) alternating electric fields necessary for their alignment, in order to avoid ionic currents inside the LCs (Materials and methods, Section 3.7.1).

### 1.4.2. Diamagnetic anisotropy

The diamagnetic susceptibility ( $\chi$ ) of a LC, owing to the anisotropic form of the molecules composing it, is also anisotropic thus having two components for each molecular axis ( $\chi_{\parallel}$  and  $\chi_{\perp}$ ). Analogously to the previous section, we can quantitatively define the effect of the field  $\mathbf{H}$  on the director  $\mathbf{n}$ . The magnetization  $\mathbf{M}$  induced by  $\mathbf{H}$  is

$$\mathbf{M} = \chi_{\parallel} \mathbf{H} \quad \text{if } \mathbf{H} \text{ is parallel to } \mathbf{n}$$

$$\mathbf{M} = \chi_{\perp} \mathbf{H} \quad \text{if } \mathbf{H} \text{ is perpendicular to } \mathbf{n},$$

and, as before,  $\mathbf{H}$  for arbitrary angles to respect to  $\mathbf{n}$  becomes

$$\mathbf{H} = \chi_{\perp} \mathbf{H} + \chi_a (\mathbf{n} \cdot \mathbf{H}) \mathbf{n}.$$

In this case, both  $\chi_{\parallel}$  and  $\chi_{\perp}$  are always negative and normally, in nematic LCs the diamagnetic anisotropy ( $\chi_a = \chi_{\parallel} - \chi_{\perp}$ ) is positive as  $\chi_{\perp}$  is normally smaller than  $\chi_{\parallel}$ . Even though most organic molecules are diamagnetic, the diamagnetism is particularly strong when the molecules have aromatic rings. When a magnetic field  $\mathbf{H}$  is applied normal to the rings plane an electron current is induced to compensate the flux going through it. As the lines of the field are distorted, the energy is raised and consequently, the molecules tend to align such that  $\mathbf{H}$  is parallel to the plane of the rings. Like in the previous section, we can write the magnetic contribution to the free energy density

$$f_m = -\frac{1}{2} \chi_{\perp} \mathbf{H}^2 - \frac{1}{2} (\chi_a) (\mathbf{n} \cdot \mathbf{H})^2.$$

As before, the first term is independent of  $\mathbf{n}$  but the second one it is not. If  $\chi_a > 0$ ,  $f_m$  is minimized when  $\mathbf{n} \parallel \mathbf{H}$ .

### 1.4.3. Optical anisotropy: Birefringence

In most crystalline solids, light travels at different speeds depending on the crystallographic direction it is propagating through. With LCs, light experiences the same phenomenon. As the orientation of the long-axes of their constituents align along a preferred direction, interacting light is resolved into two sets of rays that vibrate at right angles and travel with different velocities. Consequently, LCs present two different refractive indexes corresponding to the light rays polarized along and perpendicular to  $\mathbf{n}$  ( $n_{\parallel}$  and  $n_{\perp}$ , respectively). This double refraction effect is called birefringence and it quantifies the difference between the refractive indexes.

Birefringent materials like LCs are usually characterized by polarized-light optical microscopy (Materials and methods, Section 3.8.1). Briefly, this technique exploits the interference of the split light rays, which are re-united along the same optical path. Depending on the local orientation of the

optical axis, the interaction between the two rays will present different amount of phase shift (or retardation), which gives information about the LC director configuration throughout a sample (Fig. 8).

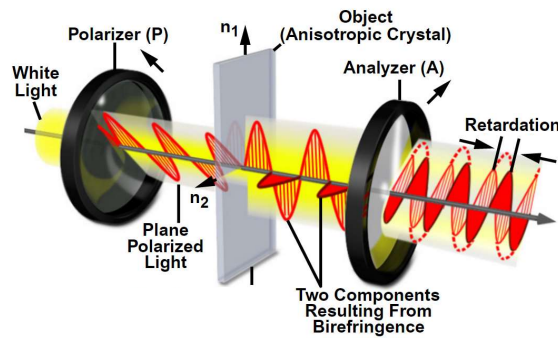


Fig. 8. Birefringent crystals between crossed polarizers. Source: ref. [19].

#### 1.4.4. Rheological anisotropy: The shear viscosity

The rheological properties of LCs are also affected by their anisotropic nature. On the one hand, the application of flows to anisotropic fluids influences the orientation of their constituents. On the other, the shear viscosity of anisotropic fluids depends on the relative orientation of  $\mathbf{n}$  with respect to the flow geometry [2,20,21].

Three fundamental flow geometries are sufficient to describe anisotropy of the shear viscosity in a LC. This can be decomposed in the three Miesowicz coefficients ( $\eta_1$ ,  $\eta_2$  and  $\eta_3$ ) that depend on the orientation of the constitutive units of the fluid to respect to the flow:  $\eta_1$  correspond to the orientations perpendicular to the flow and parallel the velocity gradient (Fig. 9a) and  $\eta_2$  and  $\eta_3$  to the two different configurations perpendicular to the velocity gradient (Fig. 9b,c).

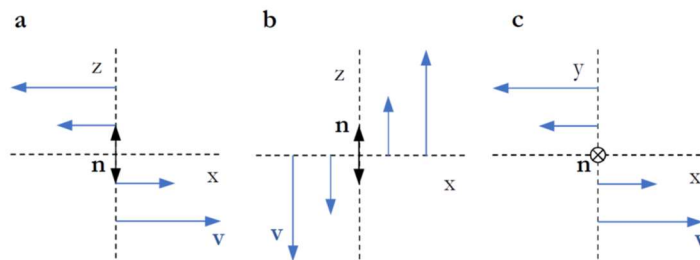


Fig. 9. Fundamental geometries for viscosity measurements. The Miesowicz coefficients ( $\eta_1$ ,  $\eta_2$ , and  $\eta_3$ ) can be tested with these experiments (a, b, c, respectively).  $\mathbf{n}$  is well-aligned along the z axis.  $\mathbf{v}$  refers to the flow velocity. Adapted from ref. [2].

While the rheological anisotropy of LCs featuring nematic phase is not usually apparent, smectic phases do show remarkable anisotropy in their rheological properties. An important part of the presented results take advantage of this behaviour, which will be described further in section 1.6.

## 1.5. Distortions in nematic liquid crystals

In equilibrium, the building blocks of an ideal nematic LC are, on average, locally aligned along one common direction  $\pm\mathbf{n}$ . However, even in equilibrium, this direction can vary from point to point due to thermal fluctuations and it can even be forced to change by imposing boundary constraints or by the action of external forces, such as shear stresses or electromagnetic fields. In most practical circumstances, the orientation in a LC changes throughout a sample and thus the order parameter becomes spatially nonuniform.

### 1.5.1. Long-range distortions: Free energy

LCs can be deformed by weak external forces, which involve changes in the internal orientation of their constituents and thus of  $\mathbf{n}$ . If the orientation in the director vector field  $\mathbf{n}(\mathbf{r})$  varies smoothly in space, i.e. the length scale of the induced distortion is much larger than the dimensions of the constituents, a LC response to deformation can be described with a version of continuum elastic theory [22–24].

In the case of nematic LCs, the director field can be distorted by mainly three types of deformation denoted as splay, where distortion occurs perpendicular to  $\mathbf{n}$  ( $\text{div } \mathbf{n} \neq 0$ ), bend, which induces a distortion parallel to  $\mathbf{n}$  ( $\mathbf{n} \times \text{curl } \mathbf{n} \neq 0$ ), and twist, where  $\mathbf{n}$  is forced to gradually rotate along the direction perpendicular to  $\mathbf{n}$  ( $\mathbf{n} \cdot \text{curl } \mathbf{n} \neq 0$ ) (Fig. 10).

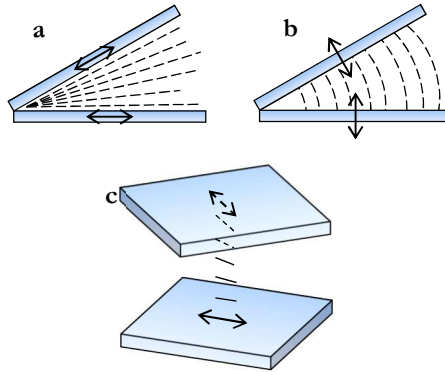


**Fig. 10. Long-range distortions of nematic liquid crystals.** a) Splay, b) bend and c) twist deformations. Arrows indicate the anchoring imposed by the walls confining the nematic (Section 1.5.2). Black lines depict the nematic orientation. Adapted from ref. [2].

The response of the material to these distortions can then be decomposed into terms based on three elastic constants  $K_1$ ,  $K_2$  and  $K_3$ , corresponding to the splay, twist and bend deformations, respectively. Then, the elastic free energy density of distortions can be constructed from the spatial derivatives of  $\mathbf{n}$ :

$$f_d = \frac{1}{2}K_1(\text{div } \mathbf{n})^2 + \frac{1}{2}K_2(\mathbf{n} \cdot \text{curl } \mathbf{n})^2 + \frac{1}{2}K_3(\mathbf{n} \times \text{curl } \mathbf{n})^2$$

### 1.5.2. LCs at interfaces: anchoring

In the absence of surfaces and applied forces,  $\mathbf{n}$  would be uniform with arbitrary orientation. Nevertheless, this never occurs in practice as LCs are always confined between interfaces that cause the director  $\mathbf{n}$  to orient in specific directions. These interfaces can be provided by solid plates, liquid volumes or gases, generally air. The interaction between the LC constituents and these interfaces conditions the orientation of the material near the surfaces [25], although this orientation propagates via elastic forces over macroscopic distances. The role of this interaction, often called LC anchoring [26], is crucial in LC science as it determines the equilibrium configuration of  $\mathbf{n}$  inside devices [27].

Depending on the orientation of the LC constituents with respect to the plane of the interface, characterized by the polar angle  $\theta$  (Fig. 11a), one can distinguish between three types of anchoring (Fig. 11b-d): planar, where constituents lay, on average, parallel to the interface ( $\theta \sim \frac{\pi}{2}$ ), homeotropic (or normal), which promotes the orientation of the LC perpendicular to the surface ( $\theta \sim 0$ ), and tilted, where LC components present an intermediate angle in between the previous configurations. The anchoring of the LC components onto surfaces depends on both the anchoring energy (physicochemical interaction), which determines  $\theta$ , and the preferred angle for the surface, or “easy axis” (physical interaction), which defines the azimuthal angle  $\varphi$  (Fig. 11a). In the majority of the cases, the interaction between the surface properties, steric effects and elastic behaviour of LCs, determine the characteristics of the anchoring [28].

In most practical conditions the surface-induced forces are strong enough to impose a well-defined direction to  $\mathbf{n}$  at the surface, regardless of the resultant elastic distortions; that is what is called a strong anchoring. Conversely, when the anchoring is weak, the surface forces enter in competition with the elastic deformation of the material. The parameter that characterizes the surface anchoring strength is the extrapolation length ( $L$ ), which is equal to the ratio of an appropriate nematic elastic constant ( $K$ ) divided by the anchoring strength coefficient ( $W$ ) [2].  $L$  represents the distance from the real surface where  $\mathbf{n}$  would coincide with the “easy axis” orientation. In strong anchoring conditions  $W$  is infinitely large thus  $L \sim 0$  and the director coincides with the easy axis orientation near the surface [29].

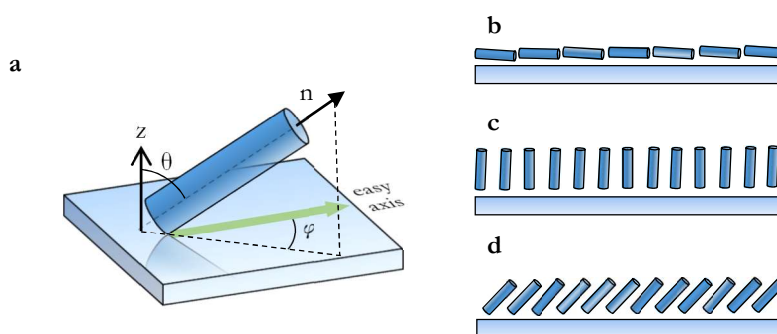


**Fig. 11. Orientation of nematic liquid crystal constituents near a solid surface.** a) position of director  $\mathbf{n}$  is determined by azimuthal ( $\varphi$ ) and polar angles ( $\theta$ ). Cylinders represent nematogens near surfaces imposing b) planar, c) homeotropic and d) tilted anchoring conditions.

In order to impose a preferred orientation to the LC, the chemical and/or physical properties of the contacting surface are usually tuned (Materials and methods, Section 3.4). In the case of nematic TLCs,

hydrophilic surfaces such as those provided by clean glass, water or some polymeric coatings/surfactants induce planar anchoring, while hydrophobic conditions usually provided by contact with air, monolayers of surfactants with aliphatic or fluorinated tails, and also some polymers, favour homeotropic anchoring of the LC molecules. Furthermore, the planar and tilted anchoring allow different variations depending on the azimuthal orientation of the LC molecules at the interface. For instance, crystals [30], mechanically rubbed surfaces [31,32], or even externally applied shear stresses [33] can impose a specific direction the LC molecules. Other interfaces can induce degenerate planar anchoring, where the molecules, although they dispose parallel to the interfacial plane, do not have a single preferred orientation.

### 1.5.3. Application of external fields: The Fréedericksz transition

As discussed in section 1.4, LCs respond to external fields, either electric or magnetic, and thus, they can be externally deformed by their action. If  $\epsilon_a$  or  $\chi_a$  are positive, when a field, applied perpendicular to  $\mathbf{n}$ , exceeds a certain value, a LC will transit from a static\* uniform  $\mathbf{n}(\mathbf{r})$  configuration, defined by the anchoring of the confining surfaces, into a perturbed state, promoted by the action of the field. Therefore, a critical field intensity must be applied in order to overcome the energetic cost of elastic deformation of the LC. This effect is called the Fréedericksz transition [34].

In the case when a magnetic field is applied normal to the easy axis of the molecules, the exerted torque  $\Gamma_M = \chi_a(\mathbf{n} \cdot \mathbf{H})\mathbf{n} \times \mathbf{H}$ , vanishes in the unperturbed situation as  $\mathbf{n} \cdot \mathbf{H} = 0$ . Thus, even with the presence of the applied field, the unperturbed configuration satisfies the conditions for local equilibrium. For larger  $\mathbf{H}$  intensities, though, practically all the molecules will tend to align with the field, except for two thin transition layers of thickness  $l$  near the surfaces that will be still influenced by the anchoring constraints (Fig. 12).

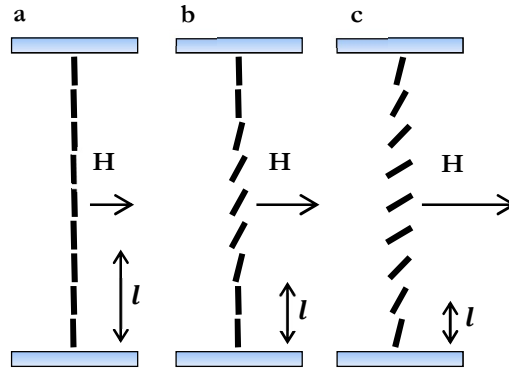


**Fig. 12. The Fréedericksz transition.** A nematic liquid crystal with  $\chi_a > 0$  is constrained to be perpendicular to its containing surfaces. A magnetic field  $\mathbf{H}$  is applied in the direction shown. **a)** Below a certain threshold value  $\mathbf{H}_{th}$ , the alignment of the molecules is not affected. **b)** Slightly above  $\mathbf{H}_{th}$ , the molecules start to align with the applied field. **c)** As  $\mathbf{H}$  is increased, the molecules deviate until they are parallel to the field and the penetration length of the anchoring constraints ( $l$ ) decreases. Adaptation from reference [35].

\* As the lengthscale over which  $\mathbf{n}(\mathbf{r})$  varies is much larger than the dimensions of the nematogens, thermal fluctuations can be neglected in this case.

### 1.5.4. Short-range distortions: Topological defects

In the previous sections, we have been considering the LCs as elastic materials deformed by long-range distortions, i.e. the distances over which significant variations of the order parameter occur are much larger than the dimensions of the LC constituents. Nevertheless, inhomogeneous distributions of the order parameter can also contain singularities or defects, where the average orientation is undefined [36]. Whenever these defects are not eliminated by continuous variations of the director field, they are defined as topologically stable, or simply called topological defects. For three-dimensional nematics, the singular regions may be either zero-dimensional (points), one-dimensional (lines), or two-dimensional (walls) [2].

As a matter of fact, the nematic mesophase was named for the apparent flexible threads (in Greek, *nema*) that these phases often present [16]. In analogy with dislocations in crystalline solids, these line singularities were called disclinations [24]. Apart from disclinations, where the director field orientation is lost along lines, there are also point-like defects, which we can find in the bulk or at the boundaries of a LC matrix. In the former case, they are called hedgehog defects and they constitute an isotropic core for complementary 3d radially or hyperbolically oriented  $\mathbf{n}$ . Point-like defects at the boundaries, or near them, have similar structures and are called boojums [37].

Defects are characterized by a topological strength,  $s$ , which describes the rotation of  $\mathbf{n}$  around the defect core. If a defect is surrounded clockwise, a polar object following  $\mathbf{n}$  will show integer (1) or half-integer ( $1/2$ ), and clockwise (+) or counterclockwise (-) rotation on itself (Fig. 13).

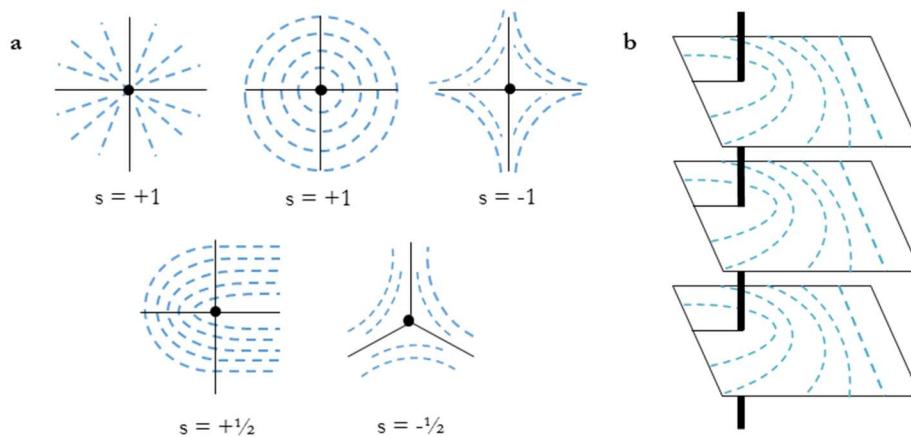


**Fig. 13. Defects in nematic liquid crystals.** a) director field configuration around defect cores with integer and semi-integer topological strengths. b) director field lines around a singular line disclinations with  $s = +1/2$ .

From an energetic perspective, defects with lower  $s$  are favored. Nevertheless, they always incur a contribution to the free energy, associated with the penalty of generating a discontinuity in  $\mathbf{n}(\mathbf{r})$ . Consequently, the concentration of defects tends to decrease by annihilation of opposite topological strengths, which are effectively attracted to each other, and in this way, minimize the free energy of the system. In the presence of well-defined boundary conditions, the sum of all the topological strengths, the so-called topological charge, is a conserved quantity. Although, at first, their name does not suggest any positive feature, LC defects have shown applicability in optical devices and materials [38–40] as well as templates for colloidal [41–44] or molecular [45] assembly.

The generation of topological defects is normally associated with the frustration of LCs by means of imposition of external constraints, which hinder a continuous evolution of  $\mathbf{n}(\mathbf{r})$  in very localized regions.

The confinement of a LC between boundary plates imposing different (hybrid) anchoring conditions [46–48] is one of the main strategies to trigger the formation of defects. The most typical case for a frustrated nematic phase is that of a nematic LC between walls with continuously degenerate (heterogeneous) boundary conditions, where the director  $\mathbf{n}$  is parallel to substrates but points in different directions. In this case, lines and point-like defects are generated, and they appear connected by dark brushes under crossed polarizers (Fig. 14). These dark branches correspond to the extinction orientation of the nematic LC. Accordingly, the director  $\mathbf{n}$  lies either parallel or perpendicular to the polarizer or analyzer axes (Materials and methods, Section 3.8.1). This is the so-called Schlieren texture [49].

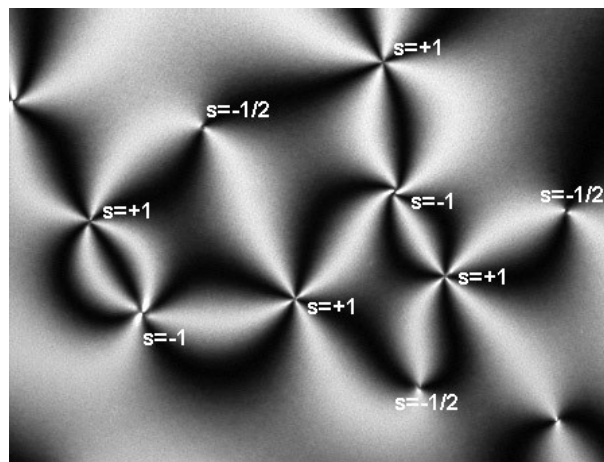


**Fig. 14. The Schlieren texture.** Nematic LC featuring degenerate planar anchoring observed between crossed polarizers. The observed patterns relate directly with the orientations of  $\mathbf{n}$  throughout the sample. Both disclinations with  $s=\pm 1/2$  and  $\pm 1$  can be found in nematics [2]. The points where four brushes meet correspond to the disclinations with  $s=\pm 1$ , and, the points with two brushes correspond to the disclinations with  $s=\pm 1/2$ . To distinguish between the disclinations of different sign, one can use the rotation of the sample with Schlieren texture between the crossed polarizers. Source: ref. [29].

Confinement inside smaller cavities with other geometries, such as spheres, is usually a robust method to generate and study topological defect configurations in LCs, which strongly depend on the anchoring forces and the radii of the spheres ( $R$ ). Droplets with  $R \ll L \sim K/W$  (Section 1.5.2), avoid spatial variations of the director  $\mathbf{n}$  at the expense of violated boundary conditions. In contrast, large droplets satisfy boundary conditions by aligning molecules along the easy directions [50]. However, even in this last situation, it is normally not possible to pack the director of a nematic LC into a spherical shape without creating one or more defects. Spherical confinement of LCs thus enhances, by itself, the generation of defects, which are an unavoidable consequence of the elastic energy of the LC and the boundary conditions at the interface with the sphere. Depending on the disposition of the LC molecules at the inner surface of the sphere, different configurations can be adopted: homeotropic anchoring induces a radial configuration with a hedgehog defect in the centre of charge  $+1$ ; planar anchoring enhances the generation of bipolar droplets with two boojum defects of charge  $+1/2$  at opposite poles of the sphere.



Other defect arrangements can be obtained by preparing nematic spherical shells, where the LC lies parallel to the surface of the sphere. In this case, the director cannot coat the surface of the sphere without singularities. From a topological point of view, and differently from nematic spheres, every possible LC configuration covering a spherical surface must have a total topological charge of  $+2$  [41]. This topological constraint leads to diverse configurations of defects, whose topological charge adds up to  $+2$ , and that have been observed in experiments [51,52]. In particular, the arrangement of four  $+1/2$  defects is of special interest as their tuneable positioning seems to be key towards improving the directionality of colloid interaction for the development of new nanomaterials [41,52]. In fact, this four-defect topological configuration has an important role in Chapter 4. Finally, twist deformations can occur in droplets and shells containing chiral nematics, which develop more complex structures [53].

Alternatively, defects can be generated by forcing an abrupt change in orientation of a perfectly aligned nematic slab. For instance, with the application of an electric field higher than the Fréedericksz threshold value, a LC may choose between two different (but equivalent) distortion patterns, which leads to the generation of two different director domains. The limit between two domains of opposite distortions involves the formation of a wall line defect, constituted by two singular line defects of charges  $s=+1/2$  and  $s=-1/2$  (Fig. 15) [2,54].

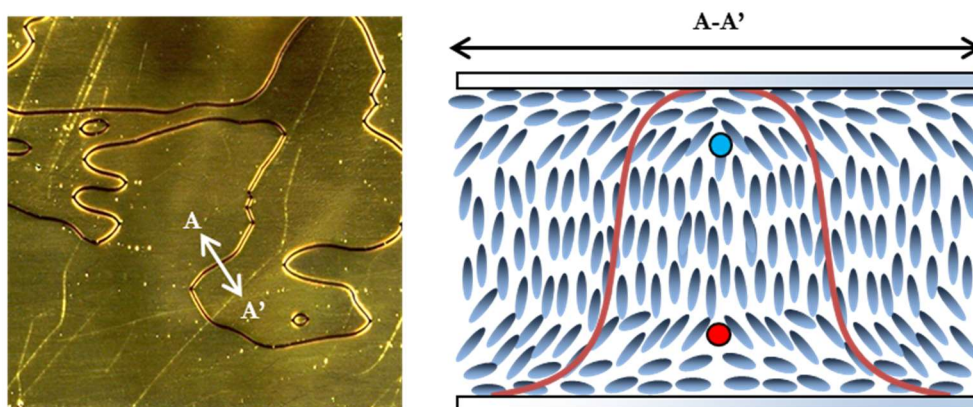


**Fig. 15. Wall line defects.** **a)** micrograph of a nematic LC just after application of a strong electric field. The image shows the presence of non-singular wall line defects. Image is 1mm wide. **b)** Schematic representation of the section of a wall line defect, constituted by  $+1/2$  (blue dot) and  $-1/2$  (red dot) disclinations. The red line stands for the average orientation of the LC constituents in the shown plane.

Finally, topological defects can also be created in a more controlled way, by imposing surface patterns with chemical gradients [55–58] or topographical features [59–61]. In addition, the application of electric or magnetic fields allows to control the formation of disclinations, whose configuration can be externally modified [58]. Finally, frustration of LCs by the addition of inclusions inside a LC matrix [62–64] induces also localized distortions of the LCs. In particular, phenomena arising from the incorporation of spherical inclusions in nematic LCs is explained in detail in the next section, as it will be of interest for forthcoming discussion in Chapter 4.

---

### 1.5.5. Spherical inclusions in nematic liquid crystals

The introduction of a micron-sized object inside a LC induces a distortion of the anisotropic host, which accommodates to the new conditions with the creation of defects close to the surface of the inclusion [65]. An inclusion inducing sufficiently strong anchoring carries a topological charge of a certain strength, and if  $\mathbf{n}(\mathbf{r})$  is uniform far away from the particle, so that the total topological charge of the whole system is zero, additional defects should be created in order to compensate the topological charge of the inclusion. Therefore, the combination of the geometry and the anchoring properties of the embedded object, together with the long-range orientation of  $\mathbf{n}(\mathbf{r})$ , determines the topological constraints that the anisotropic host must satisfy. As a result of the elastic distortions of the host, defect configurations on LC-dispersed entities enhance anisotropic interactions between these entities [62], which self-organize in structured assemblies [40,66–68].

Experimentally, either the preparation of colloidal dispersions [69], i.e. solid particles suspended in a fluid, or water-in-oil emulsions [62,64], i.e. water droplets dispersed in oil, are valid strategies for embedding micro-spheres in LCs. The control of the anchoring of the LC molecules onto the inclusions is achieved by using various amphiphilic compounds which are adsorbed at the object/LC interface. In particular, chemical functionalization of colloids, in dispersions, and coating with adequate surfactants of aqueous droplets, in emulsions, allow to induce different anchoring conditions at the surface of the dispersed spheres (Materials and methods, Section 3.6).

A spherical inclusion with strong homeotropic anchoring, is topologically equivalent to a radial hedgehog defect (Section 1.5.4). Embedded in an aligned far field director, the configuration imposed by the surface on the inclusion should conduct all the lines of  $\mathbf{n}(\mathbf{r})$  towards the central point of the sphere, resulting in a virtual\* topological defect of unit charge  $s=+1$ . In a cell with parallel boundary conditions, which has a zero charge, the addition of a single sphere lead to the generation of defects, whose configuration is controlled by the parameter  $L/R$  (Section 1.5.4). Spheres with normal strong anchoring ( $R \gg L$ ), must nucleate an additional hedgehog ( $S=-1$ ) near the inclusion in order to compensate the charge of the inner one. As a matter of fact, a zero charge can be only achieved if the second point defect is a hyperbolic hedgehog, as depicted schematically in Fig. 16a. Other topological defects, such as disclination lines called Saturn ring defects (Fig. 16b), can also satisfy the topological constraints imposed in this situation. In particular, a singular ring of a  $-1/2$  disclination, equivalent to a hedgehog with  $s=-1$ , surrounds the droplets in the equatorial plane perpendicularly to the far field (Fig. 16b). This situation is enhanced for particles inducing weak anchoring forces, thus  $R \ll L$  (Section 1.5.4) [70].

---

\* Virtual defects locate their cores out of the nematic phase. Although they are not visible, their topological influence is the same as a normal defect in the bulk of the LC.

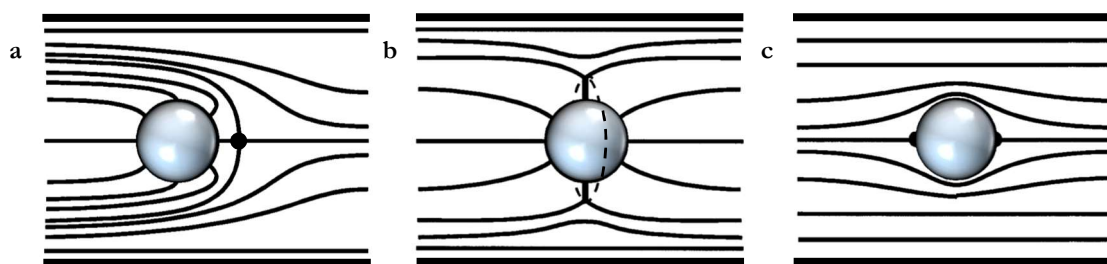


**Fig. 16. Liquid crystal defects around spherical inclusions.** a) the black dot indicates the position of a hyperbolic hedgehog, which compensates a radial hedgehog with a virtual core in the center of the inclusion. b) Saturn ring defect also satisfies the requirements for the total topological charge to be zero. c) A double boojum configuration (black semicircles) is obtained when the anchoring on the inclusion is planar. Adapted from ref. [64].

When the anchoring on the inclusions is planar, the boundary conditions are met by the creation of two boojums at the surface of the poles of the spheres [65]. They are then diametrically opposed and the align along the axis of the nematic phase (Fig. 16c).

## 1.6. Structure of the smectic-A phase: effects on rheology

Although smectic phases have been briefly introduced in section 1.2., this part is dedicated to a more detailed description of the smectic-A phase, especially focusing on its structure, main organizational configurations and consequent rheological properties.

In smectic phases, the LC constituents orient along a preferred direction, still denoted  $\mathbf{n}$ , like in the uniaxial nematic phase. Nevertheless, smectics present some positional order along  $\mathbf{n}$  that results from the disposition of the constituents in layers with a well-defined spacing between them [2,4,16,30]. Of all smectic phases, the SmA is the simplest one as there is no long-range positional order in the arrangement of the constituents within layers, where their long axes orient, on average, perpendicular to the layer planes (Fig. 17).

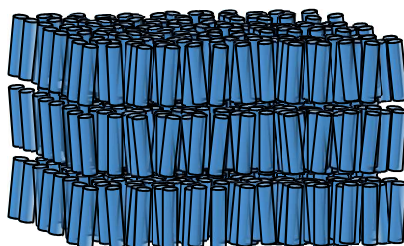


**Fig. 17. Schematic representation of the smectic-A phase.** The molecules align in a preferred direction and stack in layers, in which molecules can move freely.

In the absence of any constraints, the layers in a SmA would be flat with the constituting units lying perpendicular to the planes and parallel to one another, as their side-to-side interactions are relatively strong [35]. However, as we have seen in previous sections, unconstrained LCs do not exist in practice as, at least, they must satisfy the imposed anchoring conditions of the contacting interfaces. Therefore, realistic bulk samples do not form an idealized system of parallel layers. Rather, as the layers are uncorrelated from each other, they can bend in response to a variety of external triggers to form topological defects [4]. Depending basically on the imposed anchoring conditions, LCs featuring SmA

phase will arrange in two main types of structures: focal conic domains (either toroidal or parabolic) and the “bookshelf configuration”.

In order to conform to hybrid surface anchoring conditions, smectic planes bend and assemble toroidal focal conic domains (TFCDs), whose circular cores reside at the planar interface, where they pack in a surface-filling texture commonly called Apollonian net [71] (Fig. 18*a*). Both the size of the TFCDs and the symmetry of the net that they constitute are parameters difficult to control experimentally.

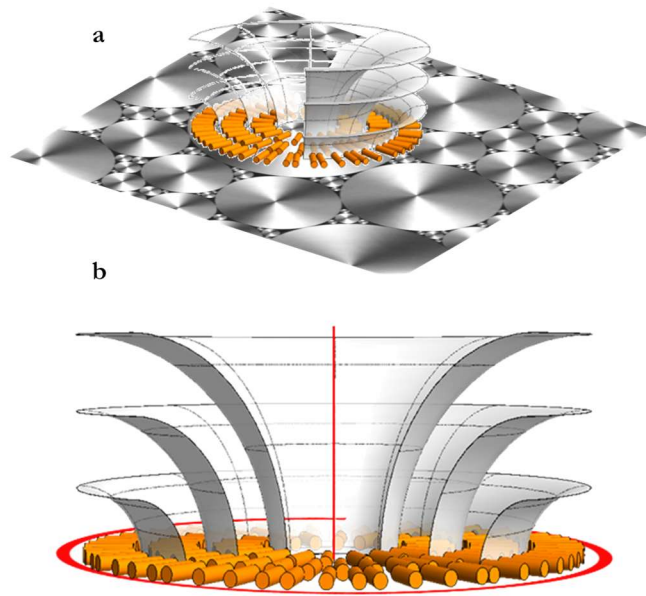


**Fig. 18. Structure of toroidal focal conic domains.** **a)** polarization micrograph shows the cores of toroidal focal conic domains lying at the interface, where molecules orient radially while constituting concentric planes. **b)** scheme of a half toroidal focal conic domain, which is constituted around two singular line-disclinations, depicted in red.

In TFCDs, the layers are arranged in toroidal rings wrapped around a straight linear singularity that extends across the entire distance between the antagonistic surfaces. The second singularity line is a circle that forms the core of the torus, which typically lies onto the interface with parallel anchoring in order to satisfy anchoring conditions (Fig. 18*b*). Therefore, at the interface inducing planar anchoring, molecules arrange radially in circular concentric planes parallel to the interface.

On the other hand, the “bookshelf configuration” would be the conformation adopted by a bound-free smectic, with parallel flat layers of aligned molecules, which lay parallel or perpendicular to the surfaces, depending on the induced anchoring, and dispose perpendicular to the layer planes (Fig. 19*a*). This configuration is formed between confining plates inducing the same anchoring conditions. However, due to imperfections of anchoring or impurities inside the LC matrix, some disclinations may appear, as well as parabolic focal conic domains (PFCDs) (Fig. 19). PFCDs are arranged such that the parallel layers are wrapped around two singularity lines that form perpendicularly facing parabolas that each pass through the focal point of the other. They are formed due to mechanical dilatation, which induces an undulation instability in the smectic layers [72].

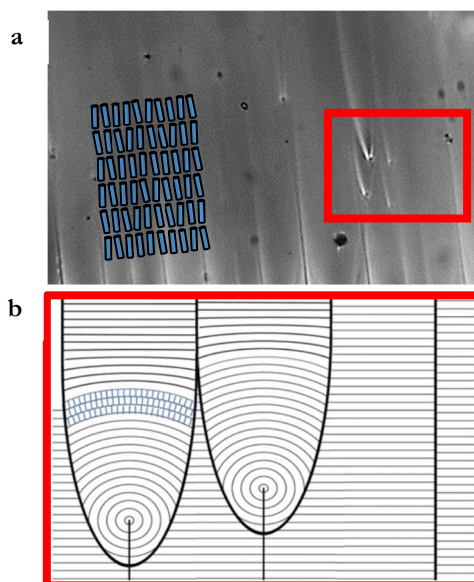


**Fig. 19. The bookshelf texture.** Smectic-A phase is aligned by an external magnetic field generating the bookshelf configuration. **a)** Polarization image shows the alignment of the LC phase in one direction. Molecules arrange parallelly in flat layers as depicted by the cylinders on the image. The red box encloses parabolic focal conic domains and disclinations that arise from local distortions in the layered structure, represented schematically in **(b)**.

As the diamagnetic anisotropy of the smectics is usually positive, i.e. molecules orient with a magnetic field, it is possible to externally force the molecules to adopt a bookshelf configuration. If the applied field is sufficiently strong it is possible to obtain this configuration regardless of the anchoring conditions. In addition, by adjusting the direction of the field, it is also possible to control the orientation of the planes in the bookshelf (Materials and methods, Section 3.7.2).

The lamellar nature of the Smectic-A structures confers remarkable properties. The most apparent in our experiments being their uniaxially-anisotropic rheological behaviour. Lamellar phases, such as those exhibited by soapy solutions or graphite, are well-known for their lubricant properties [4]. The source of this behaviour lies in the fact that molecules are free to move inside each layer, as in a two-dimensional liquid. Although they can jump from one layer to the next, this movement across layers is severely hindered. Consequently, the flow parallel to the layers is greatly facilitated compared to the flow in the perpendicular direction.

The unique rheological properties of this phase have been crucial for the successful completion of some of the main goals of this work. This will be explained in detail in chapter 3.

---

## 2. Active Matter

Active matter comprises systems constituted by self-driven units, which thus exert forces to their surroundings and move systematically and autonomously by consuming stored or ambient free energy [73]. In high density regimes, the action of the active units becomes dominated by the influence of their neighbours, and interact with each other assuming average common directions, and displaying complex collective behaviours.

Although the constituents of active systems can differ widely in their characteristic length scales, they often share common features, responsible for the observed dynamic states [74]:

- they are rather similar in shape and size
- they are usually anisometric, generally elongated objects
- they self-propel along directions that are set by their own anisotropic nature
- they move with a nearly constant absolute velocity
- they can change their direction
- they interact with their neighbours within a specific interaction range by changing their direction of motion and, in this way, involving an effective alignment.

As the influx of energy is continuous, active matter systems operate far from thermal equilibrium, giving rise to exotic steady states that involve phenomena such as collective motion [75], formation of large-scale patterns [76–78], unusual mechanical [79] or rheological [80,81] properties, topological defects [82,83] or active turbulence [84–86].

### 2.1. Main observations and experiments

Active systems are found, predominantly, in biological contexts. In the natural world, living cases of active systems abound, with characteristic length scales ranging from microns to meters. Nevertheless, conservation laws and symmetries constrain the possible dynamical behaviours of active matter systems, and thus, in spite of operating at vastly different length scales, active systems share similar properties, suggesting generality underlying their formation, morphology and dynamics [73].

#### 2.1.1. Living Active Matter systems

- Animal groups

Examples of active systems exhibiting large-scale collective phenomena include animal populations like flocking birds [87,88], insect swarms [89,90], shoals of fish [91–93], even people crowds [94–96] or other mammal herds [97,98], which can exhibit leaderless but coherent motion patterns (Fig. 20). By simply increasing the density of organisms in a group, a transition from random to directed motion is usually observed. This transition is well-described by flocking models [75,99], to which most of the previously cited works make reference. In living systems, flocking is biologically justified as animals in groups defend better against predators, they explore for resources or hunting more efficiently, and their decision making is improved [74].





**Fig. 20. Drone footage of a sheep spiral.** Interaction between components within animal groups lead to the creation of large-scale motion patterns. Photography by Tim Whitaker<sup>©</sup>.

The movement of animal flocks has been mainly tracked by camera-based techniques. Here, the observed entities are big, but the space in which they move is often unconfined. The simpler case is when the group to be observed moves only in two dimensions or when it develops in a quasi-two-dimensional space [91]. Incorporation of stereoscopic photography, i.e. 3D reconstruction of 2d images taken from slightly different positions, has allowed to record all the birds in a three-dimensional flock and reconstruct their positions [88,100], although this technique did not make the reconstruction of the trajectories of individual group members possible (Fig. 21). The appearance of advanced tracking systems like the “Global Positioning System” (GPS) or the “Acoustic Waveguide Remote Sensing” (OWARIS) has overcome this problem and, despite the cost-limitation of the research, it represents a breakthrough in the characterization of collective motion in living active systems [93,96,101].

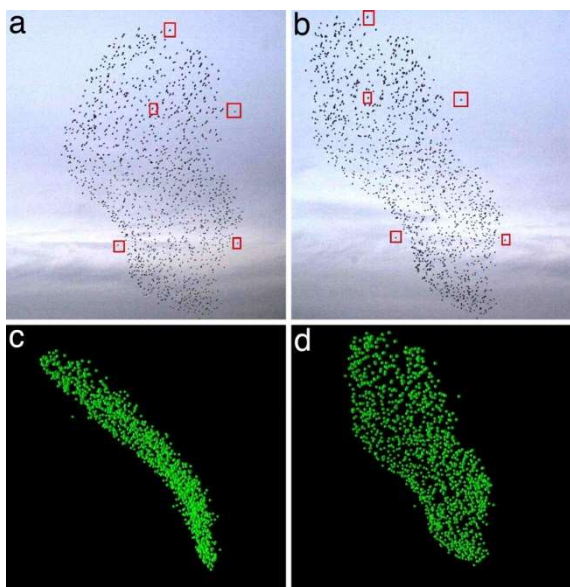


**Fig. 21. A typical starling flock and its 3D reconstruction.** (a) and (b) are photographs of one of the analyzed flocks. The pictures were made at the same moment by two different cameras, 25 meters apart. For reconstructing the flocks in 3D, each bird’s image on the left had to be matched to its corresponding image on the right. The small red squares indicate five of these matched pairs. (c,d) The 3D reconstructions of the analyzed flock from four different perspectives. (d) The reconstructed flock from the same view-point as (b). Adaptation from ref. [88].

- Colonies of bacteria

As stated previously, collective behaviours also arise at much smaller scales, which are much more easily characterizable. Microorganism colonies (such as bacterial colonies) are one of the simplest systems that consist on many interacting organisms, yet exhibit a non-trivial macroscopic behaviour [102,103]. At high concentrations, these cells assemble into co-directionally swimming clusters (Fig. 22), which often move at speeds larger than the average speed of single bacteria. Collisions and short-range hydrodynamic interactions within bacterial colonies also produce a wide variety of rich collective phenomena: among others, highly correlated turbulent states [84–86] and colony formations exhibiting patterns reminiscent of fractals [104].

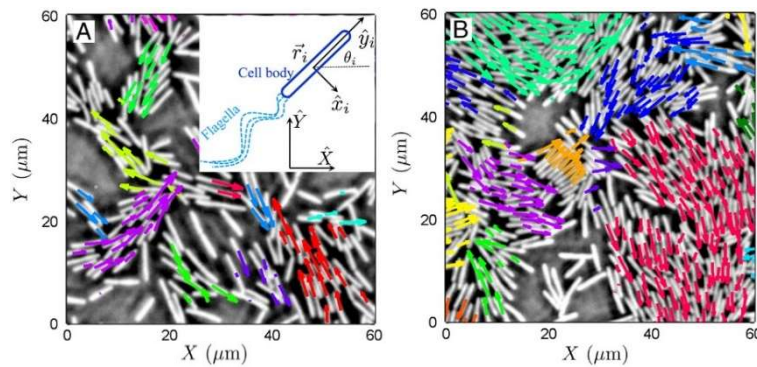


**Fig. 22. Dynamic clusters of bacteria.** Instantaneous configurations at two densities with the average total number of bacteria in the imaging window  $N_{\text{total}} = 343$  (a) and  $N_{\text{total}} = 718$  (b). Velocity vectors are overlaid on the raw images of bacteria. The length of the arrows of the same colour belong to the same dynamic cluster. Adapted from ref. [103].

- Cell tissues

In living tissues, cells move cooperatively in order to attain large-scale restructuration events, which are fundamental for processes such as morphogenesis, wound healing or tumor metastasis [105–107]. Due to cell body changes during motion, single cell migration is quite erratic. Nevertheless, in confluent cell layers migration becomes directional, even featuring glass-like dynamics due to cell-cell interactions and consequent coordinated movement of cells within a group [108–110] (Fig. 23).

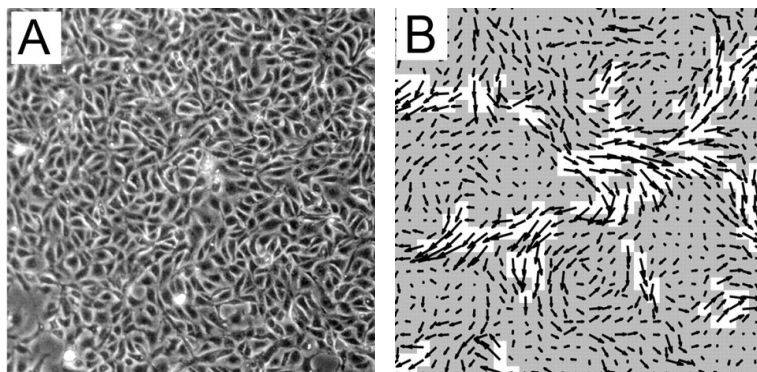


**Fig. 23. Migration of cells within a confluent monolayer.** a) Phase-contrast micrograph of a living tissue. b) Velocity vector field shows the collective dynamics within the cell sheet. White regions highlight areas with of dynamic heterogeneities. Images are 500  $\mu\text{m}$  wide. Adaptation from ref. [110].



- Subcellular structures: the cytoskeleton

Similarly, the scaffold of cells, the cytoskeleton, or other subcellular structures like cilia or flagella, organize large-scale steady state structures from random mixtures of molecules, such as filamentous protein polymers and force-generating motor proteins (Fig. 24). These entities cooperate functionally during a wide variety of processes, including intracellular transport of organelles, cell motility, spindle rotation or cytoplasmic streaming [111–114].

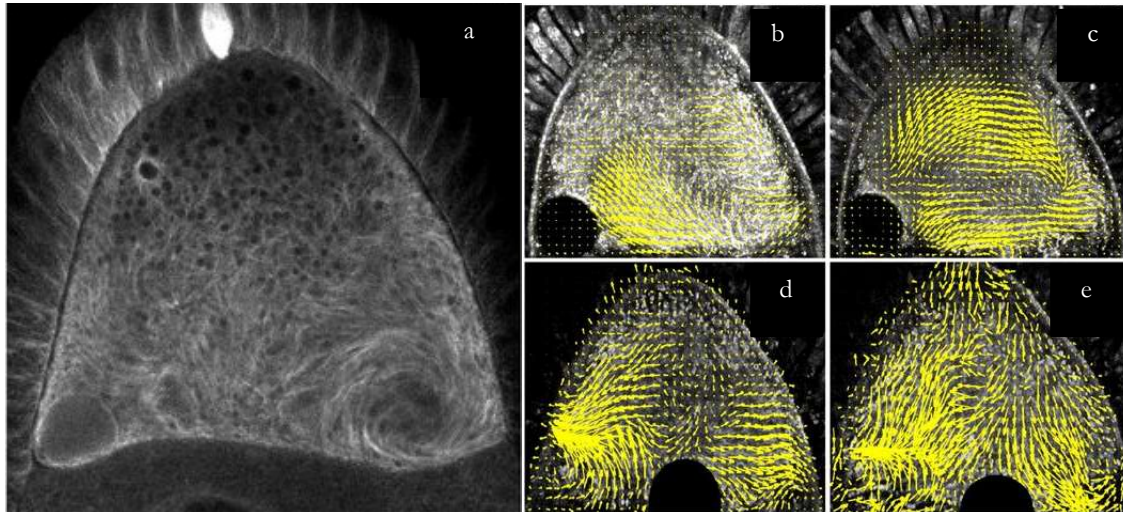


**Fig. 24. Collective patterns in cytoplasmic streaming in an oocyte of *Drosophila melanogaster*.** a) Fluorescence micrograph shows the disposition of the microtubule mesh inside the oocyte. b-e) Velocity flow fields (yellow arrow vectors) for two different oocytes at two different times. Circular black region within each oocyte is the nucleus, approximately 15  $\mu\text{m}$  in diameter. Adapted from ref. [114].

The dynamic behaviour of the cytoskeleton arises from the combination of different active and passive mechanisms. On the one hand, proteins such as actin and tubulin associate into fairly rigid linear polar structures (actin filaments and microtubules, MTs, respectively) that are fundamentally out of equilibrium (Fig. 25). In cells, continuous hydrolysis of ATP or GTP (adenosine triphosphate and guanosine triphosphate, respectively) enhance their growth in length from one end, while from the other they shrink (Fig. 26). When the polymerization and depolymerization rates are balanced, this process, known as treadmilling, results in a segment of filament seemingly moving across the cytosol [115].

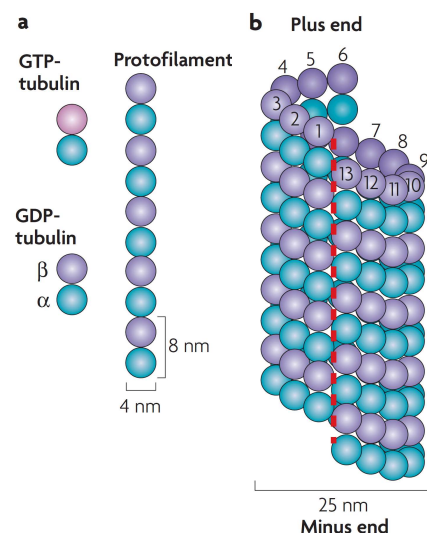


**Fig. 25. Microtubule structure.** Microtubules are composed of stable  $\alpha/\beta$ -tubulin heterodimers that are aligned in a polar head-to-tail fashion to form protofilaments (a). The cylindrical and helical microtubule wall typically comprises 13 parallel protofilaments *in vivo* (b). Adapted from ref. [115].

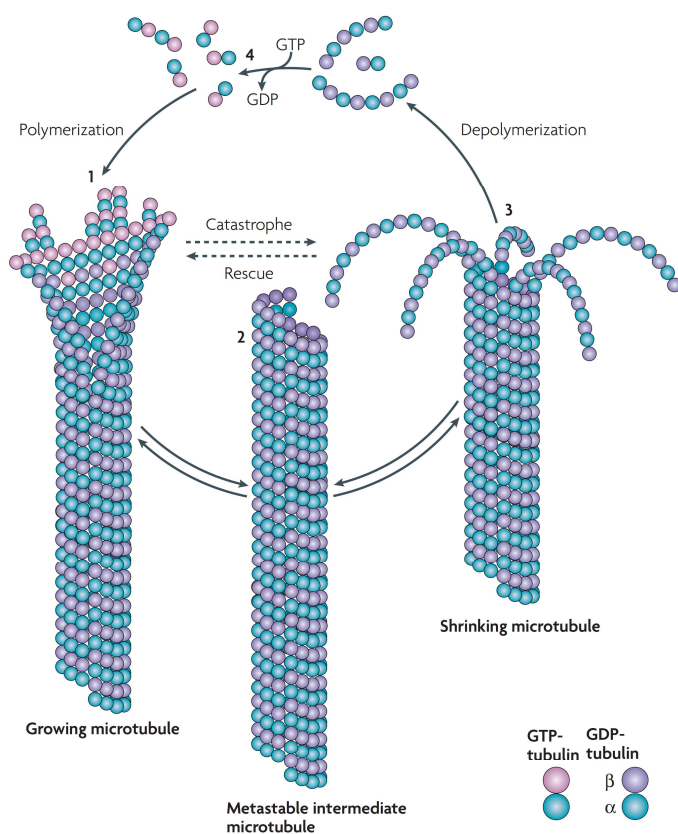


**Fig. 26. Dynamic instability of microtubules.** Polymerization and depolymerization of microtubules is driven by the binding, hydrolysis and exchange of a guanine nucleotide on the  $\beta$ -tubulin monomer (GTP bound to  $\alpha$ -tubulin is nonexchangeable and is never hydrolysed). GTP hydrolysis is not required for microtubule assembly *per se* but is necessary for switching between catastrophe and rescue. Polymerization is typically initiated from GTP-loaded tubulin subunits (1). GTP hydrolysis and release of inorganic phosphate occurs shortly after incorporation, and is promoted by burial and locking of the partially exposed nucleotide as a result of the head-to-tail assembly of dimers. Growing microtubule sheets are thus believed to maintain a ‘cap’ of tubulin-GTP subunits to stabilize the straight tubulin conformation within the microtubule lattice. Closure of the terminal sheet structure generates a metastable, blunt-ended microtubule intermediate (2), which might pause, undergo further growth or switch to the depolymerization phase. A shrinking microtubule is characterized by fountain-like arrays of ring and spiral protofilament structures (3). This conformational change, which is presumably directed by tubulin-

GDP, may destabilize lateral contacts between adjacent protofilaments. The polymerization–depolymerization cycle is completed by exchanging GDP of the disassembly products with GTP (4). Adapted from ref. [115].

On the other hand, energy-transducing motor proteins bind to cytoskeletal filaments and hydrolyse ATP to ride along the protein tracks. To do so, they undergo small conformational variations, at the expense of chemical energy, that are amplified and translated into movement via nanometer-size steps [116]. Three superfamilies of motor proteins can be distinguished: myosins, which move on actin filaments and kinesins and dyneins that move on MTs. All of them exist in different structures and feature different behaviours, which are specially designed for specific functions that can involve either the transport of organelles throughout the cell or the exertion of forces within the cytoskeletal filament network [117,118]. To better understand the relation between the behaviour of these networks and the interplay between constitutive filaments, motors and other molecules, dynamic cytoskeletal extracts have been also studied *ex vivo* [119]. Finally, non-enzymatic (passive) biofilament cross-linkers have been proven to be also necessary for force-generating mechanisms inside cells [120]. All these ingredients, namely the intrinsic filament dynamics, and the active or passive cross-linking, provide with the dynamical and structural framework to generate mechanical forces by which the cytoskeleton spontaneously remodels [121–123].

Small-scale living systems, i.e. bacteria, cells and the cytoskeleton, allow better characterization and higher-precision studies than those formed by larger units. Nevertheless, the complex interactions between and inside living organisms, together with the limitations in parameter adjustability, represent major obstacles to understand the underlying principles of ordering pathways in these Active Matter systems. Thus, simpler experimental realizations are much-needed to mimic the functionalities of these complex processes, and to control all parameters with high accuracy.

### 2.1.2. Artificial Active Matter

In the recent years, artificial active systems have been developed by engineering active but inanimate analogues of living systems by means of bottom-up approaches. Experimental realizations in artificial Active Matter can be classified in two main families: groups of motile colloids and dynamic assemblies of subcellular extracts, which comprise the so-called high-density motility assays, and active gels.

- Motile colloids

Highly populated monolayers of motile colloids, either self-propelled [124–127] or externally-activated by means of vibration [128,129] or external fields [130] give rise to collective phenomena, which share several similarities with those exhibited by groups of living organisms (Fig. 27). Here, the shape and the symmetry of the particles determine their collective dynamics as the particles do not communicate except by physical contact. Despite the absence of shape anisotropy or alignment interactions, these colloids interact forming clusters and tend to preferentially align their speed in a given direction, so that the cluster is ‘alive’ and translates and rotates through the solvent (Fig. 27). An advantageous feature of these systems is the possibility to tune the speed of their constituents either by varying fuel concentration, in the case of colloids self-propelled by auto-catalytic reactions, or by changing the amplitude or vibration frequency of the applied field, for actuated entities.

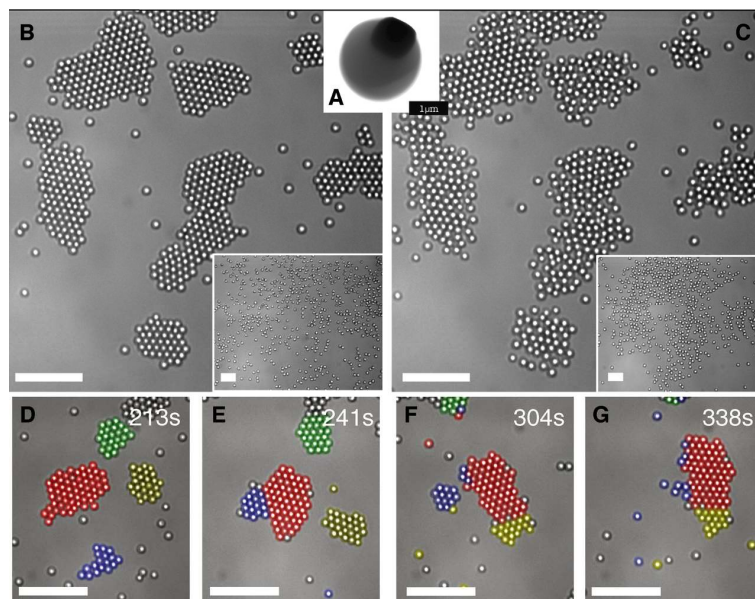


**Fig. 27. Self-organization of light-activated self-propelled colloids.** a) Scanning electron microscopy (SEM) of the bi-material colloid: polymer colloidal sphere with protruding hematite cube (dark). b) Living crystals assembled from a homogeneous distribution (inset) under illumination by blue light. c) Living crystals melt by thermal diffusion when light is extinguished: Image shows system 10 s after blue light is turned off (inset, after 100 s). (d-g) The false colours show the time evolution of particles belonging to different clusters. For (b-g), the scale bars indicate 10  $\mu\text{m}$ . Adaptation from ref. [125].

Even though the robustness of these realizations is undeniable, they still lack control variables, which could trigger the emergence of novel phenomena. To overcome these limitations, other realizations are based in *in vitro* reconstitutions of subcellular extracts, involving the smallest experimentally realized self-propelled particles so far. As previously explained, the constituents of the cytoskeleton



can exert forces at expenses of nucleoside hydrolysis, which is used to drive the formation of the far-from-equilibrium dynamic steady states of the active systems explained below.

- High-density motility assays

The first precedent of experiments of active subcellular-extracts-based active systems are the so-called motility assays, where actin biofilaments are propelled by myosin molecular motors anchored on a substrate [131,132] (Fig. 28a). Although these realizations aimed for the exploration of the basic biological functioning of molecular motors rather than exploring the dynamics of the transported filaments, they prefaced some of the most relevant experiments in the Active Matter field. In particular, by increasing the density of filaments moving over the surface, the interaction between them is greatly enhanced, thus leading to self-organized collective patterns, such as highly dynamic clusters, travelling waves or rotating swirls of actin filaments [133–135](Fig. 28b-d). These experiments have verified the existence of anisotropy in collective motion patterns and have been useful to quantify the spatiotemporal density fluctuations characteristic of active systems.

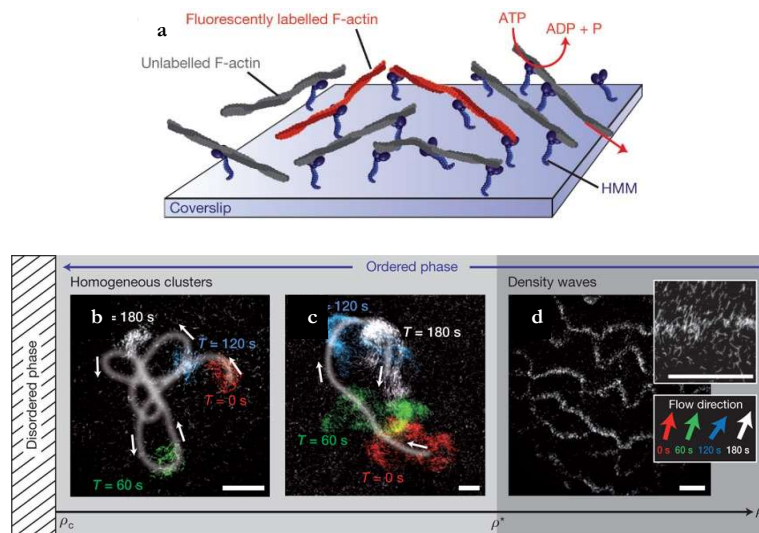


**Fig. 28. Schematic of a motility assay and phase behaviour as a function of the filament density.** a) Myosin molecular motors (HMM) are immobilized on a coverslip and the filament motion is visualized by the use of fluorescently labelled reporter filaments. For low densities, a disordered phase is found. b) and (c) Above a certain critical density,  $\rho_c$ , in an intermediate-density regime, the disordered phase is unstable and small polar nematic clusters of coherently moving filaments start to form. d) Above a threshold density,  $\rho^*$ , in the high-density regime, persistent density fluctuations lead to the formation of wave-like structures. The insets in (d) show a magnified view and a local analysis of the average flow direction. Scale bars, 50  $\mu\text{m}$ . Adapted from ref. [134].

Similar experiments have also been performed with MTs although, in contrast with those above, in these assays, MTs were not confined to two dimensions and could cross one another. This causes MTs to align locally with a relatively short correlation length. At high density, this local alignment is enough to create “intersections” of perpendicularly oriented groups of MTs that create vortices and loops [136].

These early *in vitro* realizations are simple in terms of number of ingredients and preparation, and versatile, as their control parameters can be easily modified. In fact, it is the use of proteins that confers this versatility as the system can be adjusted at the molecular level, allowing a more complete description and characterization of the underlying physical phenomena.

- Active gels

Finally, in an attempt to mimic the functionalities of the cytoskeleton, minimal active networks based on biofilaments and associated proteins have been assembled *in vitro* following bottom-up strategies. Often called active gels [73,137], these realizations combine, as the cytoskeleton does, filament dynamics, filament cross-linking and the activity of molecular motor proteins to generate the forces for the self-organization of steady state structures, out-of-equilibrium motion and flow patterns, necessary for cell functioning and development.

The first version of these dynamic networks was obtained from a suspension of MTs and clusters of kinesin molecular motor proteins, which acted as dynamic cross-linkers [138–140]. As previously explained, kinesin molecular motors attach to MTs and move along them towards the “plus” end [116], by hydrolysing ATP into ADP. In active gels, dimeric motor protein constructs attach to a pair of neighbouring MTs and, in some cases, exert forces onto them. Particularly, if linked MTs are polarity-oriented the motor protein complex moves in between the attached filaments practically without exerting any forces. On the other hand, when they exhibit opposed polarities to respect to the motor complexes, then, the latter effectively pull the MTs in different directions, displacing them apart (Fig. 29).

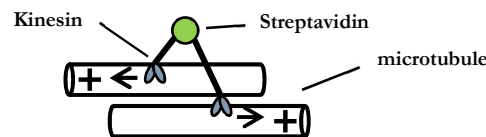


**Fig. 29. Self-organization of microtubules and kinesin motor complexes.** Schematic representation of a kinesin–streptavidin construct moving simultaneously along two microtubules. Kinesin clusters are, effectively, force-generating mobile crosslinks. Adaptation from ref. [138].

This shear forces, which are tens of pN [141] and act at the nano-scale, are responsible for macroscopic changes in cytoskeletal networks, which drive, for instance, cell reshaping events, formation of the mitotic spindle, and cell division. The dynamic interaction between MTs and motor proteins leads to the formation of polarity sorted aggregates, which are static. This polarity sorting results in large MT structures such as asters or vortices, where kinesin complexes accumulate in the centers (Fig. 30).

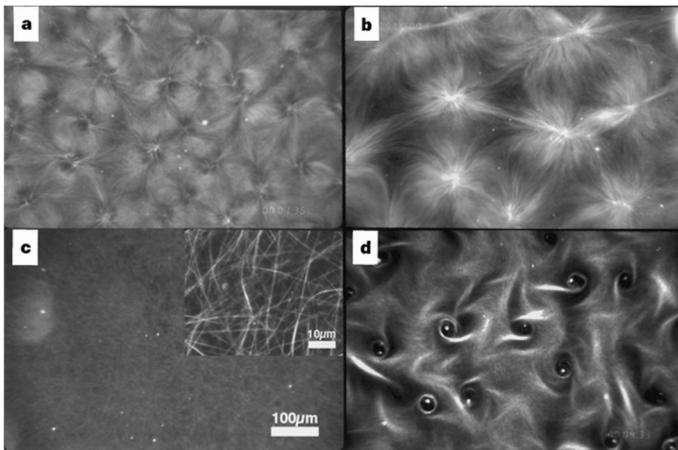


**Fig. 30. Different large-scale patterns formed through self-organization of microtubules and motors.** Initially uniform mixtures of proteins were heated to 37 °C, and patterns resulting after 7 min are shown at equal magnification. The samples differ in kinesin concentration. **a)** A lattice of asters and vortices obtained at  $\sim 25 \mu\text{g ml}^{-1}$  kinesin. **b)** An irregular lattice of asters obtained at  $\sim 37.5 \mu\text{g ml}^{-1}$  kinesin. **c)** Microtubules form bundles at  $\sim 50 \mu\text{g ml}^{-1}$  kinesin (scale bar, 100  $\mu\text{m}$ ). Insert, at higher magnification (scale bar, 10  $\mu\text{m}$ ). **d)** A lattice of vortices obtained at  $<15 \mu\text{g ml}^{-1}$  kinesin. Source: ref. [138].

---

Analogues of this active meshwork have been successfully assembled with actin filaments and myosin multimeric motor complexes. However, the main goal of these realizations has been to capture essential and general features of contractility and mechanical adaptation of cytoskeletal networks [142–145].

The contractile behaviour of these biologically inspired actin-based active gels is in sharp contrast to other realizations with microtubules, which exhibit extensile behaviour. The reason for this difference is not well understood, although it has been suggested that actin gels are contractile due to small wavelength buckling of the constituent filaments. MTs, stiffer, have much longer buckling wavelength and this might suppress generation of any contractile forces [146]. In recent experiments, described below, it has been shown how depletion interaction also plays a major role in determining the nature of tubulin-based active gels.

- Entropically-assembled active gels: depletion interaction

Both actin filaments and MTs have been also assembled just by entropically-generated soft attractive interactions [147,148]. Optical trapping has recently enabled to measure the forces involved in the bundling of a pair of MTs [149] and to even measure the friction associated with filament sliding [150]. This attractive effect enhances the aggregation of colloids and protein assemblies, even in the absence of cross-linkers, and it is known as depletion interaction (in soft matter physics and materials science) [151–153], or as macromolecular crowding (in biology) [154]. It can be understood as follows. Consider a suspension of rods and smaller non-adsorbing polymer coils, which we will call depletants and that can be represented as spheres, with a characteristic radius of gyration,  $R_g^*$ . The center of mass of each depletant can get no closer than  $R_g$  to the surface of the rods, thus creating a cylindrical shell around them, known as excluded volume, which is unavailable for the depletants. By overlapping excluded volumes, i.e. by aggregating the rods, the free volume available for the depletants is maximized and, since there are many more depletant molecules than rods, the overall entropy of the mixture is increased, thus decreasing the free energy.

From bundles of stabilized MTs, active gels are easily obtained by incorporating motor protein complexes [77,155]. As explained in the previous subsection, molecular motor multimeric clusters can exert inter-filament sliding and drive non-equilibrium dynamics, especially when motors are continuously fed by ATP. In combination with depletion interaction, cross-linked MTs form active filamentous bundles that extend, fold, buckle and subsequently fracture, generating a steady state of continuous recombination of filament aggregates, which tend to be polarity sorted [77]. At sufficiently high concentration, fractured bundles rapidly recombine with surrounding bundles with random polarity, making polarity sorting inefficient. Consequently, reformed bundles usually generate further extension and thus provide the active gel with highly-dynamic flows that can persist for hours, only limited by the protein integrity and the available chemical fuel (Fig. 31). The composition of this active gel allow variations of its most relevant parameters such as ATP, motor protein, and depletant concentrations, enabling to tune its dynamical and morphological properties [138].

---

\*The square radius of gyration ( $R_g$ ) is the average squared distance of the elements of a polymer coil from its center of gravity [218].

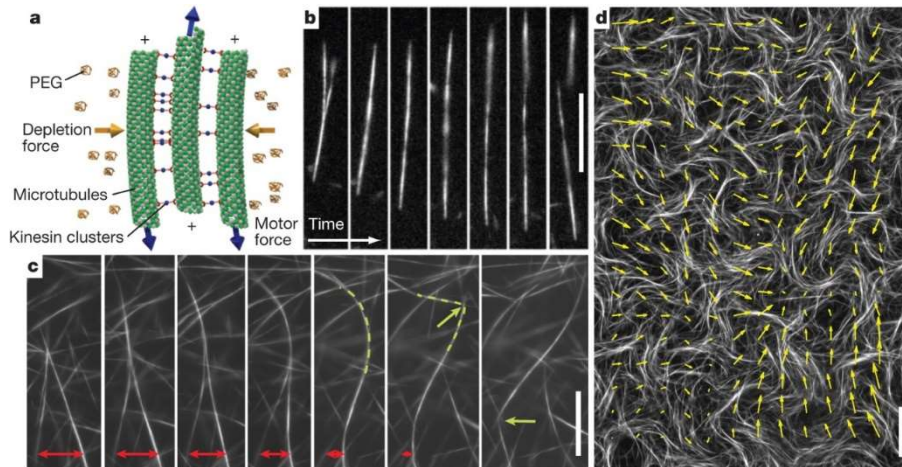


**Fig. 31. Active microtubule networks.** **a)** Schematic illustration of an extensile MT–kinesin bundle, the basic building block used for the assembly of this active gel. Kinesin clusters exert inter–filament sliding forces, whereas depleting PEG polymers induce MT bundling. **b)** Two MT bundles merge and the resultant bundle immediately extends, eventually breaking. Scale bar, 15  $\mu\text{m}$ . **c)** In a percolating microtubule network, bundles constantly merge (red arrows), extend, buckle (green dashed lines), fracture, and self-heal to produce a robust and highly dynamic steady state. Scale bar, 15  $\mu\text{m}$ . **d)** An active microtubule network viewed on a large scale. Arrows indicate local bundle velocity direction. Scale bar, 80  $\mu\text{m}$ . Adaptation from ref. [77].

The extensile nature of this composition results in spatiotemporally chaotic flows and textures that are reminiscent of those observed in animal groups, bacterial colonies or inside living cells. Therefore, these cytoskeletal minimal reconstitutions not only serve as minimal experimental realizations for basic research on pattern formation in active matter but also have become excellent models for fundamental research on cytoskeleton dynamics.

The presence of a suitably-functionalized flat fluid interface (liquid/liquid) results in an effective transport of the active gel towards the interface by means of the same depletion forces that bundle MTs together. This entropically-driven condensation of the extensile bundles forces their organization in the interfacial plane, where they self-assemble into a quasi-two-dimensional active gel that features long-range orientational order [77]. Precisely, in the next section I will focus on the description of ordered active materials, with special emphasis on this last realization, as it has been our system of study.

## 2.2. Active liquid crystals

Most of the systems that compose the Active Matter field are suspensions of self-propelled units, which, above a certain density, interact with each other leading to collective phenomena. By further increasing the constituent concentration, most of these systems, especially those formed by rod-like objects, are likely to feature a transition to a dynamic ordered state, as observed in LLCs (Section 1.1). As a matter of fact, when densified onto a surface, active units can form quasi-two-dimensional active colloidal LCs, usually called active LCs (ALCs) [73,157]. Differently from their passive analogues, an energy input on each individual constituent maintains these materials far from equilibrium, giving rise to complex behaviours and novel physical properties that conventional LCs do not present.

ALCs can either be constituted by units that are polar, endowed with head and tail, or apolar, if they are fore-aft symmetric. Polar active constituents, such as animals [88], bacteria [103,158], migrating

cells in dense layers [110], self-propelled rods [127] or biofilaments in motility assays [134], generally move along their long-axis towards their ‘head’. Conversely, apolar active units, like human melanocyte cells [108], vibrated rods [129] or internally-sheared MT bundles [77], may move back and forth but exhibit no net motion. Polar units can organize both macroscopically-moving polar ordered states, where all units point in the same direction, or zero-mean-motion nematic states, where units align locally but point in different directions. By contrast, an ordered state of apolar units always form nematic states.

### 2.2.1. Active defects and meso-scale turbulence

Just like passive LCs, ACLs also feature topological singularities, which have a crucial role in determining the dynamics of these active systems. In passive LCs, oppositely charged defects attract and annihilate each other and thus defects continuously disappear from a system as it approaches equilibrium (Section 1.5.4). Although rules concerning conservation of total topological charge are unchanged to respect to passive LCs, in ALCs defects are continuously generated because of the constant input of energy, and they will move autonomously mainly due to asymmetry in their surrounding flow field, rather than to minimize free energy [159–161]. The presence of topological defects in active systems has been identified experimentally, both for nematic [77,129] and polar active materials [135,138]. The nature of these defects, i.e. their morphology and dynamics, depends on the symmetry of the system: Nematic ALCs feature motile polar comet-like defects ( $s = +\frac{1}{2}$ ) and quasi-static threefold symmetric defects ( $s = -\frac{1}{2}$ ) (Fig. 32). On the other hand, polar phases exhibit static or rotating vortex, aster and spiral defects, endowed with integer charges ( $s = \pm 1$ ) (Fig. 30).

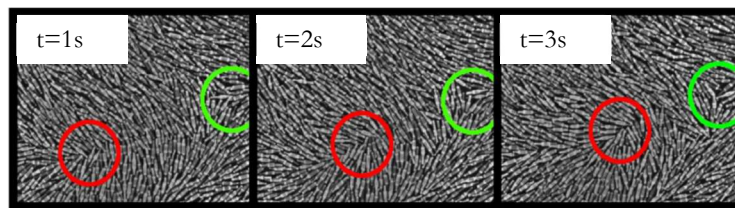


**Fig. 32. Active nematic of vibrated rods.** The time-lapse images show how the strength  $-\frac{1}{2}$  defect (encircled in green) moves very little, while the strength  $+\frac{1}{2}$  defect (encircled in red) moves substantially and systematically along its nose. Adapted from ref. [129].

In contrast to passive LCs, homogeneous states of ALCs are hydrodynamically unstable. The continuous energy input generates internal stresses that give rise to instabilities, similar to those observed in the Fréedericksz transition of passive LCs (Section 1.5.3) [162]. In the latter, tilted  $\mathbf{n}(\mathbf{r})$  configurations arise from a uniform configuration on application of a sufficiently strong external field. In the case of ALCs, there is no need for an external field to generate an instability as spontaneous active stresses can generate it. As a consequence, homogeneously oriented ALCs rapidly experience local reorientations in the director field [162,163] often generating oppositely charged topological defects [161]. These episodes share also analogies with passive LCs, where high-distortion lines, the so-called wall instabilities, “unzip” by forming pairs of defects, which move apart or annihilate (Section 1.5.4). The continuous influx of energy thus drives ALCs to steady states where topological defects are continuously created and destroyed. This results in a dynamic state featuring highly-disordered velocity fields, with a continually changing pattern of vortices [84,85], reminiscent of classical turbulent regimes in passive fluids (Fig. 33).



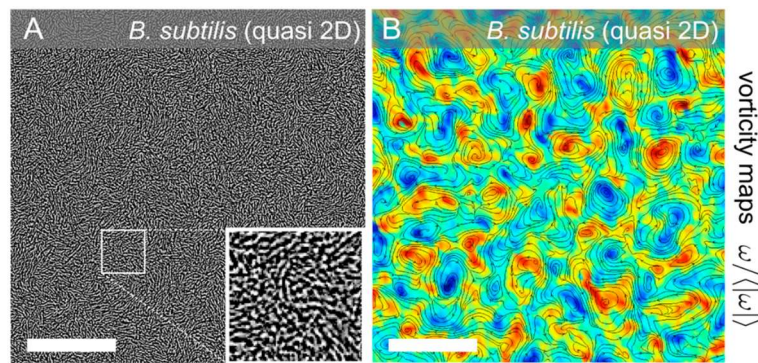


**Fig. 33. Turbulence in a bacterial bath.** Experimental snapshot (a) of a highly concentrated, homogeneous quasi-2D bacterial suspension. a) Flow streamlines  $v(t,r)$  and vorticity fields  $\omega(t,r)$  in the turbulent regime obtained from quasi-2D bacteria experiments. Adapted from ref. [85].

Nevertheless, while classical turbulence arises in systems with high Reynolds number\* ( $Re$ ) due to the dominance of inertial effects, this new “active turbulence”, also called meso-scale turbulence, is based on dissipation in systems with a low  $Re$ , where viscous forces dominate [86]. Moreover, detailed properties, such as scaling laws, seem to differ dramatically between inertia-based and active turbulence [164].

---


\* The Reynolds number ( $Re$ ) is a dimensionless quantity that calculates the balance between inertial and viscous forces in fluid flow. It is defined as  $Re = \frac{\rho v L}{\mu}$ , where  $\rho$  is the density of the fluid,  $v$  is the velocity of the fluid,  $L$  is a characteristic linear dimension and  $\mu$  is the dynamic viscosity of the fluid.

### 2.2.2. Our experimental system: The Active Nematic

As previously mentioned, our system of study is a quasi-two-dimensional active gel that features liquid crystalline order, and it is prepared from the entropically-assembled active gel, already introduced in Section 2.1.2. This active material was first developed in the laboratory of Z. Dogic (Brandeis University, MA, USA). In brief, it is based on MT bundles cross-linked by ATP-fuelled kinesin motor clusters, which form a highly-dynamic network from apolar active units. As stated, this kind of constituents can only lead to nematically-ordered materials in sufficiently high concentration regimes, which exhibit large-scale orientational coherence, resulting in long-range spatiotemporal correlations. As a matter of fact, densification of actively sheared MT bundles onto a soft interface leads to the spontaneous organization of a nematic ALC, the so-called active nematic (AN, Fig. 34).

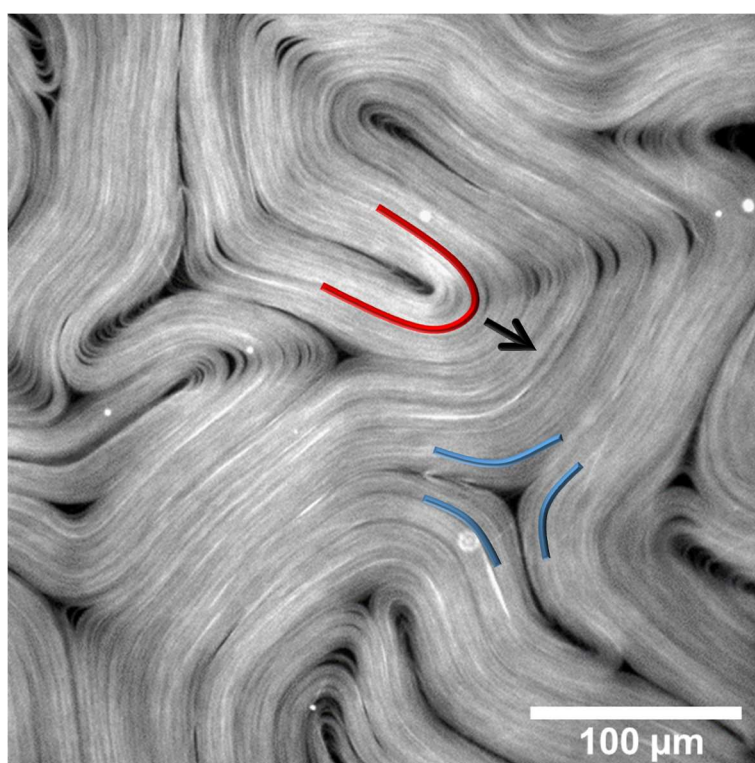


**Fig. 34. Active nematic liquid crystal.** When condensed onto an oily interface, the active gel organizes a quasi-two-dimensional system featuring liquid crystalline order. Black regions constitute active defects with positive (in red) or negative (in blue) semi-integer topological strength. The arrow indicates the direction of motion of the positive defect.

 See Video 1.

Regeneration of ATP (Materials and methods, Section 3.1.5) ensures a constant and continuous input of energy, which is dissipated as active stress through the surrounding fluids. Due to the continuous energy influx, these active suspensions with orientational order are in a state of permanent uniaxial tension and are therefore intrinsically unstable. As stated in the previous section, these instabilities, driven by active stresses, lead to the creation of topological defects (highlighted in Fig. 34), which can be easily identified as MT voids, which appear dark in the fluorescence micrographs (Materials and methods, Sections 3.1.2 and 3.8.2). Similar to topological defects in passive LCs (Section 1.5.4), these motile singularities can be characterized by a certain topological strength that depends on the configuration of the nematic director field around the singularities. Since the active phase features

nematic order, only semi-integer defects of positive ( $+\frac{1}{2}$ , Fig. 34 and Fig. 35, in red) and negative ( $-\frac{1}{2}$ , Fig. 34 and Fig. 35, in blue) charges are present.

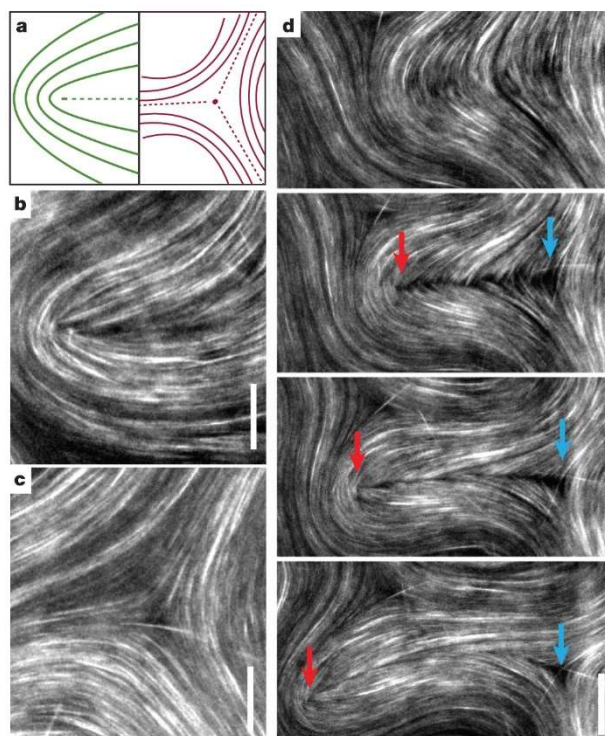


**Fig. 35. Dynamics of 2D streaming nematics confined to fluid interfaces.** a) Schematic illustrations of the nematic director configuration around disclination defects of charge  $\frac{1}{2}$  (left) and  $-\frac{1}{2}$  (right). b, c) Active liquid crystals exhibit disclinations of both  $\frac{1}{2}$  (top) and  $-\frac{1}{2}$  (bottom) charge, indicating the presence of nematic order. Scale bars,  $15\ \mu\text{m}$ . d) A sequence of images demonstrates buckling, folding and internal fracture of a nematic domain. The fracture line terminates with a pair of oppositely charged disclination defects (red arrow tracks  $\frac{1}{2}$  disclination; blue arrow tracks  $-\frac{1}{2}$  disclination). After the fracture, line self-heals and the disclination pair remains unbound. Time lapse, 15 s; scale bar,  $20\ \mu\text{m}$ . Source: ref. [77].

The asymmetry of positive “comet-like” semi-integer defects implies a strong bend deformation around their cores. This leads to an active stress that generates flow along the axis of symmetry of the defect, which becomes effectively propelled [163]. Conversely, deformations generating three-fold symmetric negative defects produce flow jets that tend to cancel out. Therefore, such defects act as effective stagnation points, mostly altering the flow directions and thus contributing to the creation of circulating flows or vortices [160]. Continuous creation, motion and annihilation of defects, reinstate nematic regions which undergo further instabilities, leading to a turbulent-like dynamic steady state. For saturating ATP concentrations, the AN flows feature average velocities much higher than maximum kinesin velocity [77,165]. In Chapter 2, these out-of-equilibrium dynamics are analysed in further detail. Finally, despite the seemingly chaotic behaviour of these out-of-equilibrium steady states, long-range correlations in the orientation of the trajectories of motile defects have been recently reported in experiments based on this active system [83]. However, the mechanism for such alignment is still controversial [166,167].

Even though some hydrodynamic theories can be extended to include more exotic ALC phases, for example, active chiral fluids [168] or active smectics [169], few experimental realizations have been able to report such phases [170]. Three-dimensional ALCs are also pursued in experiments although

---

their characterization is far more complicated. In addition, there is still lack control capabilities to ease the study of such systems *in vitro*.

### 2.3. Alteration and control of active flows: state of the art

Despite numerous efforts to characterize the morphology and dynamics of active systems, only a few recent works have focused on the development of strategies for the alteration or control of their flows. This section summarizes some of the most relevant contributions in which active flows are either conditioned or controlled by means of external constraints. Our own results have also been included in this section as I consider they represent a significant advance in this particular subject.

Strictly speaking, control of active systems goes back to the Neolithic, when wild animal groups started to be domesticated and guided, mainly by confinement [171]. Nevertheless, here, we refer to the control of the (often chaotic) flows that arise in active matter systems at the microscale, namely bacterial colonies, cell tissues, colloid swarms and active gels, whose control represents a notable challenge. In particular, actuation at the microscale will require proper application of complex materials, original strategies and the use of novel techniques, most of them still to be fully explored.

- Nutrient distribution

Under standard (favourable) conditions, animal groups do not exhibit a high level of organization. However, under certain hostile environmental conditions the complexity of these systems increases [74]. Similar behaviour is exhibited at the cellular level. Taking advantage of the chemotactic\* behaviour of bacteria like *Escherichia Coli* [172], researchers have used chemical attractants to condition the collective motion of colonies of this type of organisms. Such is the case of *E. Coli* colonies growing on agar surfaces with limited nutrients. Bacteria exhibit complex colony formation and various types of collective motion, like rotation of disk shaped aggregates or unusual motion patterns along ring shaped trajectories, as a response to this hostile environment [173,174]. Other experiments, make use of gradients of nutrient concentration to study the migration of these individuals in a more directional motion. For example, in convection-free containers such as capillaries or microchannels, bacteria collectively migrate towards regions where attractants abound, in the form of propagating concentration waves [172,175]. Similarly, temperature gradients have been useful to indirectly induce non-isotropic chemo-attractant secretion and thus wave propagation within the colonies [176]. Finally, phototactic microalgae accumulate beneath an excitation light, where collective effects lead to the emergence of radially symmetric convective flows [177].

---

\* from chemotaxis, movement of a motile cells or organisms in a direction corresponding to a gradient of concentration of a particular substance. The term *Taxis* (meaning arrangement) is referred to the movement of an organism in response to a stimulus. For instance, directed motion along gradients of light, temperature, stiffness is called photo-, thermo-, and durotaxis, respectively.



- Objects and confinement

Up to now, all the active systems described in this introduction develop flows in flat, smooth and featureless backgrounds. However, active systems in nature interact with complex environments and disorder. This can inhibit, for instance, the flocking of their constituents, and, consequently, may give rise to new alternative collective phenomena [178]. Active flows are thus obviously conditioned by the presence of static physical obstacles, which can be either dispersed within the active system or at the periphery, confining the generated flows. In the former case, it has been recently shown how, as the obstacle density increases, previously coherent flocks of rolling colloids [130] cease to be homogeneous in shape and instead reorganize in river-like flowing channels [179]. Above a critical density of obstacles, in spite of the high concentration of active constituents, order is completely lost (). Although the objects used as obstacles here are point-like, one can imagine a wide spectrum of different shape and distribution possibilities, which opens a new subfield where active matter will interact with complex landscapes.

On the other hand, how active flows behave inside confining environments is also an increasingly-studied scenario. Here, the main motivation is to explore the self-organization dynamics of active systems in adaptation to geometrical and/or topological constraints. *Per se*, confinement exists and it is effective when its characteristic dimensions and shape compete with the active flow length-scales of the studied material, which reorganizes to satisfy the imposed restrictions. Therefore, confinement represents a suitable choice not only to unveil the organizational modes of active materials under geometrical constraints, but also to investigate the role of their intrinsic length-scales.

Confinement of cellular tissues or bacterial colonies, with either circular wells [180,181] or adhesion patterns [182], respectively, has been shown to induce spontaneous circulation flows. Confining environments usually lead to highly-packed systems which feature LC-like ordered active domains and defects that must adapt to the shape of the container and satisfy the associated topological constraints [183]. Rectangular channels have provided with the framework to enhance directed motion of cell layers and groups of bacteria [184–186], where they develop unidirectional flows (Fig. 37). Similar results are obtained at lower scales in experiments where actin monomers self-assemble in nematically-ordered filament groups when they polymerize inside small enough rectangular cavities [187].

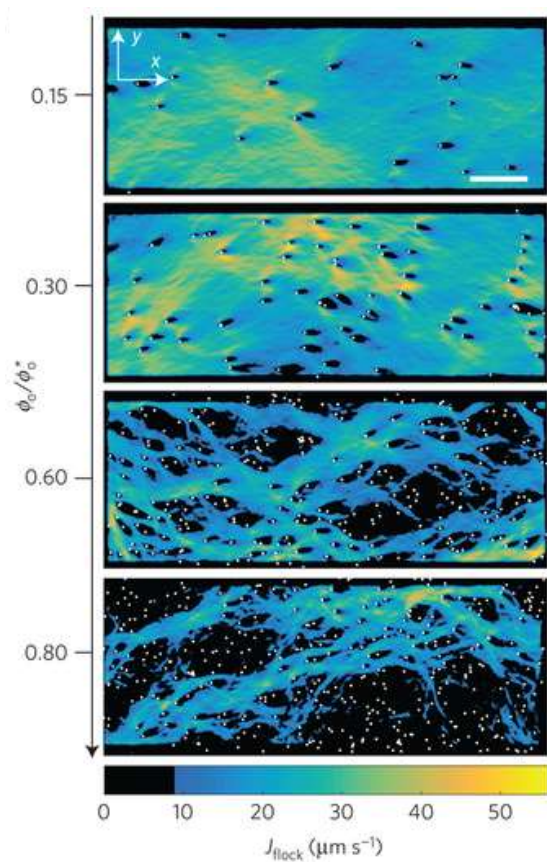


**Fig. 36. Flocks of rolling colloids through obstacle-decorated channels.** Magnitude of the flock current  $J_{\text{flock}}$  plotted for four different obstacle packing fractions. At low  $\phi_0$  colloid-depleted wakes form downstream of the obstacles. As  $\phi_0$  increases, a channel network forms and becomes increasingly sparse and tortuous. Scale bar, 200  $\mu\text{m}$ . Adapted from ref. [179].

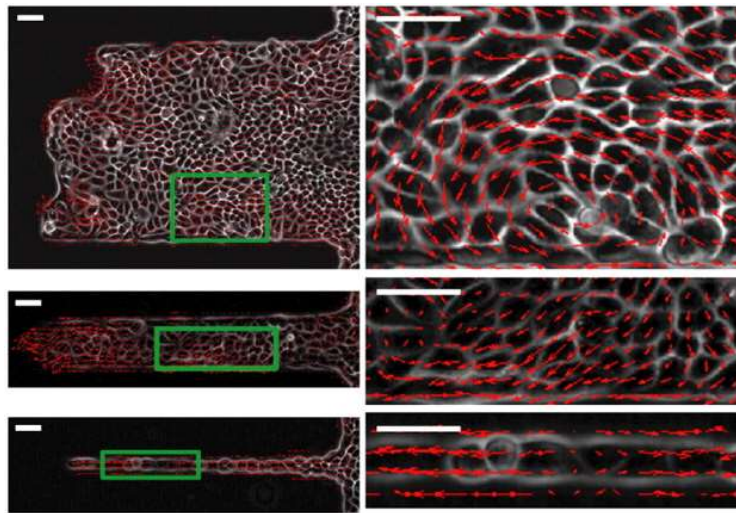


**Fig. 37. Tissue flows controlled by geometric constraints.** Micrographs of migrating cell layers and superimposed of velocity fields (red arrows). Vortex formation is observed in 400  $\mu\text{m}$  wide strips (top) but not in strips  $\leq 100 \mu\text{m}$  wide (middle and bottom). Right panels are magnified views of regions delimited by green boxes.

Of special interest is the study of how active LCs behave in spherical confinement, taking into account the rich behaviour of their passive counterparts [52]. Although the active materials exhibit more complex dynamics in three-dimensional spaces, confinement in spheres impose well-defined topological constraints (Section 1.5.4) that have been proven to be a valid strategy to regulate the spatiotemporal dynamics of nematically-ordered ALCs. MT-based active gels near equilibrium can adapt to confining walls of a sphere by bending mechanisms, which lead to structures where filaments assemble in bipolar or disk-like configurations [188] that have been also observed in encapsulated LCs in equilibrium [52]. Alternatively, highly dynamic systems, very far from thermal equilibrium, need to continuously remodel their structure in order to adapt to the frustrating environment. That is the case of an active nematic film (Section 2.2.2) in the interior of a spherical vesicle, where it develops featuring four  $+\frac{1}{2}$  defects that, due both to topological and elastic constraints, continuously rearrange, leading to oscillatory dynamics between tetrahedral and planar spatial defect configurations (Fig. 38) [82,189]. Spherical confinement suppresses further defect creation in the active nematic shell but it can induce the formation of other steady states by tuning the size and the rigidity of the container.

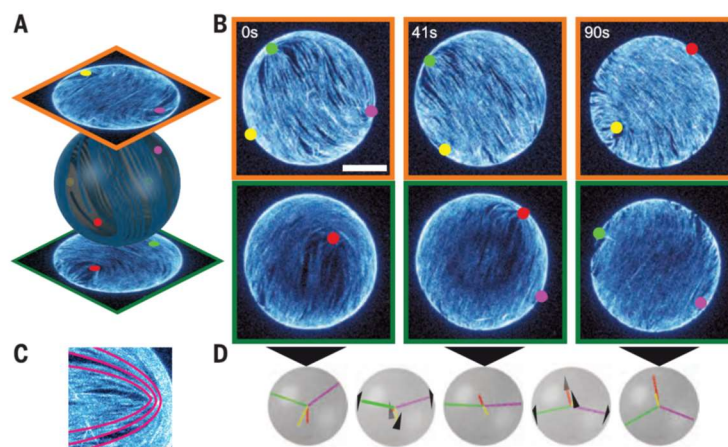


**Fig. 38. Defect dynamics of an active nematic film on the surface of a spherical vesicle.** a) Hemisphere projection of a 3D confocal stack of a nematic vesicle. The positions of four  $+\frac{1}{2}$  disclination defects are identified. b) Time series of

hemisphere projections over a single period of oscillation in which the four defects switch from tetrahedral ( $t = 0$  s) through planar ( $t = 41$  s) and back to tetrahedral ( $t = 90$  s) configurations. Scale bar, 20  $\mu\text{m}$ . **c**) Comet-like  $+\frac{1}{2}$  disclination defect with schematic of the orientation of the nematic director (red lines). **d**) Schematic of the defect configurations at the time points of **(b)** and intermediate times ( $t = 24$  s,  $t = 65$  s). The black arrowheads indicate the direction of defect motion. Source: ref. [82].

- Cell mechano-sensing

Active flows and stresses within epithelial tissues have been also controlled by modifying the adhesive properties of the substrates onto which they migrate by means of local adhesions and mechanical forces. *In situ* photo-responsive culture surfaces that allow local changes of adhesion by UV illumination is probably the most promising example [190]. Moreover, the capacity of cells to crawl vary at great extent with the mechanical properties of the substrates. As a matter of fact, some cell types (durotactic) are able to follow gradients of stiffness, a collective process that is implicated in many biological processes, which require directional cues [191,192]. *In vitro* experimental realizations have recently demonstrated this phenomenon and use it to control the directionality of tissue collective migration and growth [193].

- Hydrodynamic interactions: viscous fluids and liquid crystals

Constituents of active materials usually move inside and/or in contact with other passive materials that do not present specific interactions with the active units but that oppose to their motion. However, how this motion is affected by hydrodynamic interactions, such as viscous or friction drags, is not fully-understood yet, especially in scenarios where viscous forces dominate over inertia of the active constituents (low  $Re$ ) [73]. In these cases, the properties of the surrounding fluids and hydrodynamic interactions between active units and their environment have unavoidable effects on the organization of active systems. Recently, these effects have been considered for the alteration and command of flows arising from active materials.

Some examples include experiments with epithelial tissues that have demonstrated the influence of the viscoelasticity of the employed substrates, which induce changes in the spatiotemporal correlations in cell velocity during the movement of an epithelial monolayer [194]. Other realizations with tubulin/kinesin-based active nematics, reported by us, have also demonstrated the influence of viscosity on active materials, which have shown adaptability to the contact with high viscosity oils [195]. The second chapter of this thesis is specially dedicated to expand these observations.

Finally, by taking advantage of the strong hydrodynamic coupling effects that they experience, active materials have begun to be effectively controlled by LCs. As detailed in previous sections, the long-range orientational order exhibited by these materials results in anisotropic physical properties (Section 1.4), which have allowed to set motion directions and patterns of active flows, by imposing external (non-invasive) constraints. On the one hand, water-based non-toxic LLCs have shown applicability in the control of dense bacterial colonies, which are dispersed in the ordered fluids. Bacteria recognize subtle differences in LC deformations and thus respond to LC orientation by reorganizing both individual and collective dynamics. Further control capabilities have been possible by confining these bacterial baths between photo-responsive plates that allow to induce topological defects and impose well-defined anchoring patterns, and thus structured active flows, at specific positions [196] (Fig. 39).

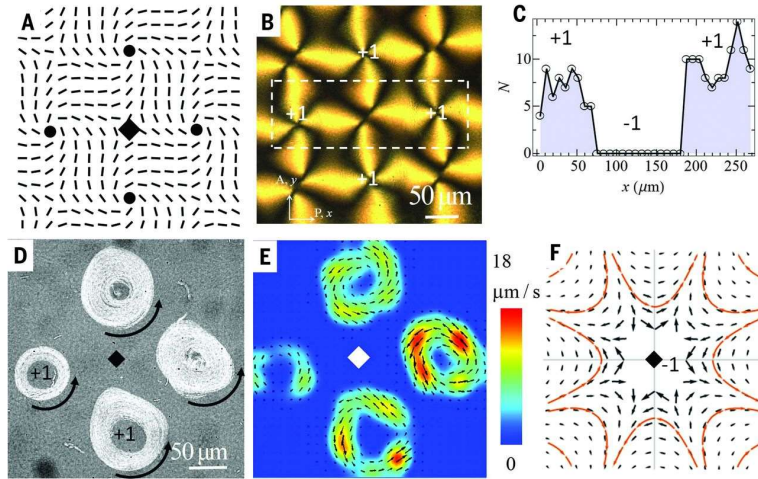


**Fig. 39. Unipolar circular flows of bacteria in a periodic pattern of defects.** **a)** Director pattern with +1 (cores marked by circles) and -1 defects (one core marked by a diamond). **b)** Polarizing optical microscopy texture of the pattern. A, analyzer; P, polarizer. **c)** Spatial modulation of the number of bacteria ( $N$ ) within the rectangular region in **(b)**. **d)** Counterclockwise trajectories of bacteria around four +1 spiraling vortices. **e)** Map of corresponding velocities. **f)** Active force calculated for a -1 defect. Source: ref. [196].

On the other hand, oily TLCs have been also used to control active flows, which in this case, will be altered by hydrodynamic coupling through a LC/water interface. In particular, our experiments with protein-based active nematics show how, by contact with smectic LCs, which exhibit marked rheological (viscous) anisotropy (Section 1.6), the active flows rapidly rearrange in well-defined dynamic structures such as rotating swirls, which adapt to circular patterns of viscosity at the interface [197]. In addition, the robust response of TLCs to anchoring conditions, temperature and external fields has allowed to reversibly change from the turbulent-like dynamics typical of active nematics to a laminar flow regime with pre-assigned unidirectional motion [198]. The results obtained from these realizations are developed in detail in Chapter 3.

In conclusion, control of active flows not only allows a better knowledge of active systems but also widens the possibilities for controlling biomaterials at different scales, and paves the way towards the use of the produced mechanical work in devices. This chapter highlights that control of active flows is usually based on confinement, patterns, gradients, and anisotropy, and, as we have seen, such influences can often be combined to obtain better responsiveness. Nevertheless, in the next decades, control of active matter will demand actuation capabilities, and, for now, only anisotropy can be *in situ* reconfigured by using LCs, which are probably the best candidates to fulfil this task.





---

## 3. Materials and methods

In this section, first, I explain in detail the procedures involved in the preparation of the active gel. I will then itemize the most relevant information about the LCs that have been used in the experiments. Subsequently, I describe the main setups with which the experimental realizations have been performed, and I include a description of the implicated surface treatments and surfactants. A fifth subsection is dedicated to the instrumentation for the application of external fields, and a sixth to describe the three microscopy techniques I have used for characterization, both their functioning fundamentals and their specific advantage for the imaging of our experiments. Finally, I summarize the basics of the algorithms and functions used for image processing and data analysis.

### 3.1. The active gel

The active gel used in all the experimental realizations is based on bundles of tubulin filaments (microtubules, MTs) and kinesin motor proteins and it has been already introduced in previous sections 2.1.2 and 2.2.2. Here, I summarize the bottom-up strategy by which this active system is prepared, from the obtaining of the main constitutive proteins to the active gel assembly.

#### 3.1.1. Purification of tubulin

Heterodimeric ( $\alpha,\beta$ )-tubulin (obtained from the Brandeis University Biological Materials Facility) was purified from bovine brain tissue through two cycles of polymerization–depolymerization in high-molarity PIPES buffer [199].

#### 3.1.2. Polymerization of microtubules

Tubulin (8 mg/mL) is incubated at 37°C for 30min in an M2B buffer (80mM PIPES, 1mM EGTA, 2mM MgCl<sub>2</sub>) (Sigma, P1851, E3889 and M4880, respectively) supplemented with the reducing agent dithiothreitol (DTT, 0.4 mM) (Sigma, 43815) and with Guanosine-5'-[( $\alpha,\beta$ )-methylene]triphosphate (GMPCPP, 0.6 mM) (Jena Biosciences; NU-405), a non-hydrolysable analogue of the nucleotide GTP\*. By controlling the concentration of GMPCPP we are able to prepare high-density suspensions of short MTs (1-2  $\mu$ m). For the characterization with fluorescence microscopy, part of the initial tubulin (3%) was fluorescently labelled with Alexa-647 (Sigma, A20006), which is attached by a succinimidyl ester linker to a primary amine on the tubulin surface. Alexa-647 yields the most photo-stable MTs while also minimizing the amount of undesirable cross-linking [200]. After incubation at 37°C, MT suspensions were allowed to sit at room temperature for 5 hours. Subsequently, MT suspension is aliquoted in small volumes, snap-frozen in liquid nitrogen, and kept at -80°C.

---

\* As GTP, GMPCPP promotes the association between tubulin heterodimers although it completely suppresses the dynamic instability of MT [219], which affects structural and mechanical properties of MTs. Moreover, MTs composed of tubulin-GMPCPP are stiffer and allow faster kinesin transports (rates  $\sim$ 30% faster) than those of tubulin-GDP MTs [220].

### 3.1.3. Expression of kinesin

*Drosophila Melanogaster* heavy chain kinesin-1, K401-BCCP-6His (truncated at residue 401, fused to biotin carboxyl carrier protein (BCCP) and labelled with six histidine tags), has been expressed in *Escherichia Coli* by using the plasmid WC2 from The Gelles Laboratory (Brandeis University, MA, USA) and purified with a nickel column [201].

In brief, a single *E. Coli* colony is grown in LB broth (Sigma, L3022), supplemented with biotin (Sigma, B4631), ampicillin (Sigma, A9518) and chloramphenicol (Sigma, C0378) until reaching an OD<sub>600</sub> of 0.60. Expression is induced at by adding 1mM IPTG (Melford Laboratories, 367-93-1). Culture is kept shaking at 22°C overnight. After pelleting cells by centrifugation at 4,000rpm and 4°C for 30 min, the pellet is resuspended in a lysis buffer and sonicated. Centrifugation at 66,000 rpm and 4°C for 15 minutes is enough to get the expressed protein in the low-speed supernatant, which is loaded into a nickel column (Ni-NTA Agarose resin, Qiagen, 30310) for purification. The resin is washed with a 50mM HEPES (Sigma, H33759) solution, supplemented with 4 mM MgCl<sub>2</sub> (Sigma, M8266), 20mM imidazole (Sigma, I5513), 10 mM β-Mercaptoethanol (Sigma, M6250) and 50 μM ATP (Sigma, A2383), and kinesin is subsequently eluted against high concentration solution of imidazole (500mM). A desalting column (Healthcare GE, PD10 Sephadex Columns, G25M, 17-0851-01) is used to exchange the buffer solution to the HEPES buffer. The protein can be concentrated with a protein concentrator spin column (Vivaspin, VS2012). At this point, the concentration is estimated by means of absorption spectroscopy ( $A_{280}$ ,  $\epsilon=30370 \text{ M}^{-1}\text{cm}^{-1}$ ). Finally, kinesin is stored at a specific concentration in a 40%wt/vol sucrose (Sigma, 84097) solution at -80°C [201].

### 3.1.4. Clustering of molecular motors

Biotin-Streptavidin pair presents one of the strongest and more specific noncovalent interactions known in biochemistry [202]. In our experiments, biotinylated kinesin motor proteins and tetrameric streptavidin (Invitrogen; 43-4301) are incubated on ice for 30 minutes at specific stoichiometric ratio (~2:1) in order to obtain kinesin-streptavidin motor clusters.

### 3.1.5. ATP hydrolysis and regeneration system

In order to walk along MTs, motor proteins undergo conformational changes that require ATPase activity, i.e. hydrolysis of one of the three phosphate groups of ATP, which, in cells, stores the energy released from oxidations of nutrients.

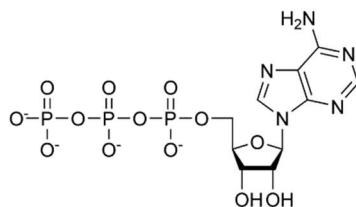


Fig. 40. Skeletal formula of deprotonated Adenosine triphosphate (ATP).

The essence of the action of ATP is its ability to lose its terminal phosphate group by hydrolysis and to form adenosine diphosphate (ADP):



Where  $\text{P}_i$  denotes an inorganic phosphate group such as  $\text{H}_2\text{PO}_4^+$ . The biological standard values for ATP hydrolysis at  $37^\circ\text{C}$  are  $\Delta_r G^0 = -31 \text{ kJ mol}^{-1}$ ,  $\Delta_r H^0 = -20 \text{ kJ mol}^{-1}$ , and  $\Delta_r S^0 = +34 \text{ J K}^{-1} \text{ mol}^{-1}$  [203]. The hydrolysis is therefore exergonic ( $\Delta_r G^0 < 0$ ) under these conditions, and  $31 \text{ kJ mol}^{-1}$  is available for driving other reactions and processes like motor protein conformational changes. The precise  $\Delta_r G^0$  for these reactions depend on ionic strength of metal ions in solution such as  $\text{Mg}^{2+}$ , which help to stabilize the ATP molecule, making it biologically active. Finally, for higher ATP concentrations  $\Delta_r G = \Delta_r G^0 - RT \log \frac{[\text{ATP}]}{[\text{ADP}] \cdot [\text{P}_i] \cdot [\text{H}_3\text{O}^+]}$  decreases, thus activity of the motors ( $\sim \log[\text{ATP}]$ ) increases.

In the active gel, ATP must be regenerated to keep its concentration constant and maintain the system out of equilibrium. The enzyme pyruvate kinase (PK) is able to transfer a phosphate group from phosphor(enol)pyruvate (PEP) to ADP generating pyruvate and ATP.

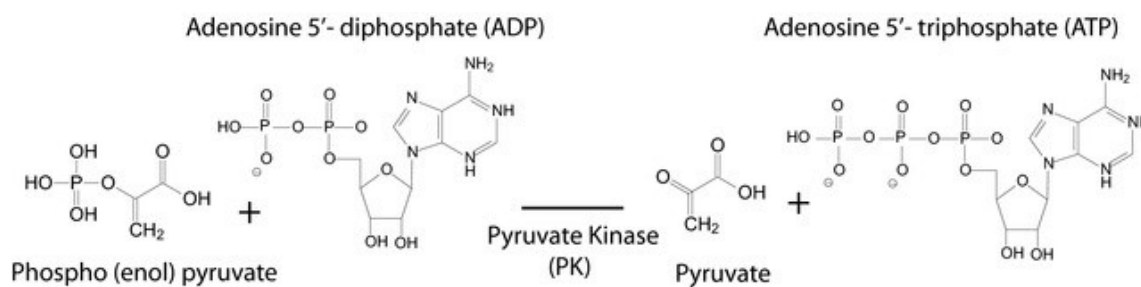


Fig. 41. Regeneration of ATP by pyruvate kinase (PK).

### 3.1.6. Active gel assembly

MTs are mixed with the motor clusters that act as cross-linkers, and with ATP (Sigma, A2383) that drive the activity of the gel. The aqueous dispersion contains a non-adsorbing polymer (poly-ethylene glycol, PEG, 20 kDa) (Sigma, 95172) that promotes the formation of filament bundles through depletion interaction. As explain above, to maintain a constant concentration of ATP during the experiments, we add an enzymatic ATP-regenerator system based on PEP (Sigma, P7127) and PK (Invitrogen; 434301), which convert ADP back into ATP. Several anti-oxidant components are also included in the solution to prevent protein residues to form disulphide bonds, to minimize the damaging of fluorophores by oxygen species, and suppress photobleaching during characterization by fluorescence microscopy. The anti-oxidants are the following: Trolox (Sigma, 238813), Dithiothreitol (DTT, Sigma, ref. 43815) and the oxygen-scavenging enzymatic mixture, which includes Glucose (Sigma, G8270), Glucose oxidase (Sigma, G2133) and Catalase (Sigma, C1345).

PEGylated surfactants must be added to procure biocompatible water/oil interfaces in subsequent steps. In experiments involving water/LC interfaces, the choice of surfactant is crucial as it determines the disposition of the LC molecules at the interface with the active aqueous suspension (Section 1.5.2). More information about the employed surfactants is given in Section 3.3.

This active gel is very robust and it can be formed over a wide range of microscopic control parameters [77,200].

Parameter	Concentration range
[PEG] (%wt/v)	0.4 – 10
[MTs] (mg·mL <sup>-1</sup> )	0.5 – 5
[Streptavidin]* (μg·mL <sup>-1</sup> )	2 – 40
[ATP] (mM)	0.1 – 2

However, concentrations for the standard experiments are chosen to assure an optimal performance of the active system, in terms of average flow velocity.

Parameter	Concentration
[PEG] (%wt/v)	0.8
[MTs] (mg·mL <sup>-1</sup> )	1.3
[Streptavidin] (μg·mL <sup>-1</sup> )	7
[ATP] (mM)	0.7 or 1.4

Other compounds with antioxidant (AO) functions or part of the ATP-regeneration (R) system are always used in the same concentrations:

Parameter	Concentration
[Trolox] (AO, mM)	2
[DTT] (AO, mM)	6
[Glucose] (AO, mg·mL <sup>-1</sup> )	0.3
[Glucose oxidase] (AO, mg·mL <sup>-1</sup> )	0.2
[Catalase] (AO, mg·mL <sup>-1</sup> )	0.04
[PEP] (R, mM)	27
[PK/LDH] (R, units PK·mL <sup>-1</sup> )	26
[MgCl <sub>2</sub> ] (mM)	3

---

\* Streptavidin concentration sets the concentration for the motor clusters.

## 3.2. The liquid crystals

In part of the experiments reported in this thesis we have combined active and passive LCs (Chapter 3 and 4). The passive analogues are always thermotropic LCs, which feature nematic and/or smectic-A phases. In general, we have mainly used two homologous alkyl-cyanobiphenyl compounds, which are chemically very stable:

- 4-pentyl-4'-cyanobiphenyl (**5CB**, Synthron Chemicals, ST00683, Fig. 42) features LC behaviour between 18 and 35°C. It exhibits a high birefringence and positive electric anisotropy.

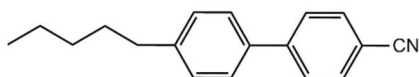


Fig. 42. Skeletal formula of 4-pentyl-4'-cyanobiphenyl (**5CB**).

- In some experiments, where electric fields were applied normal to the equilibrium director field orientation, **MLC-7029** (with  $\epsilon_a < 0$ , secret formula, Merck) has replaced 5CB, in order to be able to actuate on the nematic orientation by electric fields perpendicular to the far-field.
- 4-octyl-4'-cyanobiphenyl (**8CB**, Synthron, ST01422) features LC behaviour between 21.4 and 40.4°C. Differently from 5CB, 8CB shows both nematic (33.4 – 40.4°C) and Smectic-A phase (21.4 – 33.4°C). Like most usual organic mesogens, 8CB is diamagnetic and exhibits a positive diamagnetic anisotropy ( $\chi_a \sim 10^{-6}$  [3]). A magnetic field of the order of 1 kG will exert a torque able to align a layer of nematic 8CB.

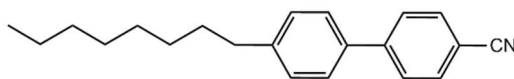
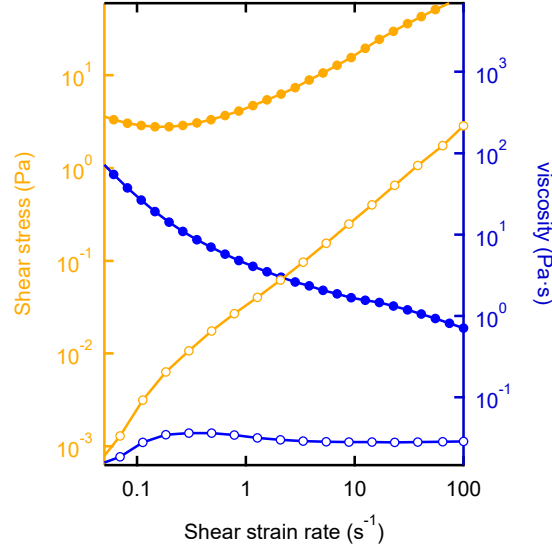


Fig. 43. Skeletal formula of 4-octyl-4'-cyanobiphenyl (**8CB**).

Depending on the desired interaction between the LC and the active material, we choose between the nematic (low viscosity, low viscous anisotropy, flow reporter) or the smectic-A phase (high viscosity, high viscous anisotropy, flow commander).

### 3.2.1. Rheological measurements of 8CB

The rheological properties of 8CB have been crucial for the experiments in Chapter 3, based on the remarkable anisotropy in the viscosity of the Smectic-A phase (Sections 1.4.4 and 1.6). Although we have not obtained the value for its viscous anisotropy, we have been able to measure its average viscosity, through shear stress measurements, when featuring nematic or smectic-A phase (Fig. 44).



**Fig. 44. Rheology measurements for 8CB.** Average steady-state shear stress (orange) and viscosity (blue) for 8CB measured in the SmA phase (25 °C, ●) and in the nematic phase (35 °C, ○). Measurements have been performed using a Thermo Haake RheoStress 1 rheometer, in constant stress mode, using cone-plate geometry with a 1°, 60 mm diameter titanium cone.

In order to determine the viscosities that the AN senses when in contact with the different 8CB phases we need to know an estimate of the shear strain rate ( $\dot{\gamma}$ ) that the AN exerts to the nematic and the Smectic-A phase. In order to obtain a rough approximation of this value, we will consider that the shear within the AN due to the motion of defects one past each other, then we can assume that  $\dot{\gamma} \sim \frac{\Delta v}{d}$ , where the velocity increment ( $\Delta v$ ) can be considered as twice the average speed of the shearing defects, and  $d$  is the distance between them ( $d \sim 2/\sqrt{n}$ , where  $n$  is the defect density).

Parameter	Nematic phase	Smectic-A phase
$\bar{n}$ ( $\mu\text{m}^{-2}$ )	$6 \cdot 10^{-5} \pm 1 \cdot 10^{-5}$	$4 \cdot 10^{-4} \pm 1 \cdot 10^{-4}$
$\bar{v}$ ( $\mu\text{m} \cdot \text{s}^{-1}$ )	$20 \pm 6$	$3 \pm 1$
$d$ ( $\mu\text{m}$ )	$187 \pm 11$	$71 \pm 12$
$\dot{\gamma}$ ( $\text{s}^{-1}$ )	$0.2 \pm 0.1$	$0.1 \pm 0.3$

From these data and the rheological measurements of 8CB at different temperatures, we can conclude that the viscosity that the AN senses when it evolves in contact with nematic and Smectic-A phase differs by a factor  $\sim 10^2$ - $10^3$  Pa·s. Experimentally, we have been able to prove that the AN evolving in contact with 8CB featuring the N $\rightarrow$ SmA phase transition shows an increase in defect density via the formation of wall instabilities (Section 2.2.1), and a decrease in defect speed, as would be predicted from the results reported in Chapter 2.

### 3.3. Experimental setups

The study of the active nematic at flat interfaces has been carried out in open-cavities, where the active material develops underneath a volume of a non-volatile, low-density, oily compound (usually silicone oils or LCs). For the characterization of spherical active nematic shells, observed in water-in-oil emulsions, flow cells have been used. In the experiments with water-in-LC emulsions, we induce specific anchoring of the LC molecules onto the substrates (Section 1.5.2) by means of coating or chemical functionalization methods (Section 3.4).

#### 3.3.1. Open cell

A block of poly-dimethylsiloxane (PDMS) with a cylindrical well of diameter 5 mm and height from 1-8 mm (depending on the experiment) is manufactured using a custom mold. The block is glued using a UV-curing adhesive (Norland, NOA81) onto a bioinert and superhydrophilic polyacrylamide (PAA)-coated glass (Section 3.5.1) that prevents the protein-based system from denaturation (Fig. 45).

The pool is first filled with  $\sim 50 \mu\text{L}$  of oil, either an isotropic silicone oil (Bluestar Silicones) or a TLC (Section 3.2). Subsequently,  $1 \mu\text{L}$  of the active gel is injected under the oil. In the experiments where we have used the LC 8CB, the system is heated up to  $35 \text{ }^\circ\text{C}$  in a homemade oven in order to promote transition to the less viscous nematic phase of the mesogen, which facilitates the spreading of the active gel onto the PAA substrate. After several minutes at room temperature, the active nematic is spontaneously formed at the flat water/oil interface. Unlike the conventional flow cells, in which a layer of the active gel is confined in a thin gap between two glass plates [77], this setup enables us to use high viscosity oils in contact with the active nematic.

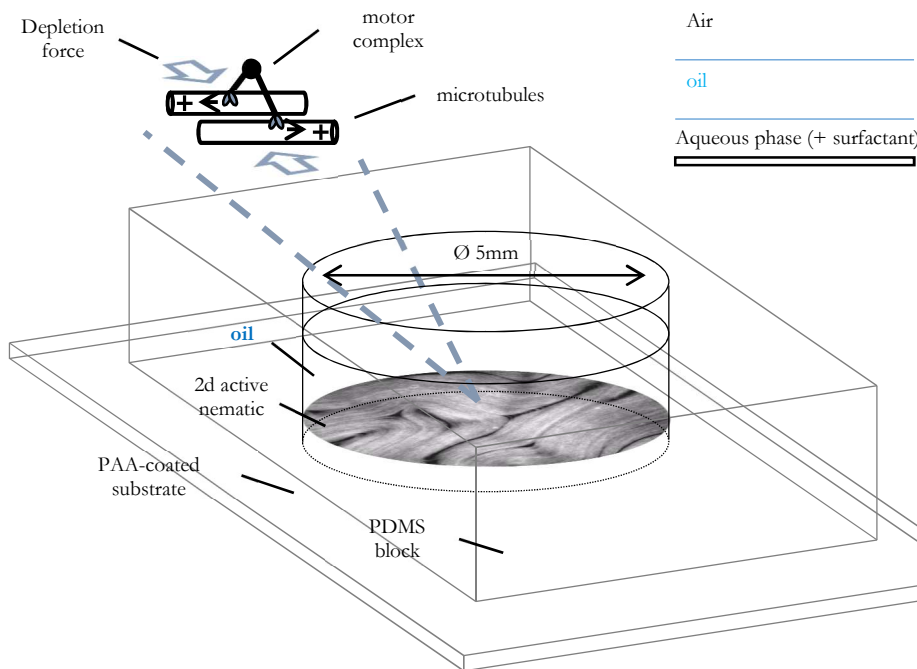


**Fig. 45. Schematic representation of the experimental setup.** The active nematic is formed between an oil volume and a Polyacrylamide (PAA)-coated substrate, which avoids protein adhesion.



### **3.3.2. LC flow cell**

Flow cells are prepared by assembling two parallel coated or functionalized (Section 3.4) glass plates with two sheets of double-sided tape (thickness 70  $\mu\text{m}$ , 3M) between them, acting as spacers. The cells are filled by capillarity with water-in-oil emulsions (Materials and methods, Section 3.4) and sealed using UV-curing epoxy glue (Norland Optical, NOA81), which confers robustness to the system. Indium Tin Oxide (ITO)-coated plates have been used for application of electric-fields normal to the plates.

## **3.4. Active emulsions**

Active water-in-oil emulsions have been prepared by mechanically mixing the active aqueous suspension in either isotropic oils or in a thermotropic nematic LCs (Materials and methods, Section 3.2) in the presence of a proper PEG-functionalized surfactant (Materials and methods, Section 3.6). For emulsions based on isotropic oils we have used the fluorinated oil 3-ethoxy-1,1,1,2,3,4,4,5,5,6,6,6-dodecafluoro-2-trifluoromethyl-hexane (3M, NOVEC-7500) supplemented with a fluorinated surfactant. For water-in-LC emulsions we have employed NLCs 5CB or MLC-7029 (Materials and methods, Section 3.2) as host fluids. In this case, surfactants are dispersed in the aqueous phase and specifically chosen to induce either planar or homeotropic anchoring to the LC molecules (Materials and methods, Section 3.6).

## **3.5. Surface treatments**

For the preparation of the experimental setups (Materials and methods, Section 3.3), substrates are always chemically and/or mechanically treated for specific reasons. On the one hand, surfaces in contact with the active material must be coated with a polymeric brush, which avoids direct contact between the constituent proteins of the active material and the glass by steric repulsion. On the other hand, plates used for LC flow cells need to impose well-defined anchoring conditions to the confined mesogens (Section 1.5.2).

### **3.5.1. Polymeric brush**

Clean and activated glass (activation with an alkaline solution or with  $\text{O}_2$  plasma treatment) is first silanized with an acidified ethanolic solution of 3-(trimethoxysilyl)propylmethacrylate (Sigma, 440159), which will act as a polymerization seed. The silanized substrates are rinsed with ethanol and deionized water and subsequently immersed in a degassed solution of acrylamide monomers (for at least 2 h) in the presence of the initiator ammonium persulfate (APS, Sigma, A3678) and  $\text{N,N,N',N'}$ -tetramethylethylenediamine (TEMED, Sigma, T7024), which catalyses both initiation and polymerization of acrylamide. Glass substrates are stored in the polymerization solutions and they are used for up to three weeks.

### **3.5.2. Hydrophobization by self-assembled monolayers of silanes**

Silane coupling agents are organosilicon compounds that are widely used to covalently bond organic materials to properly activated (hydroxylated) ceramic surfaces. Here, mainly two hydrophobic silane

compounds are used to functionalize both glass and ITO-coated plates. Both induce high water contact angles and homeotropic anchoring of contacting TLCs.

- Alkyl silanes

The surface of a glass slide or an ITO-coated glass slide (depending on the experiment) can be functionalized with Dimethyloctadecyl[3-(trimethoxysilyl)propyl]ammonium chloride (DMOAP, Fig. 46) in order to impose homeotropic anchoring conditions to a contacting TLC. The substrate is first degreased to ensure a correct functionalization. In case of using a glass plate, the substrate can be cleaned and activated at the same time using piranha solution, 1:3 H<sub>2</sub>O<sub>2</sub> (33%wt/v, Sigma 216763)/H<sub>2</sub>SO<sub>4</sub> (lab grade) v/v. The cleaning of an ITO-coated glass must be carried out with a less aggressive procedure to avoid its damage. The plate is cleaned with a diluted soap solution (Micro-90® concentrated cleaning solution from Sigma-Aldrich in purified water, 1% w/w), purified water (both followed by 2 minutes of sonication), acetone (lab grade), ethanol (Panreac, 121085.1212) and purified water again (all three require 10 minutes of sonication). The clean substrate is immersed in a very diluted DMOAP (Sigma, 435694) aqueous solution (0,01M) for 30 minutes at room temperature. The plate is then rinsed with purified water, dried with nitrogen and heated at 130°C during 1,5 hours to enhance the completion of the reaction.

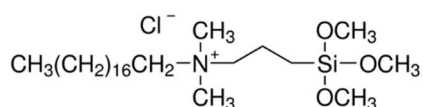


Fig. 46. Formula of DMOAP.

- Fluoroalkyl silanes

Aquapel® (PPG industries) is a solution of different chemicals including a fluoroalkyl silane. This mixture enhances fast functionalization (1-2 minutes) of clean glass at room temperature without curing step.

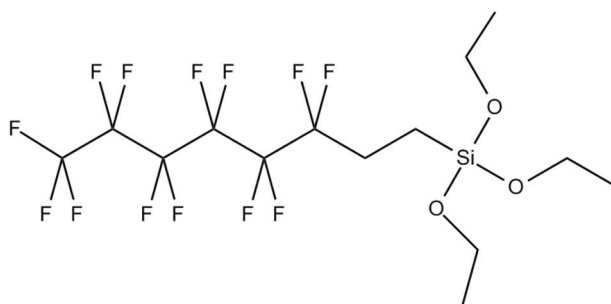


Fig. 47. Formula of a fluoroalkylsilane, the main ingredient of Aquapel®.

### 3.5.3. Polymeric coatings

Usually, polymer-coated plates are rubbed with a velvet cloth to enhance unidirectional planar anchoring of the LC molecules.

Glass slides and coverslips (ITO-coated in case we need to apply an electric field) can be coated with different polymers, such as polyimide (PI, PI-2555, DuPont-HD Microsystems) or polyvinyl alcohol (PVA, 89% hydrolysed, MW ~166,000g/mol, Sigma, 363103), to induce planar anchoring of the TLCs. The substrates are first degreased and activated by 10-minutes sonication in a diluted soap solution, ethanol (lab grade) and a sodium hydroxide solution (lab grade, 0.1M). Alternatively, more aggressive activation in piranha solution (1:3 H<sub>2</sub>O<sub>2</sub> (33%wt/v, Sigma, 216763)/ H<sub>2</sub>SO<sub>4</sub> (lab grade)) for 30 minutes has been also used. ITO-coated plates were usually activated in a mixture of 5:1:1 purified H<sub>2</sub>O/H<sub>2</sub>O<sub>2</sub> (33%wt/v, Sigma, 216763)/NH<sub>4</sub>OH (28-30%, Sigma, V000637) (v/v/v) at 70-80°C for 1,5h. The plates are rinsed, dried with a nitrogen flow and heated at 130°C for 10 minutes to get rid of any trace of water. The plate is then placed in a spin-coater (KW-4A, Chemat Scientific) and covered with the polymer solution (1-3%wt/v) using a syringe equipped with a 0.2µm-pore size nylon filter (Sigma, Z290823). The substrates are spun at 600rpm for 3 seconds and 2000 rpm for 30 seconds. Finally, the thin layer of polymer is cured at 130/300°C for PVA/PI for 2 hours, obtaining, at the end, a uniform coating of ~1-5µm thickness.

## 3.6. Surfactants

The active material used in the experiments (water-based) always develops in contact with an oil layer (Section 2.2.2 and Materials and methods, Section **¡Error! No se encuentra el origen de la referencia.**). In order to stabilize the involved water/oil interfaces, either in flat geometries (Chapters 2 and 3) or in emulsions (Chapter 4), a surfactant is required. In addition, only non-ionic surfactants have been employed, all of them necessarily functionalized with polyethylene glycol (PEG) coils to prevent direct interaction between the protein constituents of the active gel and the contacting oils. Finally, even though not fully understood, the presence of hydrophilic PEG moieties seems to enhance depletion of the active gel towards the water/oil interface.

Different PEG-based surfactants have been used in this thesis. For stabilization of water/silicone oil interfaces (Chapter 2), a copolymer surfactant (poloxamer) has been used dissolved in the active system at concentrations between 1-3%wt/v. For water/LC interfaces (Chapters 3 and 4) the same poloxamer has been used when planar anchoring of the LC molecules was desired at the interface. Conversely, for homeotropic anchoring conditions PEG-functionalized phospholipids have been used at concentrations ~1%wt/v dissolved in the aqueous phase. For a particular experiment in Chapter 4, also a Polysorbate has been used, inducing tilted degenerate anchoring at the water/LC interface of water-in-LC emulsions. Finally, for water-in-oil emulsions, a fluorinated surfactant was employed, dissolved at 2%wt/v in the oily phase.

#### - Poloxamers

A triblock copolymer consisting of a central hydrophobic block of polypropylene glycol (PPG) flanked by two hydrophilic blocks of PEG (Fig. 48). In our case, we used Pluronic F-127 (Sigma,

P2443), with approximately 101 repeat units of ethylene glycol per PEG block and approximately 56 units of propylene glycol.

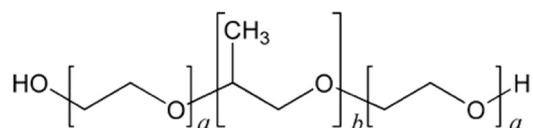


Fig. 48. Formula of Pluronic®.

- Polysorbates

In spite of its short PEG chain, PEG-20 sorbitan monooleate (Tween-80, Sigma, P4780) has been suitable for the preparation of the active nematic shells in TLCs. Usual concentration ranged between 5-10%wt/v.

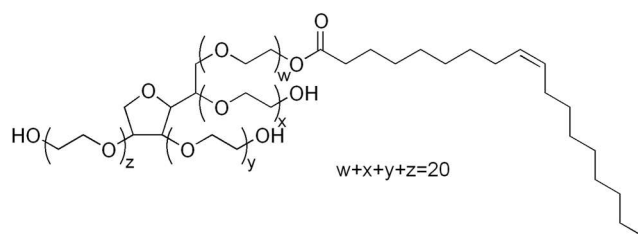


Fig. 49. Formula of Tween-80

- PEG-functionalized lipids

In our experiments, mainly highly hydrophilic PEG-functionalized phospholipids (long PEG chains) have been used (DSPE-PEG<sub>2000</sub>D<sub>3</sub>, Avanti, 880229, Fig. 50*a*). These kinds of lipids are easily dispersible and soluble in aqueous buffered solutions by vortex-stirring and short-period sonication. Nevertheless, high concentrations of these molecules at interfaces enhances the interaction both between adjacent PEG chains via hydrogen bonding, leading to gelation events that decrease the fluidity of the interface [204]. In order to prevent this phenomenon, we have employed PEG-functionalized phospholipids with unsaturated alkyl chains (DOPE-PEG<sub>2000</sub>D<sub>3</sub>, Avanti, 880130P, Fig. 50*b*), whose shape and isomerization seem to introduce more freedom and fluidity within the monolayer.

On the other hand, other lipids (without PEG, DSPC and DOPC (Avanti, 850365 and 850375, respectively, Fig. 50*c,d*) can be also added at the interface as spacers between the PEG-based molecules. In this case, direct dispersion and dissolution in the aqueous phase is not a valid option as phospholipids without PEG are highly insoluble in water. Therefore, mixed lipid vesicles must be prepared.

### 3.6.1. Preparation of lipid vesicles

PEG-functionalized and non-functionalized phospholipids are dissolved in separate glass vials at 10 mM concentration in a chloroform (J.T. Baker, 7386)/methanol (Scharlau, ME0315100)

mixture (2:1 v/v). Lipid solutions can be kept in hermetically-sealed glass vials at  $-21^{\circ}\text{C}$ . The lipid solutions are combined in a round bottom flask in an appropriate ratio (the molar fraction of the PEG-based surfactant should not be higher than 10%) in order to obtain 1 mL of the lipid solution. The solvent is carefully evaporated with a nitrogen stream (20 minutes) and vacuum (1 hour). Once it is dry, the lipid is hydrated overnight with 10mL (or 10 times the volume of the initial lipid solution) of a buffer solution (normally HEPES or phosphate buffer,  $\text{pH}\sim 6-8$ ). Subsequently, strong agitation will result in the suspension of the lipid mixture in the aqueous buffer (buffer temperature should be above the phase transition of the lipid). This procedure yields to a milky dispersion of large, multilamellar vesicles (LMVs) of a mixture of lipids at 1 mM concentration.

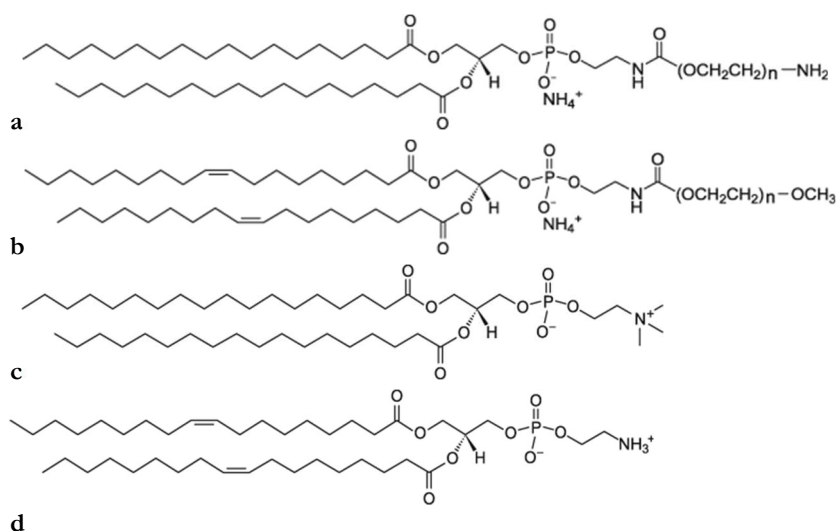


**Fig. 50. Formulas of the employed phospholipids.**

- 1,2-distearoyl-sn-glycero-3-phosphoethanolamine-N-[amino(polyethyleneglycol)] (DSPE-PEG-NH<sub>2</sub>)
- 1,2-dioleoyl-sn-glycero-3-phosphoethanolamine-N-[methoxy(polyethylene glycol)-2000] (DOPE-PEG-OCH<sub>3</sub>)
- 1,2-distearoyl-sn-glycero-3-phosphocholine (DSPC).
- 1,2-dioleoyl-sn-glycero-3-phosphoethanolamine (DOPE)

- Fluorinated surfactants

For stabilization of interfaces between water and fluorinated oil (Section 3.3.2), triblock PFTE-PEG<sub>600Da</sub>-PFTE surfactant (RAN Biotechnologies) is dispersed in the oily phase at 2%<sub>w/w</sub> concentrations.

---

## 3.7. Application of external fields and temperature control

Application of electric and magnetic fields is used for the orientation of passive LCs. The active system is not directly affected.

### 3.7.1. Electric fields

Electric fields have been applied with a function generator (Agilent Technologies DSO-X 2002A) connected to a power amplifier (TREK PZD700) and monitored with an oscilloscope (integrated in the current generator). We apply square wave AC fields (50% duty cycle) with  $f = 1.0$  kHz and amplitudes in the range 0–10 V in LC cells with coated ITO plates.

### 3.7.2. Magnetic fields

A permanent magnet assembly, compatible with microscope setups, provides homogeneous planar magnetic field with a maximum strength of 4 kG. The magnet is built as a Halbach cylindrical array [205] consisting on eight identical N52- grade NdFeB cubic magnets (cube size, 25.4 mm; K&J Magnetics; BX0X0X0-N52). The magnets are assembled, with the suitable geometric arrangement and magnetic moment orientation, using a 3D-printed poly-lactic acid (PLA) assembly (Fig. 51).

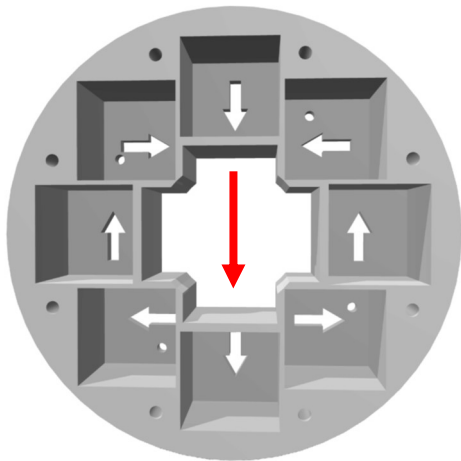


**Fig. 51. Structure for the assembly of the array of magnets.** Eight cubic magnets are placed in the holes with specific orientation (white arrows). When full of magnets, a homogeneous magnetic field is created in the direction of the red arrow.

This is an extremely cost-effective setup to generate a magnetic field that is strong and homogeneous enough to align common thermotropic LCs. The strength of the magnetic field, which is highest at the center of the magnet array (magnet midplane is engraved as a circular groove on the frame), can be adjusted by modifying the vertical position of the sample with respect to the magnets.

### 3.7.3. Temperature control

In order to control the temperature, the samples are held inside a thermostatic oven build with Thorlabs SM1 tube components and tape heater, and controlled with a Thorlabs TC200 controller.

### 3.8. Imaging

Below, I briefly describe the fundamental functioning of the three main optical imaging techniques used for the characterization of the samples involved in this work, and I give technical details about the employed setups.

#### 3.8.1. Polarized-light microscopy

The director field configuration of LCs is usually characterized by means of polarized-light microscopy, as it is the most suitable technique to image optically anisotropic (birefringent) materials (Section 1.4.3).

Polarized-light microscopy is based in two crossed polarizers (polarizer and analyzer), i.e. their easy axes are oriented at right angles with respect to each other, between which the samples are placed. When entering a LC, plane-polarized light will split in two individual wave components that are each polarized in mutually perpendicular planes. The velocities of these components, which are termed the ordinary and the extraordinary wave fronts, are different and vary with the propagation direction through the specimen (Fig. 52). After passing through the sample, the light components become out of phase, but are recombined with an interference that ranges from fully constructive to fully destructive when they pass through the analyzer [19]. These interactions will trigger variations of light intensity that provide information about the local average orientation of the sample constituents.

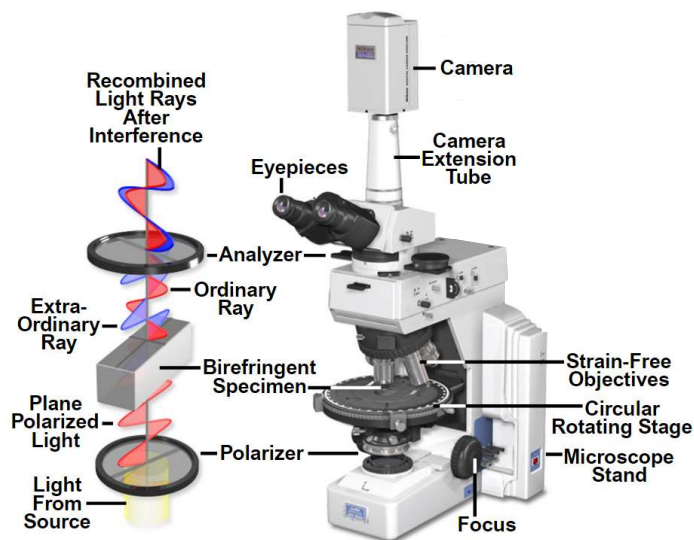


Fig. 52. Polarized-light microscopy. Adapted from ref. [19].

Polarized light microscopy is performed with a Nikon Eclipse 50iPol upright microscope. Images are acquired with an AVT Marlin 131B CMOS digital video camera.

### 3.8.2. Fluorescence microscopy

Routine observations of active samples based on fluorescently-labelled microtubules (MTs, Section 3.1.2) were normally performed by means of fluorescence microscopy.

The emission of light through the fluorescence process is nearly simultaneous with the absorption of the excitation light due to a relatively short time delay between photon absorption and emission, ranging usually less than a microsecond in duration [19]. The basic function of a fluorescence microscope is to irradiate the specimen with a desired and specific band of wavelengths, and then to separate the much weaker emitted fluorescence from the excitation light. In a properly configured microscope, only the emission light should reach the detector so that the resulting fluorescent structures are superimposed with high contrast against a very dark background [19].

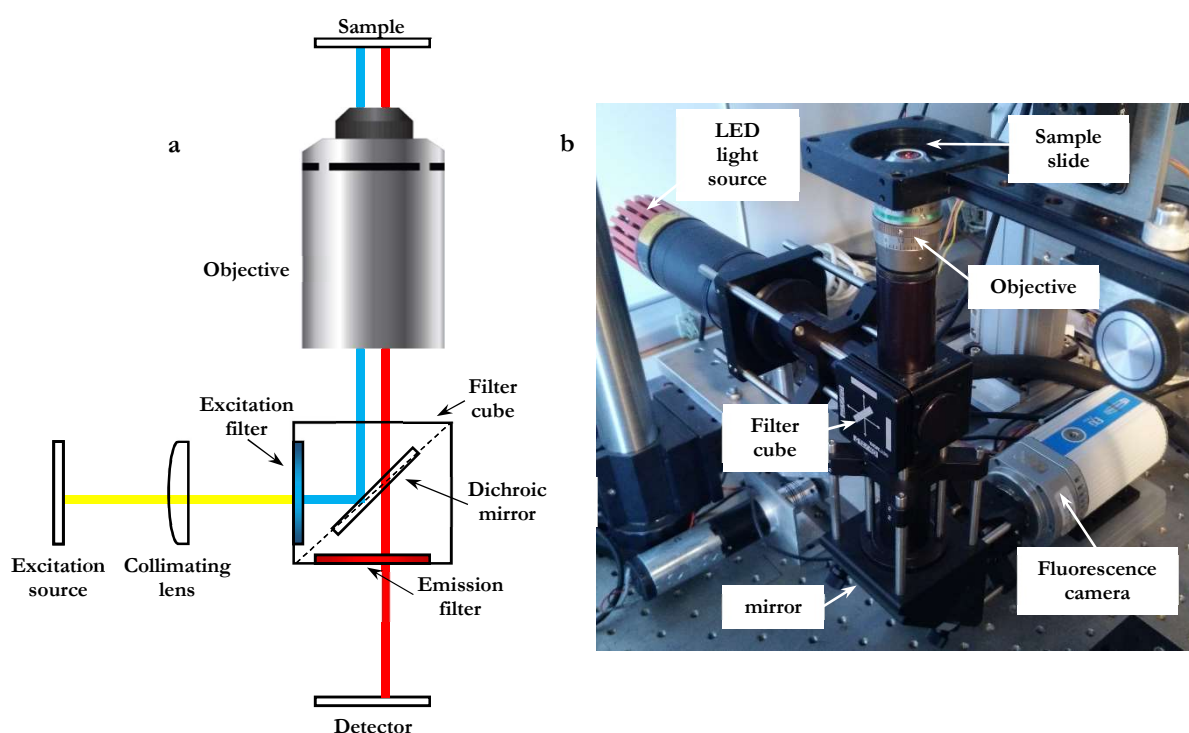


**Fig. 53. Custom-built inverted fluorescence microscope.** a) Schematic representation of the microscope, indicating its main components and the optical path for each wavelength. Yellow line indicates the path for white light. b) Photography of the microscope. Further customization of this setup has enabled to image both fluorescence and polarization channels. This is attained by adding a polarizer before the excitation filter and an analyzer between the sample and a second digital video camera.

To characterize our samples, we used a custom-built inverted microscope with a white led light source (Thorlabs MWWHLP1) and a Cy<sup>®</sup>5 filter set (Edmund Optics). Image acquisition was performed with a QImaging ExiBlue cooled CCD camera operated with ImageJ  $\mu$ -Manager open-source software.



### 3.8.3. Confocal laser-scanning microscopy

For sharper imaging of interfacial regions, we have employed confocal laser-scanning microscopy, both in reflection and fluorescence modes.

Confocal microscopy offers several advantages over conventional optical microscopy, including controllable depth of field and the elimination of image degrading out-of-focus information. Laser scanning confocal microscopes employ a pair of pinhole apertures (Fig. 54) to limit the specimen focal plane to a confined volume approximately of a micron in size. The use of this spatial filtering allows to eliminate out-of-focus light in specimens that are thicker than the plane of focus [19].

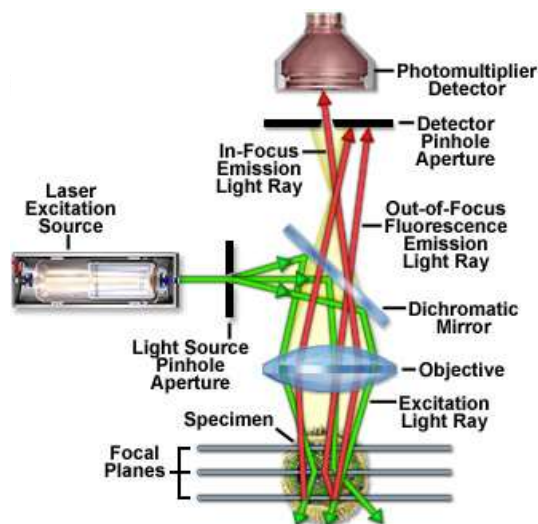


Fig. 54. Principal light pathways in confocal laser-scanning microscopy. Source: ref. [19].

While fluorescence confocal microscopy optimizes the signal/noise ratio for improved imaging of the interfacial material (Fig. 55a), we find that reflection confocal micrograph is optimal for image velocimetry of the active nematic due to the enhanced contrast of the material textures (Fig. 55b) and also its high acquisition rate. Moreover, this technique can be employed with label free active nematic, thus significantly simplifying sample preparation, reducing material costs, and, more importantly, eliminating extraneous moieties that might alter the way kinesin motors walk along the microtubules. Finally, fluorescence and reflection modes can be employed to simultaneously visualize both the active nematic and the passive liquid crystal (Chapter 3).

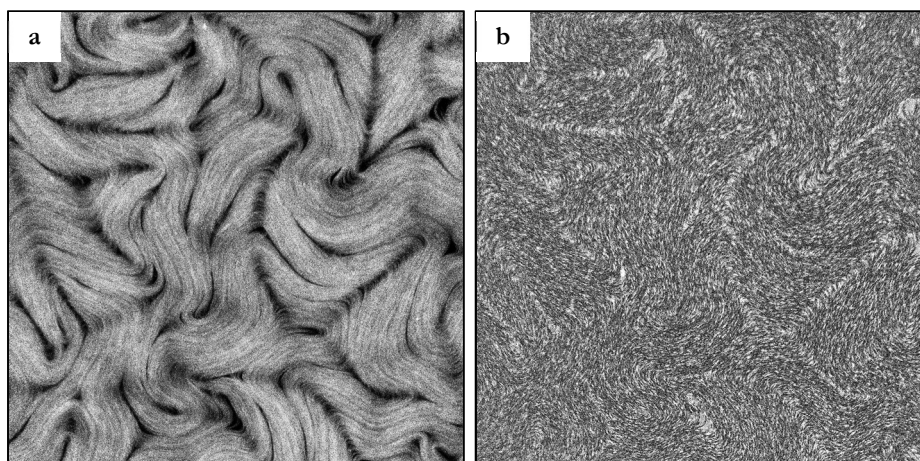


Fig. 55. Confocal micrographs in different imaging modes. Simultaneous acquisition of the active nematic images with confocal laser-scanning microscopy in fluorescence (left) and reflection (right) modes. Images are  $375\mu\text{m}$  wide.

In our experiments, we used a Leica TCS SP2 laser-scanning confocal microscope equipped with a photomultiplier as detector and a HeNe–633-nm laser as light source. A 20x oil immersion objective was employed.

---

## 3.9. Image and Data analysis

In this section, I summarize the methods used for image and data analysis.

### 3.9.1. Image velocimetry

Tracer-free velocimetry analysis of the AN has been performed by analysing consecutive pairs of confocal reflection micrographs (Section 3.8.3) with a public domain particle image velocimetry (PIV) program, implemented as an ImageJ plugin, which performs iterative PIV analysis. Basically, a pair of images is divided into smaller regions and the cross-correlation between these image sub-regions measures the optic flow (displacement or velocity of the objects) within the image pair. By progressively decreasing the size of the analysed regions, a better PIV resolution can be achieved.

### 3.9.2. Particle tracking

The active flows have been also traced by dispersing PEGylated spherical polystyrene microbeads of diameter 1.7  $\mu\text{m}$  (Micromod; 08-56-173). Manual Tracking ImageJ plugin has been used to manually track trajectories of particles or defects in the AN.

### 3.9.3. Vorticity and Okubo-Weiss fields

Further analysis of velocimetry data was performed with custom-written MatLab codes. On the one hand, we quantify the mean vorticity of the AN by extracting the vorticity ( $\vec{\omega}$ ) field and subsequently averaging the obtained vector intensities:

$$\vec{\omega} = \nabla \times \vec{v} = \left( \frac{\partial}{\partial x}, \frac{\partial}{\partial y}, \frac{\partial}{\partial z} \right) \times (v_x, v_y, v_z) = \left( \frac{\partial v_z}{\partial y} - \frac{\partial v_y}{\partial z}, \frac{\partial v_x}{\partial z} - \frac{\partial v_z}{\partial x}, \frac{\partial v_y}{\partial x} - \frac{\partial v_x}{\partial y} \right)$$

In our case, we can consider that the velocity field is quasi-two-dimensional so we can assume  $v_z = 0$ , and thus  $\vec{\omega} = \left( \frac{\partial v_y}{\partial x} - \frac{\partial v_x}{\partial y} \right) \hat{k}$ .

On the other hand, in order to differentiate between turbulent and coherent vortex regions within the vorticity field of two-dimensional (2D) turbulent flows we use the Okubo-Weiss (*OW*) criterion [164,206]. This allows to parametrize turbulence in terms of the dominance of flow deformation and flow rotation. The OW parameter is obtained as follows. In our case, we can define the stream function ( $\psi$ ) for a two-dimensional flow such that the flow velocity can be expressed as  $\mathbf{v} = \nabla \times \psi$ , where  $\psi = (0, 0, -\psi)$  if the flow vector  $\mathbf{v} = (v_x, v_y, 0)$ . In cartesian coordinates this is equivalent to  $v_x = -\frac{\partial \psi}{\partial y}$ ,  $v_y = \frac{\partial \psi}{\partial x}$ . A small local perturbation of the  $\mathbf{v}$  field thus results in

$$\begin{aligned} \delta v_x &= -\frac{\partial^2 \psi}{\partial y \partial x} \delta x - \frac{\partial^2 \psi}{\partial^2 y} \delta y \\ \delta v_y &= +\frac{\partial^2 \psi}{\partial^2 x} \delta x + \frac{\partial^2 \psi}{\partial x \partial y} \delta y \end{aligned}$$

The eigen value analysis of this system of linear equation gives  $\lambda = \pm\sqrt{OW}$ , where  $OW = \left(\frac{\partial^2\psi}{\partial x\partial y}\right)^2 - \frac{\partial^2\psi}{\partial^2x} \frac{\partial^2\psi}{\partial^2y}$ . Considering that  $\partial_x v_x = -\frac{\partial^2\psi}{\partial y\partial x}$ ,  $\partial_x v_y = \frac{\partial^2\psi}{\partial x^2}$  and  $\partial_y v_x = -\frac{\partial^2\psi}{\partial y^2}$ , then

$$OW = (\partial_x v_x)^2 + \partial_y v_x \cdot \partial_x v_y$$

OW is a measure of the relative importance of flow strain ( $OW > 0$ , hyperbolic) and vorticity ( $OW < 0$ , elliptic). For characterization of the vortex size distribution in the turbulent AN, the Okubo-Weiss (OW) parameter has been mapped also from the velocity fields obtained by image velocimetry. The vortex areas were quantified from binarized OW field images in ImageJ. Vortices on the edges of the field of view were excluded.

### 3.9.4. Active nematic director field

In order to extract the active nematic director field from fluorescence images of the filamentous material, we compute the Hough transform [207] for subsections of binarized fluorescence images  $BW$  with the Matlab function  $[H, theta, rho] = hough(BW)$ . The hough function is designed to detect lines. It uses the parametric representation of a line (Fig. 56):  $rho = x*cos(theta) + y*sin(theta)$ .

The function returns  $rho$ ,  $theta$ , and the Hough Transform,  $H$ , which is a parameter space matrix whose rows and columns correspond to  $rho$  and  $theta$  values respectively. From the matrix of  $theta$  angles for each image, we can calculate its spatial correlation function and reconstruct the director field (Fig. 57).

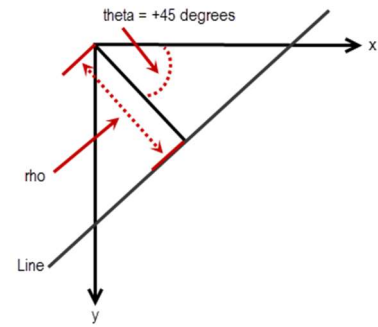


**Fig. 56. Parametric representation of a line in Cartesian coordinates.**  $rho$ , the distance from the origin to the line along a vector perpendicular to the line, and  $theta$ , from  $-90$  to  $90^\circ$ , is the angle in degrees between the  $x$ -axis and this vector.

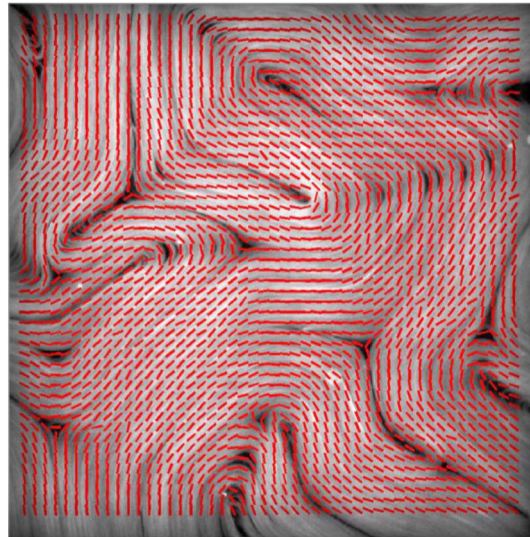


**Fig. 57. Active nematic director field.** Fluorescence micrograph of the active nematic with super-imposed director field, extracted by image processing with the Hough transform.

---

### 3.9.5. Spatial autocorrelation functions

In order to analyse the spatial behaviour of a magnitude throughout a sample we have used the two-dimensional cross-correlation method. As in our case, we will strictly calculate autocorrelation functions as we are analysing cross-correlation of a signal with itself. In particular, we will use discrete signals  $y(\mathbf{r})$  and thus the discrete autocorrelation  $c$  at lag  $\Delta\mathbf{r}$  is

$$c_{yy}(R) = \sum_{\mathbf{r} \in \mathbb{Z}} y(\mathbf{r}) \bar{y}(\mathbf{r} + \Delta\mathbf{r})$$

For a periodic array, the two-dimensional autocorrelation function of an M-by-N matrix,  $X$ , and P-by-Q matrix,  $H$ , is a matrix  $C$ , of size M+P-1 by N+Q-1. Its elements are given by

$$C(k, l) = \sum_{m=0}^{M-1} \sum_{n=0}^{N-1} X(m, n) \bar{H}(m - k, n - l)$$

where  $-(P - 1) \leq k \leq M - 1$  and  $-(Q - 1) \leq l \leq N - 1$ .

In order to calculate the spatial correlation functions of the velocity ( $\mathbf{v}$ ), vorticity ( $\omega$ ) and director angle ( $\theta$ ) we have implemented this calculation in custom-written Matlab codes. We have also employed the `xcorr2` function, which returns  $C(k, l)$ .



---

## 4. Main goal and objectives

This work aims at the development of strategies to condition active flows by means of non-invasive bounds as a tool towards the control of the intrinsic unpredictable chaotic behaviour of active matter systems. In order to achieve this goal, an initial research plan contemplated, among others, the following objectives:

- To implement a tubulin/kinesin-based active gel in our laboratory as a system of study in this project, with special interest focused on the active nematic that this material forms.
- To evaluate the influence of hydrodynamic coupling through the soft interface towards which the active material evolves via interaction with isotropic oils of different viscosities.
- To explore the adaptation of active flows to viscosity patterns at the interface by using thermotropic liquid crystals featuring lamellar phases, which display marked rheological anisotropy.
- To study the interaction between active and passive nematic liquid crystals and the possible director field coupling through the interface.
- To characterize the dynamical behaviour of active emulsions based on active nematic shells dispersed either in isotropic oils or in thermotropic liquid crystals. The latter will allow to force the coupling, if any, between active and passive defects, by means of which we envisage to control the flows from the encapsulated active material.



# Chapter 2. Interfacing the active nematic with isotropic oils





---

# Introduction

Active systems are composed of self-propelled units that interact with each other giving rise to highly-dynamic steady states (Section 2). Their constituents thus individually dissipate energy and transfer momentum to the environment by exerting forces and doing mechanical work [73,137]. Usually, in the class of active systems we will be studying, the total momentum of the system is conserved and thus it can be considered as a “wet” system [73]. Big efforts have been made to characterize the geometry of active flows in order to unveil their universal features and the intricacies of complex systems, usually in the form of active gels based on biological components [77,114]. Other studies focus on the force generation in active systems, which might have the potential to operate in devices, and drive micromachines [166,208]. However, little is known about the effects of hydrodynamic damping on active systems, especially for those that operate at low Reynolds number ( $Re$ ), where inertia plays a small role and viscosity is predominant. It is well-accepted that strategies for locomotion of organisms at high  $Re$ , such as fish, birds or insects (Section 2.1.1), do not work at the small scale. Therefore, microorganisms have developed propulsion mechanisms that not only successfully overcome drag but exploit it.

In the majority of experimental realizations with active nematics (ANs), the influence of hydrodynamics has been often neglected as viscosity of the surrounding fluids is considered to not significantly alter the dynamical behaviour of the active systems [77]. As a matter of fact, ANs have been so far experimentally studied dispersed in low-viscosity aqueous solutions and at fluid interfaces that practically do not impose any friction or flow-damping drag [77,82,83]. In addition, most of the theoretical studies have often considered “free-floating” active nematics where they develop unbounded, i.e. without any hydrodynamic coupling with their environment [160,161,164,209]. Although it is accepted that the primary mechanism by which the active constituents of these systems dissipate energy are based in the generation of motion, the behaviour of active flows evolving in constraining hydrodynamic conditions has been poorly tackled. In fact, some research groups, including ours, have just started considering the influence of hydrodynamic interactions in the organization of active soft matter [195,210], as they could provide further mechanistic insights into pattern formation in active materials, and powerful tools for the development of non-invasive strategies to condition and control biomaterials.

In this chapter, we report experiments of an AN film composed of cytoskeletal extracts (Section 2.2.2) that develops suspended in a buffered aqueous solution, and in contact with isotropic viscous oils (Materials and methods, Section 3.3). The active stresses generated within the active material are dissipated by means of active flow, further transmitted both to the solvent and to the oil, through the surfactant-decorated water/oil interface (Materials and methods, Section 3.3.1). Consequently, the active material is inevitably damped, especially due to the momentum transfer to the surrounding fluids and, therefore, the influence of damping can be varied by changing the viscosity of either the aqueous or the oily phase. On the one hand, by dissolving high concentrations of macromolecules, like methylcellulose ( $MW \sim 88,000 \text{g/mol}$ ), at the aqueous phase, we have been able to change its viscosity up to 400 times, indeed leading to slightly damped flow situations. Nevertheless, these variations in the aqueous phase imply negative effects for the components of the active gel. On the other hand, more remarkable changes are observed by condensing the active material towards

bounding isotropic oils with different viscosity, which has been varied over five orders of magnitude. With this strategy, the AN flows are effectively constrained without altering its composition, just by hydrodynamic viscous damping through the interface. The ability to dampen active flows opens a wide spectrum of possibilities to extract information about the scaling arguments that define active materials, as their speed can be varied without changing activity. For instance, the number of defects ( $n$ ) in an AN is expected to change both with variations in their own speed and with the activity, like  $n \sim \frac{|\alpha|}{\sqrt{Kv}}$ .  $\alpha^*$  is the coefficient controlling the strength of the activity, assumed to have a logarithmic dependence on Adenosine triphosphate (ATP) concentration,  $\alpha \sim \log[\text{ATP}]^{**}$ , and  $K$  is the elastic constant of the material [211].

The origin of this relation can be understood as follows. In two-dimensional active turbulence, the rate of creation of defects per unit area ( $r_c$ ) has been predicted to be  $r_c \sim (l_\alpha \tau)^{-1}$ , where  $l_\alpha \sim \sqrt{\frac{K}{|\alpha|}}$  is the active length scale determined by balancing the active and elastic stresses. It has been shown that this length scale controls the spatial correlations in the active turbulent regimes of “wet” active nematics [164]. The time scale  $\tau \sim \frac{\gamma}{|\alpha|}$  controls the relaxation of the order parameter distortions due active stresses, with  $\gamma$  being the rotational viscosity of the AN. Therefore, we can assume that  $r_c \sim \frac{\alpha^2}{K}$ . The rate of annihilation of defect pairs of opposite charge ( $r_a$ ) can be estimated as  $r_a \sim \sigma v n^2$  using simple kinetic theory arguments.  $\sigma$  is an effective cross section (a length in two dimensions) that quantifies the range of the interaction between two defects ( $n^2$ ) that move at speed  $v$ , which is assumed to scale the same way as the velocity of the fluid [211]. At steady state, the number of defects,  $n$ , saturates thus  $r_c \sim r_a$  and  $\frac{\alpha^2}{K} \sim \sigma v n^2 \rightarrow n \sim \frac{|\alpha|}{\sqrt{Kv}}$ . Here, we will focus on testing this scaling between the number of defects, their speed and the activity parameter, by adjusting the viscous damping at the interface.

The main goal of these experiments has been to demonstrate both the effective coupling of the AN through the water/oil interface and the effects of viscous damping on the morphology and dynamics of the material. By externally conditioning the active nematic, we have been able to test scaling arguments proposed in theory for active turbulent flows [161]. In addition, by combining some of our experimental data with a hydrodynamic numerical model, in collaboration with M. C. Marchetti and S. Shankar from Syracuse University (NY, USA), we have been able to probe the shear viscosity of the AN [195]. Finally, analysis of spatial correlation functions for the different material observables (velocity, vorticity and director field) and characterization of the distribution of vortex sizes has allowed to confirm the existence of a single length scale, intrinsic of active flows, as predicted by [164].

---

\* The active stress scale,  $\alpha$ , is controlled by ATP concentration and it is chosen negative for active systems predominantly extensile in character, like ours (Section 2.1.2).

\*\* Although ATPase activity for single kinesin molecular motors obeys Michaelis-Menten kinetic mechanisms [220], activity of the molecular motor-based active gels is often considered to be proportional to the chemical potential associated to ATP hydrolysis ( $|\alpha| \sim \log[\text{ATP}]$ ). See Materials and methods, Section 3.1.5.


# Results

As introduced in Section 2.2.1, ANs generate flows owing to active stress and in response to distortions in the order parameter field. The flow further disturbs the director field thus resulting in active turbulent states that feature topological semi-integer defects that are continuously created and annihilated in pairs [211]. Defects circulate throughout the flat active layer in seemingly-random walks, coherent with the active flows' length scale,  $l_\alpha$ . As they are devoid of MTs, defects of the AN appear as dark regions in fluorescence micrographs and thus they are easily traceable, and have been useful for the characterization of the AN morphology and dynamics. In particular, from tracking of positive semi-integer defects, we have both extracted their average speed and their number density. In addition, by quantifying the area covered by the dark regions, the defect area fraction has been also obtained to confirm variations in defect number. Apart from the viscosity of the interfacing oil, the activity of the AN, affected by changes in ATP concentration, has been chosen as the second variable parameter for this set of experiments.

**AN in contact with viscous oils.** First, we have prepared ANs with equal activity in contact with isotropic oils with different viscosities, which act as a bounding element for the active system. From fluorescence microscopy imaging, we observe that increasing oil viscosities lead to slower defect motion, and, as a consequence, both their density and area fraction increase (Fig. 58), as predicted for ANs with substrate friction [210].

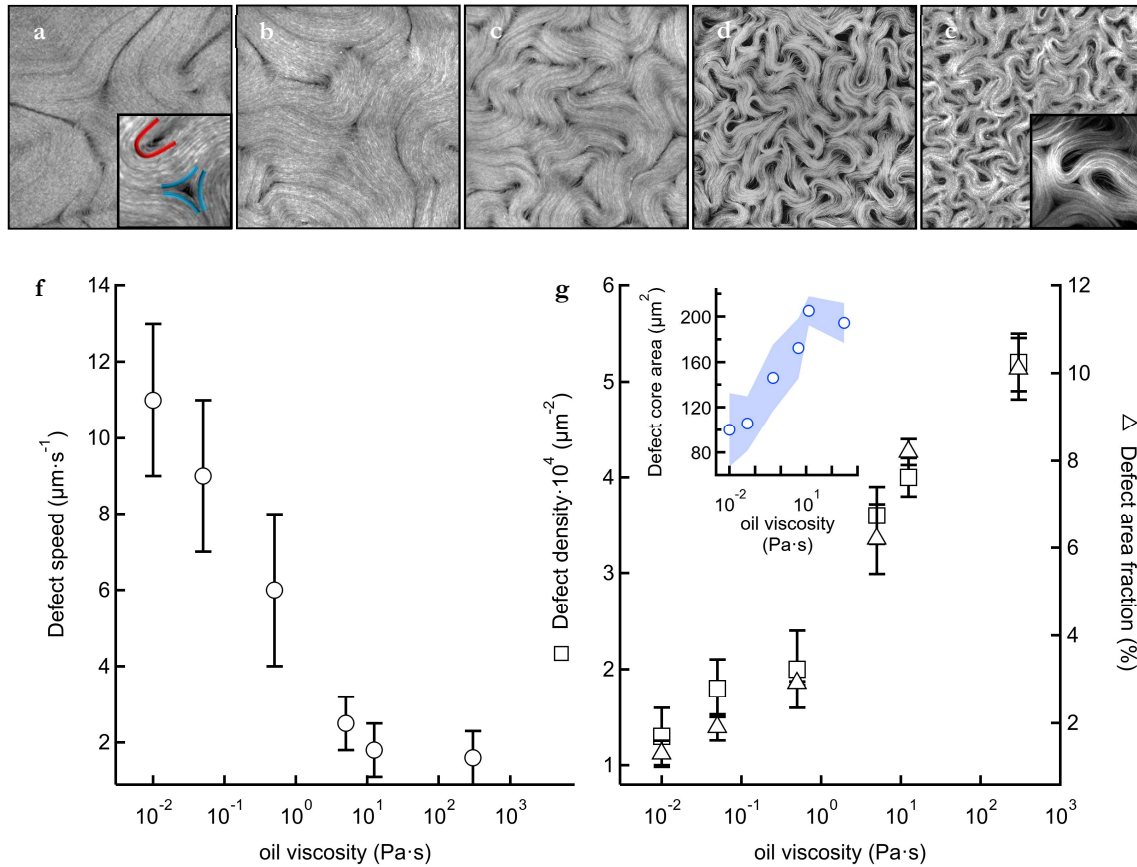


**Fig. 58. Active nematic contacting oils with different viscosities.** a) Fluorescence confocal micrographs ( $400 \mu\text{m}$  wide) show the variations in the density of defects in the active material. Oil viscosities, from (a) to (e), are  $1 \cdot 10^{-2}$ ,  $5 \cdot 10^{-2}$ ,

0.5, 5, and 300 Pa·s. ATP concentration is 1.4 mM in all the cases. Insets show sections at fourfold magnification. In the inset in (a) topological defects with  $s=+1/2$  and  $s=-1/2$  are highlighted in red and blue, respectively. f) When the ATP concentration is kept constant, the speed of the defects decreases with increasing oil viscosities. g) Both defect density ( $\square$ ) and defect area fraction ( $\Delta$ ) increase when increasing the oil viscosity. By dividing the defect area fraction by the defect density, we can estimate the area of the defect core, which also increases with higher viscosity contrasts (inset, shaded region corresponds to the error associated to the defect core calculation).  See Video 2.

The damping consequences of the viscous stresses at the interface can be easily understood as follows. Decay in the active nematic speed Fig. 58f results in more sporadic defect annihilation events and, since the ATP concentration is kept constant in all these experiments, the defect creation rate is sustained. As a consequence, the average number of defect increases Fig. 58g.

Textures in contact with oils of smaller viscosity appear more tenuous as compared to those observed for higher oil viscosities. This indicates that a large viscosity somehow concentrates the MT bundles, amplifying the size of the regions void of MTs that we identify with the cores of the defects (Fig. 58g, inset). The viscous damping could thus have some influence on the elasticity of the AN, although this is still not fully understood. Textures such as the one shown in Fig. 58e are rather disordered in the sense that the nematic order parameter would average to a small value. The system, however, still shows a characteristic structure that can be analysed in terms of nematic disclinations.

The measurements of  $v$  and  $n$  can be combined to reveal the simple scaling relationship between these two quantities. By plotting a log-log graph for the number of defects, obtained for ANs in contact with different oil viscosities, versus their average speed, we obtain a power law with exponent -0.5, consistent with the scaling arguments discussed above ( $n \sim \frac{\alpha}{\sqrt{Kv}} \sim v^{-0.5}$ ), predicted in [161]:

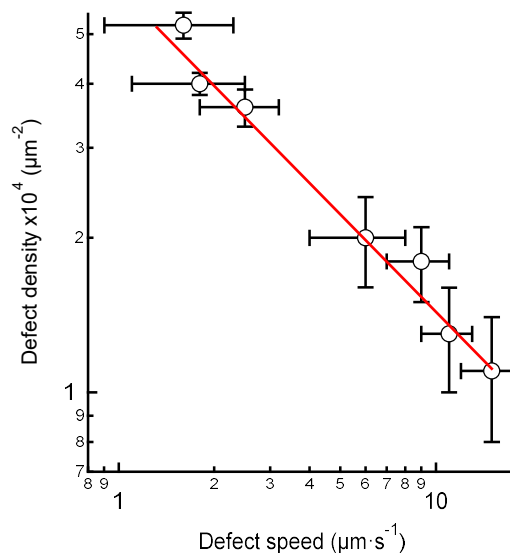


**Fig. 59. Relation between defect density and defect speed.** By combining the values for these two observables obtained for different oil viscosity conditions, we are able to analyse the relation between them. The red line is a power law with exponent  $-1/2$ .

**Estimation of the AN viscosity.** We observe that the speed of  $+1/2$  defects,  $v$ , decreases logarithmically with the oil viscosity before a saturation for the most viscous oils Fig. 58f. These data are successfully fitted with a theoretical model briefly described below, which allows us to estimate the viscosity of the AN ( $\eta_N$ ), for now, experimentally inaccessible. The model considers the

hydrodynamics of a thin layer of an AN confined between two bulk fluids (oil and water) and it is used to calculate the velocity that the director distortion due to a  $+1/2$  disclination creates at the core of the defect in regimes with different viscous damping. It is found that the presence of the bulk fluids qualitatively changes the defect velocity as compared to the previously considered cases of a “free-floating” active nematic layer [160,164,209,211].

To evaluate the defect velocity, Stokes equations for both passive surrounding fluids and the AN are written as starting point. In the Stokes equation for the AN, an active component of the stress tensor is used, being proportional to the activity parameter,  $\alpha$ , and to the nematic alignment tensor  $Q$  (Section 1.3). The structure of  $Q$  is solved around the cores of  $+1/2$  defects, as the flow is assumed to originate from these regions. By using Green’s function-based formalisms one can get an expression for the velocity of the AN flow, which we associate with the speed of  $+1/2$  defects:

$$v \sim \frac{|\alpha|}{\eta_N/l} \ln \frac{\eta_N/l}{\eta_o}$$

In this final equation, the flow velocity is predicted to be proportional to  $|\alpha|$ , in disagreement with predicted kinetic behaviour for low Re turbulence in active fluids [164], where  $v \sim |\alpha|^{-0.5}$  (see below). However, we should take into account that, in the latter case, flow velocity is calculated around one single defect core thus inevitably missing the inter-defect interaction and other consequent effects arising in ANs.

The length scale  $l \sim \frac{\eta_N}{(\eta_o + \eta_w)} \sim \frac{\eta_N}{\eta_o}$  (for  $\eta_o \gg \eta_w$ ) controls the crossover from two-dimensional surface flows to three-dimensional bulk dominated flows. Therefore, the value of  $\eta_N$  estimated by the model depends on the choice of  $l$ . A natural option is to consider  $l$  as the thickness of the oil subphase ( $\sim 1$  mm) giving  $\eta_N \sim 1.3 \cdot 10^{-4}$  Pa s m. Alternately, one could argue that our single-defect calculation should be cut off at the scale of the mean defect separation, which in turn depends on  $\eta_o$  (Fig. 58g), changing only by a factor of 2 (50–100  $\mu\text{m}$ ) over five orders of magnitude of oil viscosity. Choosing  $l \sim \eta^{-0.5}$ ,  $\eta_N \sim 6.5 \cdot 10^{-4}$  Pa s m is obtained. This value can be put into perspective with the equivalent bulk viscosity of 1 nm-thick condensed phospholipid monolayers, of order  $10^5$  Pa s [212]. In our case, we estimate a value of order  $10^2$  Pa s for an active nematic layer of thickness 1  $\mu\text{m}$ .

**Influence of activity.** Next, we introduce variations in ATP concentration, which changes the activity of the system, altering both the speed and the number of defects. In particular, higher activities lead to a major number of faster defects, whose speed has been proved to be related with activity like  $v \sim \alpha^{0.5}$  (Fig. 60) [164]. As expected, defect density also increases linearly with activity (private communication, S. J. DeCamp, Brandeis University, MA, USA). By combining changes in oil viscosity and in the ATP concentration, we have managed to explore a wide range of defect-speed situations (Fig. 60).

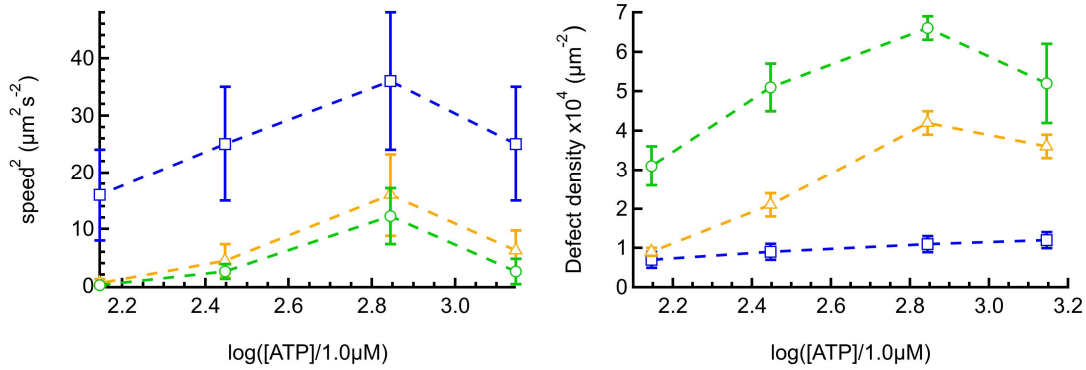


**Fig. 60. Speed and defect density variations with activity.** Linear behaviour is observed both for  $v^2$  vs  $\alpha$  (left) and  $n$  vs  $\alpha$  (right). The values for the viscosity of the oil in contact which the AN evolves are 0.5, 5 and 300 Pa·s (blue squares, orange triangles and green circles, respectively). Note that for the highest values of ATP concentration, both  $n$  and  $v^2$  values deviate from the general trends, regardless of the viscosity. We associate these values to concentrations above saturation concentration for kinesin molecular motors activity.

Further analysis can be performed by combining data of defect speeds and defect densities, obtained from multiple experiments, where both the activity and viscosity are changed. We can thus add the variation in activity as a third parameter to test  $n \sim \frac{|\alpha|}{\sqrt{Kv}}$ . By plotting the variation of  $n$  versus  $\frac{|\alpha|}{\sqrt{v}}$  we indeed observe a linear tendency between the data points corresponding to different viscosity regimes (Fig. 61). Nevertheless, we cannot reach any conclusion since the analysis is hampered by the error propagation associated to the ratio between activity and defect speed.

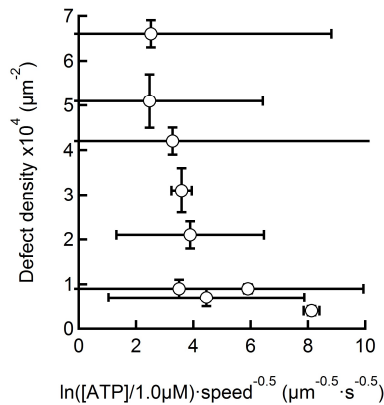


**Fig. 61. Defect density variation with a relation between activity and speed.** Seemingly linear tendency is obtained by plotting  $n$  versus  $\frac{|\alpha|}{\sqrt{v}}$ . Values for  $n$  and  $v$  are obtained from the previous experiments, where we combine activity and viscosity variations (see Fig. 60).

**Velocimetry analysis of the AN.** The complex dynamical patterns arising in these turbulent regimes are characterized by chaotic velocity fields and strong variations in vorticity [164]. The geometrical structure of active turbulent flows can be thus well-defined by these two physical observables, which have been studied for our AN, in an attempt to unveil the adaptation mechanisms of active turbulence to the contact with flow-damping fluids. By performing image velocimetry analysis of long sequences of reflection confocal micrographs, we can extract the velocity field of the AN and subsequently calculate how the vorticity ( $\boldsymbol{\omega} = \nabla \times \boldsymbol{v}$ , see Materials and methods, Section 3.9) changes in time and space.

Hydrodynamic constraints enhance the formation of defects in the AN, and it has been shown that such defects are strongly associated with vorticity generation [160]. In our experiments, it is indeed observed how, when in contact with bounding fluids, the active material self-organizes flow vortices that span a wide range of length scales. Therefore, for increasing oil viscosities, the AN develops larger number of smaller vortices (Fig. 62).

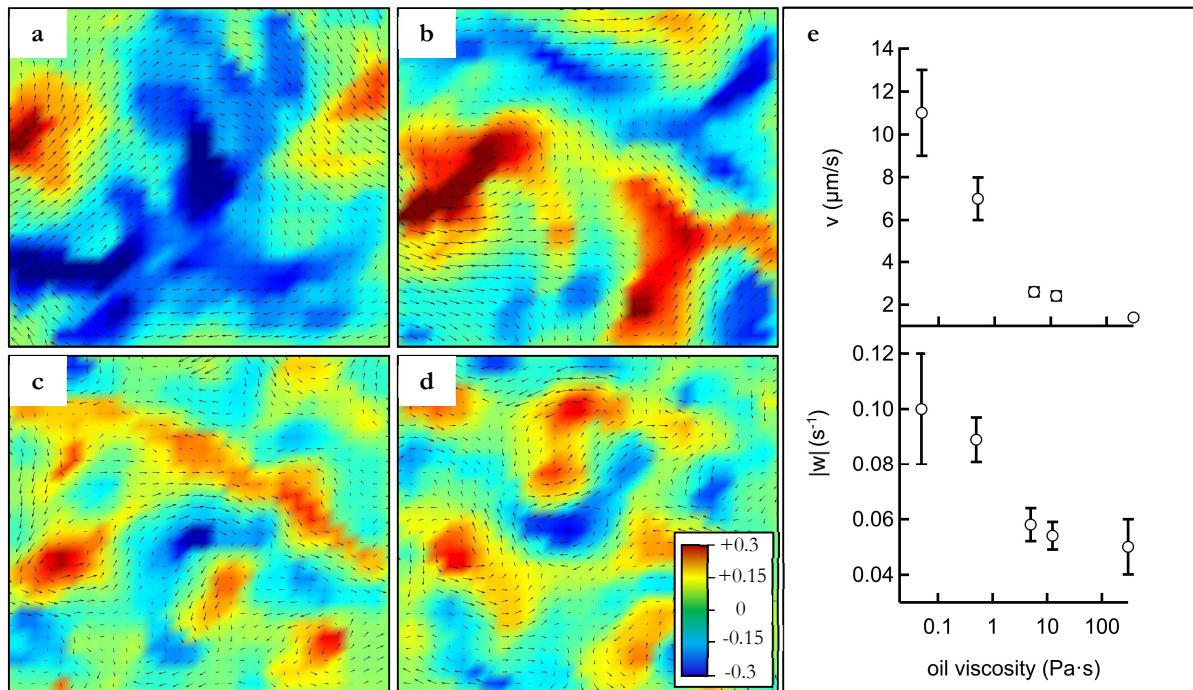



**Fig. 62. Formation of vortices in high viscosity oils.** a-d) Snapshots of superimposed velocity and vorticity fields extracted from velocimetry data for the active nematic in contact with oils with viscosities 0.05, 0.5, 5 and 12.5 Pa·s from (a) to (d). Blue and red colours correspond to clockwise and anticlockwise vorticities, respectively. ATP concentration is 1.4 mM in all cases. Analysed micrographs are 250 μm wide. e) Average velocity (top) and vorticity (bottom) extracted from thousand-image (500 s) sequences of the active nematic in contact with oils with different viscosities.

From velocimetry data, we can calculate the average speed of the active flows that decays with the logarithm of oil viscosities (Fig. 62e), as obtained from the analysis of defect tracking (Fig. 58f). We have also determined the average absolute value of vorticity, which follows a similar trend (Fig. 62e), which is mainly conditioned by the decrease in speed. Vorticity quantifies the local rotation of the fluid elements in a flow field and it might be a key tool to characterize active turbulence.



**Distribution of vortices in the turbulent AN.** It is well accepted in the literature that the spatial arrangement of ANs is determined by an intrinsic length scale  $l_\alpha$ , which establishes spatial features in the material such as the steady-state defect separation and the bending radius of the extensile MT bundles. Earlier simulations revealed that this length scale also determines the geometry of the active turbulent regime [164], where the vortex size distribution follows an exponential whose decay length is related to  $l_\alpha$ . Our experiments confirm these predictions when the AN evolves in contact with an isotropic oil. In order to test this assumption, velocimetry data are also used to obtain values of the Okubo-Weiss parameter,  $OW = (\partial_x v_x)^2 + \partial_y v_x \cdot \partial_x v_y$  (Section 3.9.3), which provides with a standard criterion for vortex location, often used in fluid dynamics, by considering the extension of each vortex to be bound by the condition  $OW < 0$  [164].

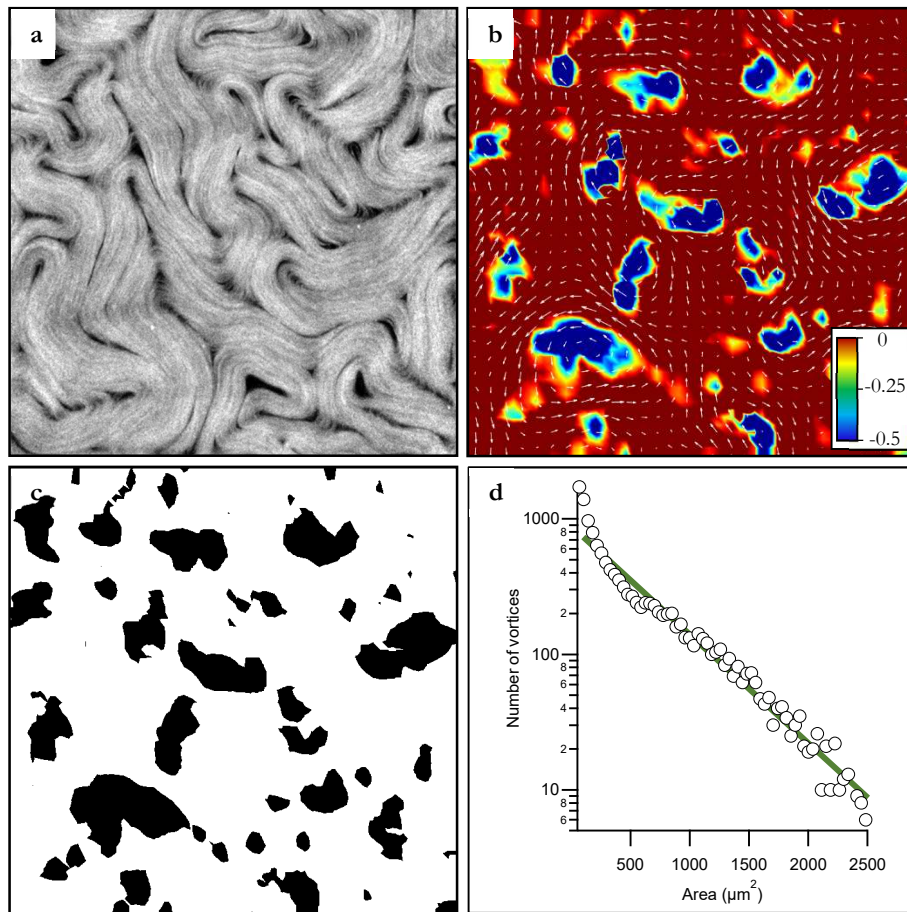


**Fig. 63. Structure of the active turbulent flow.** **a)** Confocal fluorescence micrograph of the active nematic in the turbulent regime when in contact with a high-viscosity isotropic oil. Image is  $375 \mu\text{m}$  wide. **b)** Instantaneous flow field (vector plot) and computed Okubo-Weiss parameter field (density plot), employed to determine the location and size of vortices (blue areas). **c)** Binary image corresponding to the Okubo-Weiss field. Black regions are  $OW < 0$ . **d)** Statistical analysis of the distribution of vortex sizes accumulated for a series of thousand snapshots of **(c)** during the evolution of the active turbulent flow. The range of sizes is limited by the size of the field of view. The line is an exponential fit to the data.  See Video 3.

A statistical analysis of the OW field in AN facing high-viscosity oils reveals an exponential distribution of vortex sizes (Fig. 63). This result agrees with reported analysis of the active turbulent regime in simulations of 2d nematodynamics [164] and it is consistent with the existence of a characteristic length scale ( $l_\alpha$ ), set by the balance between active and elastic stresses [161,164,213].

**Characterization of the AN director field.** In addition, the filamentous active material can be characterized in terms of the local average orientation of the filament bundles. Fluorescence micrographs of the AN are processed by image analysis codes based on object recognition [207], in this case lines (Material and methods, Section 3.9, Fig. 64). Due to the increasing number of defects, increasing oil viscosities also lead to more tangled active director fields.

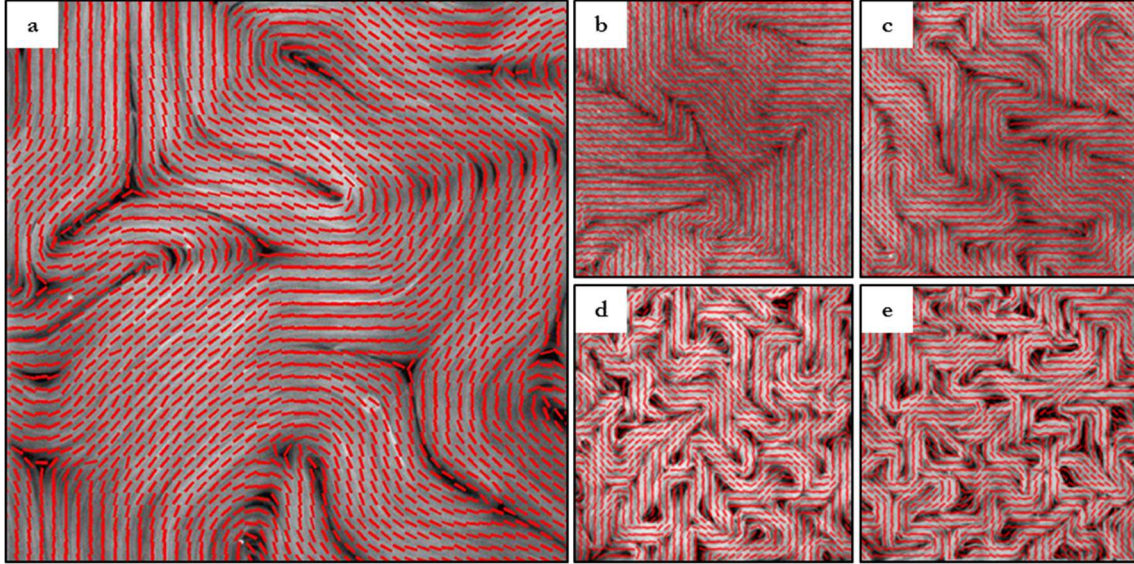


**Fig. 64. Director field of the active nematic.** Line detection allows to measure local average orientation (vector field, in red) of the active material. Viscosities of the oils in contact with the active nematics are 0.05 for (a,b) and 0.5, 5 and 12.5 Pa·s for (c-e), respectively. Images are 300  $\mu\text{m}$  wide.

**Correlation functions.** Finally, in order to deeply investigate and characterize the spatial organization of the active flow field, we measure and plot equal-time spatial correlation functions of velocity, vorticity and director fields as a function of oil viscosity. In Fig. 65 we plot the normalized the functions  $C_{vv}(\Delta r) = \frac{\langle \vec{v}(r) \cdot \vec{v}(r+\Delta r) \rangle}{\langle v(r)^2 \rangle}$ ,  $C_{\omega\omega}(\Delta r) = \frac{\langle \omega_z(r) \omega_z(r+\Delta r) \rangle}{\langle \omega_z(r)^2 \rangle}$ , and  $C_{nn}(\Delta r) = 2(\langle \cos^2(\theta(r) - \theta(r + \Delta r)) \rangle - \frac{1}{2})$  (Materials and methods, Section 3.9).

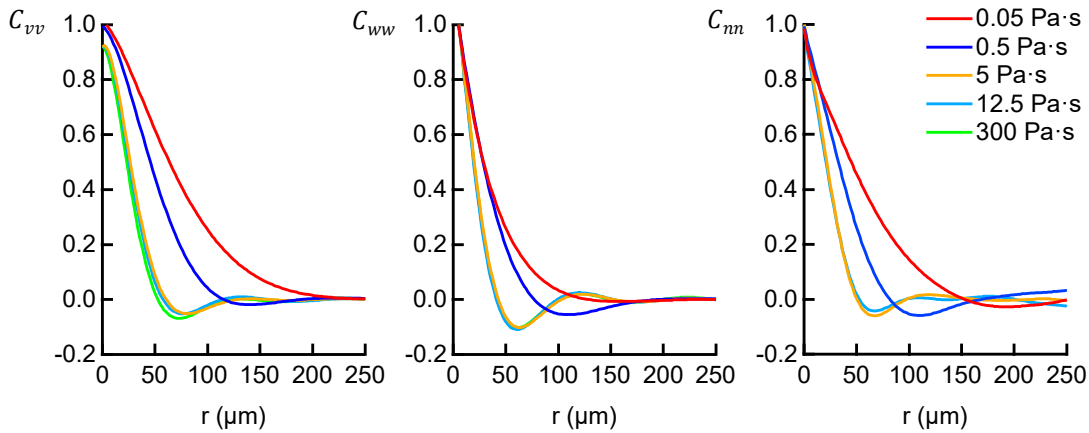


**Fig. 65. Spatial correlation functions.** From image processing, we extract the spatial correlation functions of velocity (left), vorticity (centre) and director fields (right) for ANs in contact with oils with different viscosity.

The normalized correlation functions decay becoming anticorrelated between  $\sim 60$ - $250 \mu\text{m}$ . Not all of them decay equally, revealing that the spatial structure of the generated flows depends on the viscosity of the contacting oily fluid. From the decay of the correlation functions, it is possible to define the characteristic spatial flow length scale, associated with the emergent flow. In particular, by plotting the distance corresponding to the minima for the obtained  $\langle vv \rangle$ ,  $\langle ww \rangle$  and  $\langle nn \rangle$  correlations, one can compare the influence of oil viscosity on the length scales related to each observable ( $l_v$ ,  $l_w$ ,  $l_n$ ) (Fig. 66). Moreover, this allows us to compare how the three extracted length scales vary by imposing the same constraints. As a matter of fact, the characteristic lengths appear to scale equally with viscosity, confirming the existence of a single length scale, which could be associated  $l_a$ , governing the morphology and dynamics of active flows [164].

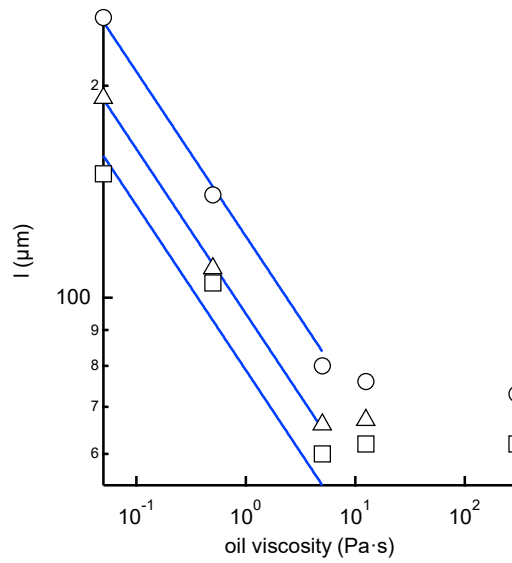


**Fig. 66. Decay lengths for active nematics in contact with different oil viscosities.** Velocity, vorticity and director filed correlation decay lengths are represented in circles, squares and triangles, respectively. Blue lines are power law fits to the data,  $l \sim \eta^{-0.2}$ .

---

# Conclusions

In this chapter, we have reported the implications of hydrodynamic coupling and consequent viscous damping in the morphological and dynamical features of ANs. To this purpose, the active material is prepared in contact with isotropic oils with different viscosities.

- Tracking of topological defects evidences the damping effects on the AN, whose speed decreases with the logarithm of the viscosity, when in contact with flow-constraining viscous fluids. Lower defect speeds hinder defect annihilation events and consequently, as activity and thus defect creation rate ( $\sim\alpha^2$ ) do not vary, the number of defects increases in ANs contacting oils with higher viscosities.
- By combining experiments with a hydrodynamic model, we show that measurements of the defect velocity can be used to estimate the shear viscosity of the active nematic.
- By extracting the average flow speed of the AN from velocimetry data, we have corroborated that the speed of the active flows decreases with the logarithm of the viscosity of the contacting bounding oil, as observed from the tracking of active defects. Thus, we can basically interpret the active flows as the velocity of defects.
- From velocimetry data, we have also extracted the vorticity field, from which we qualitatively show how the density of vortices increases when facing increasing viscosities. This can be easily understood by considering the increase in defect number, which triggers the formation of rotating flow fields. Moreover, we calculate the average vorticity for the different viscosity regimes, observing a decay with increasing oil viscosities, as shown by the average speeds.
- The Okubo-Weiss parameter has been also calculated and mapped in order to localize vortices within the velocity fields and obtain their areas. Exponential distribution of vortex sizes is reported, in agreement with recent simulations in 2d active nematics.
- Finally, spatial correlation functions of the velocity, vorticity and director fields have been measured for different viscous damping situations. Decay of such functions seems to be governed by the same length scale, which we associate with the active length scale  $l_\alpha$ , set by the balance between active and elastic stresses.



# **Chapter 3. Control of active flows with addressable soft interfaces**



---

# Introduction

Direct actuation on the flows arising from biological active matter is not easily attainable as the constitutive units practically do not respond to external fields. From this assumption, other strategies have been developed to indirectly condition the morphology and dynamics of active systems (Section 2.3). Usually consisting in confinement constraints, contact with gradients or anisotropic boundary conditions, methods to control active flows might provide with new tools to further explore the features of existing artificial active systems, and also to create new active biomaterials. In particular, strategies that allow *in situ* reconfiguration of control bounds are of great interest.

In the experiments described in the previous chapter, we have demonstrated the remarkable effects arising from the hydrodynamic interaction between our quasi-two-dimensional active nematic and passive isotropic oils. Concisely, the active LC becomes effectively damped when contacting oils of high viscosity, and it readapts to satisfy the boundary conditions. Here, by taking advantage of the reported strong hydrodynamic coupling through the soft interface, we prepare our active material in contact with anisotropic oily compounds, namely thermotropic LCs (TLCs). The main purpose of these realizations is to study the interaction between active and passive ordered fluid analogues. Parallely, we have pursued the design of strategies to control the active flows characteristic of these materials, by using the exceptional physical properties of LCs. As explained in Section 1, LCs are fluids that feature internal order, which results in anisotropy in many physical properties. Consequently, LCs allow, for instance, to optically report active dynamics by flow-induced birefringence textures (Section 1.4.3), to impose rheological patterns by taking advantage of their viscous anisotropy (Section 1.4.4), and last but not least, to tune their configuration by means of external electric and/or magnetic fields (Section 1.4.1 and 1.4.2). All these features will be of importance for the fulfilment of the posed objectives.

*In situ*-tunable control of active flows not only sets the bases for further development for the steering of biomaterials, but it eases the characterization of their intrinsic length- and timescales. As explained in Section 2.2.1, active turbulence is based on the presence and motion of defects, which gives rise to complex flow patterns that develop at length scales much larger than the size of the actual constituents of the active material. In fact, it is well accepted in the literature [164] that spatial arrangement of ANs is determined by a single intrinsic length scale  $l_\alpha$ , which establishes spatial features in the material such as the steady-state defect separation and the bending radius of the extensile MT bundles.  $l_\alpha$  is assumed to arise from a competition between active stress, which tries to establish a flow field by distorting the director field, and elasticity, which works against this deformation. The crucial role of this length scale has been stressed in the previous chapter and we should recall that its scaling behaviour has been predicted [161,213].

Earlier simulations revealed that this length scale also determines the geometry of the active turbulent regime [164], where the vortex size distribution follows an exponential whose decay length is related to  $l_\alpha$ . With the experiments reported here, we have been able to test these theoretical ideas by forcing the active material to evolve in confined situations, or along predefined directions, providing with a tool to unveil the role of  $l_\alpha$ . Moreover, by steering the orientation of active flows, we have been able



to trigger transitions between turbulent and laminar active flow regimes in ANs, each one of them featuring distinctive dependences between flow speed and activity [164].

In summary, in this chapter, experiments will focus on exploring the interaction between the AN and TLCs. Research on the coupling between active and passive LCs remains in its infancy [158,197,198] although, in our opinion, it is promising for the control of active matter and the implementation of activity-triggered forces in devices. It is not always easy to combine active and passive materials while preserving their integrity, even though, here, thermotropic LCs are proven to be suitable not only for active flow reporting but also for effective active flow commanding. Whichever it is, in our case, we claim that the effects arising from the interaction between active and passive materials are always due to the hydrodynamic coupling at the interface between the two materials.


Control capabilities have allowed us to confine active flows through the water/LC interface while re-establishing the geometrical properties of active turbulence. Furthermore, we have been able to study the topology and dynamics of active laminar flow regimes, never explored before in experimental Active Matter. Finally, “ordered” versions of the usually chaotic-like active material have eased its characterization, by which the previously stated theoretical ideas have been tested.

## Results

The results reported in Chapter 2 clearly point out to a marked effect of the interface on the active nematic, which arises from the need to accommodate the active flows to the rheological properties of the passive contacting fluid. This gives us a clear indication that the contact of the active and passive structured materials is robust, persistent, and stable enough to foresee stronger effects when the order of the passive phase is upgraded to attain anisotropic viscosity. Therefore, in the experiments shown here we use the same setup but replacing the isotropic oil by anisotropic fluids (TLCs), towards which the active nematic will form.

**Interaction between active and passive nematic LCs.** To better evaluate the influence of the contact with an anisotropic fluid on the morphology or dynamics of the AN, we first choose a low viscosity LC, featuring nematic phase at room temperature (4-pentyl-4'-cyanobiphenyl, 5CB, Materials and methods, Section 3.2), so that anisotropy can dominate over viscous-damping to constrain the active flows. However, although the passive mesophase is anisotropic, shear viscosities along different directions are of the same order of magnitude (Section 3.2), and thus do not trigger any observable effects on the AN, which features the well-known turbulent-like flow patterns. Even so, we do observe interesting phenomena arising from the flow transfer from the AN into the passive LC phase. We assume that flow-alignment of the LC molecules near the water/LC interface, generate the rich birefringence patterns observed under crossed polarizers. Especially when homeotropic anchoring is induced at the water/LC interface, due to the influence of a PEGylated phospholipid (Materials and methods, Section 3.6), the passive LC shows textures reminiscent of those exhibited by active nematic underneath (Fig. 67).

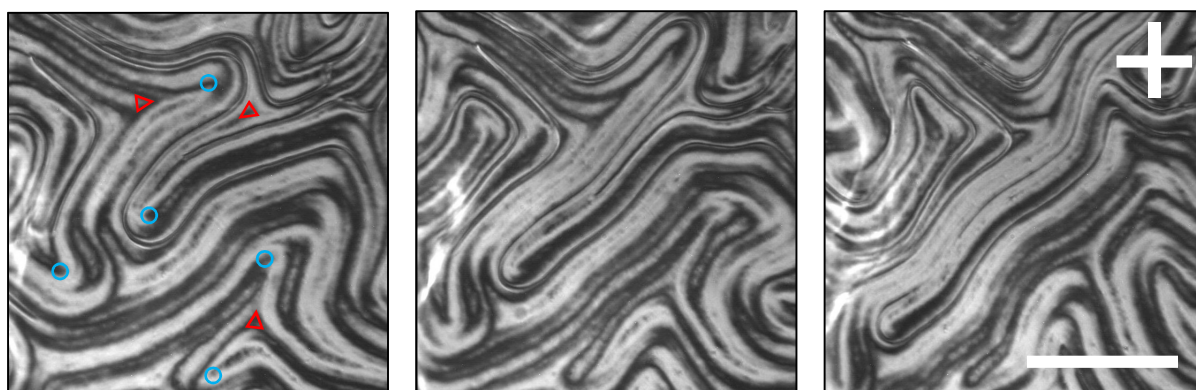


**Fig. 67. Active flows reported by a nematic liquid crystal.** Polarization micrographs showing a time sequence (7s between images) of the textures displayed by a thermotropic liquid crystal, featuring nematic phase, in contact with the active nematic. From the birefringence patterns position of the active defects can be identified (depicted in red ( $-1/2$ ) and blue ( $+1/2$ ) in the left panel). Scale bar, 100  $\mu\text{m}$ .  See Video 4.

Although this phenomenon has not been explored in detail, we have paved the way for further exploration of the molecular-scale flow-reporting capabilities of nematic TLCs.

**Conditioning the geometry of active turbulence with a patterned interface.** From the point of view of the control of active flows, far more interesting effects arise from the interaction between the AN and 4-octyl-4'-cyanobiphenyl (8CB), which features lamellar Smectic-A phase (Section 1.6) at temperatures compatible with the active material integrity. Layers in the smectic-A phase are perpendicular to the oil molecules, which, in the presence of a polymeric surfactant (Materials and methods, Section 3.6), organize parallel to the water/oil interface. Free-energy minimization constraints, related to the boundary conditions at the interfaces, result in the formation of the so-called toroidal focal conic domains (TFCDs) that organize into an Apollonian fractal tiling (Fig. 68*a* and Section 1.6). At the water/LC interface, TFCDs have a circular footprint, and are formed by concentric SmA planes perpendicular to the interface. As a result, 8CB molecules, which are both parallel to the water layer, due to the interaction with the used surfactant, and perpendicular to the SmA planes, orient radially in concentric rings. Crucially, molecules in the SmA phase can diffuse freely within a given smectic plane but their transport is severely hindered in the direction perpendicular to the planes (Section 1.6). The interfacial shear stress probed by the active material is thus markedly anisotropic, forcing active stretching of the MT bundles to occur preferentially along circular trajectories, centered in TFCDs. Swirling laminar currents now evolve within the interfacial domain limits, segregated from the rest of the large-scale flows in the system (Fig. 68*b,c*). This results in the size distribution of swirls to become commensurate with the Apollonian net. Since the latter features a power-law distribution of domain sizes, the original exponential vortex size distribution (Chapter 2, Fig. 63) in the unbound turbulent AN is now transformed into a scale-free power law (Fig. 68*d*).

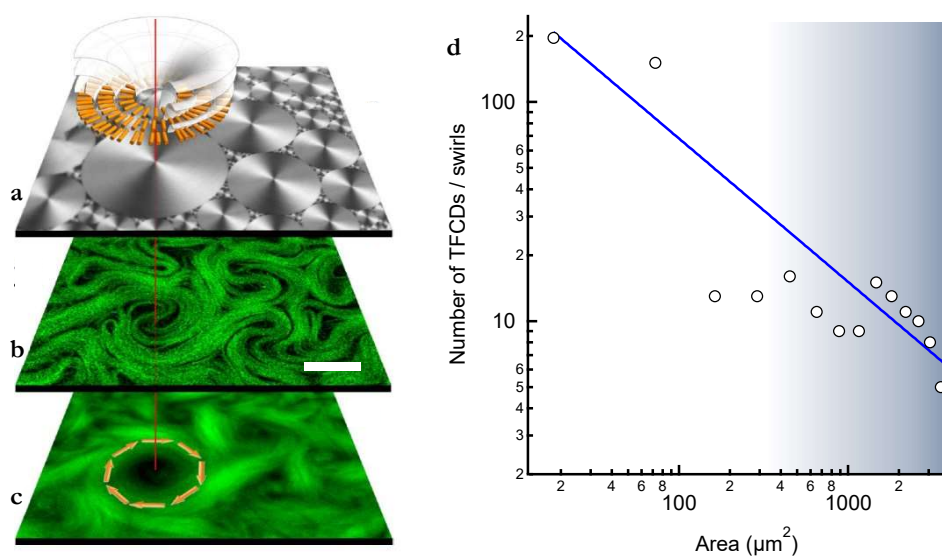


**Fig. 68. Self-assembly of the active nematic in contact with the patterned interface.** **a)** Confocal reflection micrographs of the water/liquid crystal interface reveal the tiling formed by the distribution of circular TFCDs of the liquid crystal 8CB in the Smectic-A phase. The diagram illustrates the arrangement of the mesogen molecules at the interface, which determines the active flow behaviour. **b)** Confocal fluorescence micrograph showing the rearrangement of the active nematic flow into swirls due to the hydrodynamic coupling with the anisotropic interface. **c)** Time averaged fluorescence confocal micrograph (total integration time 300 s) highlighting the patterning of the active flow due to the anisotropic interface. Arrows indicate the direction of the circular flow. Line segments through the panels identify coincident regions, showing that swirls are in registry with underlying TFCDs. Scale bar, 25  $\mu\text{m}$ . (See Video 5). **d)** Analysis of the size distribution of TFCDs in a  $500 \times 500 \mu\text{m}^2$  window. The line is a power law fit to the data with an exponent  $-0.7$ . The shaded region corresponds to the size range of domains that are able to effectively trap the active flow. The threshold can be varied by tuning the experimental control parameters (see text and Fig. 69).


**Intrinsic length scale of the confined AN.** The effectiveness of the active flow confinement depends both on the size of each TFCD and on the composition of the AN. Our experiments reveal the emergence of a cut-off length scale above which TFCDs are able to locally imprint a swirl on the AN (shaded region in Fig. 68*d*), while small domains can, at most, scatter moving defects. Indeed, defects are forced to circulate around the center of large TFCDs, following the circular easy flow directions defined by the underlying SmA phase (Fig. 69).

In order to assess the flow confinement due to a given TFCD, we define, for each  $+1/2$  defect that moves within the domain's limits, a winding number,  $Q = \frac{\Delta\alpha}{2\pi}$ , where  $\Delta\alpha$  is the accumulated angle of rotation around the TFCD center until the defect is either annihilated or it escapes from the domain. We will consider a trapping event for  $Q > 1$ , which implies that the  $+1/2$  defect has performed more than one full rotation around the domain center.

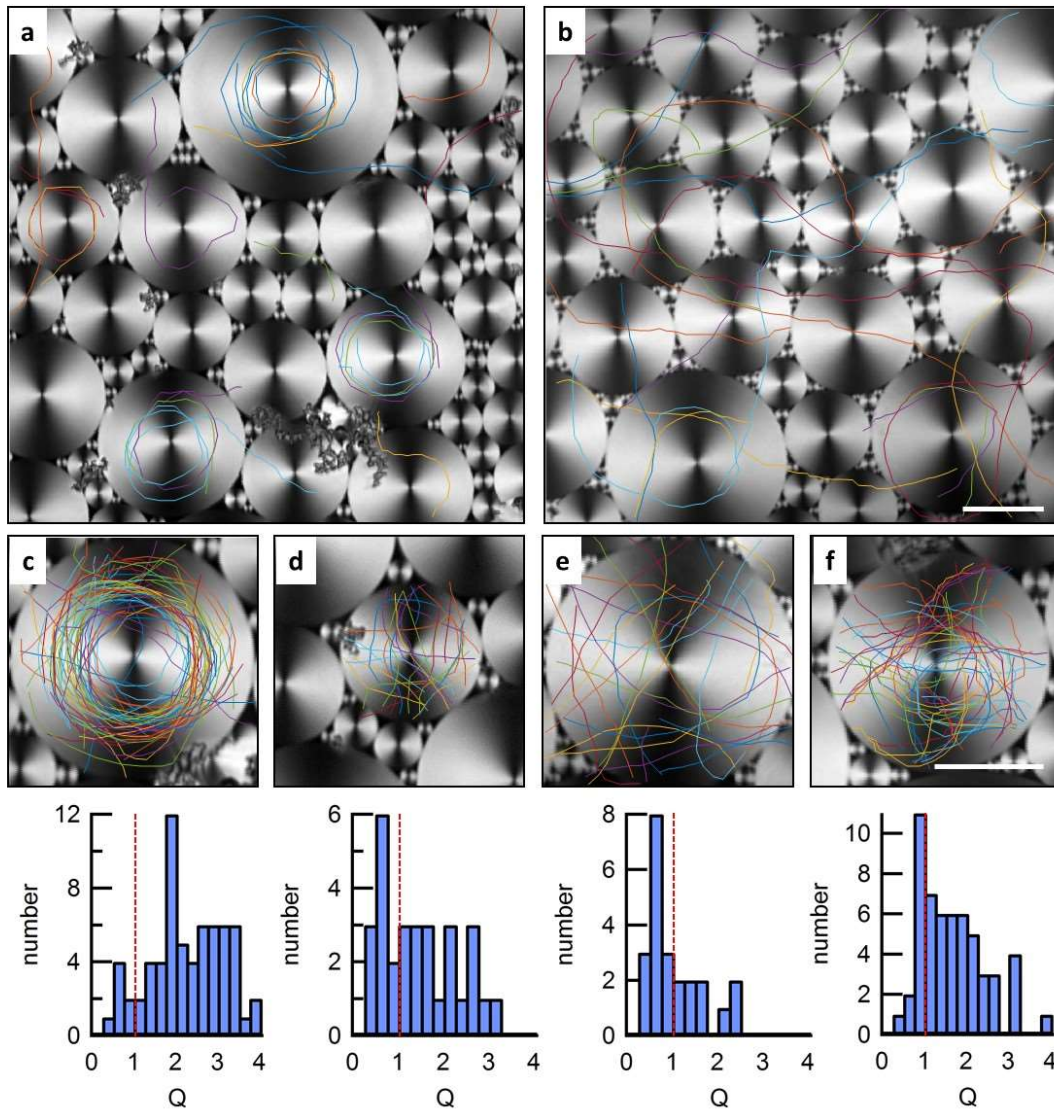


**Fig. 69. Soft confinement of the active nematic.** Confocal reflection micrographs of different TFCDs and overlaid trajectories of  $+1/2$  defects of the flowing active nematic for different experimental conditions: (a, c, and d) [ATP] = 700  $\mu\text{M}$ , [PEG] = 0.8 %w/w; (b and e) [ATP] = 70  $\mu\text{M}$ , [PEG] = 0.8 %w/w; (f) [ATP] = 700  $\mu\text{M}$ , [PEG] = 4.2 %w/w. Histograms below micrographs (c-f) include the distribution of computed winding numbers,  $Q$  (see text), corresponding




to defect trajectories shown in the respective micrographs. The dashed lines indicate  $Q = 1$ , which implies one full rotation of the moving defect. Scale bars, 25  $\mu\text{m}$ .  See Video 6).

We have analysed the influence of the concentration of ATP, which will directly modify the activity parameter ( $\alpha \sim \log[\text{ATP}]$ ), and the bending rigidity ( $K$ ) of the active bundles, which is expected to increase with the concentration of the depleting agent PEG [156]. For the reference experimental conditions ( $[\text{ATP}] = 700 \mu\text{M}$ ,  $[\text{PEG}] = 0.8 \text{ \%w/w}$ , Materials and methods, Section 3.1.6) the critical domain diameter is  $\sim 30 \mu\text{m}$  (Fig. 69a). Larger domains (Fig. 69c) are able to capture the active flows, while smaller ones (Fig. 69d) do not significantly alter the defect trajectories. A decrease in  $\alpha$  (Fig. 69b, e) or an increase in  $K$  (Fig. 69f) lead to a shift to smaller  $Q$  values for a given domain size.

**Topology of AN swirls.** In order to understand the origin of the threshold TCFD size for the effective confinement of moving filaments, we focus on how the AN self-organizes into swirls. As a characteristic feature of active turbulence, defects are permanently renovated through instabilities of the elongated filaments (Section 2.2.1), even their number may change to a small extent, continuously assembling and disassembling the core structure of each rotating swirl. From a topological perspective, the confined rotating filaments constitute a singularity of total charge  $S = +1$ , which corresponds to a full rotation around the domain centre (Section 1.5.4). However, the spontaneous folding of the extensile AN filaments can only create  $+1/2$  defects (at the tip of the fold) and  $-1/2$  defects (at the tail of the fold) (Section 2.2.1). This topological mismatch poses an additional constraint on the ensemble of AN defects that may evolve within a TCFD. At all times, a dynamic balance must be established such that the arithmetic sum of charges inside a single domain adds up to one, as dictated by topology (Fig. 70).

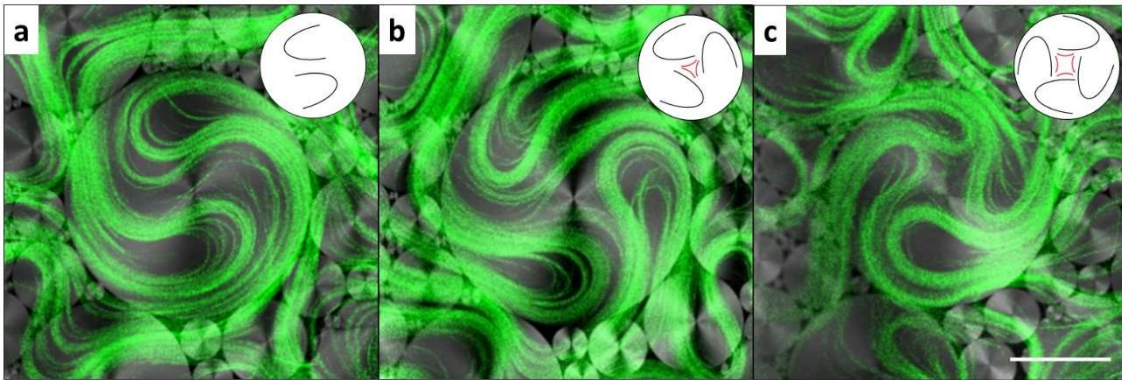



**Fig. 70. Defect structure in active nematic swirls.** Different confocal micrographs of the active nematic in contact with the lattice of TCFDs. The simultaneously acquired confocal fluorescence (green) and confocal reflection (grayscale) channels are overlaid, and show, respectively, the active nematic filaments and the SmA interface. Due to spontaneous defect unbinding and annihilation, the active flow trapped by the central domain features different topological defect configurations over time, as illustrated by the sketches on the top right corners, but always with a net topological charge balance  $S = +1$ . **a)**  $S = 2 \times (+1/2)$ ; **b)**  $S = 3 \times (+1/2) - 1/2$ ; **c)**  $S = 4 \times (+1/2) - 1$ . Scale bar, 50  $\mu\text{m}$ .  See Video 7.

Clearly, the minimum number of semi-integer defects required to organize a rotating swirl is two  $s = +1/2$  defects (Fig. 70a). Since defect spacing is regulated by  $l_\alpha$ , the above topological arguments establish a minimum size for a rotating swirl. Taking into account that the threshold domain size for effective flow trapping scales with material parameters consistently with  $l_\alpha$ , we conclude that it is indeed this active length scale that also determines the crossover from turbulent to laminar flow under confinement.

**Periodic bending instability in AN swirls.** The extensile nature of the studied AN material makes a configuration of parallel elongated filaments intrinsically unstable, leading to a defect-forming bending instability (Section 2.2.1). As observed in Fig. 71a, the distribution of the trapped active filament density around large TFCDs is heterogeneous, with a central region mostly devoid of MTs surrounded by a denser region occupied by the outer arms of the parabolic filament bundles that form  $+1/2$  defects. Since filaments are locally parallel within this region, the inner structure of organized  $s=+1$  swirls is unstable, being periodically disrupted and reconstituted (Fig. 71b-g).

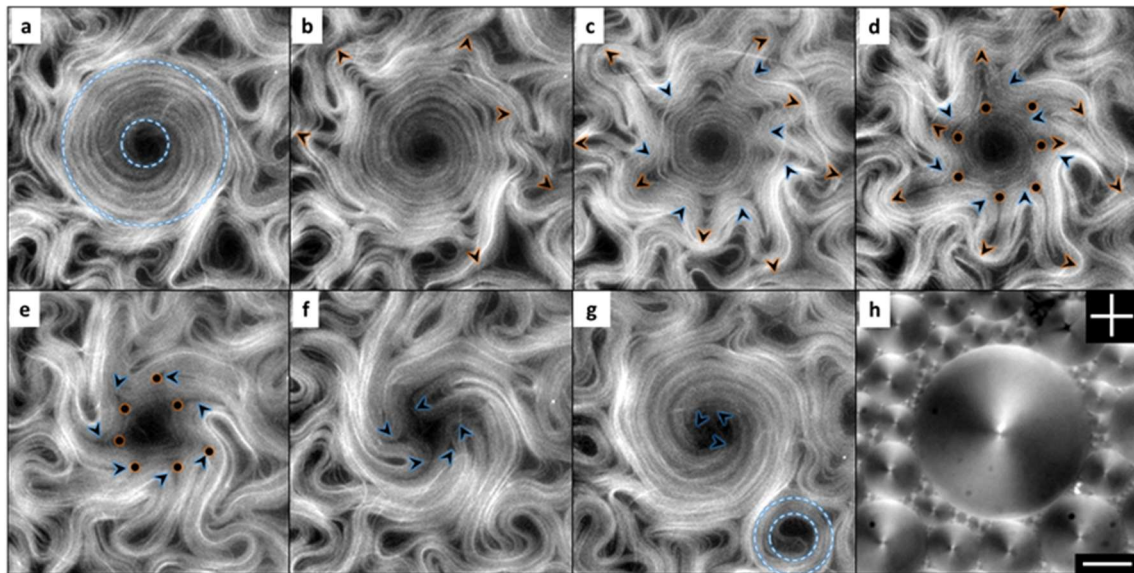



**Fig. 71. Defect dynamics in active nematic swirls.** Fluorescence confocal micrographs show the periodic reconstruction of the active nematic swirls constrained by a TFCD. **a)** Rotation of  $+1/2$  defects results in the formation of a corona of MT bundles, which align in quasi-concentric circumferences. Dashed lines depict inner and outer corona perimeters. **b-d)** radial bending instability of the aligned bundles generates pairs of complementary  $+1/2$  (black arrow heads, blue incoming, red outgoing) and  $-1/2$  (black dots highlighted in red) defects. **e-g)** Incoming  $+1/2$  defects annihilate with static  $-1/2$  defects, leading to the formation of a new swirl structure. In **(g)**, a smaller TFCD has assembled a MT corona. For clarity,  $-1/2$  defects are only highlighted in **(d)** and **(e)**. **h)** Polarizing micrograph taken between crossed polarizers (top right corner) of the local distribution of TFCDs that leads to the active flow patterns in **(a-g)**. Scale bar, 50  $\mu\text{m}$ .  See Video 8.

The emergence of this instability is made more apparent in swirls assembled by bigger TFCDs. In these situations, the AN can generate a thick annular band of circularly-aligned MT bundles (Fig. 71a). This configuration is unstable (Fig. 71b), and the filaments develop a radial buckling instability that leads to the formation of semi-integer defect pairs, moving inwards and outwards of the domain (Fig. 71c-d). Some of these new defects will eventually annihilate with existing inner ones (Fig. 71e-f), finally reorganizing the original aligned state (Fig. 71g). This sequence of dynamic events, which is also exhibited as a time periodic modulation of the velocity of the active flows inside domains, repeats with remarkable periodicity, thus revealing an intrinsic time scale of the active nematic [214]. We conjecture that this kind of periodic “avalanches” arise from the intrinsic dynamics of the sheared MTs, and provide a breakdown mechanism that the active material has at its disposition to repeatedly release the extensile tensional stress accumulated in the ordered active filamentous bands. In spite of the flow reorganization triggered by episodes of structural instability, the handedness of flow rotation inside each swirl, which is randomly selected upon self-assembly, is preserved in time.

By performing velocimetry analysis of the swirling currents together with particle tracking of passive beads (Materials and methods, Section 3.9) embedded either in the AN (Fig. 72a) or within the lamellar smectic-A planes (Fig. 72b), we have been able to evidence the synchronous flow coupling between the active and the passive LCs, and to quantify the frequency for the oscillatory dynamics of the AN swirls (Fig. 72c,d).

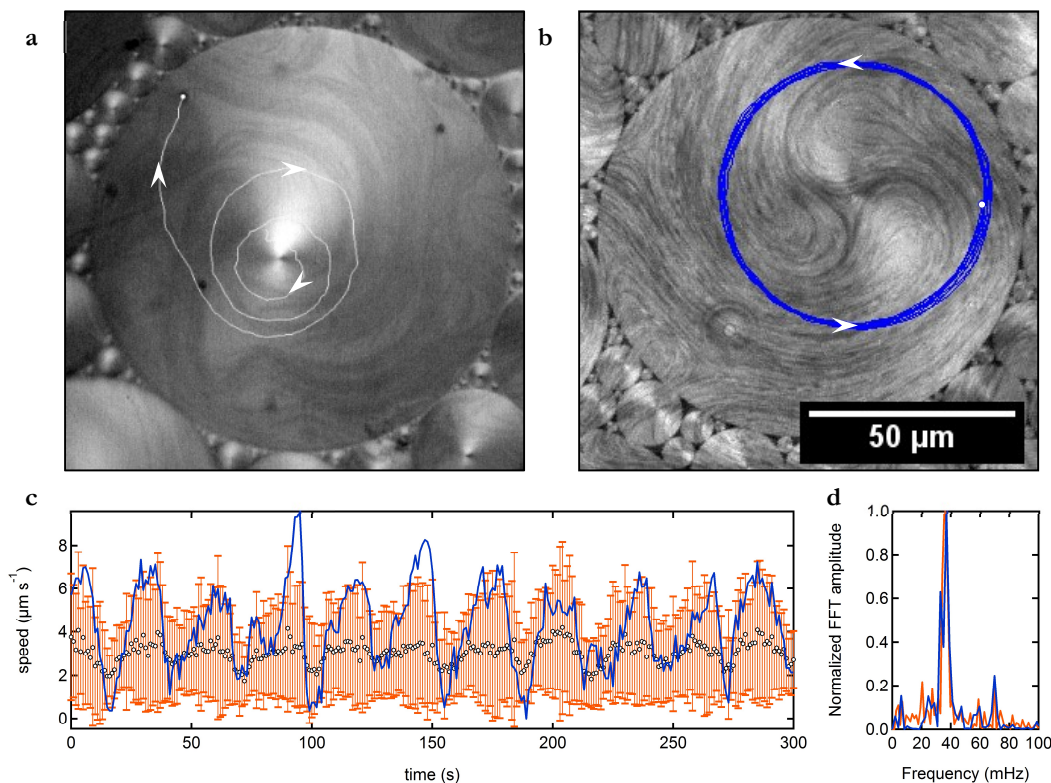


**Fig. 72. Flows induced by active nematic swirls.** In contact with big enough TFCDs, the active nematic generates swirling flows, which can effectively drag dispersed passive tracers (**a**, white dot) in spiral trajectories (white line). **b**) Particles adsorbed at the oil phase move in perfect circles within the lamellar planes (blue line). Arrows indicate the sense of the rotation. **c**) Active nematic swirls are unstable and they assemble and disassemble with striking regularity. Here, we plot the average speed of the active flows in (**b**) (white dots with orange error bars) together with the speed of the rotating tracer at the lamellar phase (blue line). **d**) Normalized power spectra for data in (**c**).  See Video 9.

Since the beads that circulate together with the active material are not bound to a circular trajectory, the tracers inside rotating swirls drift outwards while performing spiral trajectories (Fig. 72a). On the other hand, particles adsorbed at the LC phase describe a perfect circular trajectory, following the geometry of the SmA planes (Fig. 72b).

**Control of the AN with a magnetic field.** A tighter control of the active flow is achieved by directly actuating on the contacting passive oil. To this purpose, we take advantage of its (positive) diamagnetic anisotropy (Sections 1.4.2 and 3.2) that enables to align a macroscopic volume of the material with uniform magnetic fields of the order of a few kG, easily attainable with a permanent magnet array (Materials and methods, Section 3.7.2). By a slow temperature quench of 8CB (Materials and methods, Section 3.7.3) from the nematic to the lamellar (smectic-A) phase, in presence of a 4 kG magnetic field parallel to the oil/water interface, we induce the formation of a layer of oil molecules uniformly aligned with the magnetic field. In this situation, the lamellar planes are oriented perpendicularly both to the interface and to the magnetic field (Fig. 73a). This structure, so-called bookshelf geometry, robustly



kept after removal of the magnetic field, results in a liquid that flows easily when sheared along the lamellar planes, but that responds as a solid to stresses exerted in the orthogonal direction (Section 1.6). Polarizing optical microscopy confirms the formation of this aligned smectic-A layer (Fig. 73*a*) that includes dislocations in the aligned lamellar planes, which propagate into the bulk of the material with the so-called parabolic focal conic domains (PFCDs, Section 1.6). In contact with this interface, the turbulent active nematic experiences markedly anisotropic shear stresses, which result in a rapid rearrangement of the flow pattern that consists now in parallel stripes of uniform width aligned perpendicularly to the magnetic field (Fig. 73*b*). Fluorescence microscopy indicates that the bright stripes consist on densely packed microtubule bundles, while intercalated dark lanes incorporate the cores of proliferating  $\pm\frac{1}{2}$  defects, which align and move in antiparallel directions (Fig. 73*b,c*). Negative defects are, in this situation, more difficult to localize, although the global topological requirements apply here to secure a zero total charge.

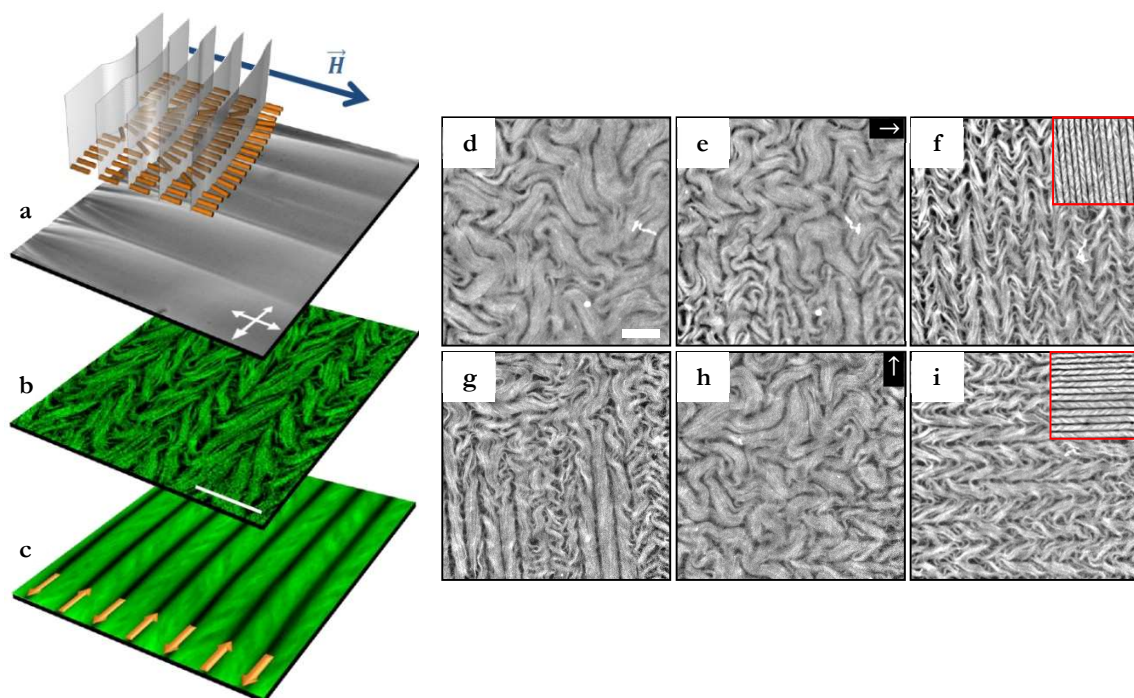


**Fig. 73. Alignment of the active nematic with a magnetic field.** **a)** Polarizing optical micrograph, and configuration of the underlying molecular planes in the SmA phase of the passive liquid crystal. **b)** Fluorescence confocal micrograph revealing the correlation between the aligned active nematic and the anisotropic SmA phase. **c)** Time average of the dynamic pattern. The arrows depict the antiparallel flow directions along the lanes of defect cores. **d-i)** Fluorescence micrographs with different configurations of the active nematic in the presence of a 4-kG uniform magnetic field (orientation is indicated by the white arrows). **d)** The active fluid is initially in contact with nematic 8CB, which is transitioned, below  $T_{N-SmA} = 33.4$  °C, into the lamellar smectic-A phase (**c**) under a horizontal magnetic field. **f)** The active nematic aligns perpendicularly to the field. By temperature cycling above (**f-h**) and below (**h-i**)  $T_{N-SmA}$  under a vertical magnetic field, the active nematic is now realigned in the orthogonal direction (**i**). Insets in (**f**) and (**i**) are time average images of the aligned states, evidencing the unidirectional orientation of the active flows. (Scale bars: 100  $\mu\text{m}$ ). See Video 10 and Video 11.


**Transition between turbulent and aligned laminar flow regimes.** Chaotic filament orientation observed under the nematic phase of 8CB (Fig. 73*d*) can now be regularized into an aligned laminar flow regime (Fig. 73*d-f*). During the slow temperature ramp that triggers the transition to the SmA phase, there is a transient state where regions with 8CB in the nematic and in the SmA phase coexist, resulting in growing areas where the AN is aligned, together with vanishing regions where it is still



disordered (Fig. 73e). The alignment process is reversible and versatile. By cycling the temperature above (Fig. 73f-h) and below 33.4 °C (Fig. 73h-i) the AN returns to the disordered state when freed from the interfacial constraints, and a new direction of alignment can be arbitrarily chosen by rotating the magnetic field (Fig. 73j).


**Bending instability in the aligned AN.** As observed in the laminar swirling flows (Fig. 71), parallel arrangement of microtubule bundles between defect lanes is prone to suffer the intrinsic bending instability of extensible active materials (Section 2.2.1). Indeed, we observe periodic outbursts of defect creation across the stripes that lead to transient transversal flow damping the average speed of the AN (Fig. 74). Regions with aligned stripes (type I regions, Fig. 75a) coexist with transient regions where alignment is lost (type II), which span arbitrary extensions that are commensurate with the stripe width. Close inspection shows that the instability originates from packed parallel microtubule bundles that bend and generate pairs of complementary half-integer defects, which either annihilate in pairs or incorporate into opposite pre-existing lanes (Fig. 75b,c). A velocimetry analysis of the dynamics of the aligned AN layer reveals that these stress-generated disrupting episodes occur with remarkable regularity, imprinting an oscillation frequency to the velocity that depends linearly on the activity (Fig. 75d-f).

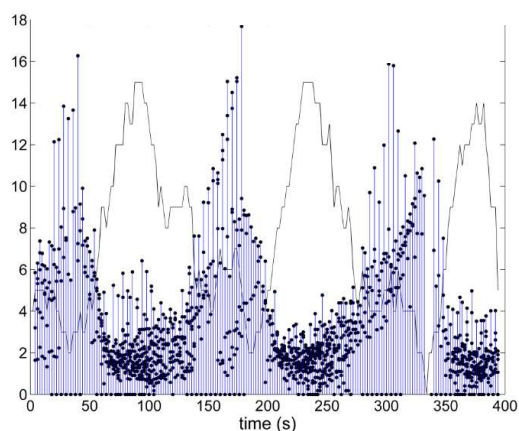


**Fig. 74. Regular destabilization of the aligned active material via bending deformations.** Instantaneous defect speed (blue lines,  $\mu\text{m}\cdot\text{s}^{-1}$ ), and total number of defects (black line) follow complementary oscillation behaviours during spontaneous alternation between type I and type II regimes.  See Video 12.

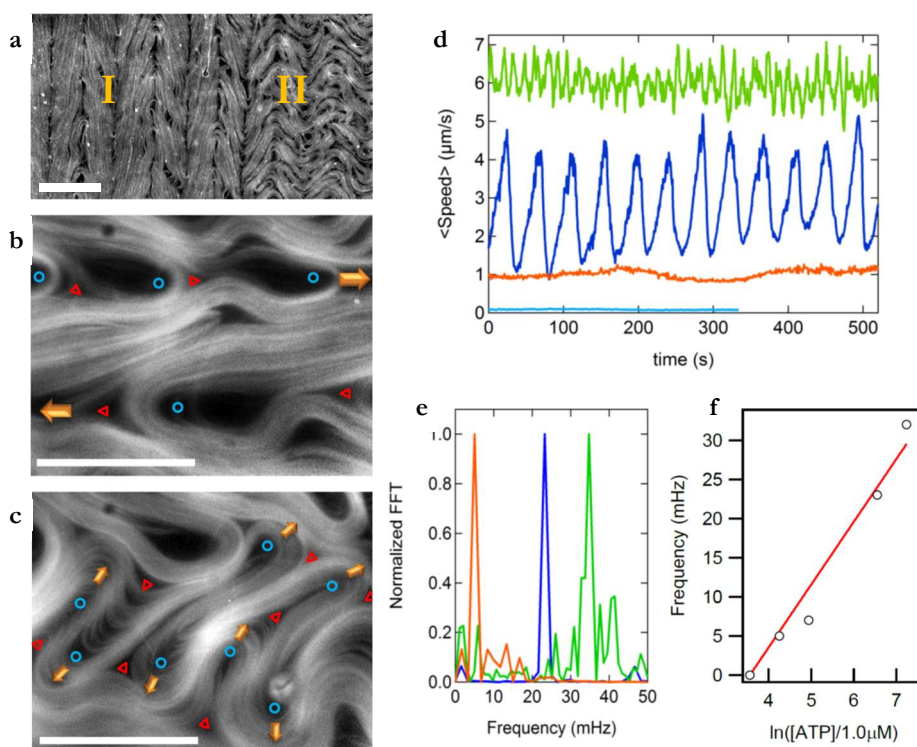



**Fig. 75. Oscillatory instability of the aligned active nematic.** a-c) Fluorescence micrographs of a horizontally aligned active nematic layer showing the two alternating dynamic regimes: (I) with aligned stripes and lanes with flowing defects,

and (II) with transversal flow. **b)** Magnified view of regime (I) with the cores of the flowing  $+\frac{1}{2}$  (blue circles) and  $-\frac{1}{2}$  (red triangles) defects highlighted. **c)** Magnified view of regime (II) with the proliferation of transversally flowing defect pairs. Scale bars, 100  $\mu\text{m}$ . **d)** Temporal evolution of the average active nematic speed, determined from velocimetry measurements for different concentrations of ATP, 1.400  $\mu\text{M}$  (green), 700  $\mu\text{M}$  (blue), 70  $\mu\text{M}$  (orange), and 35  $\mu\text{M}$  (light blue). **e)** Normalized power spectra for data in **(d)**. **f)** Linear scaling of the leading oscillation frequency with the ATP chemical potential.  See Video 13.

Also from velocimetry data of the moving active filaments, we have been able to observe that the average speed is highest along the lanes where defect cores organize and vanishes on the stripes where microtubules pack (Fig. 76*a-c*). Velocity gradients follow a complementary pattern, being the highest at the points of flow stagnation. By seeding the active nematic with colloidal microparticles (Materials and methods, Section 3.9), we put into evidence that the aligned lanes are able to actively transport biocompatible cargo (Fig. 76*d*).

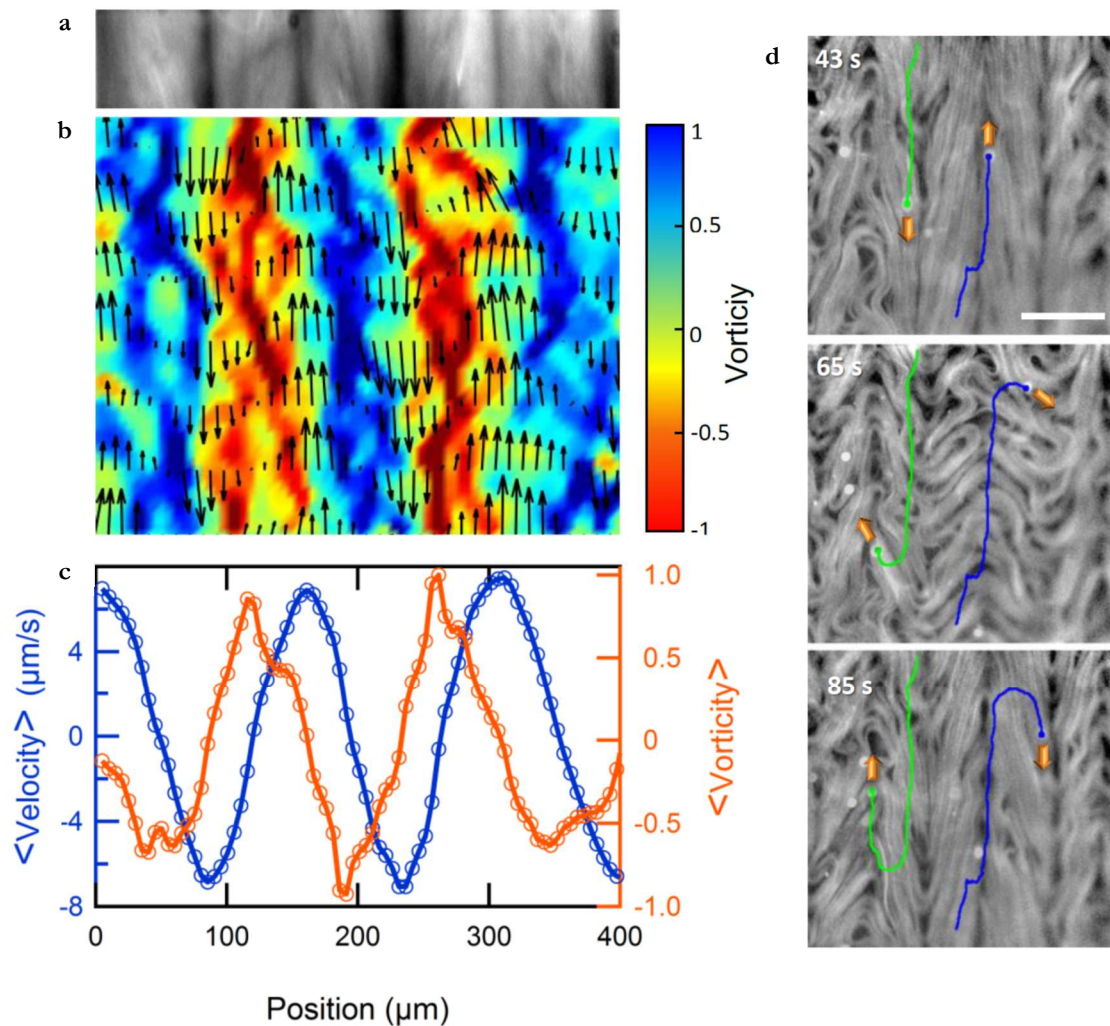


**Fig. 76. Active flow along self-organized lanes.** **a)** A transversal cut of the time-averaged fluorescence micrograph is shown. **b)** Local velocity (vector plot) and local normalized vorticity ( $\partial v_y/\partial x - \partial v_x/\partial y$ , color density plot) for the vertically aligned active nematic film. **c)** Downstream average of velocity and vorticity across the horizontal position. **d)** Fluorescence micrograph with the path of colloidal tracers being advected in neighbouring (i.e., antiparallel) flow lanes. Local instability of the aligned pattern may lead to lane jumps (Middle) and thus to velocity inversion (Bottom) of the transported particles. Scale bar, 100  $\mu\text{m}$ .  See Video 14.

**Spatiotemporal scaling behaviours.** We have analysed the AN patterns aligned under a magnetic field for different activities, characterizing the spatial periodicity in terms of the average distance between adjacent antiparallel flow lanes (Fig. 77a).

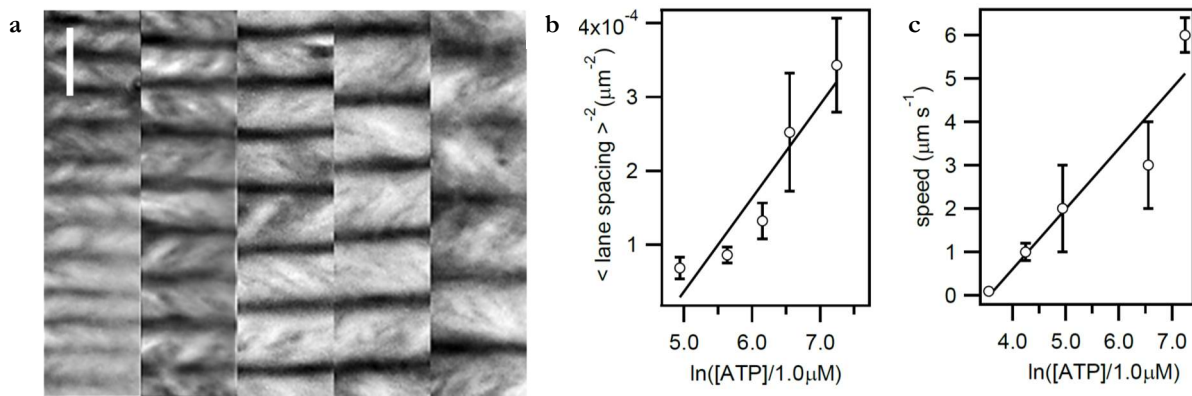


**Fig. 77. Activity dependence of the self-organized flows.** **a)** Time average of fluorescence micrographs of horizontally aligned active nematic films for different concentrations of ATP, from Left to Right, 1.400, 700, 470, 280, and 140  $\mu\text{M}$ . Scale bar, 100  $\mu\text{m}$ . **b)** Scaling of the average spacing between neighbouring lanes, and **(c)** of the maximum speed inside the flowing lanes with the ATP chemical potential.

We find that this length scale depends on the ATP concentration as predicted by the scaling relation  $l_\alpha \sim \alpha^{-1/2}$  (Fig. 77b), presented in the introduction of this chapter. Even though predicted for a free-floating AN, this relation is evidenced also in these realizations, despite the fact that our active film has a strong hydrodynamic coupling with the SmA LC, crucial to account for the described alignment mechanism.

Finally, we find that the velocity inside lanes satisfies a scaling  $v \sim \alpha$  (Fig. 77c). Existing theoretical models [164] predict this linear scaling in a laminar flow regime, whereas a dependence  $v^2 \sim \alpha$  should be expected for active turbulence. In our case, the latter regime is observed when the active nematic is in contact with nematic 8CB or with an isotropic oil (Chapter 2, Fig. 60). Therefore, we argue that the described alignment protocol provides with a reversible mechanism to transit the active nematic between the turbulent and the laminar flow regimes.

---

# Conclusions

In this chapter, we report how the disordered flow patterns of the active two-dimensional nematic can be controlled to follow preassigned directions, along which the material develops laminar flows. This is achieved by means of the anisotropic shear stress exerted at the interface by a LC layer featuring lamellar SmA phase. Either circular domains of concentric lamellae or magnetically-oriented bookshelf structures have enabled to command the turbulent behaviour of the AN. The versatility, reversibility, and robustness of such strategies should be considered as a proof of concept for the taming of active subcellular materials.

- Confinement with an anisotropic soft interface can lead to the reversible modification of the nature and geometry of active flows, whose structure is nevertheless always determined by the single intrinsic active length scale.
- In contrast with the exponential vortex size distribution observed in ANs evolving in contact with isotropic oils (Chapter 2, Fig. 63*d*), here, by contact with a patterned soft interface, active turbulence is reorganized in a scale-free power law distribution of swirl sizes that adapts to the underlying tiling (Chapter 3, Fig. 68*d*).
- Even in this regime, an intrinsic length scale resurges in the form of a minimum swirl size that is compatible with laminar AN flow.
- We have provided topological arguments that justify the existence of this minimum size, since at least two  $+1/2$  defects of the active filaments are required to organize a circulating swirl, and the defect separation is regulated by  $l_\alpha$ .
- Moreover, we have found that the scaling of this characteristic size with the material parameters  $\alpha$  and  $K$  is consistent with the one expected for  $l_\alpha$ . This evidence, along with the topological arguments presented above, let us summarize our findings as a manifestation of the different roles played by the same active length scale  $l_\alpha$ , depending on the confinement constraints.
- In addition, by confining the AN in swirls, we have been able to explore the metastable nature of these extensile active material arrangements, prone to suffer bending instabilities.
- Turbulent flows of the AN have been also regularized into an aligned laminar flow with periodic velocity oscillations, when orienting the contacting smectic LC with a magnetic field.
- Once patterned, the MT-based assembly reveals its intrinsic length and timescales, which we correlate with the activity of motor proteins, as predicted by existing theories of ANs.
- The topology and dynamics of this aligned flowing state are also studied. In brief, defects organize in parallel lanes, along which they circulate in opposite directions. Velocities reach their maximum along the trajectories of oppositely flowing defects, which generate bands of high vorticity.
- As it occurs in active swirls, unidirectional laminar flows lead to vast regions of aligned MT bundles. Release of extensile stresses within these regions generates bending instabilities that periodically distort the aligned states with outbursts of defect creation.



# **Chapter 4. Active droplets in nematic liquid crystals**



---

# Introduction

Topological defects are intrinsic of all liquid crystals, both thermotropic and lyotropic, passive (Section 1.5.4) and active (Section 2.2.1), and respectively, have a relevant role in the operation of new meta-materials and in the organization of active matter. However, how these structures interact with each other has been poorly explored, especially in cases when they originate in mesogens of different nature.

Here, with our experiments and simulations performed by M. Ravnik and Ž. Kos (University of Ljubljana, Slovenia), we report the phenomena arising from the interaction between topological defects of active (lyotropic) and passive (thermotropic) nematic liquid crystals, which hydrodynamically interact through a soft interface in water-in-liquid-crystal active emulsions. In the experiments shown here, droplets of active gel featuring an AN shell are suspended in different fluids. In contrast to large flat AN films, where defects are continuously generated and annihilated in pairs at equal rates generating seemingly-chaotic flows, simpler behaviour can be observed in well-defined confinement conditions, whose geometrical and topological restrictions constrain the dynamics of the active system. In particular, when encapsulated in micro-droplets, the tubulin/kinesin-based active material is driven towards the inner surface of the confining spheres by depletion forces. In large enough droplets, the constituent MT bundles can accommodate onto the inner surface self-assembling into a thin AN shell. As introduced in previous sections, topological rules dictate that defects for nematic shells must accumulate a total charge of  $+2$  under equilibrium conditions (Section 1.5.4). Differently from their passive analogues, defects within the AN generate stresses and move (Section 2.2.1). Therefore, because of their intrinsic dynamics, it is not possible to minimize repulsion between defects while conserving inter-defect relative distance. In addition, under a critical shell size, destabilization of the active nematic is elastically inhibited thus further creation of defects is suppressed. Free energy minimization predicts a preferred minimal defect configuration of four  $+1/2$  defects located at the corners of a tetrahedron inscribed in the sphere [41]. The presence of these four motile singularities lead to a coherent dynamic steady state, with defects circulating unceasingly at the inner surface of the sphere, where they oscillate between a quasi-tetrahedral arrangement and a (more energetic) coplanar configuration [82,189]. The arisen coherent flows are transmitted to the surrounding fluids.

Even though we will first describe the behaviour of active emulsions with isotropic oils, this chapter will focus on the study of the effects arising from the interaction of active droplets in NLCs. The latter are studied between parallel plates that induce identical anchoring conditions to the molecules of the passive LC (Materials and methods, Section 3.5), either planar or tangential, generating well-defined topological structures around the active inclusions (Section 1.5.5). In particular, we are especially interested in the accommodation of Saturn ring disclinations to the flows exerted by active droplets, and in studying the possible cross-talk between active and passive defects. According to recent numerical simulations [189], active defects in active nematic shells move following closed paths along the edges of a deformed cube, each pair of defects being cyclically symmetric about the symmetry axis of the cube. The high freedom in inscribing the embedded cube anticipates a high degeneracy of the realized trajectories. Nevertheless, in bounded situations, active shells generate strikingly coherent flows, which can only be attainable for very specific orientation of the cubic axes defining the active defect trajectories.



In summary, this chapter will tackle, on the one hand, how defect flows in active shells are transmitted to their surroundings, either isotropic or anisotropic. Particularly, the influence of active flows on passive defect structures in LC remains practically unexplored [215,216]. On the other hand, we suggest flow-damping mechanisms by which the active defect dynamics might become stabilized by physical constraints. In particular, coupling between active and passive liquid crystal topological defects not only increases our knowledge of these complex structures but it may lead to better control strategies of active matter.

# Results


ANs can be prepared in the inner surface of droplets, where they adapt to the geometrical and associated topological constraints. As it has been introduced, in a certain size range, AN spherical shells feature four  $+1/2$  motile defects that circulate throughout the shell oscillating between two well-defined defect configurations (Section 2.3 and Fig. 78). However, free AN shells imply degenerate orientations of active defect states with respect to the confining sphere. In this chapter, we present our work with active emulsions, where active shells evolve in constrained situations. First, we report preliminary experiments with active droplets in isotropic fluids, where active defect trajectories could be constrained by frictional damping. The second part, more extensive, focuses on the interaction between active droplets and passive LC defects in water-in-LC emulsions, and on the possible bounding effects of topological structures around AN shells.

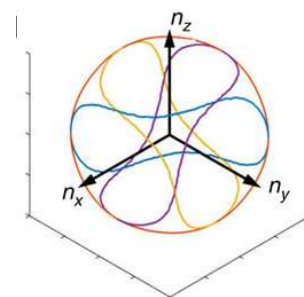


**Fig. 78. Defect trajectories in small active nematic shells.** Coloured lines are full minimally-distorted paths of the four  $+1/2$  defects. Adapted from [189].

**Active nematic shells in isotropic fluids.** It has been shown that droplets featuring an AN shell can exhibit autonomous motility when partially compressed between chamber surfaces [77]. The mechanism by which active droplets move is assumed to arise from the frictional coupling between the active shell and the contacting plates. Flow jets generated by the  $+1/2$  defects act as drop propellers when passing near a rigid surface. Here, by confining active emulsions based on low-viscosity isotropic oils (Materials and methods, Section 3.4), we notice that single small active gel droplets display very robust and practically uniform rotational motion that develops centred at a distance equal to the radius of the droplets (Fig. 79). By tracking the active defects, we are able to identify repeated defect paths that trigger the observed regular droplet motion. We presume that frictional contact with the substrate of the confining cell hampers specific trajectories of the active defects. Adaptation of defect-originated flows to the boundary conditions result in the observed motion.

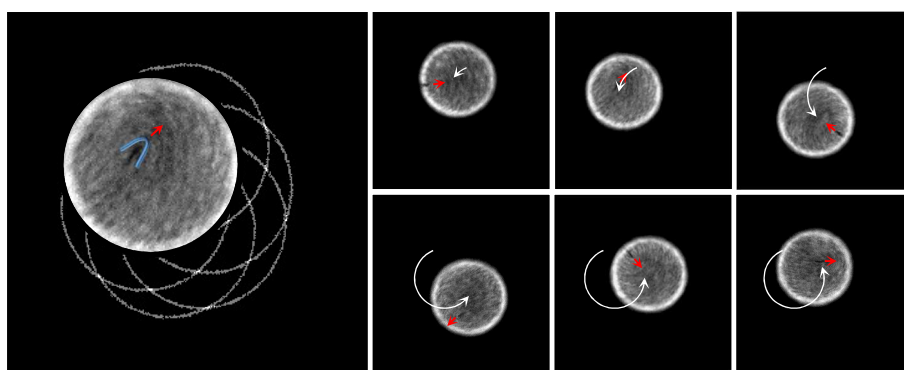


**Fig. 79. Active nematic shells in contact with a solid substrate.** Fluorescence micrographs of an active nematic shell show persistent oscillatory rotational dynamics. Motion of positive defects is indicated with red arrows. The translation trajectory of the motile droplet is depicted by the white arrow. The diameter of the droplet is  $\sim 75 \mu\text{m}$ .  See Video 15.

Hydrodynamic interaction between different droplets give rise to more chaotic dynamical states (Fig. 80), although we envisage flow coupling and synchronization for small droplets in jammed situations. Droplets with diameters larger than  $\sim 100 \mu\text{m}$ , feature AN shells punctured with both positive and negative semi-integer defects (Fig. 80). The trajectories of bigger droplets are thus much more complex. Although the topological constraint  $Q=+2$  is always satisfied in AN shells, the number of defects inevitably increases when the diameter of the shells is above the length scale at which homogeneously ordered regions are unstable to bend deformations.

**Active nematic shells in nematic liquid crystals.** More interesting is the case of imposing tuneable topological soft constraints by using passive LCs as a continuous phase for preparing the active emulsions. In the following experiments, we prepare water-in-oil emulsions based on droplets of the MTs/kinesin active gel dispersed into a thermotropic nematic LC, 5CB (Materials and methods, Section 3.4). Dispersed droplets generate a distortion of the anisotropic host, which accommodates to the imposed boundary conditions by creating topological defects close to the surface of the inclusions (Section 1.5.5). The formation of the active nematic at the inner

surface of the droplets generates flows that are effectively transmitted through the water/LC interface, driving the (typically static) topological defects far from equilibrium. By taking advantage of the oscillatory dynamics of the active nematic shells, coherent flow patterns are imposed to the passive LC topological defects. The latter couple with the flow generated by the active nematic defects and exhibit their own dynamic properties and behaviour, only constrained by topology, which impose restrictions for active defect trajectories. Therefore, active dynamics that result in a minimum distortion of surrounding passive ring-like defects are favoured. As a consequence, the interaction between active defect motion and passive topological restrictions lead to regular oscillating states that suggests a cross-talk between active and passive defects.

**Strained Saturn ring defects.** Between surfaces inducing identical anchoring, active nematic shells, coated with a PEGylated phospholipid (Materials and methods, Section 3.6), lead to the generation of closed disclination lines, with core configuration  $s=-\frac{1}{2}$ , that surround spherical inclusions in the equatorial plane, perpendicular to the planar far field (Fig. 81). These singularities are called Saturn rings (SRs) (Section 1.5.5). When surrounding droplets with a cortical active nematic shell, SRs are dragged by the flow generated inside the droplets (Fig. 82*a-c*). Active defect trajectories thus alter the shape of the outer disclinations, which are driven away from their equilibrium position and configuration (Fig. 82*a*). The flow field generated within the active nematic sphere is due to the motion of the four  $+\frac{1}{2}$  defects, which impose fast flow jets and vortices that are transmitted to the passive LC. When the trajectory

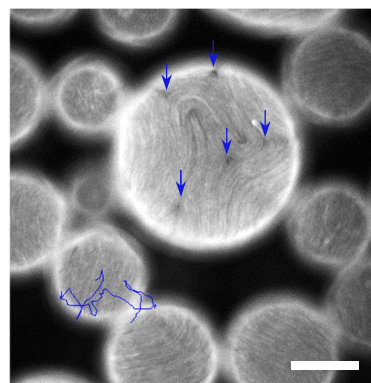


**Fig. 80. Interaction between active droplets of different sizes.**

Fluorescence micrograph of a group of contacting active droplets. Interaction between active cortical flows disrupt the otherwise rotational motion of small droplets ( $\varnothing < 100 \mu\text{m}$ ). Blue line corresponds to the random trajectory of one droplet. Big active shells allow the unfolding of defect pairs, noticeable by the presence of negative singularities, depicted by the blue arrows. Scale bar,  $100 \mu\text{m}$ .

 See Video 16.

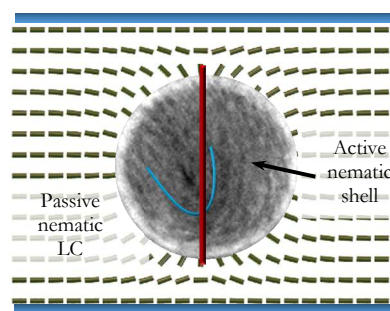



**Fig. 81. Active nematic shell in a thermotropic nematic liquid crystal.**

Fluorescence image of an active nematic shell showing a  $+\frac{1}{2}$  defect. Short rods represent the passive liquid crystal molecule and the red line depicts the equilibrium position of the induced disclination.

of a  $+1/2$  defect crosses below the SR, the disclination folds and extends in response to the active flow (Fig. 82*b,c*). In ideal conditions, active defects move around the active nematic shells and circulate as far as possible from each other, alternating between quasi-tetrahedral arrangement and a coplanar configuration. SRs wrap the active shells and remodel in order to adapt to the flows generated by the active nematic defects (Fig. 82*d*). Some of the oscillations between tetrahedral and planar arrangements will result in two of the four active defects traveling below the equator of the SR disclinations with opposite directions. The other pair of active defects follows the complementary pattern at the other pole. Consequently, dragged from the inner cortical flows, the SR exhibits a remarkable integrity as it periodically folds about its equilibrium position, in a way that reproduces with remarkable accuracy the dynamics of the active defects. While rotating in opposite directions in each side of the droplet, active defects induce the formation of a figure-of-eight structure of the wrapping ring (Fig. 82*a,c*).

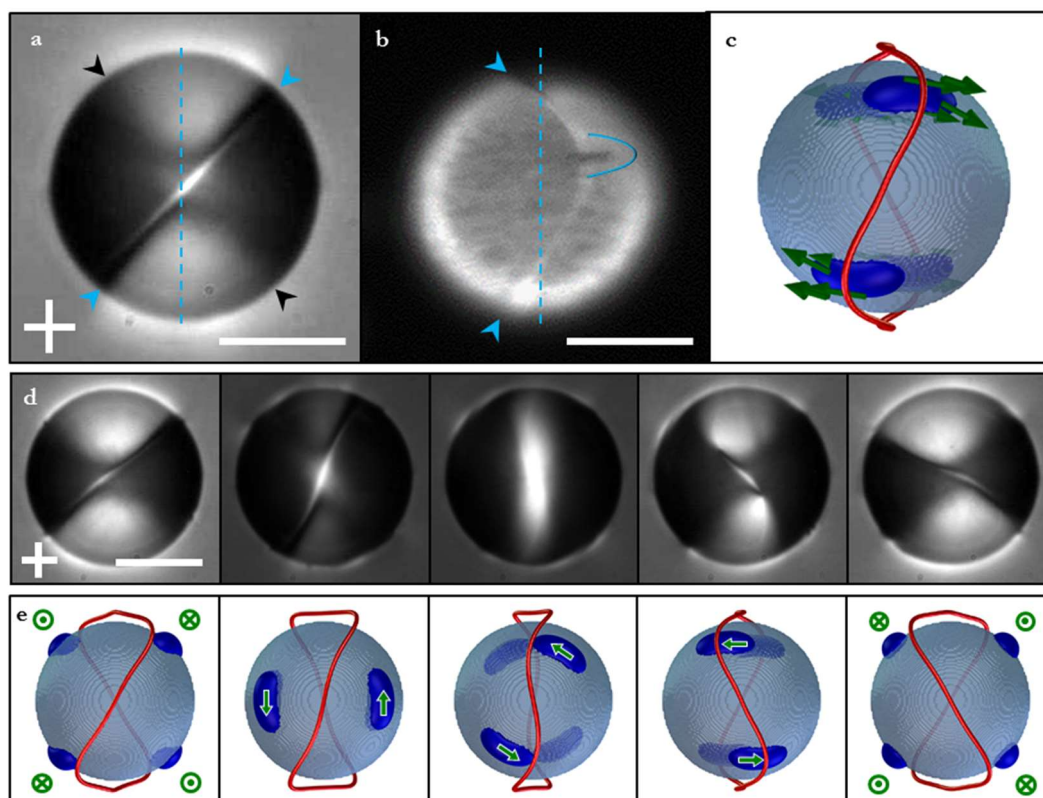


**Fig. 82. Periodically-oscillating Saturn ring defects.** **a)** Oscillating SR observed between crossed polarizers (the orientation of the polarizers is represented by the white cross). Arrow heads indicate the position of the SR in front (blue) and behind (black) the active droplet, at the maxim amplitude with respect to the equilibrium position (blue dashed line). **b)** Fluorescence micrographs allow visualization of both the active shell and the passive defect surrounding it. In the image, the SR is dragged by an active defect (dark spot), which is depicted with a blue parabola, indicating its direction. **c)** Snapshot of a simulation showing the oscillating state of a SR. Velocity field (green symbols and arrows) in the passive nematic and isosurface of its magnitude (in blue), indicating the position of the active defects below. Image sequence showing half period of the oscillation of a SR **(d)** in experiments and **(e)** in simulations. Scale bars, 50  $\mu\text{m}$ .  See Video 17 and Video 18 corresponding to **(a,c)** and **(b)**, respectively.

Either when the SRs overcome their maximum tilt configuration (up to  $\sim 60^\circ$ ), or when the flowing defects travel away from the SR position, the disclination line is able to spontaneously recover its equilibrium position (Fig. 82*d*, three first snapshots). The time SRs take to recover into the ground state depends on the nature of the experienced deformations, as well as on the viscosity and elastic constants of the confining mesogen. Repeatedly, further oscillation of the active defects through

tetrahedral and planar states will induce a new oscillation of the SR defect (Fig. 82*d*, two last snapshots). This behaviour is consistently reproduced by numerical simulations (Fig. 82*c,e*), which have been obtained by imposing predefined active defect trajectories and corresponding velocity boundary conditions [189,209] that drive the deformations of the passive nematic around the spheres.

**Angle  $\beta$ .** The orientation of the planes connecting the four  $+1/2$  defects in the planar configurations with respect to the equatorial plane of the SR has a tremendous influence on the dynamics of the passive topological defect, as well as on the free energy of the system. Choosing one of the coplanar active defect configuration, we have defined the angle formed between this plane and the SR as  $\beta$ , to which we have arbitrarily assigned the value “0” for the situation of perfect alignment (Fig. 83*a,b*). Numerical simulations demonstrate that such configuration is energetically favourable for the obtaining of the oscillating SR. Fig. 83*c* and Fig. 83*d* depict the oscillating trend of the elastic energy of the passive LC, showing that  $\beta=0^\circ$  indeed corresponds to a free energy landscape with deeper minima. A comparison between structures obtained by numerical simulations at different  $\beta$  angles and structures observed in experiments reveals that the coupling between the oscillating SR and corresponding oscillation of active defects leads to alignment between passive nematic far field and active defect trajectories only at  $\beta\sim 0^\circ$  (Fig. 83*e,f*). Conversely, the impinged SR displays irregular distortion patterns when non zero values for  $\beta$  are prescribed (Fig. 83*g,h*).

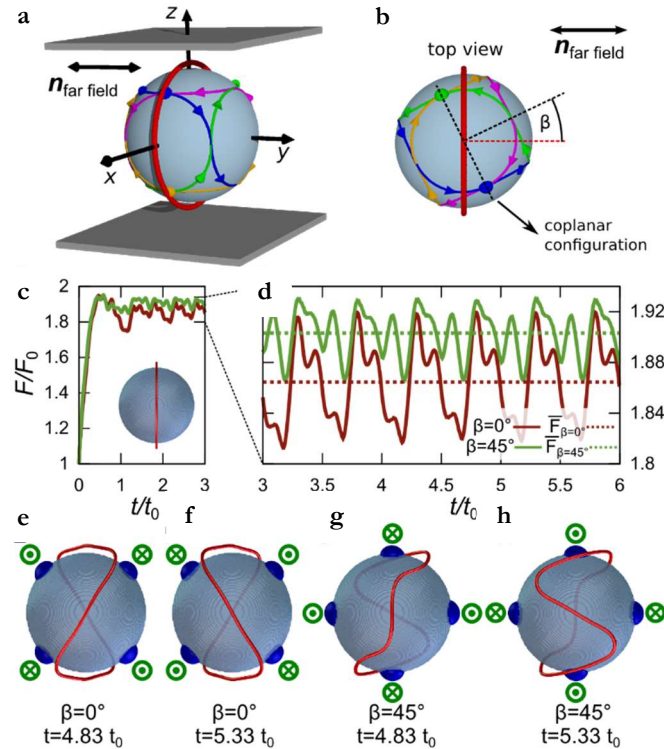


**Fig. 83. Coupling of the active defect trajectories to the passive nematic.** (a) Periodic active defect trajectories prescribed in the simulations and their orientation with respect to the passive nematic far field in a system confined between two planes that are perpendicular to the Z axis. (b) Schematics of the defect trajectories projected on the XY plane. Defects are depicted in the coplanar configuration, which defines the angle  $\beta$ , relative to the SR. (c-d) Simulations allow to compute the passive nematic elastic energy as a function of time for  $\beta = 0^\circ$  and  $\beta = 45^\circ$ , starting from the undistorted Saturn ring configuration (inset in c). (e-h) Numerical investigation of the influence of  $\beta$  on the dynamics of the SR. Snapshots of the defect structure for  $\beta = 0^\circ$  (e,f) and  $\beta = 45^\circ$  (g,h). (e,f) reveal that the oscillating Saturn ring state is only possible for  $\beta = 0^\circ$ .




In consequence, a situation where the orientation of the oscillating active defects were truly degenerate should result in a negligible fraction of droplets with  $\beta = 0^\circ$ . However, our experiments frequently show droplets exhibiting a regularly oscillating SR. This can only be possible if there is a feedback between the passive LC and the AN shell that leads to the orientation of the active defects towards the  $\beta = 0^\circ$  configuration. Similar to the previously reported case with localized friction, we propose that viscous coupling can mediate in this crosstalk between active and passive LCs, since one can expect that the viscous drag felt by the active shell will be different in the droplet regions near the ring disclination.

**External reorientation of Saturn ring defects.** The dielectric and diamagnetic behaviour of LC molecules (Sections 1.4.1 and 1.4.2), allow to tune their orientation with strong external fields. Both electric and magnetic fields (Materials and methods, Sections 3.7.1 and 3.7.2) have been applied to active emulsions based on LCs, in order to change the orientation of the passive topological defects around the inclusions. Although preliminary, experiments on the reorientation *in situ* of Saturn rings wrapping active nematic shells have not shown any noticeable changes in the active defect dynamics.

**Other configurations of forced Saturn rings.** Although regular oscillations of the SR are experimentally robust and stable over time, other regimes are experimentally observed. The oscillating SR (Fig.84a) may permanently or transiently succumb to bent conformations involving a marked increase of its length (around three-fold) (Fig.84b). In conditions where active defects perform more complicated trajectories, SRs are not able to adapt to the flow patterns imposed at the interface, and consequently, they become highly distorted, even dismantled, when they are forced to adopt arrangements that are topologically prohibited (Fig.84c). Normally these episodes ultimately lead to a crumpled configuration of the disclination that becomes nearly collapsed at one pole of the droplet (Fig.84d) [69]. In this way, the near-equilibrium distortion of the SR, still quadrupolar in the oscillating phase, is effectively transformed into a dipolar point-like, compatible with the homeotropic anchoring of the passive 5CB.

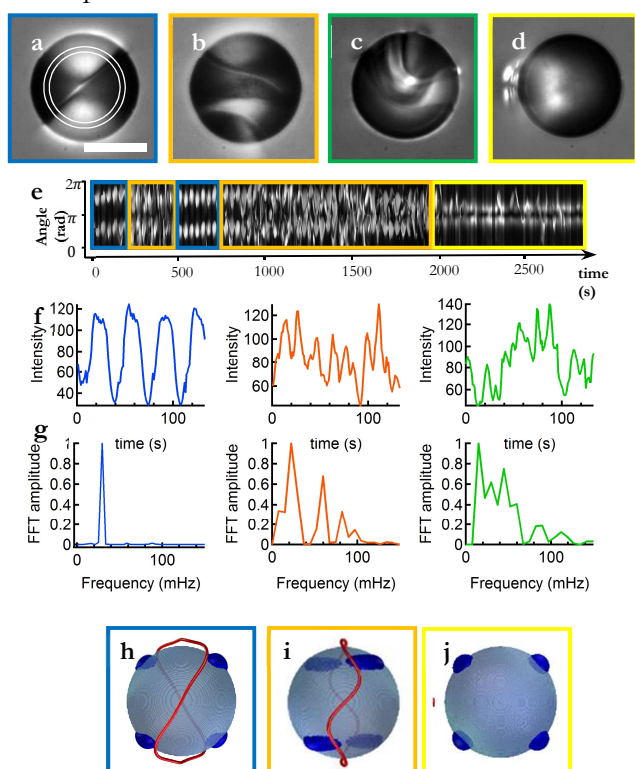



**Fig. 84. Activity-triggered Saturn ring configurations.** Polarization micrographs for periodically-oscillating (a), bent (b), distorted (c), and folded SR configurations (d) of the same droplet. Scale bar is  $50 \mu\text{m}$ .  See Video 19. (e) Space-time plot corresponding to the region within the ring depicted in (a) for a polarization image sequence showing the SR evolution over time. Frame colours relate with the corresponding SR configurations shown in (a-d). (f) Plot profiles of the average grayscale intensity inside the ring-shaped region over time. Crossed-polarized observation allows to highlight the dynamical features of the SR. Trace colours correspond to the different SR dynamic regimes in (e). (g) FFT amplitude of the oscillations in (f). The characteristic frequency corresponds to half-cycle oscillations. Simulation snapshots of the oscillating (h), bent (i), and folded (j) SR configurations.

The signature of periodic oscillations tracked during this course of events progressively fades away (Fig.84*e-g*), converting the original single frequency peak into a noisy spectrum. Simulations capture one of these deteriorated states (Fig.84*i*, corresponding to the experimental snapshot shown in Fig.84*b*), achieved numerically by arbitrarily introducing a minimal instantaneous kink in the trajectory of an active defect, which consequently turns over  $90^\circ$  in the same plane. This transition affects the overall dynamics of the active shell, which readapts into a new dynamic state. This erratic episode in active defect motion implies a mismatch between active defect dynamics and the SR oscillatory state enhancing the generation of disclination bends. Subsequent similar events can lead to an evolution back into the regularly-oscillating regime (Fig.84*e*). The seemingly chaotic phase (Fig.84*c*) is only numerically attainable by tuning the ratio between the relaxation time of the passive LC with respect to the active defect speed.

**Strained hexadecapolar arrangement.** By changing the surfactant that stabilizes the active emulsion, one can easily tune the anchoring conditions of the passive LC at the surface of the droplets, thus imposing different topological constraints on the motion of active defects. In particular, interesting effects may arise from the coupling of active flows with less labile passive defect configurations like the recently reported hexadecapolar structure [217], composed by a simultaneous pair of point-like boojums and a SR disclination. Here, by inducing conically degenerate anchoring conditions with the surfactant Tween-80 (Materials and methods, Section 3.6) we induce this configuration around the active shells. Highly-regular and stable-over-time oscillatory regimes are observed, where individual dynamics of passive defects synchronize, also with the motion of the active defects (Fig. 85*a-e*).

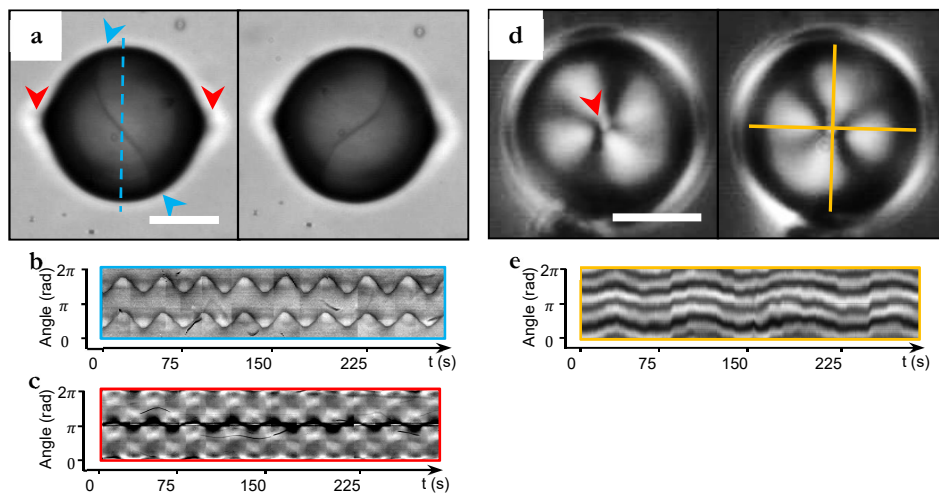



**Fig. 85. Oscillation in hexadecapolar configurations.** (a) Bright field micrographs show the evolution of an activated hexadecapolar topological configuration, formed by a SR and two surface point defects (boojum). Blue arrows indicate the position of the SR, which oscillates far from the equilibrium position (blue dashed line). Although boojums remain pinned at their location (red arrows) they also exhibit oscillations. (b,c) Space-time plots show the regular oscillating behaviour of all defects. (d) Using homeotropic anchoring of the liquid crystal, the plane of the SR is parallel to the plane of the sample, and oscillations of the boojums are better appraised. In the polarizing micrographs, the red arrow indicates the position of the boojum defect closest to the top plate. The orange cross indicates the equilibrium position for the four oscillating black brushes (e). Scale bars,  $50\mu\text{m}$ .  See Video 20.

The topological construction of such configuration seems to hamper the motion of the SR disclination, which, constrained by the presence of quasi-immobile boojums, mostly exhibits regular

oscillations. Lack of distortions in the hexadecapolar arrangement hints at a more effective cross-talk between active and passive defects as compared to the previous case. These suggests more efficient strategies for the control of encapsulated active flows. Homeotropic far-field conditions (Materials and methods, Section 3.5.2) allows to study the configuration around the point defects, which unite four brushes of an oscillating Maltese cross (Fig. 85*f-b*).


Finally, by using the polymeric surfactant Pluronic F-127 (Materials and methods, Section 3.6) planar anchoring of the LC molecules is imposed onto the active droplets. This situation induces the formation of pairs of point-like boojums (Section 1.5.5) that locate at the surface of the inclusions in diametrically opposed positions (Fig. 86*a*). Due to the inner active shell dynamics, boojums sway along short linear trajectories centred in the equilibrium position of the defects Fig. 86*b*. Although we observe short oscillating states of boojums, we suspect that this topological configuration does not impose sufficiently strong bounds to steer the dynamics of the contacting active nematic shells.

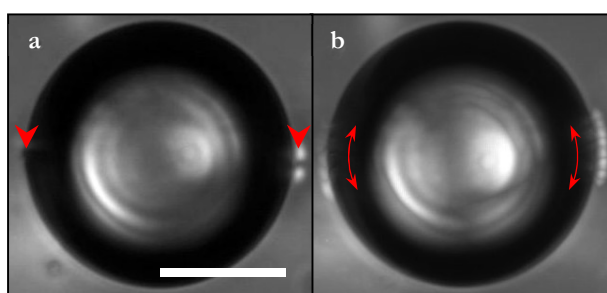


**Fig. 86. Boojum defects dragged by active flows.** Bright field micrographs of an active droplet with two boojums (**a**, red arrows) which are dragged away from their equilibrium positions. **b**) Super-imposed images from a 46 seconds sequence show the amplitude of the boojums oscillation. Red arrows here indicate the motion of passive point-like defects. Scale bar is 50  $\mu\text{m}$ .  See Video 21.

Droplets with larger diameters, featuring AN shells punctured with both positive and negative semi-integer defects, thus inducing much more complex active nematic dynamics. Consequently, when embedded in LCs, situations of chaotic-like passive defect dynamics are triggered (Fig. 87).

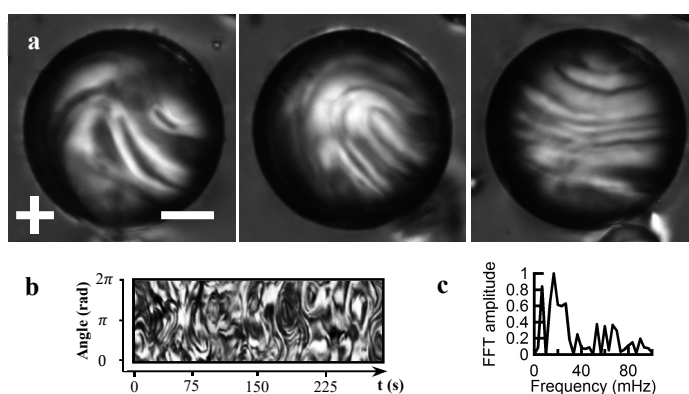


**Fig. 87. Distorted Saturn ring around an active nematic shell with irregular dynamics.** **a**) Polarized micrographs of a completely distorted SR. Corresponding disordered space-time plot (**b**), and multiple-peak FFT (**c**) support the observations. White crosses indicate the orientation of the polarizers. Scale bar is 50  $\mu\text{m}$ .  see Video 22.



## Conclusions

In this Chapter, small droplets of the tubulin/kinesin-based active gel are dispersed in isotropic and anisotropic oils in order to study their interaction with different environments. AN shells in a specific material-dependent size range feature four  $+1/2$  defects that circulate around the spherically-shaped quasi-2d layer, oscillating between tetrahedral and coplanar configurations of defects. Although the dynamical behaviour of these active nematic shells is expected to be regular, the orientation of the inter-defect tetrahedrons and planes is not fixed, thus anticipating high degree of degeneracy. Interestingly, the presence of damping boundary conditions seems to alter the dynamics of the active cortices, which, adapting to the outer constraints, generate coherent flows at the scale of the active shells. In particular, we focus on the crosstalk between active and passive defects, arising when droplets containing active nematic shells (active lyotropic) are dispersed in nematic LCs (passive thermotropic).

- In low-viscosity isotropic oils, AN shells in contact with a solid surface exhibit spontaneous rotational motion, which is robust and stable over time.
- By confining active droplets in a nematic LC we have triggered the formation of defects surrounding the inclusions. Weak homeotropic anchoring at the surface of the spheres generate Saturn ring disclinations, which couple with the active nematic flows.
- By tracking the behaviour of Saturn rings of the host matrix, we have identified a wealth of dynamical regimes induced by the sustained cortical motion.
- Experimental results and simulations indicate that, when the periodically visited planes in the trajectories of active defects are compatible with that of the Saturn ring, the former appear locked and the latter features periodic and regularly folded distortions.
- Simulations show that this situation is the most favourable energetically, even though it is prone to destabilization under sudden or unpredictable turns in the active defect paths, giving rise to quasiperiodic or even more irregular regimes of the passive defect structure.
- Preliminary experiments involving external forcing of Saturn ring defects surrounding active nematic shells did not seem to alter the cortical active defect dynamics. Nevertheless, full characterization of active defect trajectories requires more precise microscopy techniques, allowing three-dimensional reconstruction of the active shells for investigation of defect location over time. 3D confocal fluorescence microscopy would be a proper candidate despite the fact that, due to optical restrictions, it demands for low birefringence nematic LCs, which would have to be proven valid for the preparation of active emulsions.
- Finally, more stable topological structures can be induced around the AN shells. Particularly, we are able to obtain an hexadecapolar configuration of defects, composed of two diametrically opposed point-like defects simultaneously with a Saturn ring disclination. In this case, passive defects are not so easily dismantled and we find more activity-triggered oscillatory states. This could suggest that less labile topological structures are better candidates to tame active flows in spherical confinement.
- AN shells in bigger droplets are prone to suffer bending instabilities that generate defects, thus inducing much more complex dynamics. The dynamical behaviour of big active droplets has not been studied in detail, neither dispersed in isotropic nor anisotropic oils.

# Chapter 5. Closing remarks



---

# 1. Conclusions

The out-of-equilibrium dynamics exhibited by free active systems are changeable and unpredictable, a fact that neither facilitates its characterization nor allows to envisage the application of active flows. In this thesis, by imposing flow constraining conditions, we have managed to alter, pattern, and finally control the flows arising from a biologically-inspired active assembly. In particular, we have used a quasi-two-dimensional active gel based on microtubule aggregates and clusters of ATP-fuelled kinesin molecular motors. This system evolves at water/oil interfaces featuring, as other active materials at high constituent densities do, long-range orientational order, reason why we call it “active nematic”. Activity-triggered internal stresses continuously break such orientational order creating defects, in turn generating streaming flows characteristic of the so-called meso-scale or active turbulence.

First, isotropic oils with viscosities spanning five orders of magnitude have been employed to prepare the liquid interface near which the active material resides, evidencing a clear influence of the oil viscosity and thus indicating the existence of an efficient hydrodynamic coupling through the soft interface. Decrease in the flow speeds of the active nematic has revealed the existence of viscous damping. Reduction of the average velocity of the active nematic in contact with increasing viscosity oils results in an increase of the number of defects, whose annihilation becomes more sporadic. In consequence, the number of vortices of this turbulent-like material raises while obeying an exponential size distribution, in agreement with reported theoretical ideas.

Second, and foreseeing further steering of active flows, we have replaced the isotropic oils by externally-tuneable anisotropic fluids, i.e. thermotropic liquid crystals. Although liquid crystals featuring the nematic phase have not induced any remarkable effects on the active material, mesogens that exhibit lamellar (smectic-A) phase have been crucial for the achievement of our goal. The molecular arrangement of these fluids at the water/LC interface provides with patterns with a marked viscous anisotropy able to guide the active material, whose internal stretching is forced to occur along low-viscosity directions. Therefore, the previously seemingly-chaotic dynamics is organized into regimes displaying laminar flows with predefined directions. On the one hand, by imposing local circular lamellar domains at the interface, the active flows are confined into rotating swirls. By patterning the interface with a fractal tiling of these circular domains, we have effectively regularized the exponential distribution of rotational flows of active turbulence into a scale-free power law distribution of localized swirls. On the other hand, by orienting the liquid crystal molecules with an external magnetic field we have been able to generate well-oriented unidirectional lamellar structures at the interface, exhibiting robust unidirectional viscous patterns. Under this constraint, the previously swirling active material rearranges in parallel filamentous stripes with alternate flow directions, which we could easily reorient by changing the direction of the magnetic field.

Third, by dispersing small droplets of the active gel in oil we obtain active emulsions. Densification of the active material at the water/oil interface leads to the formation of active nematic spherical shells, punctured with four defects, as dictated by topology. Although the motion of these defects always leads to oscillatory dynamics between coplanar and tetrahedral configurations, the orientation of such configurations is completely degenerate. Nevertheless, in the presence of flow-damping constraints, we have observed coherent motion, only attainable for specific trajectories of the active defects. Contact with a solid surface results in active droplets moving in perfect circles pushed by flow

---

jets generated by the defects, thus suggesting stabilization of specific defect trajectories. Strikingly, by dispersing active droplets in nematic liquid crystals we have detected similar effects. Although droplets do not rotate, we have observed periodic oscillations of surrounding passive defects, mainly Saturn ring disclinations, whose deformation may impose localized viscous drag. This is a clear indication of cross-talk between active and passive defects in liquid crystal materials.

More specific conclusions for each topic have been listed at the end of the corresponding chapters.

## 2. Open questions

In the course of this work we have had the opportunity to learn about the intricacies of an active nematic and begin to understand its adaptation mechanisms to constraining situations. Although we have managed to contribute to deepen our understanding of active matter by characterizing new behaviours and regimes, numerous questions have arisen, to which we do not have an answer, yet.

For instance, little is known about how the active nematic is formed in the first place. Is it only the depletion interaction that drives the extensile system towards the interface? Apparently, it is not, since we have noticed that without activity this interfacial condensation does not happen. Furthermore, interestingly the presence of polymeric PEG chains at the interface seems to have a crucial role in driving the condensation of the three-dimensional chaotic-like active gel. We know that PEG sterically avoids direct contact between our sensitive protein-based active material and the oils, but we do not know the specific role of PEG, if any. Physico-chemically similar polymers with surfactant properties like PVA have been tested without success. Considering that the interface is inert, in principle depletion interaction should mainly depend on the geometries of the depleting and depleted units. So, why does the active nematic not form under alternative surfactant conditions?

Still in relation to this issue, it comes into play the role of the softness and fluidity of the interface where the active nematic resides. We have vaguely explored the interaction between the active nematic and solid surfaces and, in a way that we do not fully understand, the active material cannot coexist at the boundary with a solid interface. Despite being functionalized with PEG chains, solid surfaces inhibit the formation of the ordered active material, even substrates with low elastic modulus. In other experiments, by interfacing the active nematic with a non-volatile hydrocarbon with low-temperature freezing point, we have been able to perform a transition from a liquid/liquid to a solid/liquid interface *in situ* by changing temperature. Above the melting point, the interface is fluid and the active nematic evolves naturally. Once the oil is frozen, the active nematic dismantles scaping from the interface. Why does the active nematic need a fluid interface? Is it not enough to dissipate its energy by transferring momentum into the aqueous phase? Is it the no-slip condition what is incompatible with our ‘wet’ active system?

Other questions arise from the difficulties to measure the active nematic thickness. Although we have always wondered whether the active nematic evolves in the third dimension, we have considered it as a two-dimensional material and the arising flows have been only quantified in the plane of the interface. However, it is tempting to think of the consequences of increasing the thickness of the active material. Can we expect tens-of-microns-thick active gels featuring coherent bi-dimensional

---

flows? Recent experiments by the group of Z. Dogic, report thick active nematics losing orientational order but no reference to the third dimension was made whatsoever.

By preparing the active nematic in contact with lamellar liquid crystal phases, we have induced regimes where the active material evolves in preferred orientations. Interestingly, an active nematic forced to flow along one single direction adopts a strikingly perfect configuration of antiparallely flowing lanes. This regime result in the creation of regions where the active nematic is aligned and, due to the extensile nature of the system, these regions are prone to suffer bending instabilities that appear with striking regularity. What is the material property that sets this timescale apart from activity? The observed arrangement is most probably influenced by the presence of limiting boundaries but, is this interaction what generates such antiparallely-flowing laminar regimes? In order to investigate this issue, it will be interesting to prepare the active nematic under ‘periodic’ boundary conditions without limiting walls. Toroidal, cylindrical or circular geometries might be proper candidates for such experiments. Would it then be possible to suppress defect creation and lead to perfectly aligned active nematic states?

### 3. Future perspectives

The presented work is just a first step towards acquiring full control capabilities over active flows, and paves the way for further investigation both in the fundamentals of active matter, and in the commanding of active flows for their implementation in devices.

The employed tubulin/kinesin-based nematic active gel has been an excellent choice for our initiation with active soft matter. Although it lacks the simplicity and robustness of other active materials, its biological origin and the ability to vary its fundamental parameters accept an incredibly wide range of experimental possibilities, of course, impossible to tackle in one single PhD thesis.

Biologically-motivated variations of the core constituents of the active system could provide with insight of mechanically-triggered processes in cells. Further exploration, for instance, of the effects arising from the addition of other microtubule-associated molecular motors like dynein, which moves in opposite direction than kinesin, might be helpful to the unveil the possible coordination mechanisms between these two motor molecules in the cytoskeleton. Collective dynamics of active gels, if viable, powered by single-headed kinesin motors could also be interesting. In addition, implementation of other ATPase enzymatic cycles could trigger new dynamical states, controlled by kinetics. Finally, the role of depletion interaction in our active gel as in the cytoskeleton, plays a major role and must be further explored, as it could set the crossover between extensile and contractile behaviour in active gels.

At the interface between biology and physics, other projects are being considered. For instance, the evaluation of the hydrodynamic interaction between two independent active nematics as a representation of short-range cell-to-cell interactions. We have evidence that direct contact between active droplets has marked effects on their individual dynamics. We thus envisage to prepare active cortices in jammed situations where active flows will be forced to couple. Synchronization would not be unexpected.

---

Although the dynamical properties of artificial active materials obviously have got most of the attention, we are also interested in probing the viscoelastic properties of these protein-based extensile active gels. In particular, increasing interest to develop other tools for probing the rheological properties of the cytoskeleton make our system suitable for preliminary tests. Moreover, it is also interesting to quantify the force that these materials can effectively generate, from the cooperative action of thousands of motor proteins.

Finally, we are especially interested on the interaction between active nematics and passive liquid crystals and we envision great advances in relation with the implementation of anisotropic patterns to the steering of active flows. In particular, we plan to optimize the methods reported here and use anisotropy-based strategies to control other active materials featuring collective motion at interfaces, such as self-propelled colloids, bacterial colonies or cellular tissues.

---

# List of references

1. O. Lehmann, On Flowing Crystals. *Zeitschrift für Phys. Chemie.* **4**, 462–472 (1889).
2. P. G. de Gennes, J. Prost, *The Physics of Liquid Crystals* (Clarendon Press, 1995), *International Series of Monographs on Physics*.
3. P. Oswald, P. Pieranski, *Nematic and Cholesteric Liquid Crystals: Concepts and Physical Properties Illustrated by Experiments* (CRC Press, 2005), *Liquid Crystals Book Series*.
4. P. Oswald, P. Pieranski, *Smectic and Columnar Liquid Crystals: Concepts and Physical Properties Illustrated by Experiments* (Taylor & Francis, Boca Raton, FL, 2006), *The liquid crystal book series*.
5. V. Luzzati, T. Gulik-Krzywicki, A. Tardieu, Polymorphism of Lecithins. *Nature.* **218**, 1031–1034 (1968).
6. L. J. Yu, A. Saupe, Observation of a biaxial nematic phase in potassium laurate-1-decanol-water mixtures. *Phys. Rev. Lett.* **45**, 1000–1003 (1980).
7. S.-W. Tam-Chang, L. Huang, Chromonic liquid crystals: properties and applications as functional materials. *Chem. Commun.*, 1957 (2008).
8. H. Hasegawa, T. Hashimoto, Morphology of block polymers near a free surface. *Macromolecules.* **18**, 589–590 (1985).
9. C. S. Henke, E. L. Thomas, L. J. Fetters, The effect of surface constraints on the ordering of block copolymer domains. *J. Mater. Sci.* **23**, 1685–1694 (1988).
10. Z. Dogic, S. Fraden, Smectic phase in a colloidal suspension of semiflexible virus particles. *Phys. Rev. Lett.* **78**, 2417–2420 (1997).
11. Q. Liu, M. G. Campbell, J. S. Evans, I. I. Smalyukh, Orientationally Ordered Colloidal Co-Dispersions of Gold Nanorods and Cellulose Nanocrystals. *Adv. Mater.* **26**, 7178–7184 (2014).
12. L. Onsager, The effects of the shape on the interaction of colloidal particles. *Ann. N. Y. Acad. Sci.* **51**, 627–659 (1949).
13. F. C. Bawden, N. W. Pirie, J. D. Bernal, I. Fankuchen, Liquid Crystalline Substances from Virus-infected Plants. *Nature.* **138**, 1051–1052 (1936).
14. S. Fraden, G. Maret, D. L. D. Caspar, R. B. Meyer, Isotropic-nematic phase transition and angular correlations in isotropic suspensions of tobacco mosaic virus. *Phys. Rev. Lett.* **63**, 2068–2071 (1989).
15. M. Adams, Z. Dogic, S. L. Keller, S. Fraden, Entropically driven microphase transitions in mixtures of colloidal rods and spheres. *Nature.* **393**, 349–352 (1998).
16. G. Friedel, Les états mésomorphes de la matière. *Annales de Physique* **18**, 273-474 (1922).
17. H. S. and D. Demus, The Polymorphism of Liquid Crystals. *Mol. Cryst.* **2**, 81–102 (1966).



- 
18. W. Maier, A. Saupe, A simple molecular theory of the nematic crystalline-liquid state. *Z. Naturforsch. Tl. A.* **13a**, 564–566 (1958).
  19. M. Philip C. Robinson, Abramowitz, M. W. Davidson, *MicroscopyU: The source for microscopy education* (2012), (available at [www.olympusmicro.com](http://www.olympusmicro.com)).
  20. M. Miesowicz, The Three Coefficients of Viscosity of Anisotropic Liquids. *Nature*, 27–27 (1946).
  21. S. Hess, J. F. Schwarzl, D. Baalss, *J. Phys. Condens. Matter*, in press, doi:10.1088/0953-8984/2/S/042.
  22. H. Zocher, The effect of a magnetic field on the nematic state. *Trans. Faraday Soc.* **29**, 945–957 (1933).
  23. C. W. Oseen, The theory of liquid crystals. *Trans. Faraday Soc.* **29**, 883–899 (1933).
  24. F. C. Frank, I. Liquid crystals. On the theory of liquid crystals. *Discuss. Faraday Soc.* **25**, 19 (1958).
  25. C. Mauguin, Orientation of liquid-crystals by plates of mica. *C. R. Hebd. Seances Acad. Sci.* **156**, 1246–1247 (1913).
  26. B. Jérôme, Surface effects and anchoring in liquid crystals. *Reports Prog. Phys.* **54**, 391–451 (1999).
  27. D.-K. Yang, S.-T. Wu, *Fundamentals of Liquid Crystal Devices* (Wiley, 2014).
  28. D. Berreman, Solid Surface Shape and the Alignment of an Adjacent Nematic Liquid Crystal. *Phys. Rev. Lett.* **28**, 1683–1686 (1972).
  29. B. Senyuk, *Liquid Crystals: a Simple View on a Complex Matter* (2005), (available at [www.personal.kent.edu/~bisenyuk/liquidcrystals/intro.html](http://www.personal.kent.edu/~bisenyuk/liquidcrystals/intro.html)).
  30. F. Grandjean, The orientation of anisotropic liquids on crystals. *Bull. la Société Fr. Minéralogi.* **39**, 163 (1916).
  31. O. Lehmann, On Flowing Crystals. *Phys. Zeitschrift.* **7**, 578 (1906).
  32. J. L. Janning, Thin film surface orientation for liquid crystals. *Appl. Phys. Lett.* **21**, 173–174 (1972).
  33. D. M. Boudreau, H. H. Winter, C. P. Lillya, R. S. S. Stein, Conoscopic observations of shear-induced rotations in nematic liquid crystals. *Rheol. acta.* **38**, 503–513 (1999).
  34. V. Freedericksz, V. Zolina, Forces causing the orientation of an anisotropic liquid. *Trans. Faraday Soc.* **29**, 919–930 (1933).
  35. M. J. Stephen, J. P. Straley, Physics of liquid crystals. *Rev. Mod. Phys.* **46**, 617–704 (1974).
  36. A. Saupe, Disclinations and Properties of the Directorfield in Nematic and Cholesteric Liquid Crystals. *Mol. Cryst. Liq. Cryst.* **21**, 211–238 (1973).

- 
37. G. E. Volovik, Topological singularities on the surface of an ordered system. *JETP Lett.* **28** (1978), pp. 59–61.
  38. I. I. Smalyukh, Y. Lansac, N. A. Clark, R. P. Trivedi, Three-dimensional structure and multistable optical switching of triple-twisted particle-like excitations in anisotropic fluids. *Nat Mater.* **9**, 139–145 (2010).
  39. A. Honglawan *et al.*, Topographically induced hierarchical assembly and geometrical transformation of focal conic domain arrays in smectic liquid crystals. *Proc. Natl. Acad. Sci. U. S. A.* **110**, 34–9 (2013).
  40. A. Nych *et al.*, Assembly and control of 3D nematic dipolar colloidal crystals. *Nat. Commun.* **4**, 1489 (2013).
  41. D. R. Nelson, Toward a Tetravalent Chemistry of Colloids. *Nano Lett.* **2**, 1125–1129 (2002).
  42. T. Araki, H. Tanaka, Colloidal Aggregation in a Nematic Liquid Crystal: Topological Arrest of Particles by a Single-Stroke Disclination Line. *Phys. Rev. Lett.* **97**, 127801 (2006).
  43. U. Tkalec, M. Ravnik, S. Čopar, S. Žumer, I. Muševič, Reconfigurable knots and links in chiral nematic colloids. *Science.* **333**, 62–65 (2011).
  44. M. A. Gharbi, M. Nobili, C. Blanc, Use of topological defects as templates to direct assembly of colloidal particles at nematic interfaces. *J. Colloid Interface Sci.* **417**, 250–255 (2014).
  45. X. Wang, D. S. Miller, E. Bukusoglu, J. J. de Pablo, N. L. Abbott, Topological defects in liquid crystals as templates for molecular self-assembly. *Nat Mater.* **15**, 106–112 (2016).
  46. V. M. P. O. D. Lavrentovich, Patterns in thin liquid crystal films and the divergence (“surfacelike”) elasticity. *Int. J. Mod. Phys. B.* **9**, 2389–2437 (1995).
  47. D. Link, M. Nakata, Y. Takanishi, K. Ishikawa, H. Takezoe, Patterns in Hybrid Nematic Liquid-Crystal Films: Topography and Topology. *Phys. Rev. Lett.* **87**, 1–4 (2001).
  48. O. V Manyuhina, A.-M. Cazabat, M. Ben Amar, Instability patterns in ultrathin nematic films: Comparison between theory and experiment. *Eur. Lett.* **92**, 16005 (2010).
  49. J. Nehring, A. Saupe, On the schlieren texture in nematic and smectic liquid crystals. *J. Chem. Soc. Faraday Trans. 2.* **68**, 1 (1972).
  50. O. D. Lavrentovich, Topological defects in dispersed liquid crystals, or words and worlds around liquid crystal drops. *Liq. Cryst.* **24**, 117–125 (1998).
  51. V. Vitelli, A. S. Utada, D. R. Link, M. Ma, Novel Defect Structures in Nematic Liquid Crystal Shells. **157801**, 1–4 (2007).
  52. T. Lopez-Leon, V. Koning, K. B. S. Devaiah, V. Vitelli, A. Fernandez-Nieves, Frustrated nematic order in spherical geometries. *Nat Phys.* **7**, 391–394 (2011).
  53. A. Darmon, O. Dauchot, T. Lopez-Leon, M. Benzaquen, Elastic interactions between topological defects in chiral nematic shells. **62701**, 1–6 (2016).

- 
54. A. de Lózar, W. Schöpf, I. Rehberg, D. Svenšek, L. Kramer, Transformation from walls to disclination lines: Statics and dynamics of the pincement transition. *Phys. Rev. E.* **72**, 51713 (2005).
  55. V. Fazio, L. Komitov, S. Lagerwall, Alignment and alignment dynamics of nematic liquid crystals on Langmuir-Blodgett mono-layers. *Liq. Cryst.* **24**, 427–433 (1998).
  56. B. W. Lee, N. a Clark, Alignment of liquid crystals with patterned isotropic surfaces. *Science.* **291**, 2576–2580 (2001).
  57. N. Petit-Garrido *et al.*, Healing of defects at the interface of nematic liquid crystals and structured Langmuir-Blodgett monolayers. *Phys. Rev. Lett.* **107**, 177801 (2011).
  58. P. Guillamat, F. Sagués, J. Ignés-Mullol, Electric-field modulation of liquid crystal structures in contact with structured surfactant monolayers. *Phys. Rev. E.* **89**, 52510 (2014).
  59. J.-H. Kim, M. Yoneya, H. Yokoyama, Tristable nematic liquid-crystal device using micropatterned surface alignment. *Nature.* **420**, 159–162 (2002).
  60. S. Ferjani, J. Pendery, C. Rosenblatt, Mechanically generated surface chirality: Control of chiral strength. *Appl. Phys. Lett.* **97**, 121905 (2010).
  61. T. Ohzono, J. Fukuda, Zigzag line defects and manipulation of colloids in a nematic liquid crystal in microwrinkle grooves. *Nat. Commun.* **3**, 701 (2012).
  62. P. Poulin, Novel Colloidal Interactions in Anisotropic Fluids. *Science.* **275**, 1770–1773 (1997).
  63. B. Senyuk *et al.*, Topological colloids. *Nature.* **493**, 200–5 (2013).
  64. P. Poulin, D. a. Weitz, Inverted and multiple nematic emulsions. *Phys. Rev. E.* **57**, 626–637 (1998).
  65. M. V Kurik, O. D. Lavrentovich, Defects in liquid crystals: homotopy theory and experimental studies. *Sov. Phys. Uspekhi.* **31**, 196–224 (1988).
  66. U. Ognysta, A. Nych, V. Nazarenko, M. Skarabot, I. Musevik, Design of 2D binary colloidal crystals in a nematic liquid crystal. *Langmuir.* **25**, 12092–12100 (2009).
  67. I. I. Smalyukh *et al.*, Ordered droplet structures at the liquid crystal surface and elastic-capillary colloidal interactions. *Phys. Rev. Lett.* **93** (2004), doi:10.1103/PhysRevLett.93.117801.
  68. S. Hernández-Navarro, P. Tierno, J. A. Farrera, J. Ignés-Mullol, F. Sagués, Reconfigurable Swarms of Nematic Colloids Controlled by Photoactivated Surface Patterns. *Angew. Chemie Int. Ed.* **53**, 10696–10700 (2014).
  69. Y. Gu, N. L. Abbott, Observation of Saturn-Ring Defects around Solid Microspheres in Nematic Liquid Crystals. *Phys. Rev. Lett.* **85**, 4719–4722 (2000).
  70. O. V. Kuksenok, R. W. Ruhwandl, S. V. Shiyonovskii, E. M. Terentjev, Director structure around a colloid particle suspended in a nematic liquid crystal. *Phys. Rev. E.* **54**, 5198–5203 (1996).

- 
71. C. Blanc, M. Kleman, Tiling the plane with noncongruent toric focal conic domains. *Phys. Rev. E.* **62**, 6739–6748 (2000).
  72. C. S. Rosenblatt, R. Pindak, N. Clark, R. Meyer, The parabolic focal conic: a new smectic a defect. *J. Phys.* **38**, 1105–1115 (1977).
  73. M. C. Marchetti *et al.*, Hydrodynamics of soft active matter. *Rev. Mod. Phys.* **85**, 1143–1189 (2013).
  74. T. Vicsek, A. Zafeiris, Collective motion. *Phys. Rep.* **517**, 71–140 (2012).
  75. T. Vicsek, A. Czirak, E. Ben-Jacob, I. Cohen, O. Shochet, Novel type of phase transition in a system of self-driven particles. *Phys. Rev. Lett.* **75**, 1226–1229 (1995).
  76. C. Dombrowski, L. Cisneros, S. Chatkaew, R. E. Goldstein, J. O. Kessler, Self-Concentration and Large-Scale Coherence in Bacterial Dynamics. *Phys. Rev. Lett.* **93**, 98103 (2004).
  77. T. Sanchez, D. T. N. Chen, S. J. DeCamp, M. Heymann, Z. Dogic, Spontaneous motion in hierarchically assembled active matter. *Nature.* **491**, 431–4 (2012).
  78. Y. Sumino *et al.*, Large-scale vortex lattice emerging from collectively moving microtubules. *Nature.* **483**, 448–452 (2012).
  79. M. Tennenbaum, Z. Liu, D. Hu, A. Fernandez-Nieves, Mechanics of fire ant aggregations. *Nat. Mater.* **15**, 54–59 (2015).
  80. A. Sokolov, I. S. Aranson, Reduction of Viscosity in Suspension of Swimming Bacteria. *Phys. Rev. Lett.* **103**, 148101 (2009).
  81. S. Rafai, L. Jibuti, P. Peyla, Effective Viscosity of Microswimmer Suspensions. *Phys. Rev. Lett.* **104**, 98102 (2010).
  82. F. C. Keber *et al.*, Topology and Dynamics of Active Nematic Vesicles. *Science.* **345**, 1–19 (2014).
  83. S. J. DeCamp, G. S. Redner, A. Baskaran, M. F. Hagan, Z. Dogic, Orientational order of motile defects in active nematics. *Nat. Mater.* **14**, 1110–1115 (2015).
  84. C. W. Wolgemuth, Collective swimming and the dynamics of bacterial turbulence. *Biophys. J.* **95**, 1564–74 (2008).
  85. H. H. Wensink *et al.*, Meso-scale turbulence in living fluids. *Proc. Natl. Acad. Sci. U. S. A.* **109**, 14308–14313 (2012).
  86. J. Dunkel *et al.*, Fluid Dynamics of Bacterial Turbulence. *Phys. Rev. Lett.* **110**, 228102 (2013).
  87. W. K. Potts, The Chorus Line Hypothesis of Maneuver Coordination in Avian Flocks. *Nature.* **309**, 344–345 (1984).
  88. M. Ballerini *et al.*, Interaction ruling animal collective behavior depends on topological rather than metric distance: Evidence from a field study. *Proc. Natl. Acad. Sci. U. S. A.* **105**, 1232–1237 (2008).

- 
89. I. D. Couzin, N. R. Franks, Self-organized lane formation and optimized traffic flow in army ants. *Proc. R. Soc. B Biol. Sci.* **270**, 139–146 (2003).
  90. J. Buhl *et al.*, From Disorder to Order in Marching Locusts. *Science*. **312**, 1402–1406 (2006).
  91. C. Becco, N. Vandewalle, J. Delcourt, P. Poncin, Experimental evidences of a structural and dynamical transition in fish school. *Phys. A Stat. Mech. its Appl.* **367**, 487–493 (2006).
  92. A. J. W. Ward, D. J. T. Sumpter, I. D. Couzin, P. J. B. Hart, J. Krause, Quorum decision-making facilitates information transfer in fish shoals. *Proc. Natl. Acad. Sci. U. S. A.* **105**, 6948–6953 (2008).
  93. N. C. Makris *et al.*, Critical Population Density Triggers Rapid Formation of Vast Oceanic Fish Shoals. *Science*. **323**, 1734–1737 (2009).
  94. J. J. Faria, J. R. G. Dyer, C. R. Tosh, J. Krause, Leadership and social information use in human crowds. *Anim. Behav.* **79**, 895–901 (2010).
  95. M. Moussaïd, D. Helbing, G. Theraulaz, How simple rules determine pedestrian behavior and crowd disasters. *Proc. Natl. Acad. Sci. U. S. A.* **108**, 6884–8 (2011).
  96. J. L. Silverberg, M. Bierbaum, J. P. Sethna, I. Cohen, Collective Motion of Humans in Mosh and Circle Pits at Heavy Metal Concerts. *Phys. Rev. Lett.* **110**, 228701 (2013).
  97. I. R. Fischhoff *et al.*, Social relationships and reproductive state influence leadership roles in movements of plains zebra, *Equus burchellii*. *Anim. Behav.* **73**, 825–831 (2007).
  98. C. Sueur, O. Petit, J. L. Deneubourg, Selective mimetism at departure in collective movements of *Macaca tonkeana*: an experimental and theoretical approach. *Anim. Behav.* **78**, 1087–1095 (2009).
  99. J. Toner, Y. Tu, Long-range order in a two-dimensional dynamical XY model: How birds fly together. *Phys. Rev. Lett.* **75**, 4326–4329 (1995).
  100. P. F. Major, L. M. Dill, The three-dimensional structure of airborne bird flocks. *Behav. Ecol. Sociobiol.* **4**, 111–122 (1978).
  101. M. Nagy *et al.*, Hierarchical group dynamics in pigeon flocks. *Nature*. **464**, 890–893 (2010).
  102. A. Sokolov, I. S. Aranson, J. O. Kessler, R. E. Goldstein, Concentration Dependence of the Collective Dynamics of Swimming Bacteria. *Phys. Rev. Lett.* **98**, 158102 (2007).
  103. H. P. Zhang, A. Be'er, E.-L. Florin, H. L. Swinney, Collective motion and density fluctuations in bacterial colonies. *Proc. Natl. Acad. Sci. U. S. A.* **107**, 13626–30 (2010).
  104. M. Obert, P. Pfeifer, M. Sernetz, Microbial growth patterns described by fractal geometry. *J. Bacteriol.* **172**, 1180–1185 (1990).
  105. P. Friedl, Y. Hegerfeldt, M. Tusch, Collective cell migration in morphogenesis and cancer. *Int. J. Dev. Biol.* **48** (2004), pp. 441–449.

- 
106. P. Martin, S. M. Parkhurst, Parallels between tissue repair and embryo morphogenesis. *Development*. **131**, 3021–34 (2004).
  107. V. Lecaudey, D. Gilmour, Organizing moving groups during morphogenesis. *Curr. Opin. Cell Biol.* **18**, 102–107 (2006).
  108. R. Kemkemer, D. Kling, D. Kaufmann, H. Gruler, Elastic properties of nematoid arrangements formed by amoeboid cells. *Eur. Phys. J. E.* **1**, 215 (2000).
  109. Y. Arboleda-Estudillo *et al.*, Movement Directionality in Collective Migration of Germ Layer Progenitors. *Curr. Biol.* **20**, 161–169 (2010).
  110. T. E. Angelini *et al.*, Glass-like dynamics of collective cell migration. *Proc. Natl. Acad. Sci. U. S. A.* **108**, 4714–9 (2011).
  111. W. Saunders, V. Lengyel, M. A. Hoyt, Mitotic spindle function in *Saccharomyces cerevisiae* requires a balance between different types of kinesin-related motors. *Mol. Biol. Cell.* **8**, 1025–33 (1997).
  112. C. E. Walczak, I. Vernos, T. J. Mitchison, E. Karsenti, R. Heald, A model for the proposed roles of different microtubule-based motor proteins in establishing spindle bipolarity. *Curr. Biol.* **8**, 903–13 (1998).
  113. S. L. Rogers, V. I. Gelfand, Membrane trafficking, organelle transport, and the cytoskeleton. *Curr. Opin. Cell Biol.* **12** (2000), pp. 57–62.
  114. S. Ganguly, L. S. Williams, I. M. Palacios, R. E. Goldstein, Cytoplasmic streaming in *Drosophila* oocytes varies with kinesin activity and correlates with the microtubule cytoskeleton architecture. *Proc. Natl. Acad. Sci. U. S. A.* **109**, 15109–15114 (2012).
  115. A. Akhmanova, M. O. Steinmetz, Tracking the ends: a dynamic protein network controls the fate of microtubule tips. *Nat. Rev. Mol. Cell Biol.* **9**, 309–322 (2008).
  116. J. Howard, The movement of kinesin along microtubules. *Annu. Rev. Physiol.* **58**, 703–29 (1996).
  117. L. C. Kapitein *et al.*, The bipolar mitotic kinesin Eg5 moves on both microtubules that it crosslinks. *Nature*. **435**, 114–118 (2005).
  118. G. Fink *et al.*, The mitotic kinesin-14 Ncd drives directional microtubule-microtubule sliding. *Nat. Cell Biol.* **11**, 717–23 (2009).
  119. P. J. Foster, S. Furthauer, M. J. Shelley, D. J. Needleman, Active contraction of microtubule networks. *Elife*. **4**, 1–21 (2015).
  120. Z. Lansky *et al.*, Diffusible crosslinkers generate directed forces in microtubule networks. *Cell*. **160**, 1159–1168 (2015).
  121. D. Pantaloni, C. Le Clainche, M. F. Carrier, Mechanism of actin-based motility. *Science*. **292**, 1502–6 (2001).
  122. M. Schliwa, G. Woehlke, Molecular motors. *Nature*. **422**, 759–65 (2003).

- 
123. M. Dogterom, J. W. J. Kerssemakers, G. Romet-Lemonne, M. E. Janson, Force generation by dynamic microtubules. *Curr. Opin. Cell Biol.* **17**, 67–74 (2005).
  124. I. Theurkauff, C. Cottin-Bizonne, J. Palacci, C. Ybert, L. Bocquet, Dynamic Clustering in Active Colloidal Suspensions with Chemical Signaling. *Phys. Rev. Lett.* **108**, 268303 (2012).
  125. J. Palacci, S. Sacanna, A. P. Steinberg, D. J. Pine, P. M. Chaikin, Living crystals of light-activated colloidal surfers. *Science*. **339**, 936–40 (2013).
  126. W. F. Paxton *et al.*, Catalytic nanomotors: Autonomous movement of striped nanorods. *J. Am. Chem. Soc.* **126**, 13424–13431 (2004).
  127. S. Weitz, A. Deutsch, F. Peruani, Self-propelled rods exhibit a phase-separated state characterized by the presence of active stresses and the ejection of polar clusters. *Phys. Rev. E*. **92**, 12322 (2015).
  128. D. L. Blair, T. Neicu, A. Kudrolli, Vortices in vibrated granular rods. *Phys. Rev. E*. **67**, 31303 (2003).
  129. V. Narayan, S. Ramaswamy, N. Menon, Long-Lived Giant Number Fluctuations in a Swarming Granular Nematic. *Science*. **317**, 105–108 (2007).
  130. A. Bricard, J.-B. Caussin, N. Desreumaux, O. Dauchot, D. Bartolo, Emergence of macroscopic directed motion in populations of motile colloids. *Nature*. **503**, 95–8 (2013).
  131. S. J. Kron, J. A. Spudich, Fluorescent actin filaments move on myosin fixed to a glass surface. *Proc. Natl. Acad. Sci. U. S. A.* **83**, 6272–6276 (1986).
  132. Y. Y. Toyoshima *et al.*, Myosin subfragment-1 is sufficient to move actin filaments in vitro. *Nature*. **328**, 536–539 (1987).
  133. T. Butt *et al.*, Myosin motors drive long range alignment of actin filaments. *J. Biol. Chem.* **285**, 4964–74 (2010).
  134. V. Schaller, C. Weber, C. Semmrich, E. Frey, A. R. Bausch, Polar patterns of driven filaments. *Nature*. **467**, 73–77 (2010).
  135. V. Schaller, a. R. Bausch, Topological defects and density fluctuations in collectively moving systems. *Proc. Natl. Acad. Sci. U. S. A.* **110**, 4488–4493 (2013).
  136. L. Liu, E. Tüzel, J. L. Ross, Loop formation of microtubules during gliding at high density. *J. Phys. Condens. Matter*. **23**, 374104 (2011).
  137. J. Prost, F. Jülicher, J. Joanny, Active gel physics. *Nat. Phys.* **11** (2015), doi:10.1038/NPHYS3224.
  138. F. J. Nédélec, T. Surrey, A. C. Maggs, S. Leibler, Self-organization of microtubules and motors. *Nature*. **389**, 305–8 (1997).
  139. T. Surrey, F. Nédélec, S. Leibler, E. Karsenti, Physical properties determining self-organization of motors and microtubules. *Science*. **292**, 1167–71 (2001).

- 
140. R. Urrutia, M. A. McNiven, J. P. Albanesi, D. B. Murphy, B. Kachar, Purified kinesin promotes vesicle motility and induces active sliding between microtubules in vitro. *Proc. Natl. Acad. Sci. U. S. A.* **88**, 6701–5 (1991).
  141. M. J. Schnitzer, K. Visscher, S. M. Block, Force production by single kinesin motors. *Nat. Cell Biol.* **2**, 718–23 (2000).
  142. D. Mizuno, C. Tardin, C. F. Schmidt, F. C. Mackintosh, Nonequilibrium mechanics of active cytoskeletal networks. *Science*. **315**, 370–3 (2007).
  143. G. H. Koenderink *et al.*, An active biopolymer network controlled by molecular motors. *Proc. Natl. Acad. Sci. U. S. A.* **106**, 15192–7 (2009).
  144. J. Alvarado, M. Sheinman, A. Sharma, F. C. MacKintosh, G. H. Koenderink, Molecular motors robustly drive active gels to a critically connected state. *Nat. Phys.* **9**, 591–597 (2013).
  145. S. Köhler, V. Schaller, A. R. Bausch, Structure formation in active networks. *Nat. Mater.* **10**, 462–468 (2011).
  146. M. P. Murrell, M. L. Gardel, F-actin buckling coordinates contractility and severing in a biomimetic actomyosin cortex. *Proc. Natl. Acad. Sci. U. S. A.* **109**, 20820–20825 (2012).
  147. D. J. Needleman *et al.*, Synchrotron X-ray Diffraction Study of Microtubules Buckling and Bundling under Osmotic Stress: A Probe of Interprotofilament Interactions. *Phys. Rev. Lett.* **93**, 198104 (2004).
  148. A. W. C. Lau, A. Prasad, Z. Dogic, Condensation of isolated semi-flexible filaments driven by depletion interactions. *EPL (Europhysics Lett.)* **87**, 48006 (2009).
  149. F. Hilitski *et al.*, Measuring cohesion between macromolecular filaments one pair at a time: Depletion-induced microtubule bundling. *Phys. Rev. Lett.* **114**, 1–6 (2015).
  150. A. Ward *et al.*, Solid friction between soft filaments. *Nat. Mater.* **14**, 583–588 (2015).
  151. S. Asakura, F. Oosawa, Interaction between particles suspended in solutions of macromolecules. *J. Polym. Sci.* **33**, 183–192 (1958).
  152. D. Marenduzzo, K. Finan, P. R. Cook, The depletion attraction: An underappreciated force driving cellular organization. *J. Cell Biol.* **175**, 681–686 (2006).
  153. H. N. W. Lekkerkerker, R. Tuinier, Depletion interaction. *Lect. Notes Phys.* **833**, 57–108 (2011).
  154. S. B. Zimmerman, A. P. Minton, Macromolecular crowding: biochemical, biophysical, and physiological consequences. *Annu. Rev. Biophys. Biomol. Struct.* **22**, 27–65 (1993).
  155. T. Sanchez, D. Welch, D. Nicastro, Z. Dogic, Cilia-Like Beating of Active Microtubule Bundles. *Science*. **333**, 456–459 (2011).
  156. G. Henkin, S. J. DeCamp, D. T. N. Chen, T. Sanchez, Z. Dogic, Tunable dynamics of microtubule-based active isotropic gels. *Philos. Trans. R. Soc. A Math. Phys. Eng. Sci.* **372**, 20140142 (2014).



- 
157. A. Majumdar *et al.*, Perspectives in active liquid crystals Perspectives in active liquid crystals (2014).
  158. S. Zhou, A. Sokolov, O. D. Lavrentovich, I. S. Aranson, Living liquid crystals. *Proc. Natl. Acad. Sci. U. S. A.* **111**, 1265–1270 (2014).
  159. K. Kruse, J. F. Joanny, F. Jülicher, J. Prost, K. Sekimoto, Asters, vortices, and rotating spirals in active gels of polar filaments. *Phys. Rev. Lett.* **92**, 78101 (2004).
  160. S. P. Thampi, R. Golestanian, J. M. Yeomans, Velocity correlations in an active nematic. *Phys. Rev. Lett.* **111**, 2–6 (2013).
  161. S. P. Thampi, R. Golestanian, J. M. Yeomans, Instabilities and topological defects in active nematics. *EPL (Europhysics Lett.)* **105**, 18001 (2014).
  162. R. Voituriez, J.-F. Joanny, J. Prost, Spontaneous flow transition in active polar gels. *Europhys. Lett.* **70**, 7 (2005).
  163. S. a Edwards, J. M. Yeomans, Spontaneous flow states in active nematics: a unified picture. *Europhys. Lett.* **85**, 6 (2008).
  164. L. Giomi, Geometry and topology of Turbulence in active nematics. *Phys. Rev. X.* **5**, 1–11 (2015).
  165. M. J. Schnitzer, S. M. Block, Kinesin hydrolyses one ATP per 8-nm step. *Nature.* **388**, 386–90 (1997).
  166. M. F. Adamer, S. P. Thampi, J. M. Yeomans, A. Doostmohammadi, Stabilization of active matter by flow-vortex lattices and defect ordering. *Nat. Commun.* **7**, 1–9 (2016).
  167. A. U. Oza, J. Dunkel, Nematic ordering of topological defects in active liquid crystals, 1–8 (2015).
  168. S. Fürthauer, M. Stempel, S. W. Grill, F. Jülicher, Active Chiral Processes in Thin Films. *Phys. Rev. Lett.* **110**, 48103 (2013).
  169. T. C. Adhyapak, S. Ramaswamy, J. Toner, Live Soap: Stability, Order, and Fluctuations in Apolar Active Smectics. *Phys. Rev. Lett.* **110**, 118102 (2013).
  170. V. Narayan, N. Menon, S. Ramaswamy, Nonequilibrium steady states in a vibrated-rod monolayer: tetratic, nematic, and smectic correlations. *J. Stat. Mech.* **1005**, 18 (2006).
  171. M. R. Jarman, G. Clark, C. Grigson, H.-P. Uerpmann, M. L. Ryder, Early Animal Husbandry [and Discussion]. *Philos. Trans. R. Soc. London B Biol. Sci.* **275**, 85–97 (1976).
  172. J. Adler, Chemotaxis in Bacteria. *Science.* **153**, 708–716 (1966).
  173. A. Czirók, E. Ben-Jacob, I. Cohen, T. Vicsek, Formation of complex bacterial colonies via self-generated vortices. *Phys. Rev. E.* **54**, 1791–1801 (1996).
  174. R. Tokita *et al.*, Pattern Formation of Bacterial Colonies by Escherichia coli. *J. Phys. Soc. Japan.*

---

78, 74005 (2009).

175. J. Saragosti *et al.*, Directional persistence of chemotactic bacteria in a traveling concentration wave. *Proc. Natl. Acad. Sci. U. S. A.* **108**, 16235–40 (2011).
176. H. Salman, A. Zilman, C. Loverdo, M. Jeffroy, A. Libchaber, Solitary modes of bacterial culture in a temperature gradient. *Phys. Rev. Lett.* **97**, 5–8 (2006).
177. J. Dervaux, M. Capellazzi Resta, P. Brunet, Light-controlled flows in active fluids. *Nat. Phys.* **1**, 1–8 (2016).
178. C. J. O. Reichhardt, C. Reichhardt, Collective motion: Disorder in the wild. *Nat Phys.* **13**, 10–11 (2017).
179. A. Morin, N. Desreumaux, J.-B. Caussin, D. Bartolo, Distortion and destruction of colloidal flocks in disordered environments. *Nat. Phys.* **1**, 1–6 (2016).
180. H. Wioland, F. G. Woodhouse, J. Dunkel, J. O. Kessler, R. E. Goldstein, Confinement Stabilizes a Bacterial Suspension into a Spiral Vortex. *Phys. Rev. Lett.* **110**, 268102 (2013).
181. H. Wioland, F. G. Woodhouse, J. Dunkel, R. E. Goldstein, Ferromagnetic and antiferromagnetic order in bacterial vortex lattices. *Nat. Phys.* **12**, 341–345 (2016).
182. K. Doxzen *et al.*, Guidance of collective cell migration by substrate geometry. *Integr. Biol.* **5**, 1026 (2013).
183. G. Duclos, C. Erlenkamper, J.-F. Joanny, P. Silberzan, Topological defects in confined populations of spindle-shaped cells. *Nat Phys.* **13**, 58–62 (2017).
184. D. Volfson, S. Cookson, J. Hasty, L. S. Tsimring, Biomechanical ordering of dense cell populations. *Proc. Natl. Acad. Sci. U. S. A.* **105**, 15346–15351 (2008).
185. S. R. K. Vedula *et al.*, Emerging modes of collective cell migration induced by geometrical constraints. *Proc. Natl. Acad. Sci. U. S. A.* **109**, 12974–9 (2012).
186. H. Wioland, E. Lushi, R. E. Goldstein, Directed collective motion of bacteria under channel confinement. *New J. Phys.* **18**, 1–11 (2016).
187. J. Alvarado, B. M. Mulder, G. H. Koenderink, Alignment of nematic and bundled semiflexible polymers in cell-sized confinement. *Soft Matter.* **10**, 2354–64 (2014).
188. M. Pinot *et al.*, Effects of Confinement on the Self-Organization of Microtubules and Motors. *Curr. Biol.* **19**, 954–960 (2009).
189. R. Zhang, Y. Zhou, M. Rahimi, J. J. de Pablo, Dynamic structure of active nematic shells. *Nat. Commun.* **7**, 13483 (2016).
190. J. I. Eda Hiro *et al.*, In situ control of cell adhesion using photoresponsive culture surface. *Biomacromolecules.* **6**, 970–974 (2005).
191. L. a Flanagan, Y.-E. Ju, B. Marg, M. Osterfield, P. a Janmey, Neurite branching on deformable

- 
- substrates. *Neuroreport*. **13**, 2411–2415 (2002).
192. T. A. Ulrich, E. M. De Juan Pardo, S. Kumar, The mechanical rigidity of the extracellular matrix regulates the structure, motility, and proliferation of glioma cells. *Cancer Res.* **69**, 4167–4174 (2009).
193. R. Sunyer *et al.*, Collective cell durotaxis emerges from long-range intercellular force transmission. *Science*. **353**, 1157–1161 (2016).
194. M. Murrell, R. Kamm, P. Matsudaira, Substrate Viscosity Enhances Correlation in Epithelial Sheet Movement. *Biophys. J.* **101**, 297–306 (2011).
195. P. Guillamat, J. Ignés-Mullol, S. Shankar, M. C. Marchetti, F. Sagués, Probing the shear viscosity of an active nematic. *Phys. Rev. E*. **60602**, 1–5 (2016).
196. C. Peng, T. Turiv, Y. Guo, Q.-H. Wei, O. D. Lavrentovich, Command of active matter by topological defects and patterns. *Science*. **354** (2016), doi:10.1126/science.aah6936.
197. P. Guillamat, J. Ignés-Mullol, F. Sagués, Taming active turbulence with patterned soft interfaces. *arXiv*. **1611.06416**, 1–16 (2016).
198. P. Guillamat, J. Ignés-Mullol, F. Sagués, Control of active liquid crystals with a magnetic field. *Proc. Natl. Acad. Sci. U. S. A.* **113**, 201600339 (2016).
199. M. Castoldi, A. V Popov, Purification of brain tubulin through two cycles of polymerization-depolymerization in a high-molarity buffer. *Protein Expr. Purif.* **32**, 83–8 (2003).
200. T. Sanchez, Z. Dogic, in *Methods in enzymology* (Elsevier Inc., ed. 1, 2013; <http://www.ncbi.nlm.nih.gov/pubmed/23498742>), vol. 524, pp. 205–224.
201. R. Subramanian, J. Gelles, Two distinct modes of processive kinesin movement in mixtures of ATP and AMP-PNP. *J. Gen. Physiol.* **130** (2007), pp. 445–55.
202. A. Holmberg *et al.*, The biotin-streptavidin interaction can be reversibly broken using water at elevated temperatures. *Electrophoresis*. **26**, 501–510 (2005).
203. P. Atkins, J. De Paula, Physical Chemistry. *New York*. **99**, 830 (2006).
204. C. A. Naumann, C. F. Brooks, G. G. Fuller, W. Knoll, C. W. Frank, Viscoelastic properties of lipopolymers at the air-water interface: A combined interfacial stress rheometer and film balance study. *Langmuir*. **15**, 7752–7761 (1999).
205. K. Halbach, Design of permanent multipole magnets with oriented rare earth cobalt material. *Nucl. Instruments Methods*. **169**, 1–10 (1980).
206. R. Benzi, S. Patarnello, P. Santangelo, Self-similar coherent structures in two-dimensional decaying turbulence. *Energy*. **21**, 1221–1237 (1988).
207. P. V. C. Hough, Method and means for recognizing complex patterns. *US Pat. 3,069,654*. **21**, 225–231 (1962).

- 
208. R. Di Leonardo *et al.*, Bacterial ratchet motors. *Proc. Natl. Acad. Sci. U. S. A.* **107**, 9541–9545 (2010).
209. L. Giomi, M. J. Bowick, P. Mishra, R. Sknepnek, M. Cristina Marchetti, Defect dynamics in active nematics. *Philos. Trans. R. Soc. A Math. Phys. Eng. Sci.* **372**, 20130365–20130365 (2014).
210. S. P. Thampi, R. Golestanian, J. M. Yeomans, Active nematic materials with substrate friction. *Phys. Rev. E - Stat. Nonlinear, Soft Matter Phys.* **90** (2014), doi:10.1103/PhysRevE.90.062307.
211. S. P. Thampi, R. Golestanian, J. M. Yeomans, Vorticity, defects and correlations in active turbulence. *Philos. Trans. A. Math. Phys. Eng. Sci.* **372**, 431–434 (2014).
212. J. Ding, H. E. Warriner, J. A. Zasadzinski, D. K. Schwartz, Magnetic needle viscometer for Langmuir monolayers. *Langmuir*. **18**, 2800–2806 (2002).
213. S. Ramaswamy, The mechanics and statistics of active matter. *Annu. Rev. Condens. Matter Phys.* **1**, 323–345 (2010).
214. E. J. Hemingway, P. Mishra, M. C. Marchetti, S. M. Fielding, Correlation lengths in hydrodynamic models of active nematics. *Soft Matter*. **12**, 7943–7952 (2016).
215. B. T. Gettelfinger *et al.*, Flow induced deformation of defects around nanoparticles and nanodroplets suspended in liquid crystals. *Soft Matter*. **6**, 896 (2010).
216. T. Stieger, M. Schoen, M. G. Mazza, Effects of flow on topological defects in a nematic liquid crystal near a colloid. *J. Chem. Phys.* **140**, 54905 (2014).
217. B. Senyuk, O. Puls, O. M. Tovkach, S. B. Chernyshuk, I. I. Smalyukh, Hexadecapolar colloids. *Nat. Commun.* **7**, 10659 (2016).
218. P. J. Flory, *Principles of Polymer Chemistry* (Cornell University Press, 1953).
219. A. A. Hyman, S. Salser, D. N. Drechsel, N. Unwin, T. J. Mitchison, Role of GTP hydrolysis in microtubule dynamics: information from a slowly hydrolyzable analogue, GMPCPP. *Mol. Biol. Cell.* **3**, 1155–67 (1992).
220. R. D. Vale, C. M. Coppin, F. Malik, F. J. Kull, R. A. Milligan, Tubulin GTP hydrolysis influences the structure, mechanical properties, and kinesin-driven transport of microtubules. *J. Biol. Chem.* **269**, 23769–23775 (1994).



---

# List of Publications

Below, find a list of chronologically-ordered articles, which are already published (P), in press (Pp) or submitted for publication (Ps). P1-P3 do not correspond to the topic of this work.

P1. Guillamat, P., Cortés, M., Vallés, E., Gómez, E. Electrodeposited CoPt films from a deep eutectic solvent. *Surf. Coatings Technol.* **206**, 4439–4448 (2012).

P2. Guillamat, P., Sagués, F. & Ignés-Mullol, J. Electric-field modulation of liquid crystal structures in contact with structured surfactant monolayers. *Phys. Rev. E* **89**, 052510 (2014).

P3. Guillamat, P., Ignés-Mullol, J., Claret, J., Sagués, F. Patterning of Liquid Crystals with Structured Monolayers. *Macromol. Symp.* **357**, 206–209 (2015).

P4. Guillamat, P., Ignés-Mullol, J., Sagués, F., Control of Active Liquid Crystals with a Magnetic Field. *Proc. Nat. Acad. Sci. U. S. A.* **113** (20), 5498-5502 (2016).

- Highlighted in Nature Reviews Materials: A. Brotchie, *Nat. Rev. Mater.* **16043** (2016).

Pp5. Guillamat, P., Ignés-Mullol, J., Sagués, F. Control of active nematics with passive liquid crystals. Accepted in *Mol. Cryst. Liq. Cryst.* (2017).

P6. Guillamat, P., Ignés-Mullol, J., Shankar, S., Marchetti, M. C. & Sagués, F. Probing the shear viscosity of an active nematic. *Phys. Rev. E* **94**, 60602(R) (2016).

Ps7. Guillamat, P., Ignés-Mullol, J., Sagués, F., Taming active turbulence with addressable soft interfaces (2017). Submitted to *Nat. Comm.*

Ps8. Guillamat, P., Kos, Ž., Ignés-Mullol, J., Ravnik, M., Sagués, F., Activation of topological defects (2017). To be submitted to *Proc. Nat. Acad. Sci. U. S. A.*



---

# Resum

## Introducció

Sistemes compostos per grups d'animals, colònies de bacteris, teixits de cèl·lules o assemblatges d'extractes cel·lulars, mostren comportaments dinàmics complexos significativament similars<sup>1</sup>. No obstant, generen fluxos a escales espai-temps molt diverses (**Figura 1**). Aquests sistemes, anomenats sistemes actius, estan generalment formats per unitats individuals auto-propulsades que consumeixen energia de l'ambient, a partir de la qual generen forces i treball mecànic<sup>2</sup>. La interacció entre els constituents d'aquests sistemes propicia moviments col·lectius i cooperatius, així com patrons de flux que no s'observen en sistemes similars en equilibri termodinàmic.

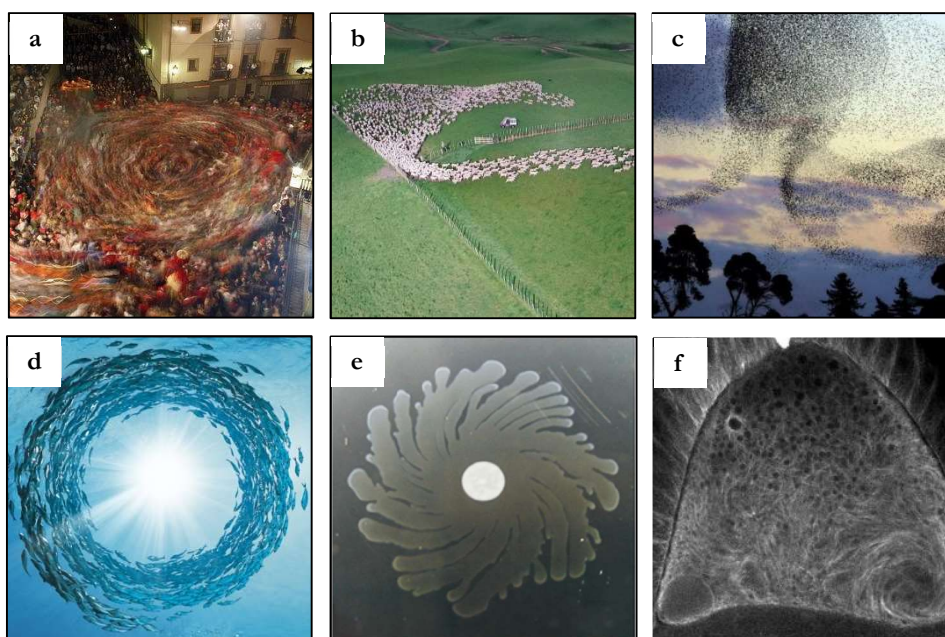


**Figura 1. Dinàmiques col·lectives en sistemes actius a la natura.** Agrupacions nombroses d'entitats actives generen moviments col·lectius degut a la interacció entre elles. Exemples de sistemes actius abunden a la naturalesa i es caracteritzen per escales de longitud que varien segons la mida dels constituents, de metres a micròmetres. Ordenats per mida dels seus constituents trobem moviments col·lectius en (a) grups de persones, (b) ramats d'herbívoros, (c) estols d'ocells, (d) bancs de peixos, (e) colònies bacterianes i (f) assemblatges de biofilaments i motors moleculars al citoesquelet.

Tot i que les característiques morfològiques i dinàmiques d'aquests sistemes s'estan estudiant amb detall, manquen encara estratègies per controlar els fluxos actius que se'n deriven. L'habilitat de controlar sistemes actius, no només en facilita la seva caracterització sinó que possibilitaria l'aplicació dels fluxos que se'n deriven, per exemple, en dispositius. Amb aquest objectiu, aquesta tesi se centra

---

<sup>1</sup> T. Vicsek, A. Zafeiris, Collective motion. *Phys. Rep.* 517, 71–140 (2012).

<sup>2</sup> M. C. Marchetti et al., Hydrodynamics of soft active matter. *Rev. Mod. Phys.* 85, 1143–1189 (2013).



en el desenvolupament d'estratègies per al condicionament i control de fluxos actius mitjançant constriccions que procuren ser no invasives per als materials implicats.

**Matèria activa artificial.** Tot i que la recerca en matèria activa es va iniciar amb l'estudi de grups d'animals, colònies de bacteris i teixits, les complicacions experimentals que suposen aquests sistemes actius "vius" o naturals han obligat a dissenyar, en els darrers anys, materials actius sintètics anàlegs a aquests sistemes amb el propòsit d'analitzar-ne els trets més fonamentals. Entre aquests materials hi trobem principalment tres famílies d'experiments:

- Col·loides dinàmics. Monocapes concentrades de partícules col·loïdals auto-propulsades<sup>3</sup> o bé activades externament mitjançant vibració<sup>4</sup> o camps externs<sup>5</sup>, donen lloc a fenòmens col·lectius que mostren similituds amb els sistemes formats per organismes vius (**Figura 2**). Únicament el contacte físic directe entre partícules esfèriques, per exemple, origina la formació de clústers mòbils que s'alineen preferentment en una direcció (**Figura 2**).

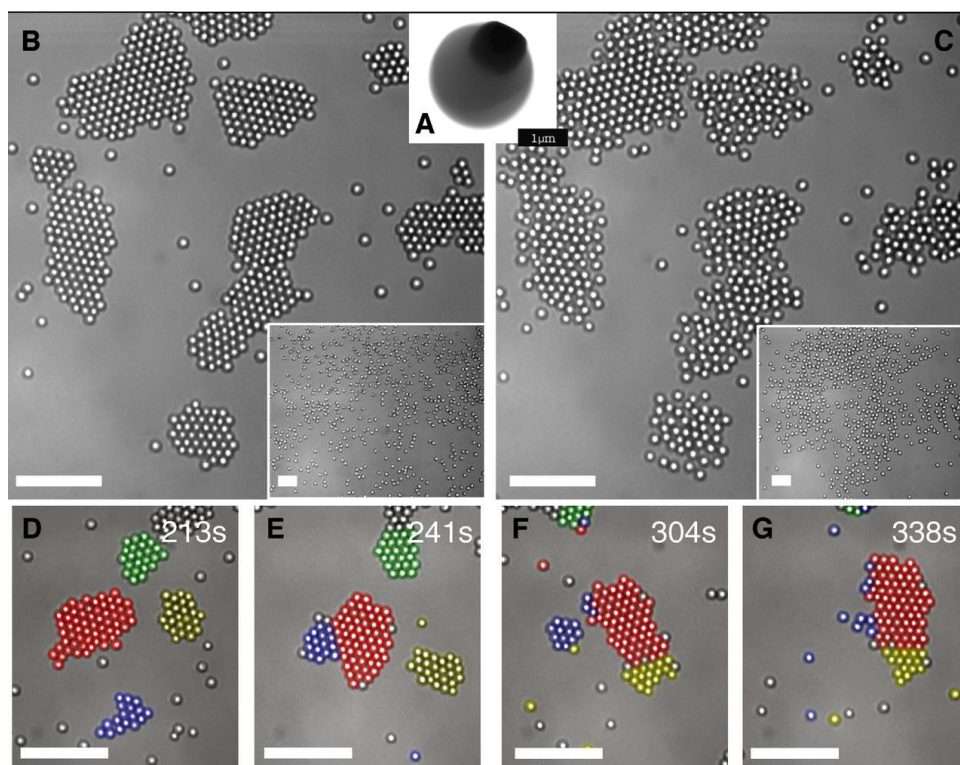


**Figura 2. Organització de col·loides auto-propulsats activats per llum.** a) imatge de microscòpia electrònica (SEM) d'una partícula biomaterial: partícula polimèrica amb hematites (fosc). b) Amb llum blava les partícules s'activen mitjançant reaccions fotocatalítiques i es formen clústers cristal·lins de partícules a partir d'una dispersió homogènia (requadre interior). c) si la llum s'apaga les partícules s'aturen i els clústers es desagrupen (requadre interior correspon a la mateixa regió 100 s després). d-g) els colors mostren l'evolució temporal de partícules que pertanyen a diferents agrupacions. Les barres d'escala indiquen 10 µm. Adaptació de la referència (3).

<sup>3</sup> J. Palacci, S. Sacanna, A. P. Steinberg, D. J. Pine, P. M. Chaikin, Living crystals of light-activated colloidal surfers. *Science*. 339, 936–40 (2013).

<sup>4</sup> V. Narayan, S. Ramaswamy, N. Menon, Long-Lived Giant Number Fluctuations in a Swarming Granular Nematic. *Science*. 317, 105–108 (2007).

<sup>5</sup> A. Bricard, J.-B. Caussin, N. Desreumaux, O. Dauchot, D. Bartolo, Emergence of macroscopic directed motion in populations of motile colloids. *Nature*. 503, 95–8 (2013).

Tot i que la robustesa d'aquests sistemes és innegable, els manquen variables de control que permetin una investigació més exhaustiva. Per tal de superar aquesta limitació, s'han dissenyat altres sistemes basats en reconstitucions d'extractes sots-cel·lulars *in vitro*. Concretament, aquests sistemes combinen macromolècules del citoesquelet capaces de generar forces mitjançant la hidròlisi dels nucleòsids Adenosina trifosfat o Guanosina trifosfat (ATP i GTP, respectivament).

- Assajos de motilitat. Els primers sistemes actius basats en extractes del citoesquelet s'anomenen assajos de motilitat, i consisteixen en filaments d'actina propulsats, en presència d'ATP, per motors moleculars tipus miosina, ancorats en un substrat sòlid<sup>6</sup> (**Figura 3a**). Tot i que aquests primers experiments tenien com a objectiu explorar el funcionament biològic bàsic dels motors moleculars, més que no pas estudiar la dinàmica dels filaments transportats, van servir de precedent per alguns dels experiments més rellevants en el camp de la matèria activa. En particular, incrementant la densitat de filaments s'incrementa la interacció entre ells, propiciant l'auto-organització de patrons col·lectius com ara clústers dinàmics, ones transversals o remolins de filaments<sup>7</sup> (**Figura 3b-d**). Aquests experiments han verificat l'existència d'anisotropia en patrons de moviments col·lectius i han estat útils per quantificar les fluctuacions de densitat característiques dels sistemes actius.

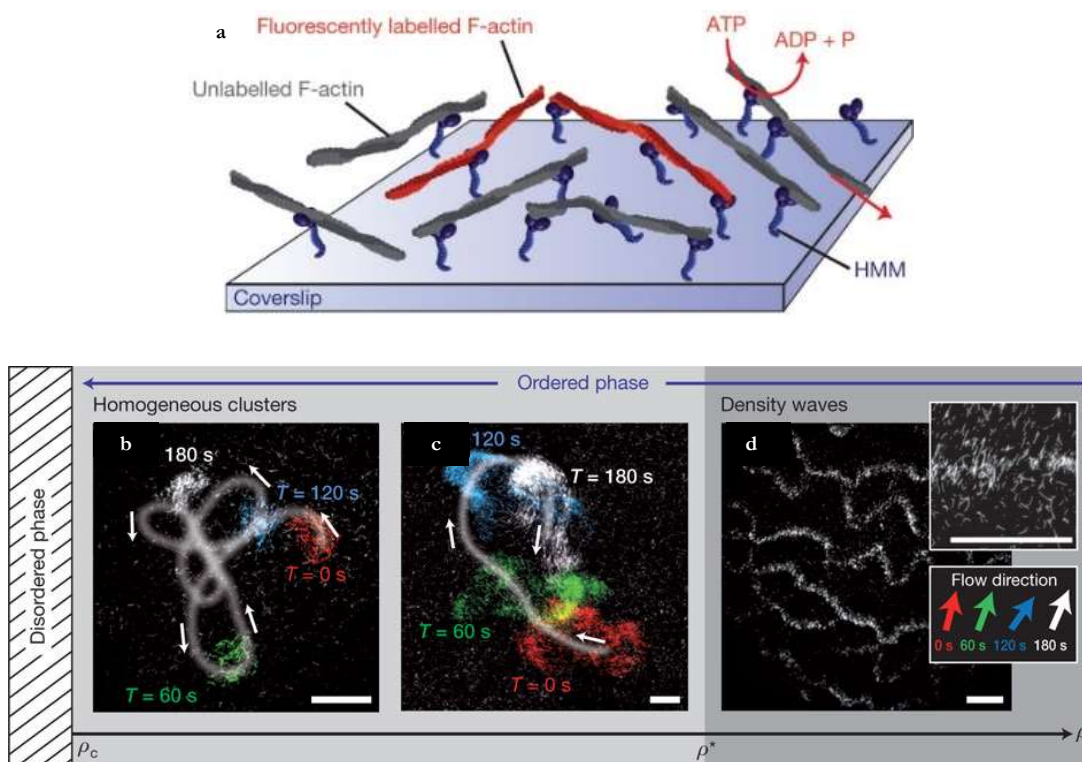


**Figura 3. Esquema d'un assaig de motilitat i diagrama de fases en funció de la densitat de filaments.** a) Motors moleculars miosina (HMM) s'immobilitzen en un substrat i per tant, són capaços de desplaçar filaments d'actina, alguns fluorescents per fer possible la seva visualització mitjançant microscòpia de fluorescència. A densitats baixes de filaments, la mobilitat és desordenada. b,c) Per sobre la densitat  $\rho_c$ , es comencen a formar clústers de filaments. d) per sobre  $\rho^*$  s'observen fluctuacions de densitat persistents que porten a la formació d'estructures tipus ona. Barres d'escala indiquen 50  $\mu\text{m}$ . Adaptació de la referència (7).

<sup>6</sup> S. J. Kron, J. A. Spudich, Fluorescent actin filaments move on myosin fixed to a glass surface. *Proc. Natl. Acad. Sci. U. S. A.* 83, 6272–6276 (1986).

<sup>7</sup> V. Schaller, C. Weber, C. Semmrich, E. Frey, A. R. Bausch, Polar patterns of driven filaments. *Nature.* 467, 73–77 (2010).

Experiments similars s'han dut a terme amb microtúbuls i els seus motors moleculars associats (quinesina), tot i que, degut a diferències en la rigidesa dels filaments, els microtúbuls mostren variacions respecte a la dinàmica observada amb els filaments d'actina. Sistemes basats en extractes del citoesquelet, són simples pel que fa al nombre d'ingredients i són versàtils ja que presenten forces paràmetres de control fàcilment modificables. En particular, és el fet d'emprar proteïnes el que confereix aquesta versatilitat a aquests sistemes, que permeten ajustos a escala molecular.

- Gels actius. Finalment, amb l'objectiu d'imitar les funcionalitats del citoesquelet, xarxes compostes per biofilaments i motors moleculars associats s'han preparat *in vitro* mitjançant estratègies *bottom-up*. Tal i com ho fan les cèl·lules, aquests sistemes, anomenats gels actius, combinen la dinàmica pròpia dels biofilaments, reticulació activa amb complexos de motors

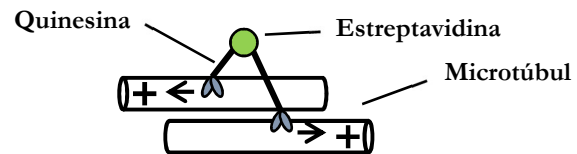


**Figura 4. Clúster de motors moleculars tipus quinesina.** Representació esquemàtica de la generació de forces entre microtúbuls, exercida per un clúster de motors moleculars.

moleculars i altres interaccions físiques, per tal de generar les forces necessàries pel seu moviment. El primer gel actiu es va obtenir a partir d'una suspensió de microtúbuls i clústers de motors moleculars quinesina, enllaçats mitjançant un nucli d'estreptavidina<sup>8</sup>. Com s'ha vist prèviament, els motors moleculars s'acoblen als filaments i exerceixen forces sobre ells. Clústers dinàmics de motors moleculars actuen com a reticulants actius ja que enllacen diferents microtúbuls i a més, exerceixen forces locals entre ells (**Figura 4**). Aquestes forces entre biofilaments, de l'ordre dels pN, són les responsables dels canvis macroscòpics que es produeixen en el citoesquelet, involucrats en processos fonamentals com la remodelació de les cèl·lules, la formació del feix mitòtic o la divisió cel·lular. En els gels actius, la interacció entre microtúbuls i clústers de motors porta a la formació d'estructures complexes quasi-estàtiques com remolins o àsters en què els motors s'acumulen als centres (**Figura 5**).

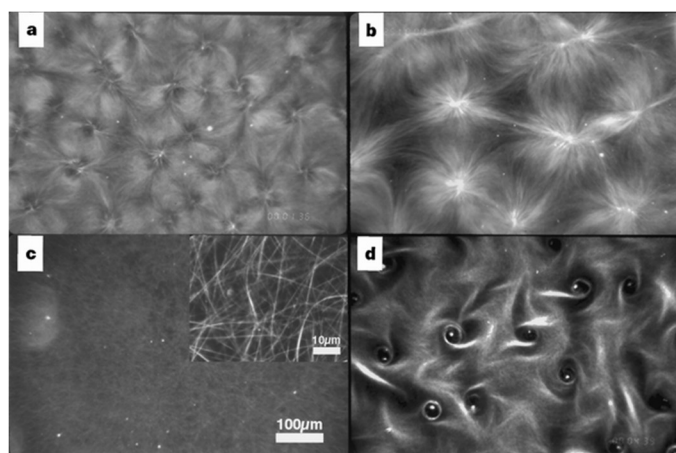


**Figura 5. Estructures formades a partir de l'auto-organització de microtúbuls i motors.** Diferent concentració de quinesina afavoreix la formació (a) de xarxes d'àsters i remolins, (b) àsters, (c) feixos de filaments o (d) remolins. Adaptació de la referència (8).

<sup>8</sup> F. J. Nédélec, T. Surrey, A. C. Maggs, S. Leibler, Self-organization of microtubules and motors. *Nature*. 389, 305–8 (1997).

Tal i com s'explica a continuació, molt diferent és el que succeeix quan entren en joc altres forces externes que afavoreixen la agrupació de filaments sense necessitat dels reticulants, com ara forces de depleció.

**El sistema experimental d'estudi.** El sistema experimental emprat en aquesta tesi correspon a un material actiu sintètic del tipus gel actiu, compostat per proteïnes del citoesquelet i un agent de depleció, creat al grup de Z. Dogic (Brandeis University, MA, USA) al 2012<sup>9</sup>. El sistema està basat en agregats de microtúbuls, reticulats per complexos de motors moleculars (**Figura 6a**). A diferència dels gels actius descrits prèviament, el sistema emprat en aquest estudi incorpora forces de depleció que propicien (entròpicament) l'agregació dels filaments. En presència d'Adenosina trifosfat (ATP), els complexos motors exerceixen forces de cisalla locals entre els microtúbuls que, globalment, provoquen l'extensió, flexió i trencament dels agregats filamentosos (**Figura 6b,c**). Gràcies a l'acció de les forces de depleció els agregats poden recombinar-se, tornant a repetir el cicle dinàmic anterior repetidament fins a l'esgotament del combustible. La interacció entre els agregats filamentosos extensils genera fluxos desordenats a escales de l'ordre dels centenars de micròmetres (**Figura 6d**), longituds molt més grans que les pròpies de les unitats constitutives del material.

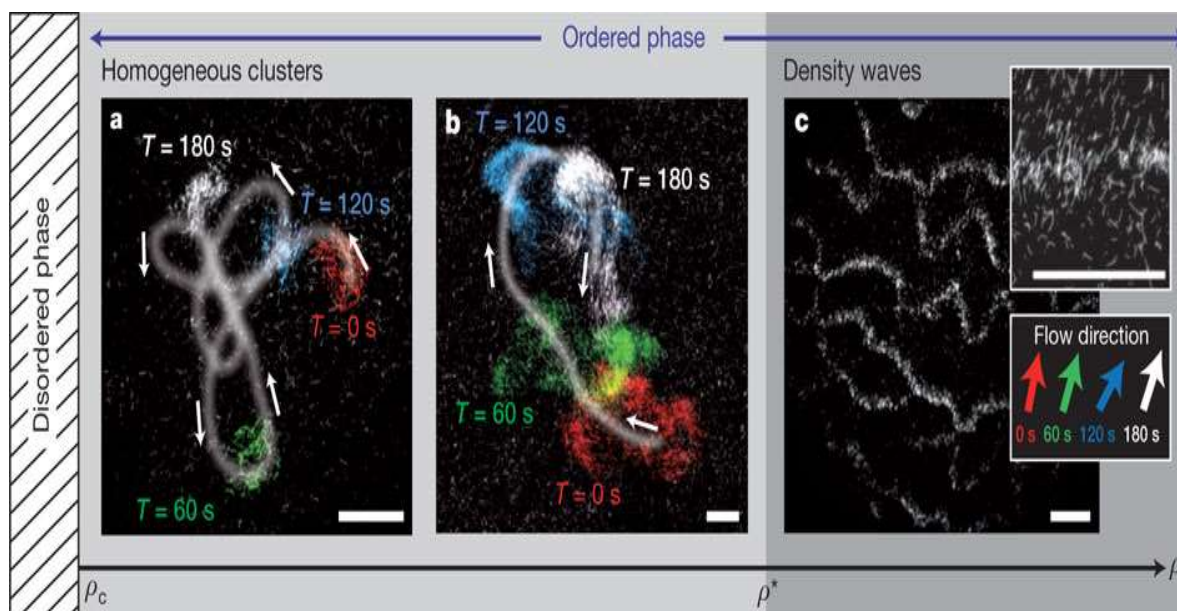


**Figura 6. Gels actius de microtúbuls.** a) Il·lustració esquemàtica d'un agregat extensil de microtúbuls, el component bàsic d'aquest gel actiu. b) Dos agregats es fusionen i s'estenen immediatament, eventualment trencant-se. c) En aquest sistema els feixos de microtúbuls constantment s'agrupen (fletxes vermelles), s'estenen, es col·lapsen, es fracturen (fletxa verda), i es recombinen amb altres agregats de filaments generant un estat molt dinàmic. La barra d'escala indica 15  $\mu\text{m}$ . d) Gel actiu observat a pocs augments. Les fletxes grogues indiquen la velocitat local dels filaments. La barra d'escala indica 80  $\mu\text{m}$ . Adaptació de la referència (9).

<sup>9</sup> T. Sanchez, D. T. N. Chen, S. J. DeCamp, M. Heymann, Z. Dogic, Spontaneous motion in hierarchically assembled active matter. *Nature*. 491, 431–4 (2012).



D'altra banda, en presència d'una interfície aigua/oli correctament funcionalitzada, el gel es densifica, desenvolupant els seus fluxos en contacte amb la fase oliosa. D'aquesta manera, s'obté un material actiu quasi-bidimensional molt dens, en el qual els filaments interaccionen entre si i s'organitzen en el pla, donant lloc a un gel actiu amb ordre orientacional (**Figura 7**). El fet que els constituents d'aquests fluids presentin interaccions entre si i, de retruc, ordre intern, recorda als cristalls líquids (CLs). En particular, l'existència, únicament, d'ordre orientacional, és un tret característic de les anomenades fases nemàtiques, fet pel qual s'ha anomenat a aquest material, CL nemàtic actiu, o senzillament, nemàtic actiu.

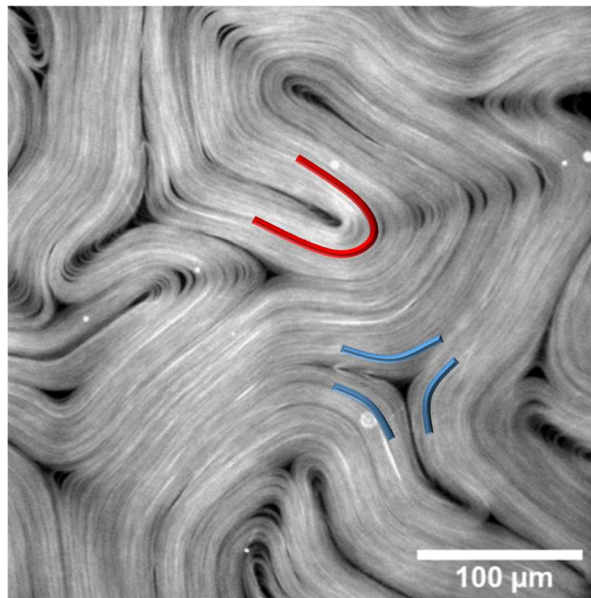


**Figura 7. El nemàtic actiu.** Imatge de microscòpia de fluorescència mostra la morfologia del material que aquí s'estudia. Les estructures negres constitueixen defectes en el si del material. Depenent de la simetria dels defectes distingim entre defectes positius (en vermell) i negatius (en blau). Degut a la seva geometria, només generen fluxos els defectes positius, mentre que els negatius es mouen principalment per fenòmens advectius.

A diferència dels CLs nemàtics tradicionals en equilibri, en què els constituents es troben ordenats i presenten mínimes distorsions, els CLs actius estan constituïts per unitats que dissipen energia de forma contínua, generant forces internes que suposen el trencament constant de l'ordre orientacional. Aquestes situacions de no equilibri generen singularitats o defectes en el camp d'orientacions, que a la vegada, en el cas dels materials actius, generen fluxos de tipus turbulent dominat per la presència de vòrtexs.

## Muntatge experimental

L'experimentació amb aquest material habitualment s'havia dut a terme en cel·les de flux d'espais no superiors als 100  $\mu\text{m}$ , molt útils per el confinament de fluids de viscositats reduïdes. Per dur a terme els experiments que aquí es presenten, ha calgut dissenyar un sistema experimental que permetés la utilització d'olis de viscositats molt diverses per a la preparació de la interfície aigua/oli on el material actiu es desenvolupa.

Un bloc de polidimetilsiloxà (PDMS) amb una cavitat cilíndrica de diàmetre 5 mm i alçada entre 1-8 mm (depenent de l'experiment) s'enganxa en un substrat bioinert i superhidrofílic de poliacrilamida (PAA) que prevé la desnaturalització de les proteïnes del material (**Figura 8**).

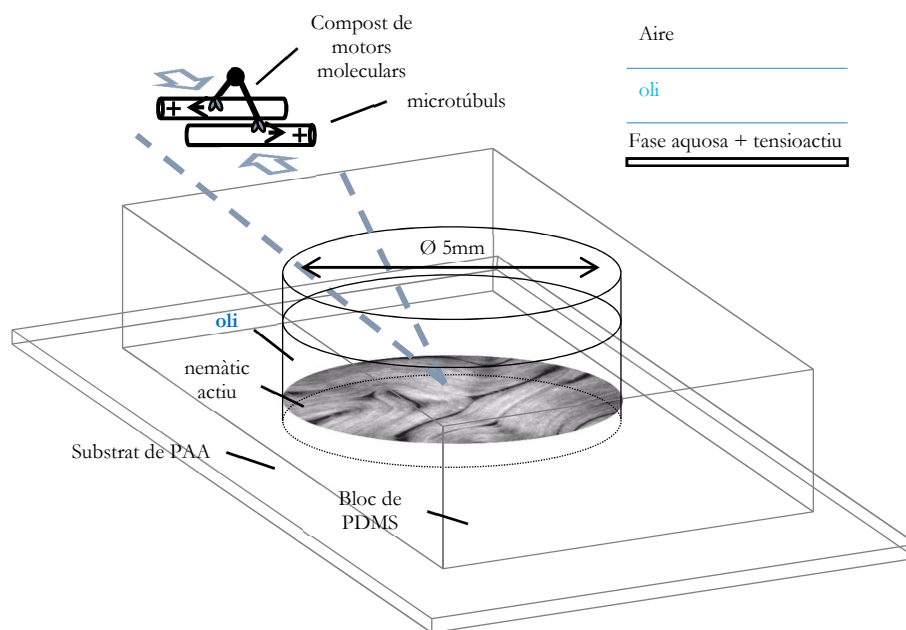


**Figura 8. Sistema experimental.**

La cavitat s'omple inicialment amb uns 50  $\mu\text{L}$  d'oli. Seguidament 1  $\mu\text{L}$  del gel actiu s'injecta a la part inferior, de manera que, en contact amb el substrat de PAA la gota mulla i s'extén. Al cap d'uns minuts el nemàtic actiu es forma espontàniament a la extensa interfície aigua/oli.

## Resultats

Aquesta tesi s'ha centrat en el desenvolupament d'estratègies per al condicionament, regularització i, finalment, control dels fluxos actius del material quasi-bidimensional descrit anteriorment. Mitjançant canvis en les propietats dels olis en contacte amb els quals el nemàtic actiu es desenvolupa, hem pogut evidenciar la importància de les condicions reològiques del seu entorn. En particular, s'ha estudiat l'efecte de la interacció d'aquest sistema amb fluids viscosos isotròpics, amb patrons reològics imposats per cristalls líquids i en confinament, com a eines per al control dels fluxos, fins ara, aparentment caòtics i impredecibles d'aquests sistemes actius.

**Adaptació al contacte amb fluids viscosos.** Mitjançant la preparació del nemàtic actiu en contacte amb olis isotròpics de diferents viscositat s'ha evidenciat l'existència d'un fort acoblament hidrodinàmic a través de la interfície aigua/oli. La interacció dels fluxos actius en diferents contrastos viscosos resulta en una readaptació del material, que reestructura les seves característiques morfològiques i dinàmiques<sup>10</sup>. En aquest cas, la viscositat dels olis actua en contra dels fluxos actius, que disminueixen la velocitat en contacte a l'augmentar el contrast viscos (Figura 9). Conseqüentment, s'observa un creixement en el nombre de defectes (Figura 9), tal i com prediuen algunes teories per nemàtics actius en contacte amb substrats friccional<sup>11</sup>.

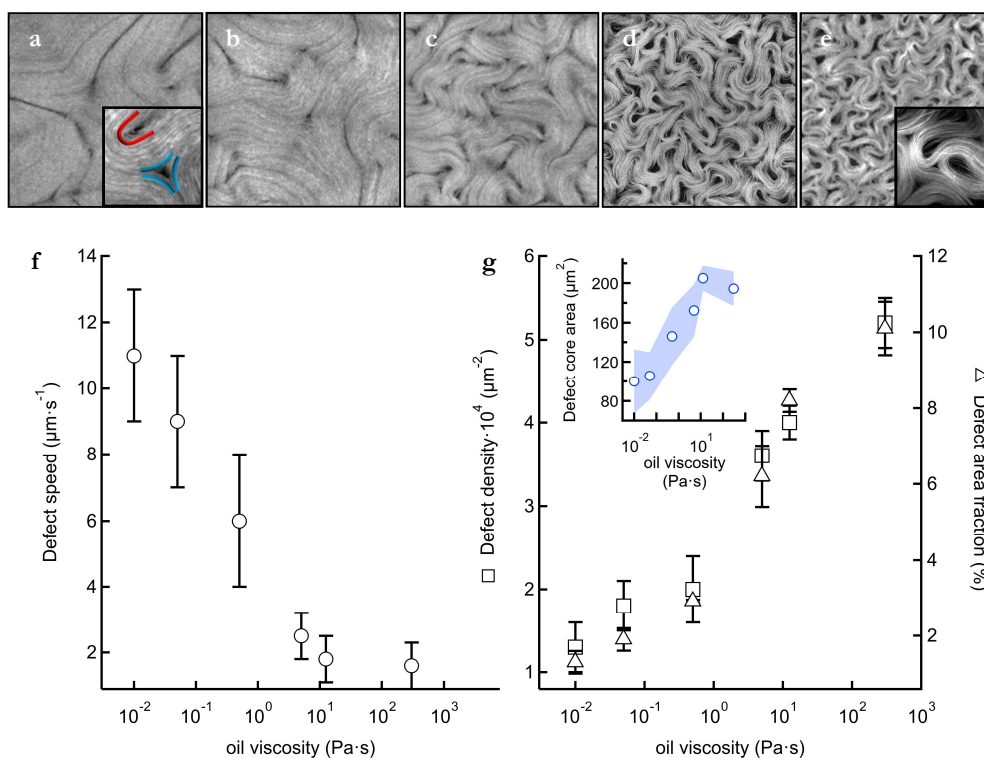


**Figura 9. El nemàtic actiu en contacte amb olis de diferents viscositats.** a) Imatges de microscòpia de fluorescència (400  $\mu\text{m}$  d'ample) mostren les variacions en la densitat de defectes en el material. Les viscositats d'(a) a (e) són  $1 \cdot 10^{-2}$ ,  $5 \cdot 10^{-2}$ , 0.5, 5, i 300 Pa·s. La concentració d'ATP és 1.4 mM en tots els casos. Els requadres interiors mostren imatges quatre

<sup>10</sup> P. Guillamat, J. Ignés-Mullol, S. Shankar, M. C. Marchetti, F. Sagués, Probing the shear viscosity of an active nematic. *Phys. Rev. E.* 60602, 1–5 (2016).

<sup>11</sup> S. P. Thampi, R. Golestanian, J. M. Yeomans, Active nematic materials with substrate friction. *Phys. Rev. E.* 90 (2014), doi:10.1103/PhysRevE.90.062307.

vegades augmentades **f)** Quan la concentració d'ATP es manté constant, la velocitat del material decreix en contacte amb olis més viscosos. **g)** Tant la densitat ( $\square$ ) com la fracció d'àrea ( $\Delta$ ) corresponent als defectes augmenten en contacte amb majors viscositats. Dividint l'àrea entre el nombre de defectes obtenim una aproximació de l'àrea dels defectes, que també augmenta amb majors contrastos viscosos (requadre interior).

Les conseqüències de l'acoblament amb olis més viscosos és fàcilment comprensible. Reducció de la velocitat del material actiu (**Figura 9f**) és conseqüència directa de l'acoblament i això resulta en una reducció de la taxa d'aniquilació de defectes (proporcional a la velocitat del material). Com que la concentració d'ATP es manté constant en tots els experiments, la taxa de creació de defectes, no varia. En conseqüència el nombre mitjà de defectes augmenta (**Figura 9g**).

**Geometria del règim turbulent.** En condicions d'acoblament isotròpic amb la fase oliosa, el nemàtic actiu desenvolupa fluxos turbulents, donant lloc a un règim dinàmic que s'ha establert com a referència durant el transcurs d'aquesta tesi. La distribució de mides d'aquests vòrtex està determinada per una escala de longitud intrínseca del material ( $l_a$ ) que estableix la geometria del règim turbulent<sup>12</sup>, caracteritzada per una distribució exponencial de les mides dels vòrtexs. Els nostres experiments han confirmat aquesta predicció mitjançant l'estudi dels camps de velocitat del material, a partir del qual s'ha extret el paràmetre d'Okubo-Weiss,  $OW = (\partial_x v_x)^2 + \partial_y v_x \cdot \partial_x v_y$ , molt útil per a la identificació de vòrtexs (**Figura 10**). En particular, s'estableix que l'extensió dels vòrtexs està sotmesa per la condició  $OW < 0$ <sup>12</sup>.

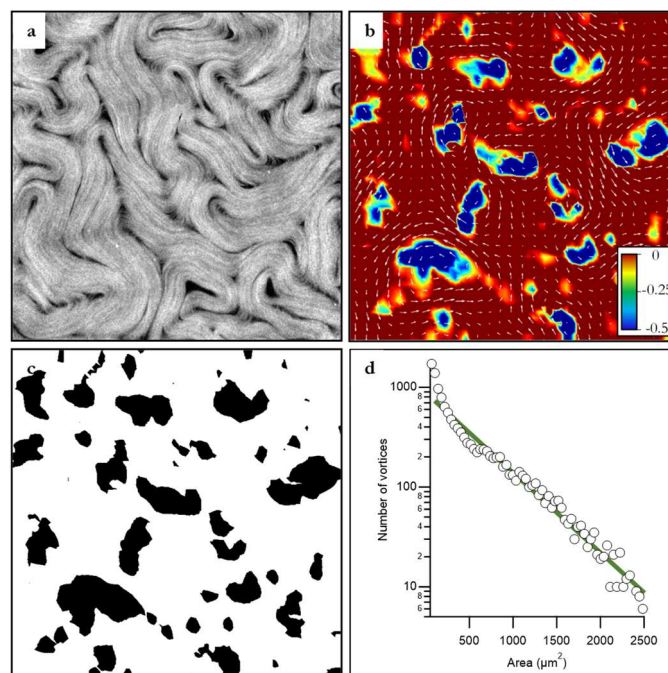


**Figura 10. Estructura de la turbulència activa.** **a)** Imatges de microscòpia confocal de fluorescència del nemàtic actiu en el règim turbulent. La imatge fa 375  $\mu\text{m}$  d'ample. **b)** Camp de velocitats (vectors) i del paràmetre OW (mapa de color), emprat per a determinar la posició i mida dels vòrtexs (àrees blaves). **c)** imatge binària corresponent al camp d'OW. **d)** Anàlisi estadístic de la distribució de la mida dels vòrtexs per una seqüència de mil imatges. La línia és un ajust exponencial a les dades.

<sup>12</sup> L. Giomi, Geometry and topology of Turbulence in active nematics. *Phys. Rev. X*, 5, 1–11 (2015).



L'anàlisi del camp d'OW extret del nematic actiu revela una distribució exponencial de la mida dels vòrtexs, en concordança amb prediccions realitzades a partir de simulacions del regim turbulent de nematics actius. Així doncs, l'estudi realitzat és també coherent amb l'existència d'un longitud característica  $l_\alpha$ , regida pel balanç entre forces actives i les propietats elàstiques del material<sup>12,13</sup>.

**Ús de cristalls líquids per a la regularització del règim turbulent.** Amb l'objectiu de pre-definir les direccions de flux del nematic actiu, s'imposen patrons de viscositat a la interfície, reemplaçant l'oli isotròpic emprat en apartat anteriors per un CL termotròpic, un fluid anisotròpic a temperatura ambient fàcilment controlable mitjançant camps externs. Els compostos emprats mostren fases d'estructura lamel·lar (esmèctiques), en les quals les molècules s'organitzen en plans paral·lels. Aquesta disposició té un efecte molt significatiu en les propietats reològiques del material, que flueix molt més fàcilment en la direcció dels plans (baixa viscositat) que en la direcció perpendicular.

El primer patró reològic estudiat consisteix en una xarxa de dominis circulars formats per anells concèntrics de plans moleculars. En contacte amb aquesta configuració, el material actiu ràpidament organitza remolins en les posicions on es troben dominis de mida superior a un valor l·lindar (**Figura 11**).

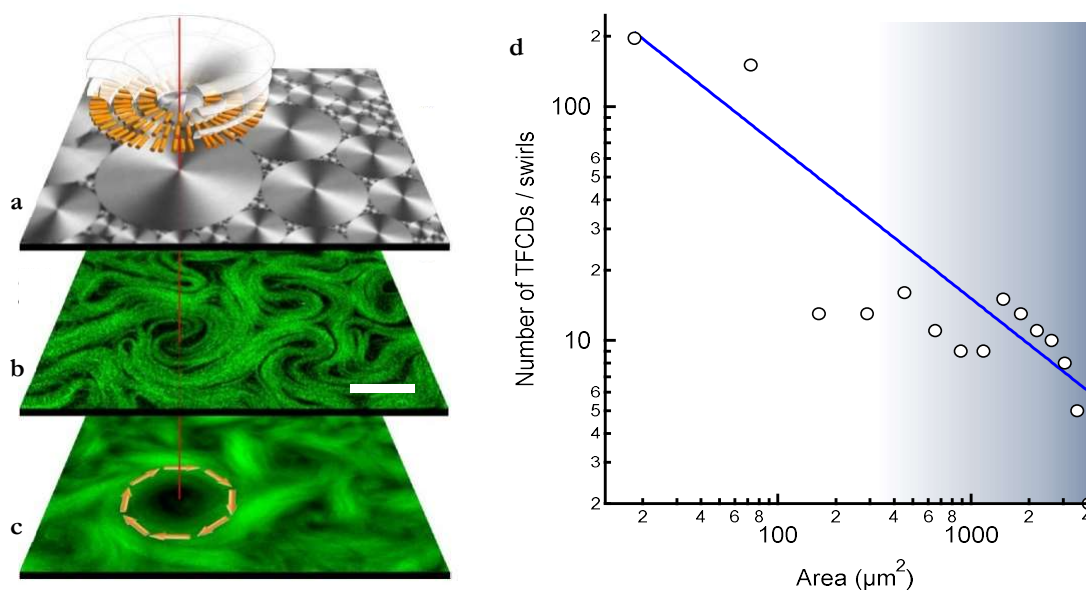


**Figura 11. Organització del nematic actiu en contacte amb patrons reològics.** a) Micrografies confocal en mode reflexió de la interfície aigua/cristall líquid revelen el patró format pels dominis circulars. El diagrama superior il·lustra la disposició de les molècules a la interfície definint la dinàmica dels fluxos actius. b) Imatges de microscòpia confocal en mode fluorescència mostren com el nemàtic actiu s'organitza en remolins molt localitzats degut a l'acoblament hidrodinàmic amb els patrons de la interfície. c) Seqüència de 300 micrografies de fluorescència sobre-imposades evidencien l'efecte dels patrons interfacials. La barra d'escala indica 25  $\mu\text{m}$ . d) Anàlisi de la distribució de mides dels dominis circulars. La línia correspon a l'ajust a una llei de potències amb exponent -0.7. La regió ombrejada correspon a la mida dels dominis capaços de confinar els fluxos actius.

<sup>13</sup> S. P. Thampi, R. Golestanian, J. M. Yeomans, Instabilities and topological defects in active nematics. *Europhys. Lett.* 105, 18001 (2014)

Conseqüentment, la distribució exponencial de mida de vòrtexs intrínseca dels sistemes bidimensionals turbulents es converteix en una distribució tipus llei de potències regida per la distribució de mida dels dominis a la interfície.

**Alineació del nemàtic actiu.** Mitjançant l'aplicació d'un camp magnètic extern, les molècules del cristall en contacte amb el material actiu s'alineen donant lloc a una estructura unidireccional de plans. La viscositat esdevé inferior el la direcció paral·lela als plans, perpendicular a les molècules i al camp magnètic. En contacte amb aquesta estructura, el nemàtic actiu organitza els seus fluxos preferentment en la direcció menys viscosa, donant lloc a un règim dinàmic basat en fluxos laminars unidireccionals<sup>14</sup> (Figura 12).

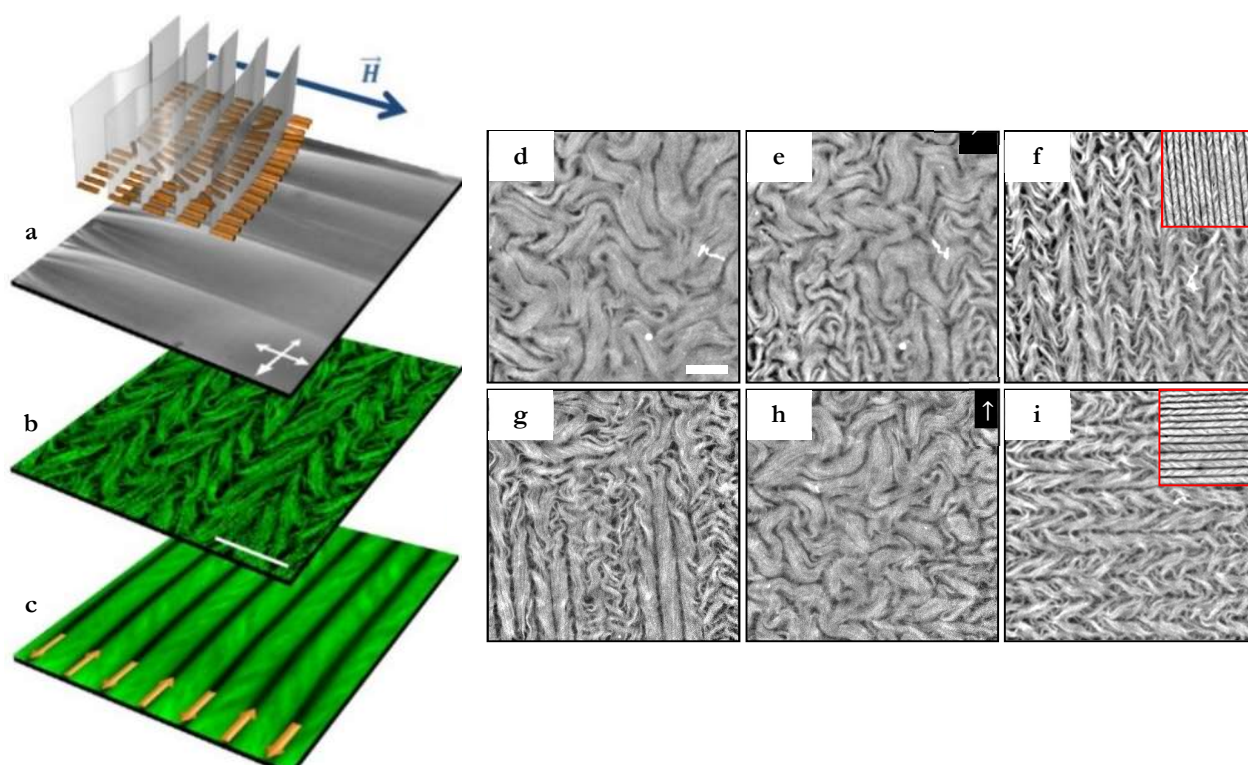


**Figura 12. Alineació del nemàtic actiu amb un camp magnètic extern.** a) imatges de microscòpia de polarització i configuració dels plans de molècules de cristall líquid. b) Micrografies confocal en mode fluorescència revelen la correlació entre el nemàtic alineat i la fase passiva. c) Sobre-posició d'imatges de fluorescència mostren la disposició regular dels defectes en el nemàtic alineat. Les fletxes indiquen la direcció de moviment dels defectes. d-i) Imatges de microscòpia de fluorescència del nemàtic actiu en diferents configuracions. d) El material actiu es troba en el inicialment en el règim turbulent propiciat pel contacte amb la fase nemàtica (menys anisotropia viscosa) del cristall líquid. e,f) Baixant la temperatura, obtenim de nou la fase esmèctica que, en presència d'un camp magnètic (fletxa n'indica la orientació), actua sobre el material actiu que reorganitza els seus fluxos perpendicularment al camp. Un increment de temperatura (f-h) i posterior reducció (h-i) en presència d'un camp magnètic, ara vertical, induueix la re-alineació dels fluxos actius en la orientació perpendicular a l'anterior. Requadres en (f) i (i) són seqüències d'imatges sobre-imposades recalcant la direcció dels fluxos. Barres d'escala indiquen 100  $\mu\text{m}$ .

<sup>14</sup> P. Guillamat, J. Ignés-Mullol, F. Sagués, Control of active liquid crystals with a magnetic field. *Proc. Natl. Acad. Sci. U. S. A.* 113, 201600339 (2016).

Degut a la naturalesa extènsil del material, les regions alineades de nemàtic actiu (**Figura 13a**, regió I) són inestables. En particular, són propenses a patir deformacions que resulten en la creació espontània de defectes en la direcció perpendicular a la orientació de la regió alineada (**Figura 13b,c**). Així doncs, regularment (**Figura 13d-f**), les regions alineades del material pateixen fluxos transversals (**Figura 13a**, regió II) que distorsionen el règim laminar.

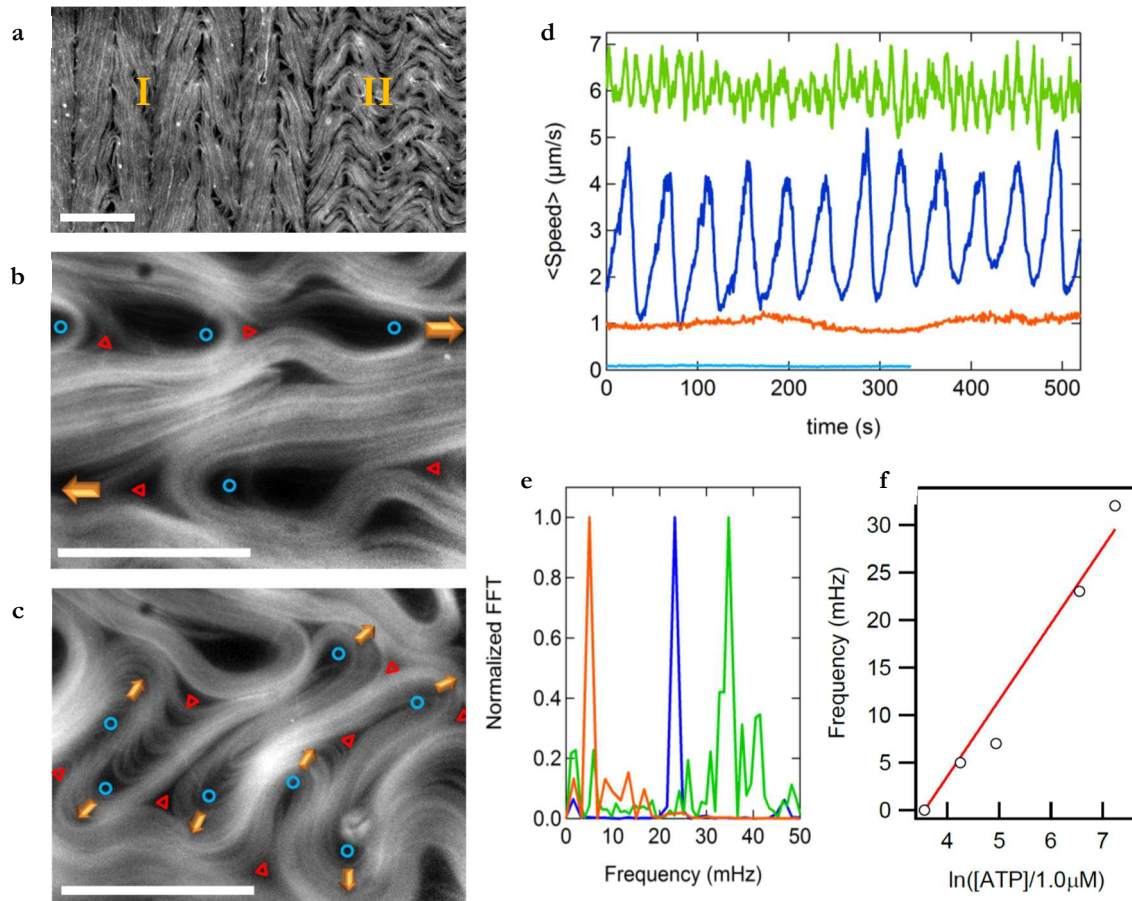


**Figura 13. Inestabilització periòdica de les regions alineades del nemàtic actiu.** a-c) Imatges de microscòpia de fluorescència mostren coexistència de regions alineades (a, I) i regions amb fluxos transversals (a, II). Les barres d'escala indiquen 100  $\mu\text{m}$ . d) Evolució temporal de la velocitat mitjana dels fluxos actius emprant concentracions d'ATP, 1,400  $\mu\text{M}$  (verd), 700  $\mu\text{M}$  (blau fosc), 70  $\mu\text{M}$  (taronja) i 35  $\mu\text{M}$  (blau clar). e) Espectre FFT mostra la dependència de la freqüència de les oscil·lacions amb la concentració d'ATP (f).

**Emulsions actives.** La dispersió de petites gotes de gel actiu en olis permet l'obtenció d'emulsions actives. De la mateixa manera que en els casos anteriors, el gel actiu es densifica a la interfície. En aquest cas però, aquest procés dóna lloc a una escorça esfèrica de nemàtic actiu. En aquesta situació de confinament la dinàmica del material té lloc en condicions de restricció geomètrica i topològica. Gotes en un interval definit de mides mostren escorça nemàtica activa amb quatre defectes. Aquests circulen per la superfície l'esfera donant lloc a dinàmiques oscil·latòries (**Figura 14**) en què els defectes es disposen en un pla o bé en configuracions tetraèdriques<sup>15,16</sup>.

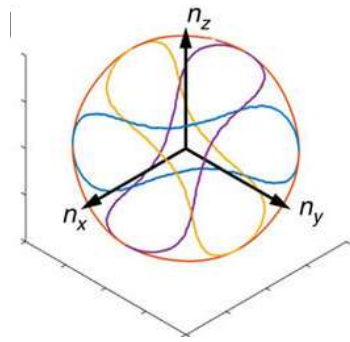


**Figura 14. Trajectòries dels defectes en una escorça de nemàtic actiu.** Les línies de colors representen la trajectòria dels quatre defectes al nemàtic actiu en confinament. Adaptació de la referència (16).

S'ha demostrat que gotes actives es desplacen en fluids de baixa viscositat quan es troben confinades entre superfícies sòlides<sup>9</sup>. El mecanisme pel qual aquestes gotes actives presenten aquest caràcter dinàmic s'associa a l'acoblament entre els fluxos corticals i el substrat. En els experiments que es mostren a continuació, es dispersen gotes actives en fluids isotròpics de baixa viscositat per estudiar el moviment de gotes actives amb còrtex amb dinàmica oscil·latòria. Com es pot observar a la **Figura 15**, gotes individuals de mides inferiors als  $\sim 100 \mu\text{m}$ , mostren moviments rotacionals persistents (**Figura 15**). Deduïm que, degut a la fricció amb el substrat, algunes direccions de flux estan menys afavorides, propiciant així, la dinàmica observada.

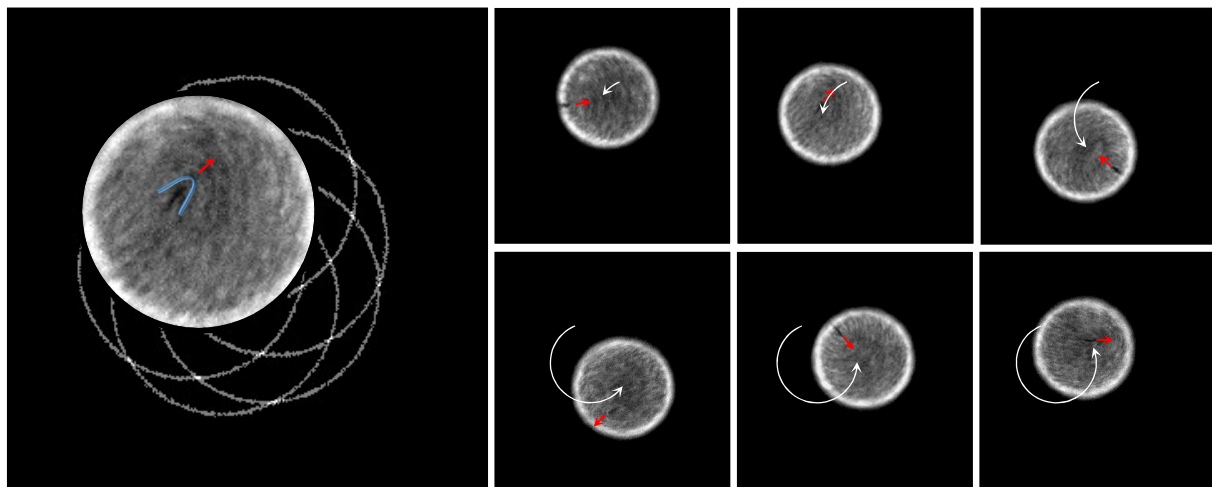


**Figura 15. Gotes actives en contacte amb un substrat sòlid.** Imatges de fluorescència de gotes actives mostren una dinàmica rotacional estable en el temps. Les fletxes vermelles indiquen la direcció del moviment dels defectes mentre que les fletxes blanques fan referència a la translació de la gota. El diàmetre de la gota és de  $\sim 75 \mu\text{m}$ .

<sup>15</sup> F. C. Keber et al., Topology and Dynamics of Active Nematic Vesicles. *Science*. 345, 1–19 (2014).

<sup>16</sup> R. Zhang, Y. Zhou, M. Rahimi, and J. J. de Pablo, *Nat. Commun.* 7, 13483 (2016).



La addició d'aquestes gotes en CLs termotròpics en fase nemàtica permet forçar l'acoblament entre els defectes actius de l'escorça nemàtica amb els defectes passius generats al voltant de les inclusions esfèriques. En particular, s'ha estudiat amb detall la interacció entre els fluxos actius i defectes tipus anell de Saturn (Figura 16a,b). En contacte amb el material actiu, aquests defectes són arrossegats pels fluxos generats a la superfície de les gotes i oscil·len reproduint la dinàmica dels defectes actius (Figura 16d). Simulacions realitzades pel grup del professor M. Ravnik (Universitat de Ljubljana, Eslovènia) han permès reproduir les nostres observacions (Figura 16c,e).

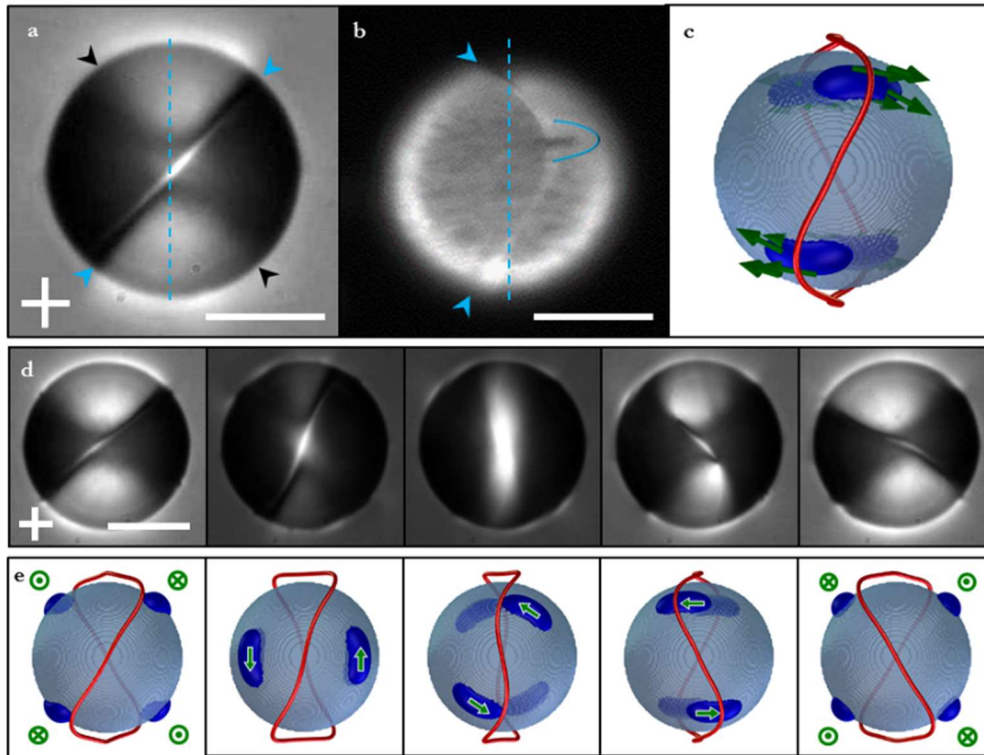


**Figura 16. Interacció entre defectes actius i defectes passius.** **a)** Micrografies de polarització mostren una gota activa rodejada per un defecte tipus anell de Saturn. Els fluxos generats a la superfície de les gotes allunyen el defecte lluny de la seva posició d'equilibri (línia blava). Les fletxes indiquen la posició del defecte a davant (blaves) i darrera (negres) la gota. **b)** Imatges de fluorescència permeten veure com els defectes actius (punt negre) arrosseguen el defecte passiu. **c)** Imatge de la simulació d'una gota activa en un cristall líquid. El defecte generat mostra oscil·lacions periòdiques. Els símbols i fletxes verdes representen el camp de velocitats dels defectes actius (en blau). Seqüències d'imatges mostren mig període de la oscil·lació del defecte passiu en experiments (**d**) i simulacions (**e**). Les barres d'escala indiquen 50  $\mu\text{m}$ .

Tot i la coherència aparent dels fluxos actius en aquesta situació de confinament, cal tenir en compte que, tot i oscil·lar entre estats planar i tetraèdric molt ben definits, la orientació dels plans de defectes és totalment aleatòria. No obstant, mitjançant les dades obtingudes a partir de simulacions s'ha pogut constatar que la oscil·lació del defecte extern és només possible quan el seu pla equatorial es troba alineat amb un dels estats planar que formen els defectes actius. El fet de veure repetidament aquesta oscil·lació porta a pensar sobre l'existència d'un acoblament bidireccional en que els defectes passius regularien la orientació de les dinàmiques actives.

---

## Conclusions

La dinàmica dels sistemes actius és canviant i impredecible, fet que dificulta la seva caracterització o fins i tot, plantejar-se la seva aplicació en dispositius. En aquesta tesi, mitjançant la imposició de constriccions de flux, s'ha aconseguit condicionar, regularitzar i finalment dominar els fluxos generats per un material actiu inspirat en el citoesquelet. En particular, s'ha emprat un gel actiu quasi-bidimensional basat en agregats de microtúbuls i complexos de motors moleculars.

En primer lloc, la utilització d'olis isotròpics de diferents viscositats ha permès avaluar l'efecte de l'acoblament hidrodinàmic a través de la interfície en contacte amb la qual el material actiu es desenvolupa. S'ha observat que a l'augmentar la viscositat de l'oli en contacte amb el material actiu, la velocitat dels fluxos disminueix, fet que comporta canvis en la morfologia del material. La caracterització dels camps de velocitat dels fluxos actius ha permès estudiar-ne la geometria.

En segon lloc, amb l'objectiu d'obtenir un millor control sobre els fluxos del material, s'han substituït els olis isotròpics per fluids anisotròpics ajustables externament (cristalls líquids termotròpics). Concretament, s'han emprat cristalls líquids en fase esmèctica en la que les molècules s'organitzen en plans. A la interfície, l'organització lamel·lar del cristall líquid té una forta repercussió en la dinàmica del material actiu, ja que s'imposen condicions de viscositat marcadament anisotròpiques. El material actiu tendeix a moure's en la direcció menys viscosa. D'una banda, la preparació de dominis lamel·lars circulars a la interfície, ha permès confinar el material actiu en remolins molt localitzats. Mitjançant la preparació de fractals basats en aquests dominis, s'han aconseguit regularitzar els fluxos turbulents, dominats ara per vòrtexs que segueixen la distribució de mides del fractal. D'altra banda, mitjançant la orientació de les molècules amb un camp magnètic extern s'han obtingut estructures de plans amb anisotropia viscosa unidireccional. Sota aquestes condicions els fluxos actius es desenvolupen en una direcció que es pot variar fàcilment canviant l'orientació del camp magnètic.

Per últim, s'han dispersat gotes de material actiu en diferents fluids, fet que ha permès l'obtenció d'emulsions actives. La dispersió de gotes en fluids isotròpics de baixa viscositat ha permès caracteritzar la dinàmica rotatòria de gotes actives en contacte amb substrats sòlids. Paral·lelament, s'han estudiat dispersions de gotes en cristalls líquids nemàtics, que generen defectes al voltant de les inclusions. En aquest darrer cas, els fluxos generats a l'interior de les gotes es transmet als defectes exteriors, que condicionen la dinàmica dels fluxos actius.

En conclusió, el control de fluxos actius mitjançant constriccions de flux ha resultat ser una estratègia efectiva. En particular, l'ús de materials anisotròpics sembla prometedor i es planteja optimitzar-los i desenvolupar-ne variants per a la seva aplicació en altres materials actius en interfícies com ara monocapes de col·loides auto-propulsats, colònies de bacteris o teixits epitelials.



---

# Acknowledgements

The thesis is done and it seems like yesterday when I first entered in the lab for the first time. During these years, I have had the opportunity not only to do great and beautiful science and to discover but also to meet incredible people. Despite these last three months of exhausting and hurried writing I think my experience during these last years has been absolutely awesome.

First of all, I would like to thank my advisors, Francesc and Jordi for giving me the opportunity to work with active matter and for believing in me for starting this amazing active project in the lab. Francesc, gràcies per contagiar-me amb la teva passió per saber més, per estar sempre disponible, per la teva predisposició a ensenyar i pel teu suport durant aquests anys. Gràcies també per les xocolatines suïsses! Jordi, gràcies per la teva constant dedicació al laboratori, per la paciència, pel teu entusiasme i el bon humor que et caracteritzen. Sempre disposat a ajudar, i sempre amb bona cara, has sabut guiar-me al llarg dels darrers 6 anys, des del projecte final de carrera fins ara. Tot i ser un pèl desordenat, no trobar les ulleres i agafar puntes de pipeta sense guants, la teva metodologia i les teves idees sempre han estat molt clares. Als dos, gràcies per les llargues estones de reunions aferrissades, a vegades un pèl turbulentes, però sempre enriquidores. Per a mi, sou dos exemples com a professors, com a investigadors i com a persones, i un immillorable tàndem per fer i dirigir recerca.

My sincere thanks also go to Zvonimir, who provided me an opportunity to join his team in Brandeis, and who gave complete access to the laboratory and research facilities. Especially grateful to Steve and Bernard, who made my learning possible during the stay. Without their support it would not have been possible to conduct this research. Thanks also to other lab members, Andrew and Joia, who made me feel at home. Thanks to Karl for hosting me and showing me around in Waltham. Thanks also to Kirby and Catie for your kind hospitality.

We have been very lucky to count on the collaboration from other groups and people from the University of Barcelona, without which this research would not have been possible. En primer lloc, gràcies als professors J. Casademunt, I. Pagonabarraga i M. Pons per formar part de la meva comissió de seguiment. Gràcies al grup del professor M. Pons (PCB), en especial a l'Anabel-Lise i al Guillermo, per ajudar-nos a expressar i purificar els nostres motors. Gràcies al professor Jordi Ortín (Facultat de física) per deixar-nos els primers olis de silicona, i a la Laura Casanellas per ajudar-nos amb les mesures reològiques. Gràcies a la Roser i a la Gemma (de BlueStar Silicones) per subministrar mostres de diferents olis. Gràcies també al Manel per descobrir-nos la microscòpia confocal de reflexió. Gràcies al grup de X. Trepal (PCB), en especial al Raimon, per ajudar-nos amb el cultiu de cèl·lules sobre cristalls líquids. Agrair també als òptics, Raúl, Estela i Mario l'oportunitat de realitzar mesures de l'elasticitat del nostre material. Per últim, gràcies també a la Professora J. Martínez (Facultat de biologia) i al seu grup pel cultiu de *Bacillus Subtilis*.

I would like to thank all my fellow labmates, with whom we have shared lots of hours and funny moments. Als primers compis, Sergi i Alba, gràcies per ajudar-me a començar i ensenyar-me com anava tot. Gràcies a en Marc pels seus ànims i el seu bon humor. A en Pepet Maria, ja com un germà gran, per fer-m'ho passar de conya al lab i a Montserrat, tot i baixar un pelet el meu rendiment. També gràcies a la Berta per revolucionar el galliner, al Jerome per el seu *savoir faire* i les classes (breus) de francès, i al Mohammad per deixar d'utilitzar els meus pòsters per les seves pregàries. Mil gràcies als orgànics pel nitrogen que us pispo de tant en tant. En especial gràcies a l'Omar, per ser-hi durant tots aquests anys i donar-me suport i bons consells. Gràcies a en Tomeu, per donar-nos la tranquil·litat illenca que tan ens manca a vegades. A en Clément per les *fondues*, els vinets i els mentolats, al Lewis, for your black humor, i a l'Albert, pel seu bon rotllo i la seva divertida manera de gaster-se la pasta. Gràcies a tots, de tot cor, per ser el meu pa de cada dia durant tot aquest temps, per tots els moments genials que hem passat junts, converses de tots colors, birres de divendres i farres posteriors.



---

During conferences, courses and a summer school I have had the opportunity to discover new places and, more importantly, to know really nice people, with whom we have had fruitful discussions and unforgettable moments. Especially, thanks to Arthur, best roommate I could have ever had in Varena, and Marko and Milos as part of the night crew.

Out of the university, I have always had the best possible company. Thanks to my best (some of them very old) friends for being there at any time. Gràcies Roger per ser-hi cada dia des de fa més de dues dècades, i per preocupar-te per si vindré a sopar... Gràcies també per organitzar les seccions d'aquesta tesi. Gràcies Sara per fer-me ballar, pel teu suport incondicional, i per voler saber sobre cristalls líquids. Gràcies als naps, en especial al Roger, Ricard i David, per fer-m'ho passar tant bé durant tants anys. Gràcies també Meri, Carlota, Clàudia, Júlia, i Marta, per ser-hi des de fa tant temps. Gràcies també a tots els meus compis de pis, Sergi, Robert, Roger, Àlex i Sintes, que no netegen massa però són molt macos. Finalment, a tu Cristina, gràcies per totes les coses bones que hem passat i passem junts. Gràcies pel suport que m'has donat durant tots aquests anys i especialment aquests últims mesos... Ara et toca a tu, i espero estar, com a mínim, a la teva alçada, espero que no a massa distància. T0, ja ho saps.

Last but not the least, I would like to thank my family for supporting me throughout all these years, during the writing of this thesis, and during my life in general. A la Mariona, gràcies per la classes de fa uns anys i per ser la meva doctora de seguiment particular. Gràcies també al Jordi, a la Lali, a la Caterina i a l'Agnès per deixar-me explicar. I especialment a vosaltres, pare i mare, moltes gràcies per fer-me, per animar-me a estudiar i per recolzar-me en tot, en tot moment. Pare, moltes gràcies per la teva tranquil·litat, per la teva pintura i per la meva portada. Mare, gràcies per la teva empenta i energia. Gràcies també per trucar per saber com em va i si menjo bé. Gràcies als dos per l'interès que sempre heu mostrat en el que he anat fent al laboratori tot i que, comprensiblement, mai ho heu volgut acabar d'entendre. Marc, gràcies a tu també per aguantar-me tots aquests anys. Us estimo.

Pau  
April 2017

